TECHNISCHE UNIVERSITÄT WIEN

Dissertation

Process Simulation for Laser-Assisted Additive Manufacturing

carried out for the purpose of obtaining the degree of Doctor technicae (Dr.techn.), submitted at TU Wien, **Faculty of Mechanical and Industrial Engineering**,

by

Dipl.-Ing. Constantin Zenz, BSc.

Mat.No.: 01227264

under the supervision of

Univ.Prof. Dipl.-Phys. Dr.-Ing. Andreas Otto
Institute of Production Engineering and Photonic Technologies, TU Wien

reviewed by

Univ.-Prof. Dr.-Ing. habil. Jean Pierre Bergmann
Department of Mechanical Engineering, Technische Universität Ilmenau

and

Prof. Frank Pfefferkorn, PhD
Department of Mechanical Engineering, University of Wisconsin-Madison

Chair of the Examination Board

Univ.Prof.in Dr.-Ing.in Stefanie Elgeti
Institute of Lightweight Design and Structural Biomechanics, TU Wien

Wien, 17.04.2026

Constantin Zenz

Andreas Otto

This work has been funded by the TU Wien Doctoral School within the Doctoral College "DigiPhot" and by the European Union's Horizon 2020 research and innovation programme within the project CUSTODIAN, under grant agreement number 825103.

I acknowledge, that I am only entitled to print my work under the title **Dissertation** with the approval of the examination board.

Affidavit

I declare in lieu of oath, that I wrote this thesis and carried out the associated research myself, using only the literature cited in this volume. If text passages from sources are used literally, they are marked as such.

I confirm that this work is original and has not been submitted for examination elsewhere, nor is it currently under consideration for a thesis elsewhere.

I acknowledge that the submitted work will be checked electronically-technically using suitable and state-of-the-art means (plagiarism detection software). On the one hand, this ensures that the submitted work was prepared according to the high-quality standards within the applicable rules to ensure good scientific practice "Code of Conduct" at the TU Wien. On the other hand, a comparison with other student theses avoids violations of my personal copyright.

Wien, 17.04.2026

Constantin Zenz

Acknowledgements

First and foremost, I want to thank my advisor and mentor, Prof. Dr. Andreas Otto, for providing the opportunity of pursuing this work, and for his constant support and trust. I am grateful for the many deep scientific discussions, for giving me the freedom to pursue my own ideas, and for teaching me to always think outside the box and to dare giving unconventional ideas a chance.

I want to thank Prof. Dr. Jean Pierre Bergmann and Prof. Dr. Frank Pfefferkorn for reviewing this thesis and I want to thank Prof.in Dr.in Stefanie Elgeti for chairing the Examination Board.

Furthermore, I want to thank Rodrigo Gómez Vázquez, for his mentorship and support. His dedicated, hard work provided the foundation for many of the concepts developed and examined in this thesis. Also, I want to deeply thank my "academic siblings" Michele Buttazzoni and Tobias Florian, for countless hours of discussions about crazy and not-so-crazy scientific ideas and tricky C++ programming problems. Their daily feedback and insight on my ideas and problems was invaluable.

I am very grateful for all the hard and dedicated work of my colleagues and co-authors. Very special thanks go to Dr. Salem Mosbah, for the countless early mornings of online-live-coding sessions and his patience with my moderate programming skills, and to Dr. Peter Cook for an endless number of interesting and very fruitful discussions despite the enormous time difference between Melbourne and Vienna.

The Research Group for Process Simulation, where I conducted my research, is a truly supportive and collaborative environment, mainly owing to all the great people who work (or have worked) there. I want to thank all my colleagues and friends at the group for their continued support and for making the last couple of years fun. Here, I want to especially thank Dr. Robert Bielak, Katherine Crespo, Carlos Durán and Laszlo Vörös.

I am deeply grateful towards my parents, Bettina and Peter, for their unconditional support throughout my entire life, and towards my sisters, Anna and Theresa, for their lifelong encouragement.

Lastly, I want to thank Lena, the love of my life, for always being there for me.

"All models are wrong, but some are useful."

George E. P. Box

"Academic time conversion requires you to multiply by two and then go up one order of magnitude. That is, in academic research anything you think will take you two hours will realistically take four days. Planning to finish a task in one week? That will be two months!"

(freely adapted from) Rodrigo Gómez Vázquez

Contents

Abstract

Physics-based simulation models for laser-based additive manufacturing processes become increasingly important due to the high complexity of the underlying coupled physical phenomena and the large (and increasing) number of tunable process parameters and materials of interest for applications. To gain understanding of the underlying coupled multiphysical problem, the onset of defects, and the consequence of process parameter settings, material choice and their interaction, simulation models with high predictive capabilities are essential.

For this purpose, a high fidelity, physics-based simulation model for the prediction of laser-based manufacturing processes was developed, including process-specific model additions that enable the simulation of the most widespread metal additive manufacturing process, laser-based powder bed fusion. Starting from the basic principles of conservation of mass, momentum and energy, a multiphysical framework for the simulation of laser-based material processing at the scale of the melt pool is developed and validated against experimental results for different processing conditions and materials. The simulation framework is then further expanded by incorporating process-relevant features such as non-equilibrium solidification, multi-layer recoating in powder bed fusion, weakly coupled solid mechanics and grain envelope tracking. Furthermore, the model's ability to predict liquid film cavitation within the mushy zone during solidification is turned into a new metric for hot crack susceptibility and validated.

The simulation model is applied to reduce crack susceptibility of non-weldable nickel-based alloys in an application-oriented study. This is achieved via introduction of a secondary, low-intensity laser beam aiming at a cooling rate reduction.

The predictive capabilities of the here-developed model are shown to outperform the previous state of the art due to increased coupling between condensed and gaseous matter, especially during laser-induced evaporation and condensation events.

Building and extensively validating a high-fidelity simulation framework that does not need empirical calibration, and incorporating multiphysical and multiscale aspects inherent to AM processes, this thesis presents important groundwork on the way towards digital process twins for laser-based additive manufacturing.

Kurzfassung

Physik-basierte Simulationsmodelle für lasergestützte additive Fertigungsprozesse gewinnen zunehmend an Bedeutung. Dies ist auf die hohe Komplexität der zugrunde liegenden, gekoppelten physikalischen Phänomene, und die große (und wachsende) Anzahl einstellbarer Prozessparameter und anwendungsrelevanter Materialien zurückzuführen. Um ein Verständnis für die zugrunde liegenden physikalischen Phänomene, die Entstehung von Defekten und die Auswirkungen von Prozessparametereinstellungen, Materialauswahl und deren Wechselwirkungen zu erlangen, sind Simulationsmodelle mit hoher Vorhersagekraft notwendig.

Zu diesem Zweck wurde ein physik-basiertes Simulationsmodell zur Vorhersage laserbasierter Fertigungsprozesse entwickelt, einschließlich prozessspezifischer Modellergänzungen, welche die Simulation des am weitesten verbreiteten additiven Fertigungsverfahrens für Metalle, dem pulverbettbasierten Laserstrahlschmelzen, ermöglichen. Ausgehend von den Grundprinzipien der Masse-, Impuls- und Energieerhaltung wird ein multiphysikalisches Modell für die Simulation der lasergestützten Fertigung auf Skala des Schmelzebads entwickelt und gegenüber experimentellen Ergebnissen für verschiedene Bearbeitungsbedingungen und Materialien validiert. Das Modell wird durch die Einbeziehung prozessrelevanter Merkmale wie Nichtgleichgewichtserstarrung, Pulverschichtauftrag beim Pulverbettschmelzen, schwach gekoppelte Festkörpermechanik und Kornwachstum weiter ausgebaut. Darüber hinaus wird aus der Fähigkeit des Modells, die Kavitation des Flüssigkeitsfilms innerhalb der Mushy Zone während der Erstarrung vorherzusagen, ein Modell für die Wahrscheinlichkeit für Heißriss-Initiierung konzipiert und validiert.

Das Simulationsmodell wird in einer anwendungsorientierten Studie eingesetzt, um die Rissanfälligkeit von nicht schweißbaren Nickelbasislegierungen zu verringern. Dies wird durch die Einführung eines sekundären Laserstrahls mit geringer Intensität erreicht, der auf eine Verringerung der Abkühlungsgeschwindigkeit abzielt.

Die Vorhersagefähigkeiten des hier entwickelten Modells übertreffen nachweislich den bisherigen Stand der Technik. Der Grund dafür liegt vorwiegend in der erhöhten Kopplung zwischen kondensierter und gasförmiger Materie, insbesondere während laserinduzierter Verdampfungs- und Kondensationsvorgänge.

Diese Arbeit entwickelt und validiert ein hochpräzises Simulationsmodell, das keine empirische Kalibrierung erfordert und Multiphysik- und Multiskalen-Aspekte von additiven Fertigungsprozessen miteinbezieht. Diese Grundlagen sind ein wichtiger Schritt auf dem Weg zur Entwicklung digitaler Prozesszwillinge für die laserbasierte additive Fertigung.

1 Introduction

Additive manufacturing (AM) is a manufacturing technique that allows for the fabrication of near net-shape parts directly from a three-dimensional model, enabling unlimited complexity in geometrical designs and simplified assembly designs with lower part count. Furthermore, part customization can be achieved with virtually no additional effort or steps and concepts such as manufacturing-on-demand, mass-customization and decentralized production are enabled through the adoption of AM [1]. Another advantage often associated with AM is the reduction of material waste, as material is only added where needed, as opposed to subtractive manufacturing processes such as milling or turning [2], although in practice, especially powder-based AM processes raise questions of powder reusability and performance of parts fabricated with reused powder [3]. With respect to AM of metallic materials, the two main types of processes currently in use are various forms of Powder Bed Fusion (PBF) and Direct Energy Deposition (DED). In the former method, metal powder is fused selectively using either a laser or electron beam in a layer-wise fashion, with the build platform being lowered and a new powder layer being added after the processing of each layer. In DED, the material to be added is delivered directly towards a heat source (electric arc, laser or electron beam) in the form of wire or powder, melted and hence added to the part [2]. The aforementioned advantages of AM have led to its adoption across many industries, especially aerospace, automotive, energy and medical industries [1] and the global metal AM market grew by 875% between 2013 and 2018 [4]. With a global market size of USD 20.51 billion as of 2023, and a projected growth to more than USD 80 billion by 2030 [5], AM technologies have long surpassed the stage of being a tool for rapid prototyping and are becoming increasingly important in production.

Focusing on laser-based AM of metals, the two main processes (laser-based direct energy deposition, DED-LB and laser-based powder bed fusion of metals, PBF-LB/M) share many similarities in their underlying physical principles: A focused, high-energy laser beam is used as heat source, selectively melting (and often even partially vaporizing) both the newly added material (which is present in the form of a powder bed in PBF-LB/M or directly delivered to the laser-material interaction zone in the form of powder or wire in the case of DED-LB) and the previously deposited material. Upon solidification, the material fuses to form the desired part geometry. The target part shape is divided into two-dimensional scan trajectories, to be completed layer-by-layer in the third (usually vertical) dimension. Many of the underlying process characteristics and physical phenomena are identical to those encountered in laser beam welding (LBW). Essentially, wire-based DED-LB can be seen as a long, continuous LBW process with a filler wire. Furthermore, in academic studies, fundamental insights into process behavior of PBF-LB/M are often gained through so-called bare-plate experiments, i.e., scans on a bare metal plate not involving powder; on the other hand, fundamental research on LBW processes is mostly performed experimentally through so-called bead-on-plate welds. Both of these configurations are virtually identical, highlighting the similarities and common process fundamentals shared between PBF-LB/M and LBW.

The underlying physical phenomena in any laser-based manufacturing process

pose a coupled multiphysical problem, which makes it challenging to predict and control these processes. Consequently, laser-based manufacturing processes are often prone to lead to defects such as spatter, porosity, lack of fusion, surface irregularities, part distortion or cracking, to name just a few. Additionally, parts built via AM often exhibit a strong anisotropy of mechanical properties [6]. Mostly, these defects are not due to stochastic uncertainties beyond our control but a direct consequence of the deterministic (but chaotic) nature of the process. When considering PBF-LB/M in particular, another challenge is added to the multiphysical problem: the multi-scale aspect of the process [7]. Phenomena that occur on time and length scales of the order of the melt pool (and well below) can lead to failures at scales of the entire printed part. When considering an entire PBF-LB/M process, relevant timescales range from the (sub-)microsecond regime (laser-material interaction, smallest fluid dynamical time scales) up to multiple hours (build time of a part). Similarly, relevant length scales cover many orders of magnitude, ranging from metallurgical length scales in the (sub-)micrometer regime up to tens of centimeters (printed part dimensions). While the multiphysical and multi-scale aspect of the process leads to challenges in modeling, prediction and optimization of PBF-LB/M processes [7], another key aspect poses both a challenge and an opportunity: the large number of tuneable parameters in PBF-LB/M. Typical parameters to be selected include laser power, spot size, scan velocity, powder layer height, hatching distance, scanning trajectory within each layer and scan strategy across multiple layers, to name merely a few [8–12]. Due to the high dimensionality of this parameter space, parameter sets are in practice often found through "trial-and-error" [7, 13]. Within recent years, the advent of "beam shaping" extended the parameter space of the laser intensity distribution from a single number (the spot size) to its own high-dimensional parameter space. Beam shaping refers to the possibility of choosing arbitrary spatial laser intensity distributions ("static beam shaping", cf. [14] for an example) and even modulating these arbitrarily over time ("dynamic beam shaping", cf. [15] for an example). Hence, both gaining a thorough understanding of underlying cause-effect relationships between chosen process parameters, the resulting process characteristics and the finally obtained part properties, and being able to predict process results without the need for large experimental campaigns are becoming increasingly important. Physics-based simulations are a powerful tool for this purpose, complementing experimental investigations as they allow for the resolution of phenomena that are experimentally difficult or even impossible to observe, or to conduct simulative experiments under idealized conditions, isolating the contribution of individual phenomena to a process [16]. In early phases of process development, physics-based simulations with high predictive power can even substitute experimental campaigns, saving time and cost.

Figure 1 exemplarily shows a top view of a single PBF-LB/M scan track, simulated using the simulation model developed throughout this thesis. Powder particles of an aluminum alloy are melted (red–yellow–white color map shows liquid metal colored by temperature) to form a continuous solid geometry upon solidification. In the front of the melt pool, a narrow and deep vapor depression (a *keyhole*) can be seen. This capillary is held open by the newly evaporated material's recoil pressure acting upon the liquid in the region where the focused laser beam is currently irradiating the

material. Many thousands of such scan tracks, performed over the course of hundreds of layers of powder typically make up a PBF-LB/M process. A schematic illustration of an entire PBF-LB/M process is provided in Figure 2.

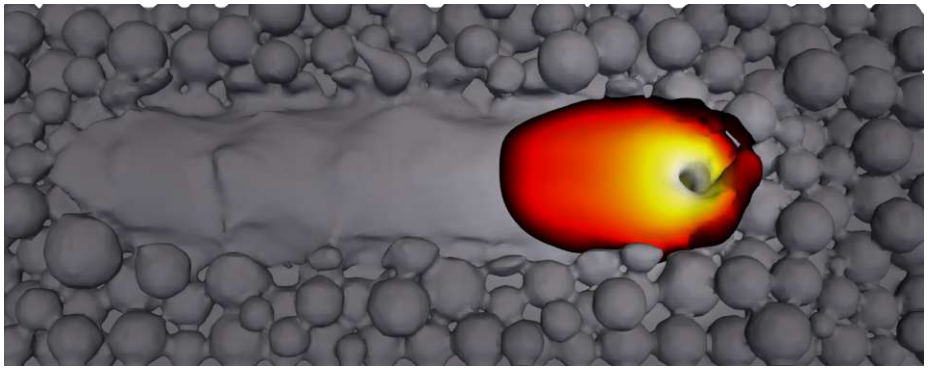

Figure 1: Simulation (using the model developed throughout this work) of a single scan track of PBF-LB/M of an aluminum alloy, featuring a keyhole (vapor depression formed through evaporative recoil pressure) in the front of the melt pool. Individual powder particles are resolved within the continuum domain, which are molten and hence added to the melt pool, colored by temperature in red–yellow. The single melt track depicted here represents the fundamental "building block" of a PBF-LB/M process, with multiple of these performed per layer, and many layers being processed to build an entire part.

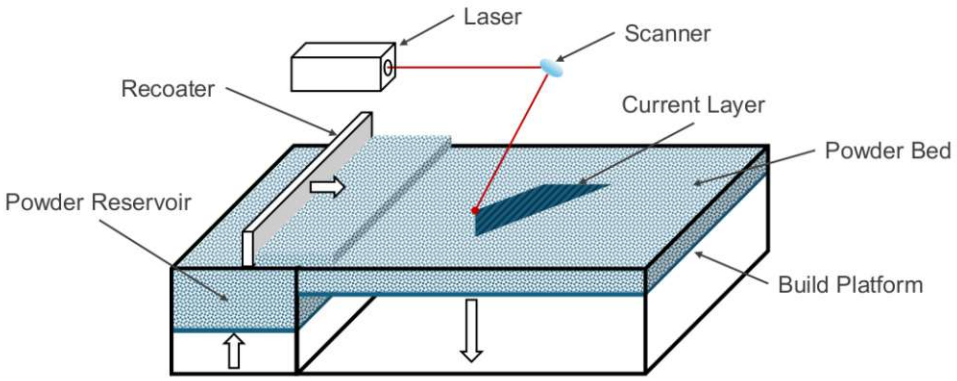

Figure 2: Schematic illustration of a PBF-LB/M process. The build platform is lowered, a layer of powder is evenly spread across the build platform by a recoater, and the laser beam selectively melts the respective quasi-2D slice of the to-be-built part. Then, the process is repeated for the next layer.

1.1 Problem

When modeling PBF-LB/M, a number of simplifications and assumptions is usually employed. One of the most common simplifications employed in virtually all studies, even at very small scales of the melt pool and keyhole is the omission of gaseous phases, employing phenomenological models to account for the effect of gaseous matter on condensed phases, especially with respect to evaporation, condensation and the resulting thermo-fluid-mechanical phenomena [17]. When going from the scale of the melt pool towards multiple layers of a PBF-LB/M process, models are often further reduced to a mere problem of heat conduction [18, 19]. However, such assumptions subsequently require careful model calibration to still yield correct results, reducing the model's predictive capabilities. Furthermore, a re-calibration can be necessary when using the same model to simulate slightly altered processing conditions. One example for such a calibration is elaborated in [20], where a coefficient in the phenomenological equation for evaporation-induced recoil was fitted to reproduce experimentally obtained results, requiring a different coefficient value for different laser beam shapes. Obviously, tasks like finding a suitable beam shape to improve a process through simulations are not possible in such a case. Similarly, in [21], this coefficient is fitted to different values for different materials to reproduce experiments.

Investigations of Shu et al. [22] showed that even for low-intensity laser melting in pure conduction mode (shallow melt pool without generation of a keyhole), computational models ignoring convective heat transport yield inaccurate three-dimensional melt pool shapes and thermal histories. Even if such models are calibrated to yield correct two-dimensional melt pool shapes (e.g., by reproducing the shape revealed by etching experimentally generated cross-sections of the weld bead, which is a commonly employed model calibration and validation method), they do not predict the correct three-dimensional shape and spatiotemporal temperature profile. However, these are essential for predicting part properties such as microstructure, residual stresses or crack susceptibility. In practice, AM via laser-based powder bed fusion (PBF-LB/M) is performed within process windows where not only melt pool convection plays a non-negligible role, but even evaporation and the associated generation of a vapor depression or keyhole becomes relevant, with a significant vapor depression being present even in low depth-to-width ratio melt pools [23]. These points highlight the complexity of the underlying multiphysical problem, even for the "moderate" conditions encountered in PBF-LB/M (compared to more "extreme" processes, such as deep penetration LBW).

Another problem is posed by the fact that many alloys of industrial interest for AM applications are classified as non-weldable due to their high susceptibility to hot cracking under the extreme cooling rates present in laser-based manufacturing. In this context, non-weldability can be seen as non-printability in PBF-LB/M processes [24]. Examples are many Nickel-based superalloys [25] or high strength aluminium alloys [26]. Simulation tools are needed to understand the role of process parameters and material composition in the onset of hot cracks, to optimize processes and subsequently enable crack-free additive manufacturing of such materials.

Looking at ongoing and future developments of laser-based material processing beyond the above-described emergence of beam shaping, concepts like hybrid additive-subtractive manufacturing with continuous wave lasers and picosecond-long

laser pulses as demonstrated by Holder et al. [27] to overcome spatial resolution and surface finish issues present in PBF-LB/M underline the growing need for universal simulation models capable of accurately predicting process phenomena across historically distinct regimes (such as, in this case, processing with continuous wave or short pulsed laser energy).

Consequently, a need for physics-based simulation models with high predictive capabilities can be identified, which should advance the state of the art, especially in terms of handling phase transitions and the resulting sources of heat, mass and momentum, challenging the long-standing norm of employing calibrated, phenomenological sub-models instead. Furthermore, with respect to PBF-LB/M in particular, additional challenges are present due to the multiphysical and multiscale aspects specific to this process. These include the need for accurate large-scale models (encompassing multiple scan tracks and printing layers), while still featuring all relevant physical phenomena and not relying on calibration towards specific process windows. Also, to bridge the knowledge gap between process behavior and resulting part properties, it is necessary to address physical phenomena such as (but not limited to) non-equilibrium solidification, crystallographic grain growth, residual stresses, or hot crack initiation, in addition to the thermo-fluid-mechanical problem commonly considered in modeling of laser-based manufacturing at and around the scale of the melt pool.

1.2 Objectives

Based on the above-described set of challenges encountered today and expected in the future, the objective of this work is to advance the state of the art in physics-based simulation of laser material processing, and particularly AM via PBF-LB/M as follows.

A physically and mathematically consistent, universal, interface-resolved multi-phase simulation framework for laser-based manufacturing processes shall be developed. For this purpose, the idea of directly tracking the evolution of mass and energy of a set of compressible fluids initially conceptualized and developed by Otto et al. [28–30], shall be formulated into a consistent mathematical and numerical framework, and validated through suitable test cases of increasing complexity. The aim of the tests is to both ensure the consistency and accuracy of the numerical framework (by comparing simulation results to analytical solutions or those of reference numerical solvers) and that of the physical model (by comparing simulation results to experimental data). The focus of the application-oriented testing on real-world data is on assessing the model's predictive capabilities, aiming at a universal model that does not need application-specific calibration steps.

The thus developed model shall be benchmarked and systematically compared against a commonly used state of the art solver for an AM case. At this opportunity, the model's capabilities of resolving evaporation and condensation and coupling evaporation rates with local pressure on the vapor side shall be leveraged to analyze and gain a deeper understanding of the physical phenomena leading to instabilities of a thermocapillary, and hence the generation of a stable or unstable keyhole in laser-based AM. New insights on the coupling between vapor-sided pressure, evaporation and condensation rates and dynamic keyhole morphology evolution shall be obtained, which are only possible through the here-developed model.

Then, a series of extensions to the simulation model shall be implemented which aim at increasing the model's ability to specifically predict the process of PBF-LB/M (or rather, the underlying physics). For this purpose, multi-track and multi-layer simulations without a reduction in the included physical phenomena shall be developed, to allow the prediction of accurate thermal histories (including events such as vaporization) at scales of individual sub-geometries of a printed part, such as a thin wall. Furthermore, solidification of an alloy across a temperature range shall be implemented for non-equilibrium conditions relevant to the extremely high cooling rates encountered in laser-material processing. Additional extensions to be implemented in the model are weakly coupled solid-body thermomechanics and tracking of crystallographic grain growth, to advance the model's capabilities of predicting part properties directly from simulated process conditions.

Finally, the important issue of solidification cracking (also termed hot cracking), which poses a complex multiphysical problem encompassing fluid-, thermo- and solid-body mechanical, and metallurgical aspects, shall be addressed. For this purpose, a new model for the prediction of hot crack susceptibility that can be recovered by leveraging the here-developed model without the need for empirical calibration parameters shall be derived and implemented.

By addressing all objectives laid out here, we shall arrive at the foundation for a comprehensive physics-based simulation framework of laser-assisted additive man-

ufacturing, that can be used both for gaining deep understanding of process fundamentals and for solving complex real-world tasks of solving defects and optimizing processes.

1.3 Methodology

The main objective of this work is the development of new simulation models and approaches. To achieve this, the methodology mainly followed throughout the work consists of working with test cases of different levels of complexity. These cases should either address a very specific, isolated subdomain of the full multiphysical problem, or the entire coupled multiphysical problem. Hence, there are two broad types of test cases used throughout this work:

- Simple, analytically solvable physical problems and entirely constructed ("made up") cases, termed *type 1*

- Real-world cases of high multiphysical complexity, with (ideally) detailed and quantified experimental results that were obtained under well-documented conditions, termed *type 2*

The aim of the first class of test cases is to assess mainly the correctness of individual physical sub-models, and especially their algorithmic and numerical implementation within the entire simulation framework. Illustrative examples of such a cases are the one-dimensional one- and two-phase shock tube scenarios used in Publication 1. These cases possess an analytical solution, and can hence be used for assessing the accuracy of a simulation model. However, the analytical solution is not that of a real physical experiment, but that of the underlying mathematical equations. The aim is therefore, to implement the same physical model equations (e.g., the ideal gas and Tait equation as equations of state for gaseous and condensed phases, respectively) and then assess whether the implementation (both from an overall solution algorithm standpoint and in terms of numerically solving the respective equations) is sound. Therefore, if the simulation model's prediction matches the analytical solution of the two-phase shock tube, we have shown that, e.g., the implementation of the chosen equations of state, the advection of different phases and their sharp interface in highly compressible scenarios, the coupling of velocity, pressure, temperature, etc. is accurately implemented. Another example of such a test case is the usage of temperature–solid fraction curves predicted by solving a one-dimensional Stefan Problem, and comparing them to the predictions of state-of-the-art software for such calculations to validate correct handling of non-equilibrium solidification of an alloy in Publication 4. Here, the conceptual algorithmic implementation of phase changes, and the implementation of a given non-equilibrium phase change model were assessed. However, none of these results tells us much about the predictive capabilities of the multiphysical model (as we have implemented the same equations as the underlying analytical models). Illustratively, the latter test case shows that the model correctly predicts solidification behavior as expected from a Gulliver-Scheil model, but does not address the question of whether the Gulliver-Scheil model accurately predicts physical reality during laser-assisted manufacturing.

The second class of test cases assesses the model's predictive capabilities, not in the sense of its numerical accuracy or algorithmic implementation, but rather testing whether the coupled multiphysical *model* accurately mirrors the *real* multiphysical problem encountered in nature (i.e., in the laboratory or during a manufacturing

process). Therefore, such problems should ideally cover a range of conditions (e.g., different laser intensities, different materials) to verify that the model is not over-fit, for example to a certain process regime or material. Examples of such cases are the stationary illumination of a titanium alloy sample under different laser intensities and high power welding of copper in Publication 1. These two cases span two very different materials and a broad range of laser intensities: While titanium has a very low thermal conductivity and relatively low reflectivity of light at the chosen wavelength, copper is highly reflective and its thermal conductivity is higher by approx. two orders of magnitude. Furthermore, the chosen laser intensities differ by an order of magnitude (between cases) and are also varied within one case. To possess true predictive capabilities, the model should not need any process- or material-specific fitting parameters to yield correct results. It should only require the correct setting of initial and boundary conditions, process conditions (such as the laser parameters) and the material properties of a certain material. While the material properties can per se be seen as a part of the model and the accuracy of simulation results depends strongly on scarce and difficult-to-measure material properties, they should not be varied once set. This means, for a given material, different simulations under different process parameters must be conducted with the same material properties to use the model as a predictive tool.

At the beginning of this work, new methods were developed and implemented to accurately model compressible multiphase flows undergoing phase change. Here, several well-known fluid mechanical benchmark cases of type 1 were simulated during model development. The results of some of these benchmarks ended up in publications of this work, such as the single-phase and two-phase shock tube in Publication 1. Examples of other fluid-mechanical test cases that were extensively used to assess aspects of the numerical solution algorithms developed in Publication 1 were the well-known dam break case, advection of a disk in a prescribed velocity field or a so-called depth charge (evolution of a high-pressure gas bubble within a liquid). However, they did not end up in the publications for reasons of brevity and conciseness. Furthermore, across all developments and tests undertaken in this work, conservation of mass and energy was always precisely monitored to ensure the model's inherent traits of being mass- and energy conservative are not violated through the algorithmic or numerical implementation. Other uses of type 1 cases were to iteratively test different implementations of the numerical solution algorithm, to assess numerical stability and also physical stability (coupling of individual sub-problems of the multiphysical problem) with respect to large time steps, as a key requirement towards the model was that large Courant Numbers of ≈ 1 can be used. Other numerical aspects where simple (often made-up) type 1 cases were used include parallelization and adaptive mesh refinement (topics that are usually "hidden" from the reader in final publications once they work seamlessly, but requiring much attention during model development). These aspects of adaptive mesh refinement, workload parallelization on many CPUs and load balancing between CPUs during re-meshing are especially crucial for the efficient simulation of PBF-LB/M due to its multiscale nature: Throughout the simulation of many tracks and layers of a part, fine spatial resolution is needed only in a small fraction of the entire computational domain at any given time, with the location of this highly dynamic zone changing constantly

throughout the simulation. An example of the dynamically refined mesh used in a multilayer simulation of PBF-LB/M is shown in Figure 3. An example of highly-specific, entirely made up type 1 cases is the artificial two-dimensional test structure used for the continuum powder recoating model presented in Publication 4, which was used to asses suitable parameter values and numerical approaches to efficiently solve the underlying equation.

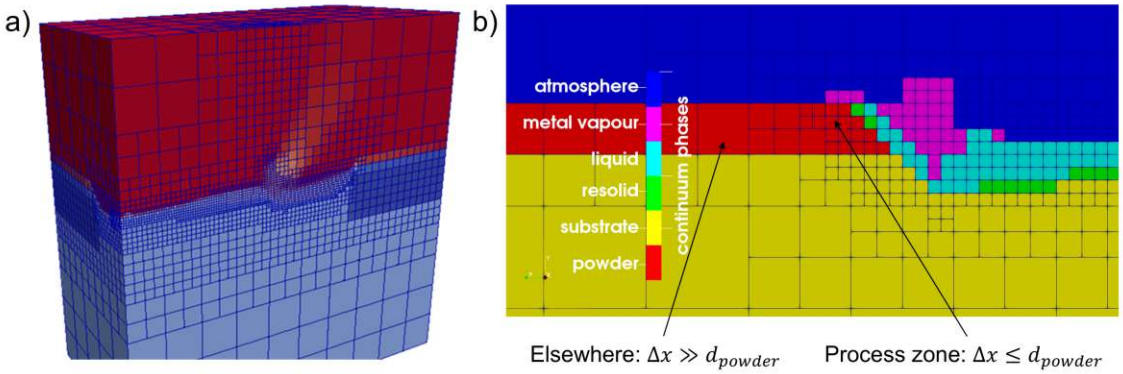

Figure 3: Exemplary computational mesh used during a multilayer PBF-LB/M simulation: a) Cut through domain during processing, showing mesh colored by the primarily present phase (red: ambient gas, dark blue: metal powder, light blue: solid bulk metal, beige tones: liquid and gaseous metal); b) close-up two-dimensional view of exemplary mesh during processing of the first layer of a PBF-LB/M process (scanning from right to left).[1]

After gaining confidence in each of the specific sub-models and the numerical solution algorithm employed in the simulation framework, predictive capabilities of the multiphysical model were assessed by comparing to experimental data for type 2 cases. Here, high-speed in situ synchrotron x-ray imaging has emerged as a valuable technique to obtain information of the dynamic behavior of the process within the material, which is not observable with conventional sensors or high speed cameras [31]. A particularly important set of experiments was the stationary illumination experiments performed by Cunningham et al. [23], as these feature process conditions and a material highly relevant to PBF-LB/M, but in a simplified setting lacking powder and without relative movement between laser and material. Furthermore, the usage of different laser spot sizes and powers made it possible to assess predictive capabilities, as the same model setup (mesh, material properties, boundary and initial conditions) could be used to simulate different processes. While only the results of two of these parameter combinations ended up in publications, many more were initially tested and it became obvious, that if one of the experiments is precisely matched, the others are also well reproduced, highlighting the model's predictive capabilities. Going to processes with even higher dynamics, deep penetration welding of pure copper was chosen as a further type 2 case as the material (due to its low absorptivity of infrared wavelengths and its high thermal conductivity) typically yields a highly unstable process with many chaotic events. As the dynamicity of deep penetration copper

[1]Images from C. Zenz et al.: Multi-Scale Simulation of Laser-Based Powder Bed Fusion Using a Continuum Mechanics Approach. 9th GACM Colloquium on Computational Mechanics, 09/2022, Essen, Germany.

welding surpasses that of most scenarios typically encountered in PBF-LB/M, this was seen as a good representative of an "extreme" test case. Furthermore, the overarching goal always remained to simulate laser-material processing in general, with the model predicting an unstable deep penetration welding process if such should also arise in reality under the given conditions. While these tests provide us with a high level of confidence in the model itself, there is always some level of uncertainty in any given application with respect to material properties or achievable spatial resolution (within reasonable computational times). Publication 2 shows a typical validation step undertaken in an application-oriented investigation, where experimental in-situ observation is unfeasible, but the model uncertainty in terms of not fully known material parameters, the continuum powder model (modeling powder particles as a continuum with average properties) and spatial discretization need to be assessed. Here, ex-situ measurements of the weld bead size and shape experimentally obtained through analyzing cross sections of samples were compared to the predictions from the simulation model. Also, the prediction of a dynamic event could be verified ex-situ by correctly simulating the occurrence of the so-called balling defect.

In Publication 5 and Publication 6, the methodology of implementing model aspects trough working with type 1 cases of increasing complexity, each aiming at the assessment of an individual physical or numerical sub-problem, culminating in complex, real-world type 2 scenarios was again repeated.

On a technical level, the simulation methods developed herein are of the category of continuum mechanical models, where coupled partial differential equations are formulated in the form of conservation equations and then solved using the Finite Volume method. Throughout this work, the developed models are implemented using the open source C++ Finite Volume library `OpenFOAM` [32]. Post-processing of simulation results is mainly done using the software `ParaView` [33].

1.4 Synopsis

The publications included in Chapter 2 are building upon and complementing each other in the following way:

Publication 1 establishes a basis in the form of a universally applicable simulation model for laser-based manufacturing with continuous wave lasers. Publications 2 and 3 present application case studies, where the model is used to gain application-oriented knowledge and solve engineering challenges at different scales. Publications 4 and 5 expand the universal model by adding features that are relevant to specific physical sub-problems or process-specific aspects relevant to AM and PBF-LB/M in particular. Publication 6 critically analyses the model's capabilities, puts them in relation to the previous state of the art and uses the model to gain knowledge of fundamental physical phenomena of AM at the melt pool scale.

Below, the papers are summarized briefly. Some Figures are reproduced here solely for illustrative purposes to support intuition for more abstract concepts discussed in the text and should not be interpreted as presenting key findings or conclusions.

Publication 1

In Publication 1, a universal simulation framework is derived and validated, with the aim of predicting various laser-material-processing scenarios, with emphasis on (but not limited to) continuous wave laser processes such as additive manufacturing and welding. To allow for high predictive capabilities and applicability across the broad range covered by modern laser-based manufacturing, the number of process-specific assumptions is aimed at a minimum.

Starting from the basic principles of conservation of mass, momentum and energy, a homogeneous equilibrium mixture formulation is used to model the behavior of an arbitrary number of phases. This means, all phases locally share a common velocity, pressure and temperature. In contrast to the widely used Volume-of-Fluid method, where volume fractions of individual phases are tracked to calculate the mixture density and energy (a step only strictly conservative for incompressible phases), the Mass-of-Fluid (MoF) method is introduced. Herein, the evolution of mass and energy of each individual phase are directly modeled through conservation equations, leading to an inherently mass and energy conservative framework even in highly compressible scenarios or those involving phase change. Figure 4 illustrates some key elements of the Mass-of-Fluid method at the example of an exemplary phase change event. Considering two phases j and k with local phase-specific mass densities ρ_j and ρ_k, exchanging some amount of mass $S_{M,j} = -S_{M,k}$ via a phase change process, we will end up with either of two states, compression or expansion. These are characterized by a value greater or less than one for "naively" calculated volume fractions via each phase's material density $\langle\rho\rangle_i$ (i.e., the temperature-dependent, but otherwise constant, material parameter), cf. Figure 4c. In the general case of different bulk moduli $K_j \neq K_k$, the true new composition of volume fractions established after the phase change event needs to be numerically determined in a process termed phase-norming within Publication 1. Herein, a bisection method is used to calculate a pressure difference Δp which will lead to all phases' volume fractions summing to

one, which is needed to calculate material properties of the mixture from individual phases' properties, or to keep track of the topological evolution of phase interfaces (needed, e.g., to calculate surface tension forces).

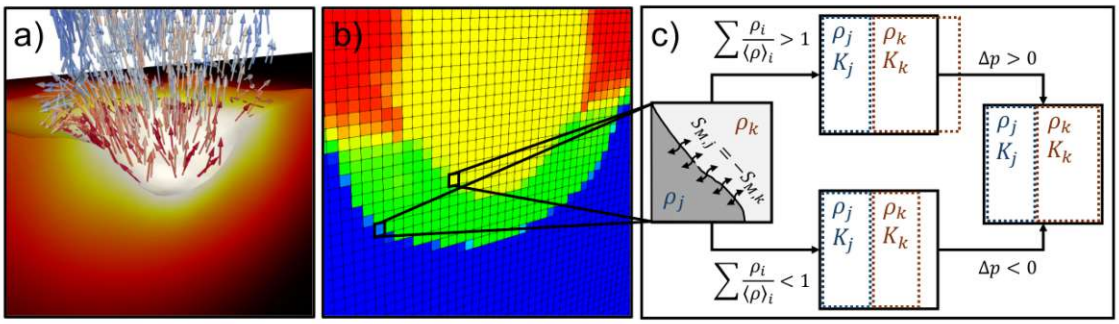

Figure 4: Illustration of the Mass-of-Fluid approach at the example of phase change: a) Exemplary laser-induced phase change process. b) Phase distribution in control volumes. c) Schematic illustration of phase transitions via exchanges of phase-specific mass density ρ_i leading to a change in volumetric phase distributions; either compression ($\Delta p > 0$) or expansion ($\Delta p < 0$) is necessary to calculate volume fractions α_i fulfilling $\sum \alpha_i = 1$ for a given set of ρ_i after phase change, obtained via phase-norming and each phases' equation of state. Reproduced from [34] with permission from Springer Nature.

Key physical models are then incorporated within this framework, such as the equations of state (using an ideal gas assumption for gaseous phases and the Tait equation for condensed matter), latent heat-based melting and solidification following an equilibrium assumption in the case of an alloy, or pressure-based evaporation and condensation using the Hertz-Knudsen model and the Clausius-Clapeyron equation to calculate the underlying saturation pressure. The MoF method and its implementation are shown to be accurate for predicting the pressure-velocity-energy evolution of highly compressible and scenarios involving phases with a large density ratio by solving first a one-phase and then a two-phase shock tube problem. At this point, to showcase also physical predictive capabilities (rather then "just" the correct implementation of a set of given model equations), a type 2 test case is solved, where the supersonic flow of gas through a converging-diverging nozzle is solved and compared to experimental data.

The propagation of laser energy and its interaction with material in the form of absorption and reflection is introduced into the model at the example of a Gaussian laser beam, calculating a heat source corresponding to the amount of laser energy absorbed by the phases over time. While the implementation is laid out at the example of a Gaussian beam, the option of using arbitrary measured or pre-calculated spatial (and temporal) laser intensity distributions was also implemented to facilitate the simulation of arbitrary beam shapes (e.g., to facilitate the simulations involving static and dynamic beam shaping in [34]).

The full model's predictive capabilities were finally tested by reproducing two parameter combinations of the stationary illumination experiments of Cunningham et al. [23], showing excellent agreement in terms of keyhole development over time. One chosen parameter combination features a distinct transition from a steady, low-fluctuation drill regime, where surface tension force and evaporative recoil pressure are

well balanced, to a highly fluctuating, unbalanced drill regime. Correctly predicting mean drill rates for both regimes, amplitude of fluctuations in the second regime, and the point of onset of the strong fluctuations, the model successfully passes this validation benchmark. Adding yet another level of complexity by going towards a moving laser beam, the copper welding experiment of Schricker et al. [35] is simulated. The model is in good agreement with experimental results in terms of size and shape of the keyhole and its dynamic evolution. Hereby, the model was shown to be valid for different processing conditions and entirely different materials without any empirical calibration steps, which was one of the key requirements.

Omitting common modeling assumptions such as incompressibility, the exclusion of gaseous phases or phenomenological models for evaporation-induced recoil, the here-presented framework greatly advances the state of the art in physics-based modeling of laser-material-processing and enables prediction of various dynamic processes across processing regimes and materials.

In this publication, C. Zenz was the lead author.

Publication 2

In Publication 2, the developed model is applied to the simulation of PBF-LB/M of two crack-prone nickel-based alloys. Within this work, the aim is to optimize the spatial intensity distribution of the used laser energy (mainly by addition of a large low-intensity secondary beam) to reduce the material's susceptibility towards hot cracking. The secondary laser beam incorporates additional pre- and post-heating of the process zone, with the aim of reducing of cooling rates within a material-dependent critical temperature range. The chosen metric of comparing cooling rates within a critical temperature interval poses a simple, relative hot cracking criterion not relying on empirical calibration parameters other than the material's critical temperature range. The model's accuracy is pragmatically validated by reproducing cross-sectional weld bead shapes (depth and width) obtained ex-situ from experiments. Furthermore, the so-called balling defect is accurately predicted for an unsuitable process parameter set, which is validated again by comparing to ex-situ images of the scan track top surface and cross-sections of the weld bead.

The technology chosen to facilitate the static beam shaping approach (Multi-Plane-Light-Conversion, MPLC) is a passive, optical solution that can be retro-fitted to existing PBF-LB/M machines, but requires an approximate preliminary design of beam shapes prior to being manufactured. Hence, it is unfeasible to design suitable beam shapes via experiments only and simulations with high predictive power (as the simulations are in part "blind", happening – at least for the conditions involving beam shaping – before the experiments) are needed. In fact, if the simulation model required beam shape-specific calibration, it would not qualify for this application. While the chosen optimization criterion is somewhat straightforward, aiming to reduce cooling rates within a material-specific temperature range, the process still needs to be kept stable, avoiding fluid dynamical instabilities such as spatter and keyhole porosity that could be introduced via the secondary beam's heating effect, or as another example (as shown within the study) balling, i.e., surface tension-driven formation of sphere-like structures that do not bond well with the substrate. Hence, it is not feasible to choose a simpler simulation tool such as a pure heat conduction model or one with a

phenomenological evaporation and condensation model.

Different combinations of power and size of primary and secondary beams were tested. As it was not obvious whether a small volume of processed material experiencing extremely high cooling rates or a large volume experiencing high, but not extreme cooling rates was more critical (i.e., which of the two peaks of the green curve in Figure 5 would be more critical), the optimization criterion was chosen as follows. The maximum cooling rates dT/dt occurring within the critical temperature range in each computational cell over the course of the simulation were recorded and then plotted in a histogram (volume over maximum cooling rate). The aim was then to shift the geometrical center of the histogram towards lower cooling rates. In this way, an optimum could be found, within the restrictions of limited computational time (i.e., number of simulations), maximum spatial laser beam dimensions achievable with the MPLC device, maximum laser power available and not inducing any process defects through the beam shaping strategy. An example of these cooling rate plots is provided in Figure 5, where the orange curve would be considered most favourable, and the green curve least favourable in terms of crack susceptibility.

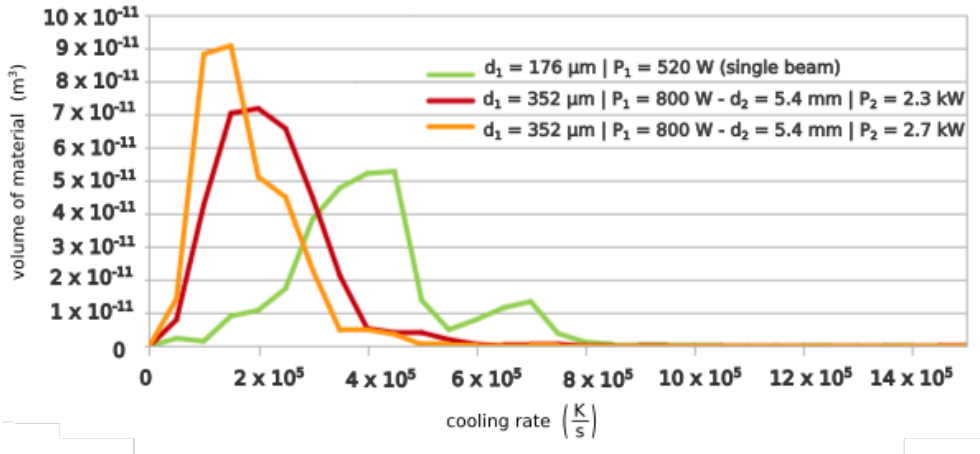

Figure 5: Exemplary cooling rates for the reference condition without beam shaping strategy, and two different combinations of primary and secondary beam parameters achieved via beam shaping. The orange plot is regarded as the best out of the three depicted ones, as its geometrical center is furthest left. Reproduced from Publication 2.

The optimized beam shapes were then tested experimentally, by printing dense samples. While not fully eliminating cracks, the number of cracks could be drastically reduced compared to the single beam reference setup. In summary, this publication presents a case study of utilizing the model presented in Publication 1 to solve an industrial challenge encountered in additive manufacturing.

In this publication, the first-authorship was shared between C. Zenz and M. Buttazzoni, with process-specific aspects of the work relevant to PBF-LB/M being led and mainly contributed by C. Zenz. During the underlying project, another co-lead-authored publication was produced [36], where, vice versa, process-specific aspects of the work relevant to laser beam welding were mainly contributed by M. Buttazzoni. All simulation-related work has been carried out at the Research Group of Process Simulation, TU Wien, while physical validation experiments were conducted by M.

Martínez Ceniceros, J.R. Blasco Puchades and L. Portolés Griñán at AIDIMME, Spain.

Publication 3

Publication 3 consists of an excerpt from a book chapter [34] and contains a part of results initially presented at two invited talks[2,3] given by C. Zenz. The investigation can be seen as a direct extension of (or appendix to) Publication 2, dealing with the multi-scale aspect of the problem and addressing the question whether process parameters optimized via single track simulations or experiments can be used at part scale. Here, multi-track and multi-layer simulations of PBF-LB/M are conducted, investigating the occurrence of defects that do not manifest in single track simulations or experiments, but build up due to heat accumulation. It was shown, that optimized secondary beam shapes delivering satisfactory results in single track simulations and experiments led to irregular layer surfaces when the scope was extended beyond single tracks towards an entire printing layer.

Furthermore, the dependence of thermal histories on process parameters across several printing layers is investigated, showing that parts of the build can, for the same single track process parameter settings, either remelt over the course of two or three layers, depending on the chosen scanning strategy or location in the sample. Also, the cooling rates during the final solidification event differ greatly, depending on strategy and location. These are however highly relevant for final built part properties, not only with respect to cracks but also its microstructure and resulting part properties. These insights were previously not available due to numerous simplifications (e.g., simplified equivalent heat sources, or treating the process as a pure heat conduction problem) usually undertaken when performing scan track-resolved multilayer simulations.

While Publication 3 only contains results, the used methodology is described in depth in Publications 1 (simulation model), 2 (material and processing parameters, context of investigation) and 4 (multi-layer printing model), and in the full text of [34]. In Publication 3, C. Zenz was the sole author.

Publication 4

In Publication 4, the universal laser material processing model presented in Publication 1 is extended in terms of multiphysical and multiscale aspects relevant specifically to the simulation of PBF-LB/M.

First, a non-equilibrium solidification model is incorporated in the MoF-framework to account for the extremely high cooling rates typically encountered in PBF-LB/M, where element diffusion in the solid phase can be neglected. The alloy concentration hence changes over the course of the solidification, leading to much lower solidus temperatures than under equilibrium conditions. The implementation within the MoF

[2]C. Zenz et al.: Multi-Scale Simulation of Laser-Based Powder Bed Fusion Using a Continuum Mechanics Approach. 9th GACM Colloquium on Computational Mechanics, 09/2022, Essen, Germany.

[3]C. Zenz et al.: Residual Stress Modelling in Laser-Based Powder Bed Fusion using a Fluid Mechanical Analogy Model. Sim-AM 2023, 07/2023, Munich, Germany.

framework is validated by reproducing temperature-solid fraction curves for different concentrations of an Al-Cu alloy and comparing them to a reference solution. Furthermore, a weakly coupled model for solid body deformation of the solidified (and substrate) material was incorporated, to allow for a direct simulation of thermally induced residual stresses and deformation of a part within the fluid-mechanical simulation. To allow for the efficient simulation of multiple layers of a PBF-LB/M process with a continuum model for the powder, a recoating model is conceptualized and implemented that enables efficient addition of powder during the simulation only in locations that can in reality be reached by powder particles (e.g., not filling previously formed pores).

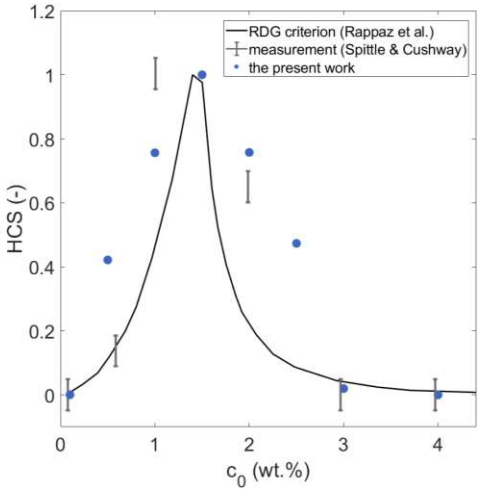

Figure 6: Hot cracking susceptibility (HCS) of different Al-Cu compositions as predicted by the RDG model [37], measured by Spittle and Cushway [38] and predicted by this work's model in a one-dimensional Stefan problem. As the plotted HCS is a relative metric, the location of its peak depends strongly on the choice of data points for investigation, hence the lack of experimental values at both models' peaks could explain the peak offset. Reproduced from Publication 4.

Then, a new model for the prediction of relative hot crack susceptibility is outlined, implemented and validated on a well-known benchmark. The main assumption within the model is that hot crack initiation begins with cavitation-induced rupture of the interdendritic liquid film due to a shrinkage- and deformation-induced pressure drop. In contrast to other criteria using the same conceptual idea, the event of cavitation within the mushy zone is an inherent feature of the underlying multiphysical simulation model and naturally arises due to the pressure drop in the mushy zone and the blockage of fluid flow to account for the low pressure via liquid backfill. Through the introduction of accurate temperature-solid fraction curves via a suitable solidification model and the introduction of an estimate of solid body deformation contribution following linear thermal expansion, the model was shown to provide accurate predictions for the crack susceptibility of Al-Cu alloys of different composition, reproducing their well-known Λ-shape, cf. Figure 6, notably without the need for fine tuning of empirical constants.

Finally, some applications of the model on PBF-LB/M scenarios at different scales are shown. These include single track scans, comparing crack susceptibility with a

significantly preheated substrate to the case of no substrate preheating, with much lower relative crack susceptibility in the case of no preheating, showing that the hot cracking model is not only sensitive towards alloy composition, but also processing conditions. Furthermore, simulations of multiple adjacent tracks and multiple layers of a PBF/LB-M process are shown.

In Publication 4, C. Zenz was the lead author.

Publication 5

Publication 5 introduces a novel particle-based simulation framework for tracking grain envelopes during solidification from melt to predict crystallographic microstructures.

Relevant model aspects are validated carefully against a number of well-known benchmarks of increasing complexity. These include the growth of a single grain envelope under a constant thermal gradient, one-dimensional solidification of a binary alloy, and the solidification of a two-dimensional crystal where the competition between adjacent grains is benchmarked against a well-known experiment and numerical reference solution to show the model's convergence with spatial discretization. Moving to more complex benchmarks, competitive growth during directional solidification of a three-dimensional polycrystal is simulated for different initial conditions and thermal gradients and compared to high-fidelity phase field simulation results from literature. Furthermore, the columnar-to-equiaxed transition of a large binary alloy ingot is successfully simulated and compared to a reference experimental and numerical simulation result.

A new, simple, quasi-two-dimensional simulation of melting and re-solidification mimicking power beam melting (e.g., laser-based additive manufacturing) is proposed and simulated to assess the ability of accurately reconstructing the solid-liquid interface during remelting and subsequently initiate re-solidification to yield microstructure evolution as encountered during laser-based partial melting and subsequent solidification. The results of this simulation are reproduced in Figure 7. Finally, the model is one-way coupled with the simulation framework of Publication 1 to predict grain growth during laser beam welding of stainless steel.

This publication contains important ground work towards the direct prediction of as-built microstructures in additively manufactured parts, which is a complex challenge given its characteristics of rapid melting and solidification, repeated remelting, heat accumulation and strongly anisotropic heat conduction conditions. The particle-based implementation of the tracking algorithm is intended for large-scale parallelization in the future, to leverage modern computer architectures when simulating large problems such as multi-layer AM.

The lead author of this publication was S. Mosbah. C. Zenz was responsible for the conceptualization and investigation of the original application cases, and conducted the investigation of the verification and validation cases under supervision of S. Mosbah and R. Gómez Vázquez. The grain growth model itself was conceptualized by S. Mosbah, with C. Zenz in a supporting role during model development and implementation.

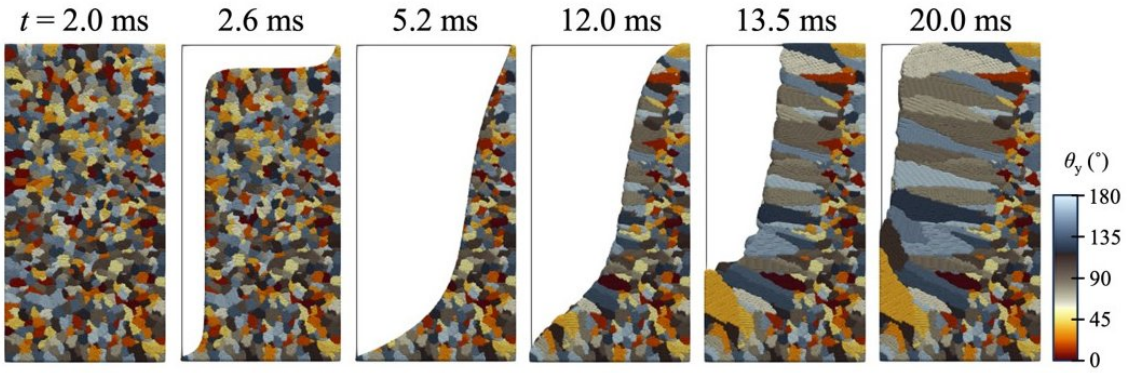

Figure 7: Grain structure at different time steps of the quasi-2D power beam melting and solidification simulation, with grains colored by their crystal orientation θ_y (since the grains have random three-dimensional orientations, the chosen color scale is mostly illustrative). The domain represents half (assuming symmetry) of a cross-section undergoing melting and solidification as induced by a power (e.g., laser or electron) beam. Reproduced (and rearranged to fit format) from Publication 5 with permission from Elsevier.

Publication 6

Publication 6 systematically investigates the differences between the newly developed simulation model of Publication 1 and a widely used, so-called one-fluid model, where incompressibility is assumed for all phases, gaseous matter is omitted, and its effect of condensed matter is accounted for through boundary conditions, reducing the level of coupling and hence presumably the predictive capabilities. The one-fluid model can be seen as a state-of-the art model for the simulation of laser-based additive manufacturing at the scale of the melt pool and is hence a good choice to benchmark the newly developed model of Publication 1 against.

To verify there is no disagreement between the two models in basic physical subproblems of heat conduction, melting and solidification and surface tension, these model components are validated by solving well-known analytically solvable benchmark problems.

Then, a simple bare plate laser melting and vaporization case is conceptualized which consists of process conditions relevant to laser-based additive manufacturing. The complexity of the problem is increased step-by-step by increasing the laser power and/or adding model features such as, e.g., Marangoni convection or the tracking of multiple laser reflections. In this way, regimes are identified where the two models yield similar or identical predictions and the threshold, at which the two models' results start to diverge in terms of both average process result and dynamical behavior. The two main areas of difference identified here are the treatment of evaporation and condensation rates and subsequently yielded evaporative recoil pressure, and the treatment of surface tension forces at the three-phase line of solid, liquid and gas. Especially the latter could be identified as an area where future research is urgently needed. Surface heat loss via radiation was identified as playing a negligible role in the laser-based AM scenarios of the work, and it was shown that convective and conductive cooling effects by the surrounding ambient gas could be approximated well by applying a calibrated heat transfer coefficient in a one-fluid model.
Finally, the stationary laser illumination case exhibiting a transition from a stable

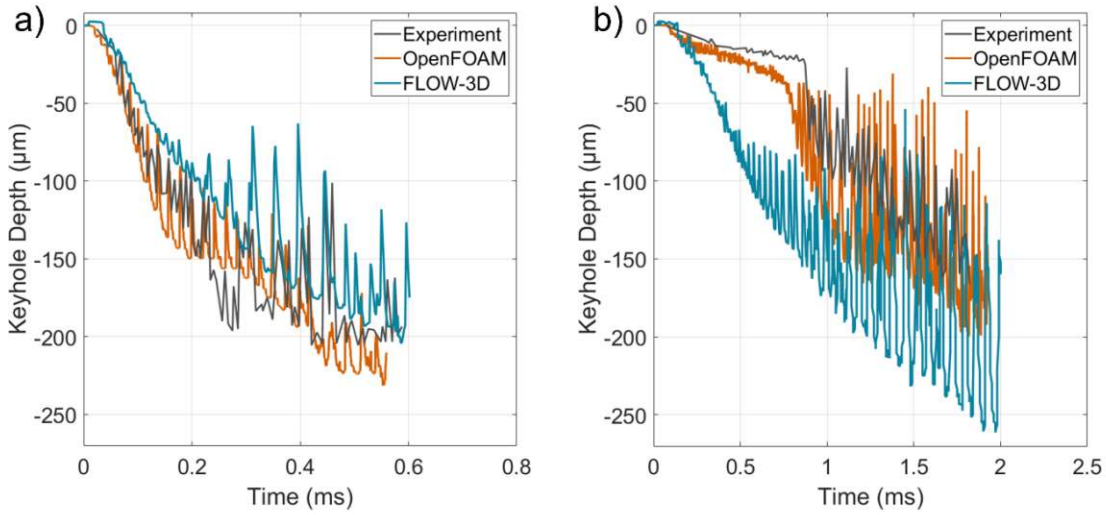

Figure 8: Comparison of keyhole evolution over time predicted by work's two-fluid model (termed OpenFOAM) and a state-of-the-art one-fluid model (termed FLOW-3D) with experimental results from [23] for laser spot sizes of (a): 95 µm, and (b): 140 µm. Reproduced from Publication 6 with permission from Springer Nature.

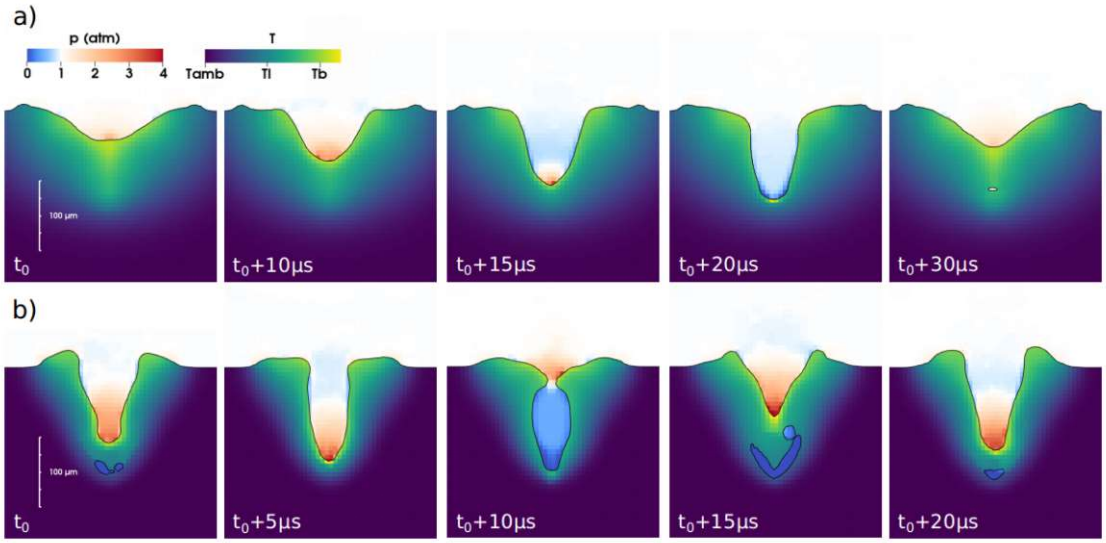

Figure 9: Keyhole morphologies predicted by work's two-fluid model for a) 140 µm spot size case, and b) 95 µm spot size case over one drill – collapse cycle during fluctuating process phase ($t >$ 1 ms for (a), $t > 0.2$ ms for (b)). Gaseous phases are coloured by pressure and condensed phases by temperature. Reproduced from Publication 6 with permission from Springer Nature.

to an unstable keyhole from Publication 1 is revisited to compare the two models. Figure 8 shows a comparison of the models' predictions of the keyhole depth evolution over time with the respective experimental data. In addition to comparing the model's predictive capabilities, the dynamic evolution of vapor pressure across a large range of values within the keyhole during the drill-collapse cycles are closely analyzed through the two-fluid model of Publication 1. Figure 9 shows the evolution of vapour pressure and keyhole shape throughout one exemplary drill–collapse cycle for both spot sizes. It becomes evident that a coupling of the evaporation rate with local pressure on the vapor side of the evaporating interface is necessary to accurately predict laser-induced vaporization events, or, if staying within a confined process regime, by properly calibrating a simpler, phenomenological model. This could be shown setting respectively different evaporative recoil coefficients in the one-fluid model's phenomenological evaporative recoil pressure model. The findings highlight the relevance of the work conducted throughout Publications 1–3, and the need for complex multiphysical models with high predictive capabilities even under "moderate" conditions such as encountered in laser-based additive manufacturing, although the additional predictive capabilities are found to come at approximately 10 times increased computational costs.

In this publication, lead authorship was shared between C. Zenz (responsible for two-fluid model aspects) and P.S. Cook (responsible for one-fluid model aspects).

1.5 Scientific Contribution

The key scientific contributions and findings of this thesis can be briefly summarized as follows.

- A consistent, interface-resolved multiphase simulation framework for the simulation of laser-material processing was developed.
  - The framework is inherently mass- and energy-conservative across phase change and compressible mass transport including discontinuities such as sharp interfaces and shocks.
  - It was shown that the predictive capabilities of the model outperform the previous state-of-the-art, as no calibration parameters in the evaporation and condensation equations were needed to accurately predict highly dynamic events over a range of intensities and materials. This could be shown by comparing simulation results with temporally and spatially highly resolved in-situ synchrotron x-ray images of the respective processes.
  - The potential future impact of these developments is high. One example of further work enabled through this contribution is the recent work of Florian et al. [39] on highly dynamic pore formation mechanisms in laser beam welding of copper, where agreement between high-speed in-situ synchrotron x-ray images and the corresponding simulations (notably across different process parameters) was sufficient to allow for the simulation to be seen as digital twin of the experiment, analyzing (usually) hidden information such as three-dimensional, transient velocity and pressure fields in liquid and gaseous phases. The here-developed model thus opens up the possibility of explaining experimental observations in detail by making accessible the underlying cause-effect relationships.
- Systematic comparison with a state-of-the-art one-fluid (not interface-resolved) simulation model showed that significant differences in simulation results are present even in low to moderate intensity AM scenarios.
  - The discrepancies stem mainly from fundamental differences in the degree of coupling of the evaporation (and condensation) equations and surface tension forces at the three-phase line.
  - While modeling aspects related to radiative heat loss and convective cooling were shown to be insignificant and can be accounted for via simple, calibrated sub-models, it was shown that the fundamental lack of coupling between vapour-sided pressure and the resulting evaporation and condensation rate usually present in most models can only be accounted for via a calibration step within narrow process bounds. Re-calibration is necessary when altering processing conditions.
  - The additional predictive capabilities of the here-developed model however come with the downside of computational costs being higher by approximately a factor of 10.

  - These findings provide guidelines for researchers and engineers on the implications of model choice and validity bounds of models calibrated to specific process regimes in the simulation of AM. They serve as foundation for the development of multi-fidelity modeling approaches, which are needed to efficiently address the inherent multi-scale nature of AM processes.

- The transient behaviour of the pressure distribution throughout the vapor capillary has been analyzed.
  - Its coupling with evaporation and condensation rates have been shown to pose a self-limiting process and hence explain lower drill rates than predicted by one-fluid models in stationary laser illumination experiments.
  - These findings represent unprecedented insights into the dynamics and coupling of pressure, evaporation and thermocapillary instability, showing for the first time the transient and highly dynamic evolution of pressure within a thermocapillary under quasi-steady state conditions.
  - Challenging the typical assumption of a constant vapour-sided pressure, these insights could play a crucial role in the development of new, improved phenomenological evaporation models to be used in faster, lower-fidelity simulation frameworks.

- The use of a high-fidelity simulation model for process optimization of PBF-LB/M, for cases where experimental optimization is not feasible, was demonstrated.
  - The addition of a secondary, large-area, low-intensity laser beam in PBF-LB/M was shown to reduce cooling rates in a critical temperature range, leading to lower hot cracking susceptibility for two crack-prone, usually non-weldable Ni-superalloys.
  - Experimental tests of the beam shapes found through simulations showed that near-zero crack densities could be achieved, which was previously not possible using a standard Gaussian laser beam. These findings unlock previously non-weldable materials of high industrial relevance for PBF-LB/M applications.
  - Besides fulfilling the optimization target (in this case, to lower cooling rates), the high-fidelity simulation model was shown to predict onset of defects such as balling in the case of insufficient energy input, or heat-accumulation-induced and scan parameter-related defects that only manifest over the course of many tracks or even several layers.
  - These findings present important groundwork on the way towards physics-based digital process twins and simulation-based process development.

- A new model for the prediction of relative hot crack susceptibility was conceptualized and developed, where the vapor cavitated within a critical solid fraction range of the mushy zone was seen as a model for hot crack initiation.

  - While akin to the well-known Rappaz-Drezet-Gremaud criterion in underlying physical assumptions, it does not rely on empirical parameters and arises implicitly from the underlying multiphase simulation framework. The concept of liquid film cavitation within the mushy zone is directly simulated.
  - The model is shown to be sensitive towards alloy composition and processing conditions and can be employed at various scales.
  - These findings represent a contribution to physics-based hot cracking models and a key element of a holistic physics-based simulation model of AM, as many materials of interest for AM are crack-prone.

- A continuum-mechanical model for efficient scan track-resolved simulation of several layers of each several tracks of a PBF-LB/M process was developed. This is accomplished wihtout reducing the degree of incorporated physics compared to high fidelity melt pool scale simulations.
  - Detailed, scan track-resolved thermal histories across several layers were obtained for different scan strategies and at different locations of a simple rectangular geometry.
  - It was shown that thermal histories over the build of a structure depend on the location and the chosen scan strategies, for example regarding the number of remelting events and cooling rates during the final solidification step. This highlights the need of expanding investigations using high-fidelity simulation models towards larger scales to accurately predict thermal histories, which are in turn decisive for the resulting mechanical properties of a final part.
  - These developments bridge the gap between currently employed high-fidelity models used at small scales of single or several adjacent tracks and those used at larger multi-layer scales typically featuring a significantly lower degree of physics and predictive capabilities.

- A new, particle-based grain envelope tracking scheme for the prediction of crystalline grain growth was developed, extensively validated and coupled with the multiphysical simulation model of laser-material processing.
  - As parts built by PBF-LB/M typically exhibit strong anisotropy, the correct prediction of grain structures is a key element of a holistic simulation framework of PBF-LB/M and these contributions represent groundwork on the way towards simulation-based grain structure (and thereby part property) optimization.
  - The particle-based implementation allows to leverage modern computer architectures in the future, to scale grain growth simulations towards the dimensions needed to simulate AM processes.

Outlook

Future work should focus on increased coupling between solid- and fluid mechanical models to further increase the accuracy of the here-developed hot cracking model, and in a next step also incorporating information obtained from the coupled grain growth model.

The role of surface tension forces at the three-phase-line in PBF-LB/M should receive further attention, developing accurate, efficient modeling strategies.

Furthermore, a multi-fidelity simulation chain should be established to enable fast predictions across broad parameter spaces, working with simple, calibrated sub-models where sufficiently accurate. Using multi-fidelity modeling strategies, future efforts should aim at unlocking true part-scale simulations, where the printing process of an entire AM part is simulated while still resolving relevant phenomena at the melt pool scale.

Many material properties which are difficult or nearly impossible to measure within the needed temperature ranges and material states have a strong influence on the resulting process behaviour. To allow for highly accurate simulations, simulation-based identification of such material properties through a calibration against experimental in-situ observations could be used to build a database of simulation-relevant material properties for materials of interest to PBF-LB/M applications.

Not only relevant to AM but laser-material-processing in general, additional physical phenomena such as multi-component evaporation and species diffusion could be integrated within the simulation framework to expand its applicability across the vast variety of laser-based manufacturing processes encountered today.

1.6 References

[1] T. DebRoy, H. Wei, J. Zuback, T. Mukherjee, J. Elmer, J. Milewski, A. Beese, A. Wilson-Heid, A. De, and W. Zhang. "Additive manufacturing of metallic components – Process, structure and properties". In: *Progress in Materials Science* 92, 2018, pp. 112–224. DOI: https://doi.org/10.1016/j.pmatsci.2017.10.001.

[2] K. Kanishka and B. Acherjee. "Revolutionizing manufacturing: A comprehensive overview of additive manufacturing processes, materials, developments, and challenges". In: *Journal of Manufacturing Processes* 107, 2023, pp. 574–619. DOI: https://doi.org/10.1016/j.jmapro.2023.10.024.

[3] M. J. Yadegari, A. Martucci, S. Biamino, D. Ugues, L. Montanaro, P. Fino, and M. Lombardi. "Aluminum Laser Additive Manufacturing: A Review on Challenges and Opportunities Through the Lens of Sustainability". In: *Applied Sciences* 15, 2025. DOI: https://doi.org/10.3390/app15042221.

[4] B. Goldense. "Metal AM: Metal Additive Manufacturing Hits Critical Mass". In: *Machine Design*, July 2018, p. 72.

[5] NMSC. *Additive Manufacturing Market*. Feb. 2025. URL: https://www.nextmsc.com/report/additive-manufacturing-market (visited on 05/22/2025).

[6] Y. Kok, X. Tan, P. Wang, M. Nai, N. Loh, E. Liu, and S. Tor. "Anisotropy and heterogeneity of microstructure and mechanical properties in metal additive manufacturing: A critical review". In: *Materials & Design* 139, 2018, pp. 565–586. DOI: https://doi.org/10.1016/j.matdes.2017.11.021.

[7] M. Bayat, W. Dong, J. Thorborg, A. C. To, and J. H. Hattel. "A review of multi-scale and multi-physics simulations of metal additive manufacturing processes with focus on modeling strategies". In: *Additive Manufacturing* 47, 2021, p. 102278. DOI: https://doi.org/10.1016/j.addma.2021.102278.

[8] E. Malekipour and H. El-Mounayri. "Scanning Strategies in the PBF Process: A Critical Review". In: vol. Volume 2A: Advanced Manufacturing. ASME International Mechanical Engineering Congress and Exposition. Nov. 2020, V02AT02A055. DOI: https://doi.org/10.1115/IMECE2020-24589.

[9] A. Martucci, A. Aversa, F. Bondioli, P. Fino, and M. Lombardi. "Synergic strategies to improve the PBF-LB/M processability of a cracking-sensitive alloy". In: *Materials & Design* 224, 2022, p. 111396. DOI: https://doi.org/10.1016/j.matdes.2022.111396.

[10] D. Bartels, M. E. Albert, F. Nahr, and M. Schmidt. "On the Influence of Volumetric Energy Density and Inter-Layer Time on the Material Properties of Case-Hardening Steels". In: *Alloys* 2, 2023, pp. 168–183. DOI: https://doi.org/10.3390/alloys2030013.

[11] J. Kluczyński, B. Sarzyński, T. Dražan, J. Łuszczek, R. Kosturek, and I. Szachogłuchowicz. "Influence of Process Parameters on Selected Properties of Ti6Al4V Manufacturing via L-PBF Process". In: *Materials* 17, 2024. DOI: https://doi.org/10.3390/ma17174384.

[12] H. Panzer, J. Diller, F. Ehrenfels, J. Brandt, and M. F. Zäh. "Experimental investigation of process parameter variations on the microstructure and failure behavior of IN718 structures in PBF-LB/M". In: *Journal of Laser Applications* 36, Jan. 2024, p. 012015. DOI: https://doi.org/10.2351/7.0001232.

[13] Y. Qiao, M. Grad, and A. Nonn. "Toward an Efficient and Robust Process–Structure Prediction Framework for Filigree L-PBF 316L Stainless Steel Structures". In: *Metals* 15, 2025. DOI: https://doi.org/10.3390/met15070812.

[14] J. Bayol and G. Pallier. "Advances in laser powder bed fusion thanks to beam shaping: Beam shaper based on multi-plane light conversion enables new forms of material processing". In: *PhotonicsViews* 19, 2022, pp. 52–55. DOI: https://doi.org/10.1002/phvs.202200045.

[15] R. Weber, J. Wagner, A. Peter, C. Hagenlocher, A. Spira, B. Urbach, E. Shekel, and Y. Vidne. "Basic Properties of High-Dynamic Beam Shaping with Coherent Combining of High-Power Laser Beams for Materials Processing". In: *Journal of Manufacturing and Materials Processing* 9, 2025, p. 85. DOI: https://doi.org/10.3390/jmmp9030085.

[16] A. Otto, H. Koch, K.-H. Leitz, and M. Schmidt. "Numerical simulations - a versatile approach for better understanding dynamics in laser material processing". In: *Physics Procedia* 12, 2011, pp. 11–20. DOI: https://doi.org/10.1016/j.phpro.2011.03.003.

[17] P. S. Cook and A. B. Murphy. "Simulation of melt pool behaviour during additive manufacturing: Underlying physics and progress". In: *Additive Manufacturing* 31, 2020, p. 100909. DOI: https://doi.org/10.1016/j.addma.2019.100909.

[18] Y. Zhang, Q. Chen, G. Guillemot, C.-A. Gandin, and M. Bellet. "Numerical modelling of fluid and solid thermomechanics in additive manufacturing by powder-bed fusion: Continuum and level set formulation applied to track- and part-scale simulations". In: *Comptes Rendus. Mécanique* 346, 2018, pp. 1055–1071. DOI: 10.1016/j.crme.2018.08.008.

[19] S. D. Proell, P. Munch, M. Kronbichler, W. A. Wall, and C. Meier. "A highly efficient computational approach for fast scan-resolved simulations of metal additive manufacturing processes on the scale of real parts". In: *Additive Manufacturing* 79, 2024, p. 103921. DOI: https://doi.org/10.1016/j.addma.2023.103921.

[20] S. Jabar, Q. Hayat, A. B. Barenji, G. Chianese, H. Kotadia, D. Ceglarek, and P. Franciosa. "Investigations of weld profiling and intermetallic formation in laser welding of steel-to-aluminium: a multi-physics CFD approach using beam shaping". In: *Procedia CIRP* 124, 2024, pp. 559–564. DOI: https://doi.org/10.1016/j.procir.2024.08.174.

[21] A. A. Lassila, E. Lundell, T. Andersson, D. Lönn, K. Salomonsson, and R. Ghasemi. "Experimental and numerical investigation of process-induced recoil force in keyhole laser welding: Insights for validating multi-physics process simulations and modelling assumptions". In: *Journal of Materials Processing Technology* 341, 2025, p. 118895. DOI: https://doi.org/10.1016/j.jmatprotec.2025.118895.

[22] Y. Shu, D. Galles, O. A. Tertuliano, B. A. McWilliams, N. Yang, W. Cai, and A. J. Lew. "A critical look at the prediction of the temperature field around a laser-induced melt pool on metallic substrates". In: *Scientific Reports* 11, 2021, p. 12224. DOI: https://doi.org/10.1038/s41598-021-91039-z.

[23] R. Cunningham, C. Zhao, N. Parab, C. Kantzos, J. Pauza, K. Fezzaa, T. Sun, and A. D. Rollett. "Keyhole threshold and morphology in laser melting revealed by ultrahigh-speed x-ray imaging". In: *Science* 363, 2019, pp. 849–852. DOI: https://doi.org/10.1126/science.aav4687.

[24] M. Mohsin Raza and Y.-L. Lo. "Experimental investigation into microstructure, mechanical properties, and cracking mechanism of IN713LC processed by laser powder bed fusion". In: *Materials Science and Engineering: A* 819, 2021, p. 141527. DOI: https://doi.org/10.1016/j.msea.2021.141527.

[25] M. Henderson, D. Arrell, R. Larsson, M. Heobel, and G. Marchant. "Nickel based superalloy welding practices for industrial gas turbine applications". In: *Science and Technology of Welding and Joining* 9, 2004, pp. 13–21. DOI: https://doi.org/10.1179/136217104225017099.

[26] N. T. Aboulkhair, M. Simonelli, L. Parry, I. Ashcroft, C. Tuck, and R. Hague. "3D printing of Aluminium alloys: Additive Manufacturing of Aluminium alloys using selective laser melting". In: *Progress in Materials Science* 106, 2019, p. 100578. DOI: https://doi.org/10.1016/j.pmatsci.2019.100578.

[27] D. Holder, M. Henn, M. Buser, C. Hagenlocher, V. Onuseit, and T. Graf. "Bridging additive and subtractive manufacturing: Exceeding the limits of conventional manufacturing with combined continuous-wave and ultrafast lasers". In: *PhotonicsViews* 21, 2024, pp. 50–53. DOI: https://doi.org/10.1002/phvs.202400022.

[28] A. Otto, H. Koch, R. Gómez Vázquez, Z. Lin, and B. Hainsey. "Multiphysical Simulation of ns-Laser Ablation of Multi-Material LED-Structures". In: *Physics Procedia* 56, 2014, pp. 1315–1324. DOI: https://doi.org/10.1016/j.phpro.2014.08.057.

[29] R. Gómez Vázquez, H. Koch, and A. Otto. "Multi-Physical Simulation of Laser Welding". In: *Physics Procedia* 56, 2014, pp. 1334–1342. DOI: https://doi.org/10.1016/j.phpro.2014.08.059.

[30] A. Otto and R. Gómez Vázquez. "Fluid dynamical simulation of high speed micro welding". In: *J. Laser Appl.* 30, 2018, p. 032411. DOI: https://doi.org/10.2351/1.5040652.

[31] W. Lu, L. Zhao, Z. Su, J. Li, and Q. Hu. "Recent progress on in-situ characterization of laser additive manufacturing process by synchrotron radiation". In: *Journal of Materials Science & Technology* 217, 2025, pp. 29–46. DOI: https://doi.org/10.1016/j.jmst.2024.07.047.

[32] H. G. Weller, G. Tabor, H. Jasak, and C. Fureby. "A tensorial approach to computational continuum mechanics using object-oriented techniques". In: *Computers in physics* 12, 1998, pp. 620–631. DOI: https://doi.org/10.1063/1.168744.

[33] J. Ahrens, B. Geveci, and C. Law. "ParaView: An End-User Tool for Large Data Visualization". In: *Visualization Handbook*. ISBN 978-0123875822. Elesvier, 2005.

[34] A. Otto, M. Buttazzoni, C. Durán, T. Florian, and C. Zenz. "Universal Numerical Simulation Model for Laser Material Processing". In: *Scaling of Laser Processing – Making Light Matter*. Ed. by J. Bonse and A. F. Lasagni. Cham, Switzerland: Springer, 2026. The final authenticated version will be available online in the Springer Series in Optical Sciences: https://link.springer.com/book/9783032171320.

[35] K. Schricker, L. Schmidt, H. Friedmann, C. Diegel, M. Seibold, P. Hellwig, F. Fröhlich, J.-P. Bergmann, F. Nagel, P. Kallage, A. Rack, H. Requardt, and Y. Chen. "Characterization of keyhole dynamics in laser welding of copper by means of high-speed synchrotron X-ray imaging". In: *Procedia CIRP* 111, 2022, pp. 501–506. DOI: https://doi.org/10.1016/j.procir.2022.08.079.

[36] M. Buttazzoni, C. Zenz, A. Otto, R. Gómez Vázquez, G. Liedl, and J. L. Arias. "A Numerical Investigation of Laser Beam Welding of Stainless Steel Sheets with a Gap". In: *Appl. Sci.* 11, 2021, p. 2549. DOI: https://doi.org/10.3390/app11062549.

[37] M. Rappaz, J.-M. Drezet, and M. Gremaud. "A new hot-tearing criterion". In: *Metallurgical and materials transactions A* 30, 1999, pp. 449–455. DOI: https://doi.org/10.1007/s11661-999-0334-z.

[38] J. Spittle and A. Cushway. "Influences of superheat and grain structure on hot-tearing susceptibilities of AI-Cu alloy castings". In: *Metals Technology* 10, 1983, pp. 6–13. DOI: https://doi.org/10.1179/030716983803291226.

[39] T. Florian, K. Schricker, C. Zenz, A. Otto, L. Schmidt, C. Diegel, H. Friedmann, M. Seibold, P. Hellwig, F. Fröhlich, F. Nagel, P. Kallage, M. Buttazzoni, A. Rack, H. Requardt, Y. Chen, and J.-P. Bergmann. "Combining in situ synchrotron X-ray imaging and multiphysics simulation to reveal pore formation dynamics in laser welding of copper". In: *International Journal of Machine Tools and Manufacture* 204, 2025, p. 104224. DOI: https://doi.org/10.1016/j.ijmachtools.2024.104224.

2 Publications

This chapter contains the full text of the following articles:

Publication 1
C. Zenz, M. Buttazzoni, T. Florian, K. E. Crespo Armijos, R. Gómez Vázquez, G. Liedl, A. Otto (2024):"A compressible multiphase mass-of-fluid model for the simulation of laser-based manufacturing processes". *Computers & Fluids* Vol. 268, 106109.
doi: https://doi.org/10.1016/j.compfluid.2023.106109

Publication 2
C. Zenz, M. Buttazzoni, M. Martínez Ceniceros, R. Gómez Vázquez, J. R. Blasco Puchades, L. Portolés Griñán, A. Otto (2023): "Simulation-based process optimization of laser-based powder bed fusion by means of beam shaping". *Additive Manufacturing* Vol. 77, 103793.
doi: https://doi.org/10.1016/j.addma.2023.103793

Publication 3
C. Zenz: "Multi-Scale Simulation of PBF-LB/M". Excerpt from: A. Otto, M. Buttazzoni C. Durán, T. Florian, C. Zenz (2026): "Universal Numerical Simulation Model for Laser Material Processing". *Preprint accepted for publication* in: J. Bonse and A. F. Lasagni (Eds.): *Scaling of Laser Processing – Making Light Matter*, Springer, Cham, Switzerland. The preprint is available at: https://doi.org/10.48550/arXiv.2509.22666. The final authenticated version will be available online in the Springer Series in Optical Sciences: https://link.springer.com/book/9783032171320

Publication 4
C. Zenz, C. Durán, T. Florian, R. Bielak, A. Otto (2024): "Multiphysical simulation of hot cracking in Laser-Based Powder Bed Fusion". *Procedia CIRP* Vol. 124, pp. 341–346.
doi: https://doi.org/10.1016/j.procir.2024.08.130

Publication 5
S. Mosbah, R. Gómez Vázquez, C. Zenz, D. Tourret, A. Otto (2025): "A particle-based approach for the prediction of grain microstructures in solidification processes". *Computational Materials Science* Vol. 255, 113918.
doi: https://doi.org/10.1016/j.commatsci.2025.113918

Publication 6
C. Zenz, P. S. Cook, L. Vörös, A. Otto (2025): "A critical comparison of one- and two-fluid approaches for the simulation of laser-induced melt pool formation and vaporisation". *Discover Materials* Vol. 5, 266.
doi: https://doi.org/10.1007/s43939-025-00434-0

A compressible multiphase Mass-of-Fluid model for the simulation of laser-based manufacturing processes

Constantin Zenz[a,*], Michele Buttazzoni[a], Tobias Florian[a], Katherine E. Crespo Armijos[a], Rodrigo Gómez Vázquez[a,b], Gerhard Liedl[a], Andreas Otto[a]

[a]Institute of Production Engineering and Photonic Technologies, TU Wien, Getreidemarkt 9, 1060, Vienna, Austria

[b]LKR Light Metals Technologies, Austrian Institute of Technology, Giefinggasse 2, 1210, Vienna, Austria

*Corresponding author

This version of the article has been accepted for publication, after peer review, but is not the Version of Record. The Version of Record is available online at: https://doi.org/10.1016/j.compfluid.2023.106109. Some typographical errors contained in the Version of Record have been corrected in this version, as published in the corrigendum available online at: https://doi.org/10.1016/j.compfluid.2024.106529

Abstract: A new model for compressible multiphase flows involving sharp interfaces and phase change is presented, that uses a variant of the Volume-of-Fluid model to track phases by advecting their respective mass, and is hence called Mass-of-Fluid model. The framework is aimed at predicting the coupled multi-physical phenomena involved in most processes encountered in laser material processing, with the aim of minimizing a priori assumptions on the nature of the process. Emphasis is put on the multiphase fluid flow model, especially on the treatment of compressibility and phase change. The model's accuracy and suitability is demonstrated on problems of increasing complexity, including well-known benchmarks and problems encountered in laser material processing, where simulation results are compared to experimental observations.

Keywords: laser material processing; multiphase flow; compressibility; OpenFOAM; Volume-of-Fluid; Mass-of-Fluid

1 Introduction

High power lasers are widely used within various industries for a broad variety of manufacturing processes due to their versatility. Some examples of the many applications include welding, cutting, powder bed fusion, drilling and cladding [1, 2]. Accurate, physics-based models for laser-material interaction, and the resulting physical phenomena are needed to understand, design and optimize these processes [3]. Due to the multi-physical nature of the process, mechanistic modeling poses a complex challenge. In Figure 1, an illustrative example of a laser material processing simulation conducted with the here-presented model is given, highlighting some of the involved phenomena and the complexity of the process. Another example for a

process is shown in Figure 2, where nanosecond long laser pulses are used for the ablation of copper, where the molten copper is entrained by shock waves that form in the ambient gas. Although both processes are very different in terms of time- and length scales and the dominant physical processes at play, they follow the same underlying physical principles and can both be efficiently simulated using the same model.

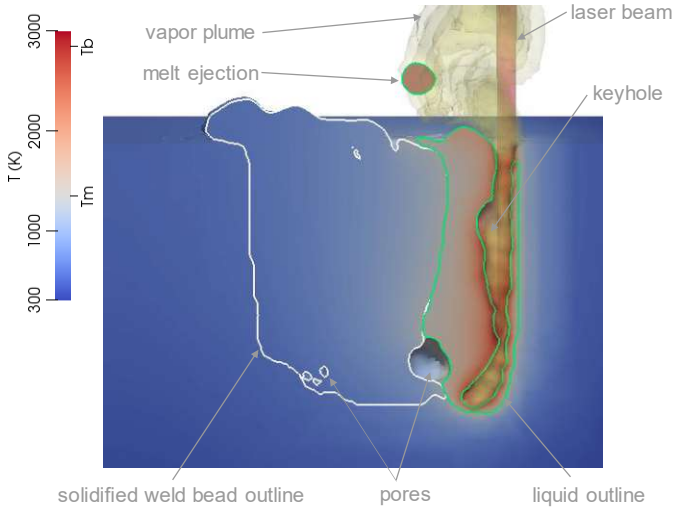

Figure 1: Three-dimensional simulation (longitudinal section) of copper processing through laser beam welding (result from simulation presented in Section 4.5).

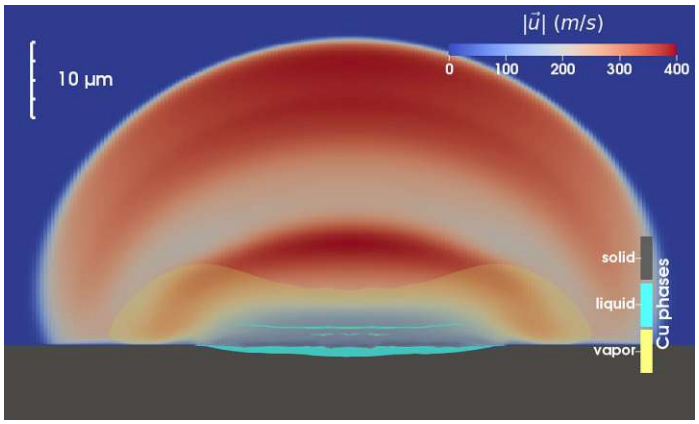

Figure 2: Two-dimensional simulation of copper processing through laser ablation using nanosecond pulses. Shock waves form due to the rapid expansion of heated gas, entraining liquid copper.

Laser-material processing models are typically dedicated to one process, where historically the focus has been mainly on laser welding, and more recently also on additive manufacturing processes, such as laser powder bed fusion or direct energy deposition. Those process-specific models typically employ assumptions which are justified in the context of the respective process or investigation but limit their validity to a narrow set of applications. An example is the laser cutting model of Zhao and Cheng [4], where evaporation and the thus induced recoil pressure are neglected, limiting its applicability, according to the authors, to cutting of sufficiently thin

sheets. Regarding more general approaches, Cho and Na [5] modeled keyhole welding with a pulsed laser source taking into account Fresnel absorption and multiple reflections within the keyhole, not taking into account any vapor phases and employing an explicit recoil pressure only depending on local temperature and constant far field pressure and evaporation efficiency. Courtois et al. [6] modeled beam propagation through the Maxwell equations and included the gas phase in their model, but did not distinct between ambient gas and metal vapor, assuming incompressible gas phases. They furthermore neglected the temperature dependency of surface tension, and hence Marangoni convection. Tan and Shin [7] incorporated a compressible description of the gas phases and included their flow description in the model, but explicitly calculated the recoil pressure, applying it in the form of a boundary condition at the interface between gaseous and condensed matter, assuming a constant evaporation efficiency. Ai et al. [8, 9] included the gas phase in their model, assuming incompressibility and not differentiating between ambient gas and metal vapor, modeling the effect of recoil pressure explicitly and only depending on the local temperature of the liquid. Similarly, Yu and Zhao [10] also assume incompressibility and incorporate the gas phase in their model and explicitly handle forces between gaseous and condensed matter. One widely used tool for the simulation of various laser-based material processing scenarios is the commercial software *Flow-3D*, where incompressibility is assumed and gaseous phases are neglected and their effect on condensed matter (e.g., in the form of recoil pressure) is modeled explicitly through boundary conditions [11–13]. Some studies report the use of frameworks very similar to that of *Flow-3D* but do not provide information on which software framework (or in-house code) was used to implement the model. One such example is the model of Feng et al. [14] used to simulate partial and full penetration keyhole welding. Flint et al. [15, 16] presented a model including component-wise phase changes of different elements of, e.g., an alloy. Although employing an incompressibility assumption for all phases, they modified the continuity equation through a volume dilation term accounting locally for the compression and expansion during evaporation and condensation, where thus the recoil pressure is an implicit result of the volume dilation. The rate of evaporation and condensation is a function of temperature only (without taking into account local pressure). Yu and Zhao [10] also included gas phases and their flow description in their model, again assuming incompressibility and incorporating an explicitly calculated recoil pressure, focusing on accurate spatial resolution of evaporation phenomena.

The studies mentioned here represent only a brief and non-comprehensive overview of some more recent multiphysical models and their main fluid-mechanical assumptions. For a wider overview on the state of the art and typical model assumptions employed in modeling of laser-material processing, we refer the reader to the review of Dal and Fabbro [17] focused on the process of laser beam welding, and the review of Cook and Murphy [18] focused on selective laser melting (i.e., powder bed fusion).

It was recently shown by Shu et al. [19] that even for low power additive manufacturing scenarios, where no keyhole is present (conduction-mode laser melting), accurate modeling of convective heat transport, and therefore melt flow, is needed to correctly predict the thermal history and three-dimensional weld bead shape of a part (even if results of a non-convective model are validated by comparing against experimental

weld bead cross sections). This once more highlights the need for multi-physical modeling, even in fairly simple scenarios of laser material processing. A truly universal model for laser material processing should, like the corresponding real-world process, only need process and material parameters, and initial and boundary conditions as inputs and be able to then predict the process. This necessity of a universal model requires the number of process-specific assumptions to be minimized. We therefore omit typical assumptions [17] such as the incompressibility of fluid phases or the exclusion of vapor phases.
Over the course of developing a universal multi-physical model for laser-based manufacturing, covering both micro- and macroscopic processes using continuous wave [20–27] and pulsed lasers [28–30], a novel approach to model compressible segregated multiphase flows undergoing phase changes was derived. The model, which we call Mass-of-Fluid model, is presented in Section 2. Details on the numerical implementation are provided in Section 3. Then, simulation results from a series of test cases of increasing complexity are presented, with the aim of validating the model and its implementation and demonstrating its universality.

2 Model Description and Governing Equations

We employ a homogeneous equilibrium mixture model for the fluid-mechanical multiphase problem, where the Navier-Stokes equations and energy equation are solved for a mixture of N phases, locally assuming average thermophysical properties and a shared velocity, pressure and temperature. In this context, each phase i corresponds to one aggregation state of one material. Therefore, in a typical application within laser material processing of a single material (e.g., *metal*), we encounter the phases *solid metal*, *liquid metal*, *metal vapor* (or multiple instances of these, in the case of multi-material simulations) and *ambient gas*. Additionally, we denote the phase *resolidified material*, i.e., solid material which solidified from melt, as this proves convenient for post-processing simulation results, e.g., visualizing the weld bead depth. Furthermore, this gives the opportunity of employing different material properties for the green state material and the processed (molten and solidified) material.

2.1 Momentum Equations

The continuity and momentum equations for the mixture of phases read

$$\frac{\partial \rho}{\partial t} + \nabla \cdot (\rho \boldsymbol{u}) = 0, \tag{1}$$

and

$$\begin{aligned} \frac{\partial (\rho \boldsymbol{u})}{\partial t} + \nabla \cdot (\rho \boldsymbol{u}\boldsymbol{u}) = \\ -\nabla p + \nabla \cdot \boldsymbol{\tau} - \boldsymbol{S}_B + \boldsymbol{S}_S + \boldsymbol{S}_D, \end{aligned} \tag{2}$$

where $\boldsymbol{u}$, p, ρ, and $\boldsymbol{\tau}$ denote velocity, pressure, density, and viscous stress tensor of the mixture, respectively. Furthermore, The source $\boldsymbol{S}_D$ is modeled as a porous bed

through Darcy's law [31] following the Carman-Kozeny equation as [32]

$$\boldsymbol{S}_D = -\frac{\mu}{A_{perm}} \frac{(\alpha_{solid})^2}{(1-\alpha_{solid})^3 + \delta} \boldsymbol{u}, \tag{3}$$

where α_{solid}, and μ denote the volume fraction of solid material, and the viscosity of the mixture, respectively. A_{perm} is the permeability area of the porous bed which is employed to model the mushy zone, usually set to $A_{perm} \approx 10^{-12}$ m^2, and $\delta = 10^{-6}$ is a small constant to prevent a division by zero.
Surface energies at phase-pair interfaces are calculated from individual phases' surface energies σ_i, assuming non-polar solid surfaces, as [33]

$$\sigma_{i,j} = \sigma_i + \sigma_j - 2\sqrt{\sigma_i \sigma_j}, \tag{4}$$

with $\sigma_i = f(T)$ typically being temperature-dependent, from which we calculate a continuum surface tension force [34] as

$$\boldsymbol{S}_S = \sum_{i,j \forall i<j} \nabla \cdot \left[\sigma_{i,j} \left(\alpha_j \nabla \alpha_i - \alpha_i \nabla \alpha_j\right)\right], \tag{5}$$

where α_i denotes the volume fraction of phase i, thus $\boldsymbol{S}_S$ only takes values within interface regions of finite thickness. However simple the surface tension force model of Eqs. (4)-(5) is, it bears the advantage of only requiring individual phases' surface energy values (i.e., the phase-vacuum interface values of surface tension) as input parameters, without having to specify contact angles or interface properties.
Body forces include only the gravitational force and are modeled as

$$\boldsymbol{S}_B = \boldsymbol{g} \cdot (\boldsymbol{h} - \boldsymbol{h}_{ref}) \nabla \rho, \tag{6}$$

where $(\boldsymbol{h} - \boldsymbol{h}_{ref})$ denotes the position in space with respect to an arbitrary reference point $\boldsymbol{h}_{ref}$ and $\boldsymbol{g}$ is the gravity vector. Forces due to evaporation-induced recoil pressure are not explicitly modeled as they are an implicit result of the compressible multiphase model (phase change issues a change in volume due to the difference in phases' densities, resulting in a change in pressure). The same holds for forces due to thermally induced expansion and contraction. The here-presented model is, to the authors' best knowledge, the only published fluid-dynamical model of laser material processing to date that is not relying on an explicitly calculated evaporation-induced recoil pressure, except for the model of Flint et al. [15], where the incompressible continuity equation is modified through a source term active at phase interfaces during evaporation to account for the associated volumetric change and thus recoil pressure.

2.2 Mass-of-Fluid Method

One of the most predominant models for the simulation of segregated phases using the Finite Volume Method (FVM) is the Volume-of-Fluid (VoF) method, developed by Hirt and Nichols [35]. Within that framework, phase volume fractions are tracked via advection on a previously obtained velocity field. The thus obtained phase volume fraction distribution is used to update the spatial distribution of material properties

such as the density. As this approach is not inherently mass conservative for compressible phases, we propose an altered scheme which we call *Mass-of-Fluid* (MoF) method. Here, we directly track the conserved quantity of the phases' mass, which leads to mass conservative advection and phase changes even in highly compressible scenarios. The implementation of phase changes between phase-pairs is relatively straightforward within this framework.
We define a quantity ρ_i for each phase i of an N-phase problem as

$$\rho_i = \frac{m_{i,CV}}{V_{CV}}, \tag{7}$$

where $m_{i,CV}$ is the mass of phase i within a control volume V_{CV}. Note that CV denotes the hypothetical concept of a control volume, and ρ_i is a function continuous in space and time governed by Eq. (9). The mixture density ρ (i.e., average density of the mixture of N phases) is obtained through summation as

$$\rho = \sum_{i=1}^{N} \rho_i. \tag{8}$$

We introduce a conservation equation for each phase's local mass density reading

$$\frac{\partial \rho_i}{\partial t} + \nabla \cdot (\boldsymbol{u}\rho_i) = \dot{\rho}_{i,m} + \dot{\rho}_{i,s} + \dot{\rho}_{i,e} + \dot{\rho}_{i,c}, \tag{9}$$

where the four source terms on the RHS of Eq. (9) represent the change in ρ_i due to melting, solidification, evaporation and condensation, respectively. Eq. (9) represents phase-wise contiuity equations that always fulfill Eq. (1), i.e., global continuity, due to Eq. (8) and the fact that for any phase pair i, j undergoing phase change, the source terms on the RHS of Eq. (9) sum to zero. For example, for i, j denoting a solid and liquid phase that exchange mass through melting, $\dot{\rho}_{i,m} = -\dot{\rho}_{j,m}$. Hence,

$$\textstyle\sum_i^N \dot{\rho}_{i,m} = 0, \tag{10}$$
$$\textstyle\sum_i^N \dot{\rho}_{i,s} = 0, \tag{11}$$
$$\textstyle\sum_i^N \dot{\rho}_{i,e} = 0, \tag{12}$$
$$\textstyle\sum_i^N \dot{\rho}_{i,c} = 0. \tag{13}$$

The four source terms on the RHS of Eq. (9) representing phase changes are defined in Section 2.4. Eq. (9) provides a full description of the temporal and spatial distribution of phases within the mixture.
While the mixture density is obtained from Eq. (8), other properties of the mixture (e.g., thermophysical properties) are obtained through volume-weighted averaging based on the individual phase volume fractions, α_i. Generally, we choose different physically motivated averaging approaches for different physical quantities (e.g., harmonic averaging is often reasonable in the case of thermal conductivity), but for the sake of simplicity we only use arithmetic averaging throughout this work s.t. for any mixture physical property ϕ,

$$\phi = \sum_{i}^{N} \alpha_i \phi_i, \tag{14}$$

where ϕ_i denotes the physical property value of the respective phase i and α_i is the volume fraction of phase i. The relationship between density and pressure of all phases is modeled via the Tait equation [36, 37] as

$$\rho_{th,i}(p) = \rho_{ref,i} \sqrt[\gamma_i]{\frac{p + B_i}{p_{ref} + B_i}}. \tag{15}$$

Here, $\rho_{th,i}$ denotes the density of phase i, i.e., a temperature- and pressure-dependent material property of phase i, not to be confused with ρ_i. Furthermore, $\rho_{ref,i} = \rho_{th,i}(p_{ref})$ is the temperature-dependent density of phase i at reference pressure p_{ref}, which is the temperature-dependent density value reported in the respective Tables of Section 4 and Appendix A as simulation input parameter, with $p_{ref} = 10^5$Pa. B_i and γ_i are empirical constants (Tait pressure and heat capacity of a liquid, respectively), where we use the bulk modulus K_i to define $B_i = K_i/\gamma_i$. The parameter γ_i influences the compressibility behaviour of the phase, where $\gamma_i = 1$ yields the case of an ideal gas, and $\gamma_i = 7.15$ is a typical value for water. Gaseous behaviour that diverges from that of an ideal gas can conveniently be accounted for by choosing an appropriate value for γ. Regarding condensed phases, it is difficult to obtain a value for γ for fluids other than water, but the difference only becomes relevant for extreme pressure changes. Therefore, for most scenarios, if no other data is available, we choose $\gamma_{cond} = 7.15$ for all condensed (solid and liquid) phases. Especially for solid phases, the value of γ is not too relevant in most cases, as the absolute value of K (and thus B) is of several orders of magnitude higher than that of a liquid. Figure 3 shows the relationship between a pressure change and the resulting change in volume (represented by the volume fraction) as determined by Eq. (15) for different values of γ and for the assumption of a constant compressibility (and hence bulk modulus).
The volume fraction α_i needed for evaluation of Eq. (14) is implicitly defined through ρ_i and $\rho_{th,i}$.

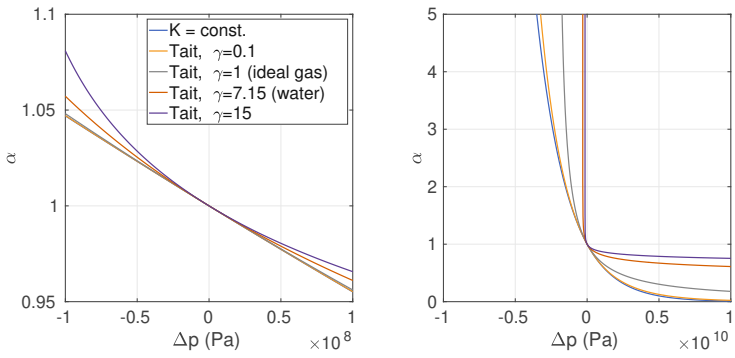

Figure 3: Comparison of α with respect to Δp for liquid water, using different assumptions of bulk modulus-pressure dependence, dK/dp. Left and right plot are identical, except for the value range of Δp.

2.3 Energy Equation

Due to the homogeneous equilibrium mixture assumption, all phases share a common temperature T, with the gradient of T being relevant for heat conduction. Convective

transport however, is associated with the individual phases and their motion. We thus decouple convective and conductive transport of energy in the following manner. Convective transport of energy is ensured through N equations of the form

$$\begin{aligned} \frac{\partial H_i}{\partial t} + \nabla \cdot (\boldsymbol{u} H_i) + S_{p,i} = \\ Q_{abs,i} + \dot{H}_{i,m} + \dot{H}_{i,s} + \dot{H}_{i,e} + \dot{H}_{i,c}, \end{aligned} \tag{16}$$

where $H_i = \rho_i h_i$ denotes the energy of phase i, with h_i denoting the specific energy of phase i. The last four source terms on the RHS of Eq. (16) represent the change in energy of phase i due to phase change, analogously to Eq. (9). The energy of the mixture is obtained through summation, i.e.,

$$H = \sum_{i=1}^{N} H_i. \tag{17}$$

The source term $Q_{abs,i}$ in Eq. (16) denotes the laser energy absorbed by phase i. The simplest way of distributing the absorbed laser energy, Q_{abs}, among phases, which we use here, is via

$$Q_{abs,i} = \frac{\rho_i}{\rho} Q_{abs}, \tag{18}$$

which represents an energy conservative distribution due to Eq. (8). As some materials, such as glass, are highly transparent in their solid state, we usually employ a distribution based on the phases' optical densities (e.g., the simulations presented in [30]), which we do not consider here for the sake of simplicity. For details on the calculation of Q_{abs}, cf. Section 2.5. The source term $S_{p,i}$ represents thermal-pressure coupling, again distributed in an energy-conserving manner among phases i, and reads

$$S_{p,i} = \frac{\rho_i}{\rho} \left(\frac{\partial (\rho k)}{\partial t} + \nabla \cdot (\rho \boldsymbol{u} k) - \frac{\partial p}{\partial t} \right) \tag{19}$$

with $k = 0.5(\boldsymbol{u} \cdot \boldsymbol{u})$. Heat conduction is modeled through

$$\frac{\partial (\rho c_p T)}{\partial t} = \nabla \cdot (\lambda \nabla T), \tag{20}$$

where λ, ρ, and c_p denote mixture thermal conductivity, density and specific heat capacity, respectively.

2.4 Phase Change

Phase changes are modeled as transfer of mass and energy between two phases, making these processes inherently mass- and energy conservative. Furthermore, associated effects such as evaporative cooling or recoil pressure are an implicit result of the phase change model, as the transfer of energy, between two phases issues a change in temperature due to the latent heat separating the phase energies, and a mass transfer between two phases of different densities issues a change in volume, and thus pressure. The phase change model therefore only needs to yield how much mass (and associated energy) is to be exchanged between two phases depending on the local temperature and pressure.

2.4.1 Melting - Solidification

Melting and solidification are modeled as energy-based mass transfer. Denoting solid and liquid phase of a material undergoing melting or solidification with the subscripts s and l, respectively, we define the excess energy for melting or solidification, following the Enthalpy-porosity method [38], as

$$\Delta E_{melt} = H_s - \rho_s h_s(T_{solidus}), \tag{21}$$

$$\Delta E_{solidif} = \rho_l h_l(T_{liquidus}) - H_l, \tag{22}$$

where $h_i(T)$ denotes the specific heat at temperature T, and H_i is the energy of phase i (cf. Section 2.3). We then define the rate of melting and solidification as

$$\dot{\rho}_{l,m} = -\dot{\rho}_{s,m} = \rho_s \frac{\Delta E_{melt}}{L_{fus}} \frac{1}{\tau_{prop}}, \tag{23}$$

$$\dot{\rho}_{s,s} = -\dot{\rho}_{l,s} = \rho_l \frac{\Delta E_{solidif}}{L_{fus}} \frac{1}{\tau_{prop}}, \tag{24}$$

where L_{fus} is the latent heat of fusion and τ_{prop} is a propagation time. For pure elements, which undergo phase change at a dedicated melting temperature, we set $T_{liquidus} = T_{solidus} = T_{melting}$, whereas alloys typically feature a melting interval between $T_{solidus}$ and $T_{liquidus}$, within which the material is in a mushy state. In Figure 4, the results for a simple one-dimensional Stefan problem are shown, for an alloy and a pure element of constant heat capacity (where, in this case, the melting temperature of the pure element equals the liquidus temperature of the alloy). The resulting solidification behaviour is in agreement with metallurgical theory [39].

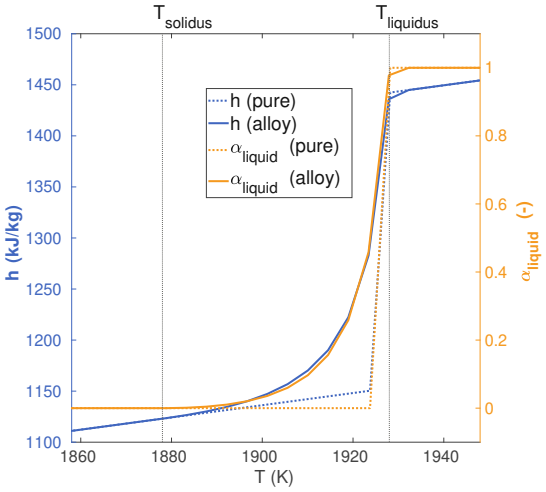

Figure 4: Illustration of melting and solidification: Liquid volume fraction α_{liquid} and mass-specific energy h for an alloy featuring a melting interval, and a pure element, over Temperature T in a one-dimensional domain, where one boundary is set to $T_{hot} > T_{liquidus}$ and one boundary is set to $T_{cold} < T_{solidus}$. The results are plotted after a steady state is reached.

2.4.2 Evaporation - Condensation

We consider pressure-driven evaporation and condensation, as

$$\dot{\alpha}_v = |c_1| \left(p_{sat} - p_{ext}\right), \tag{25}$$

where α_v is the volume fraction of the vapor phase of a liquid-vapor phase pair l, v, undergoing evaporation or condensation, p_{sat} denotes the local saturation pressure, which is calculated according to the Clausius-Clapeyron law as

$$p_{sat}(T) = p_{ref} \exp\left(\frac{M L_{vap,eff}}{T_b R}\left(1 - \frac{T_b}{T}\right)\right), \tag{26}$$

with T_b, $L_{vap,eff}$, M and R denoting the material's boiling temperature, effective latent heat of vaporization, molar mass and the universal gas constant, respectively. The reduction of latent heat of vaporization from its reference value L_{vap} towards the critical point T_{crit} is modeled through the Watson equation [40] as

$$L_{vap,eff} = L_{vap}\left(\frac{T_{crit} - T}{T_{crit} - T_b}\right)^{0.38}. \tag{27}$$

Furthermore, p_{ext} denotes local external vapor pressure, and c_1 is a constant obtained from the Hertz-Knudsen model, related to the theoretical maximum instantaneous evaporation (or condensation, depending on the sign of the pressure difference in Eq. (25)) rate,

$$c_1 = \begin{cases} \varepsilon_e \sqrt{\frac{M}{2\pi RT}} \frac{1}{\xi \cdot \rho_{ref,l}(T)} \forall (p_{sat} > p_{ext}) \\ -\varepsilon_c \sqrt{\frac{M}{2\pi RT}} \frac{1}{\xi \cdot \rho_{ref,v}(T)} \forall (p_{sat} < p_{ext}) \end{cases}. \tag{28}$$

Here, subscripts l and v denote again the liquid and vapor phase of the material undergoing phase change and ξ is the thickness of the liquid-vapor interface. The model fully resolves the vapor phase and pressure increases, associated with evaporation, are directly linked to a reduction of the evaporation rate via an increase of p_{ext} in Eq. (25). Hence, no evaporation efficiency is needed and we set $\varepsilon_e = 1$. To account for the need for heterogeneous nucleation in condensation processes (or significant subcooling in the case of homogeneous nucleation) we set the condensation efficiency as $\varepsilon_c = \max(\sum \alpha_{cond}, 10^{-6})$, with $\sum \alpha_{cond} \leq 1$ denoting the sum of volume fraction of condensed matter, promoting condensation in the vicinity of condensed matter. The change in ρ_l and ρ_v due to evaporation and condensation is then given by

$$\dot{\rho}_{l,e} = -\dot{\rho}_{v,e} = -\rho_l \dot{\alpha}_v^+, \tag{29}$$

$$\dot{\rho}_{l,c} = -\dot{\rho}_{v,c} = \rho_v \dot{\alpha}_v^-. \tag{30}$$

Note that here (and throughout this work), for any quantity x, x^+ and x^- are defined as

$$x^+ = \begin{cases} |x| & \forall x \geq 0 \\ 0 & \forall x < 0 \end{cases}, \tag{31}$$

$$x^- = \begin{cases} 0 & \forall x \geq 0 \\ |x| & \forall x < 0. \end{cases} \tag{32}$$

2.5 Laser Beam Propagation and Laser-Material Interaction

Only a brief overview on the beam propagation and laser-material interaction model is provided here, as the focus of this work lies on the fluid mechanical model. The main

quantity of interest with respect to the fluid mechanical problem is the absorbed laser energy Q_{abs}, which is introduced as source term in the convective energy transport equation (16) and distributed among phases i in a manner equivalent to Eq. (18). We outline the model here at the example of a Gaussian laser intensity distribution, but in principle, any other type of intensity distribution for which an analytical or numerical (e.g., in the case of an experimentally measured laser beam profile) description is available can be treated analogously.
Utilizing the paraxial approximation and using cylindrical coordinates r, z, where z denotes the distance from the beam's focal point along its optical axis and r denotes the radial distance from the optical axis, the axisymmetrical intensity distribution $I(r, z)$ of a Gaussian laser beam is defined as [41]

$$I(r,z) = I_0 \left(\frac{w_0}{w(z)}\right)^2 \exp\left(\frac{-2r^2}{w(z)^2}\right), \tag{33}$$

where $I_0 = I(r = 0, z = 0)$ is the intensity at the focus, $w(z)$ is the beam's radius, with $w_0 = w(z = 0)$ being the focal radius, i.e., its minimum value. The radius is usually defined as the distance from the optical axis, at which $I = \exp(-2)$, i.e., approx. 86% of laser intensity lies within the radius. The axial profile of the radius is defined as [41]

$$w(z) = w_0 \sqrt{1 + \left(\frac{z}{z_R}\right)^2}, \tag{34}$$

where z_R is the Rayleigh length, reading

$$z_R = \frac{n\pi w_0^2}{M^2 \lambda_0}, \tag{35}$$

with n denoting the refractive index of the medium through which beam propagates, λ_0 denoting the vacuum wave length of the laser beam and M^2 being a quality factor describing the divergence of a real laser beam with respect to a perfect Gaussian beam. The case of $M^2 = 1$ is associated with a perfect Gaussian beam, and $M^2 > 1$ holds true for real beams. The radius of curvature of the propagating beam's wavefront, R_c, is defined as [41]

$$R_c(z) = z\left(1 + \left(\frac{z_R}{z}\right)^2\right). \tag{36}$$

Utilizing the above beam description, we now define a unit vector $\boldsymbol{r}$ which is aligned with the laser beam's local direction of propagation, i.e., a unit vector normal to the wavefront of the laser beam, as

$$\boldsymbol{r}(r,z) = \frac{\cos(\theta)\boldsymbol{e}_z + \sin(\theta)\boldsymbol{e}_r}{|\cos(\theta)\boldsymbol{e}_z + \sin(\theta)\boldsymbol{e}_r|}, \tag{37}$$

with

$$\theta(r,z) = \arcsin\left(\frac{r}{R_c(z)}\right). \tag{38}$$

Up until initial incidence (first interaction between laser beam and condensed matter) we model beam propagation through a set of coupled steady-state Radiative Transport Equations (RTE) for laser intensity propagating through gaseous and condensed

phases, respectively, I_g and I_{cond}, reading

$$\begin{aligned}\nabla \cdot (\boldsymbol{r} I_g) = \\ &- (\zeta_g + \zeta_{plasma})\, I_g \\ &- \frac{[\nabla \cdot (\boldsymbol{r}\alpha_{cond})]^+}{\alpha_g} I_g \\ &+ (1-R)\,\frac{[\nabla \cdot (\boldsymbol{r}\alpha_{cond})]^-}{\alpha_{cond}} I_{cond},\end{aligned} \tag{39}$$

and

$$\begin{aligned}\nabla \cdot (\boldsymbol{r} I_{cond}) = \\ &- \zeta_{cond} I_{cond} \\ &- \frac{[\nabla \cdot (\boldsymbol{r}\alpha_{cond})]^-}{\alpha_{cond}} I_{cond} \\ &+ (1-R)\,\frac{[\nabla \cdot (\boldsymbol{r}\alpha_{cond})]^+}{\alpha_g} I_g.\end{aligned} \tag{40}$$

Here, the steady-state assumption is motivated as the timescales of propagating light (at the speed of light) are much smaller than any thermo-fluid-mechanical timescales encountered within the process. Distinguishing between propagation through gaseous and condensed matter is necessary to consider partial reflection upon incidence on condensed matter, which is accounted for through the second and third source term on the RHS of Eqs. (39) and (40), respectively. The subscripts *cond* and g denote condensed and gaseous matter, respectively. Hence, $\alpha_{cond} = \sum_i^{N_{cond}} \alpha_i$ and $\alpha_g = \sum_i^{N_g} \alpha_i$ denote the volume fractions of condensed and gaseous matter, respectively. R denotes the material's reflectivity which is calculated based on the laser beam's incident angle using the Fresnel Equations [42],

$$R_S = \left| \frac{cos(\beta) - \underline{n}\sqrt{1 - sin^2(\beta)/\underline{n}^2}}{cos(\beta) + \underline{n}\sqrt{1 - sin^2(\beta)/\underline{n}^2}} \right|, \tag{41}$$

$$R_P = \left| \frac{\underline{n}cos(\beta) - \sqrt{1 - sin^2(\beta)/\underline{n}^2}}{\underline{n}cos(\beta) + \sqrt{1 - sin^2(\beta)/\underline{n}^2}} \right|, \tag{42}$$

$$R = \frac{R_S + R_P}{2}, \tag{43}$$

where $\underline{n} = n + \mathrm{i}\kappa$ denotes the complex refractive index (consisting of refractive index n and extinction coefficient κ of the material, with i being the imaginary unit in this context), and β is the local angle of incidence, defined as $\beta = \arccos(\boldsymbol{n}_{cond} \cdot \boldsymbol{r})$, with $\boldsymbol{n}_{cond} = (\nabla\alpha_{cond})/(|\nabla\alpha_{cond}|)$. ζ_g and ζ_{plasma} are the absorptivity of gas and plasma, respectively, which are irrelevant for all cases investigated hereafter, as the absorptivity of vapor is set to zero in all subsequent test cases (as the gaseous phases' extinction coefficient κ is zero, and hence $\zeta_g = 0$), and no plasma forms, hence $\zeta_{plasma} = 0$. The interested reader is referred to [29] for more information on our plasma absorption model. The absorptivity of condensed matter, ζ_{cond} is modeled as

$$\zeta_{cond} = \frac{\sum_i^{N_{cond}} \alpha_i \left(\frac{4\pi\kappa_i}{\lambda_0} + \zeta_{i,NL} \right)}{\sum_i^{N_{cond}} \alpha_i}, \tag{44}$$

with $\zeta_{i,NL}$ denoting nonlinear absorption terms, which are not relevant for the materials and laser intensities investigated within this work, and are therefore being neglected hereafter for the sake of brevity. Hence, $\zeta_{i,NL} = 0$. Subsequent reflections after the initial incidence described by Eqs. (39)-(40) are accounted for through a ray tracing model. Within the ray tracing model, reflections at the ($\alpha_{cond} = 0.5$)-isosurface are calculated again angle-of-incidence-dependent using Eqs. (41)-(43). We finally obtain the absorbed laser energy from the input laser energy Q_{input} as $Q_{abs,I} = I_{cond}Q_{input} + Q_{abs,MR}$, with $Q_{abs,MR}$ denoting the amount of laser energy absorbed due to multiple reflections after initial incidence. The main advantage of splitting the beam propagation model into initial incidence following a set of RTEs and subsequently, a multiple reflection model, is the fact that the converging-diverging caustic of a laser beam can hence be accounted for. A pure ray tracing-based approach cannot account for the spatial change in beam divergence that is inherent to laser beams. On the other hand, neglecting multiple reflections would lead to unrealistically low absorption values, as in the case of a vapor depression or keyhole, or in the case of complex work piece geometries, multiple reflections are crucial for absorption and thus should not be neglected.

3 Numerical Methods

The governing equations laid out in Section 2 are solved using a pressure-based, segregated Finite Volume Method. Details on the Finite Volume Method and its implementation in `OpenFOAM` can be found, e.g., in [43–46]. In this Section, we briefly lay out the numerical implementation and solution algorithm, with emphasis on parts that differ from the numerical implementation of the VoF solver `multiphaseInterFoam` [47, 48] (the N-phase extension of the VoF solver `interFoam` [49]), which is the initial starting point for the numerical implementation of this work's model. The solution algorithm within one time step k of the transient solution procedure is summarized briefly in Table 1. Details regarding the most crucial steps of the solution procedure laid out in Table 1 are provided in Sections 3.1-3.5. Here, the superscript $k-1$ denotes the solution of the previous time step and superscript k denotes the solution of the current time step.

3.1 Courant Number

As laser material processing is not always a convection-dominated problem (e.g., low intensity conduction-mode heating without melting, or wait times between scan tracks and layers in additive manufacturing via powder bed fusion, etc.), we limit the time increment by the maximum of convective and diffusive Courant numbers, ensuring

$$\mathrm{Co} = \max\left(\frac{\lambda \Delta t}{c_p \rho \Delta x^2}, \frac{|\boldsymbol{u}|\Delta t}{\Delta x}\right) \leq 1, \tag{45}$$

with λ, c_p, and ρ denoting mixture values of thermal conductivity, specific heat capacity, and density, respectively, and Δx denoting in this context the minimum dimension of a computational cell.

`for each timestep` k`, do:`	
	Update time increment Δt^k based on Eq. (45)
1	**Phase and energy advection**
	1a Solve Eq. (46) for $\rho^k_{i,conv}$ using $\boldsymbol{u}^{k-1}$ and α^{k-1}_i
	1b Solve Eq. (48) for $H^k_{i,conv}$ using $\boldsymbol{u}^{k-1}$, $Q^{k-1}_{abs,i}$, and $S^{k-1}_{p,i}$
	1c Calculate T^k_{conv} from H^k_{conv} as laid out in Section 3.2
	1d Phase-norming by minimizing Eq. (58) for $\alpha^k_{i,conv}$
2	**Beam propagation**
	2a Solve steady-state RTEs (39) and (40) iteratively using $\alpha^k_{i,conv}$, where in each iteration j, (39) is solved for I_g using I^{j-1}_{cond} and subsequently, (40) is solved for I_{cond} using I^j_g, until $\lvert(I_g + I_{cond})^j - (I_g + I_{cond})^{j-1}\rvert/(I_g + I_{cond})^{j-1} < \delta$
	2b Calculate $Q^k_{abs,I}$ from I^k_{cond}
	2c Calculate $Q^k_{abs,MR}$ via ray tracing algorithm using $Q^k_{abs,I}$ and $\alpha^k_{i,conv}$
	2d Calculate absorbed laser energy $Q^k_{abs} = Q^k_{abs,I} + Q^k_{abs,MR}$
3	**Heat conduction**
	3a Solve Eq. (20) for $T^k_{conduct}$ from T^k_{conv}
	3b Update $H^k_{i,conduct}$ from $T^k_{conduct}$ via Eq. (50)
4	**Phase change**
	4a Evaluate Eqs. (65)-(68) using $T^k_{conduct}$ and $H^k_{i,conduct}$
	4b Obtain ρ^k_i via Eq. (63)
	4c Obtain H^k_i and thus H^k via Eq. (70) and obtain T^k from H^k as laid out in Section 3.2
	4d Phase-norming by minimizing Eq. (58) for α^k_i
	4e Calculate Ψ^k from Eq. (62) using α^k_i
5	**PISO-Loop**
	5a Evaluate momentum predictor (75) using current values
	5b Solve pressure equation (77)
	5c Calculate $\boldsymbol{u}^k$ from Eq. (76) , calculate $S^k_{P,i}$ for use in timestep $k+1$
`end timestep`	

Table 1: Overview of solution algorithm within a time step k.

3.2 Phase and Energy Advection

We modify Eq. (9) by omitting the RHS terms related to phase change which are accounted for by explicit updating of ρ_i values in a separate step of the solution procedure denoted *Phase Changes* (step 4 in Table 1). Furthermore, we introduce an interface compression term following the widely used Weller scheme [45] to keep a sharp interface between condensed and gaseous phases, yielding

$$\frac{\partial \rho_i}{\partial t} + \nabla \cdot \left[\left(\boldsymbol{u}^{k-1} + \boldsymbol{u}_c^{k-1} \right) \rho_i \right] = 0, \tag{46}$$

where $\boldsymbol{u}_c$ represents an artificial interface compression velocity only active at the phase interface of condensed phases, defined as

$$\boldsymbol{u}_c = c_\alpha \boldsymbol{u} \frac{\nabla \alpha_{cond}}{|\nabla \alpha_{cond}|} \alpha_{cond}(1 - \alpha_{cond}). \tag{47}$$

Here, $c_\alpha = 0$ corresponds to no interface compression, and $c_\alpha > 0$ introduces interface compression to counteract numerical diffusion. Usually, a value between 1 and 1.5 gives good results, in accordance with the findings of [45]. Throughout this work, a value of $c_\alpha = 1$ is chosen.
Convective transport of energy on a predetermined velocity field is ensured by solving Eq. (16) in the form

$$\frac{\partial H_i}{\partial t} + \nabla \cdot \left[\left(\boldsymbol{u}^{k-1} + \boldsymbol{u}_c^{k-1} \right) H_i \right] + S_{p,i}^{k-1} = Q_{abs,i}^{k-1}, \tag{48}$$

where again phase change-related sources on the RHS of Eq. (16) are omitted and accounted for in step 4. After solving Eq. (48) to obtain $H_{i,conv}^k$, we calculate the mixture energy after convection, H_{conv}^k, via Eq. (17). Then, following the manner of temperature recovery methods [39], we determine the distribution of T_{conv}^k through a Newton-Raphson iteration of the form

$$T_{n+1} = T_n + \frac{H - H_n}{C_{p,n}}, \tag{49}$$

where

$$H_n = \sum_{i=1}^{N} \rho_i h(T_n) \tag{50}$$

is the energy achieved by summation of phase energies at temperature T_n. Note that n denotes an iteration index within this context. The converged temperature value after the above iteration is then denoted $T_{conv}^k = T_{n,final}$, the temperature after convective heat transport.

3.3 Phase-Norming

Each time we change the distribution of ρ_i (i.e., after solving Eq. (48) or after explicitly updating ρ_i in step 4), we need to obtain the distribution of phase volume fractions, α_i. We now utilize the relationship between ρ_i and α_i implicitly laid out in Section 2.2 to derive a numerical scheme to obtain α_i for any given ρ_i, which we call *phase-norming*.
We define a quantity

$$A_i = \frac{\rho_i}{\rho_{ref,i}}, \tag{51}$$

which is not to be confused with the volume fraction α_i. Here, $\rho_{ref,i}$ again denotes the temperature-dependent density of phase i at reference pressure p_{ref}. In contrast to a volume fraction, A_i is (in the general case) of non-unitary sum, i.e.,

$$\sum_{i=1}^{N} A_i \neq 1. \tag{52}$$

Two mechanisms can lead to $\sum A_i \neq 1$: Firstly, mass can enter or leave a control volume through convection, changing ρ_i, and secondly, $\rho_{ref,i}$ can change through phase changes or with temperature following thermal expansion or contraction. Generally,

we encounter two different cases, which are schematically illustrated in Figure 5: a) expansion, characterized by $\sum A_i < 1$, and b) compression, characterized by $\sum A_i > 1$. In Figure 5, we consider two phases of different bulk moduli K_i, with $K_1 > K_2$. For the same pressure change Δp, phases with lower bulk modulus K_i experience a larger volumetric change ΔV (and vice versa). Phase-norming aims at

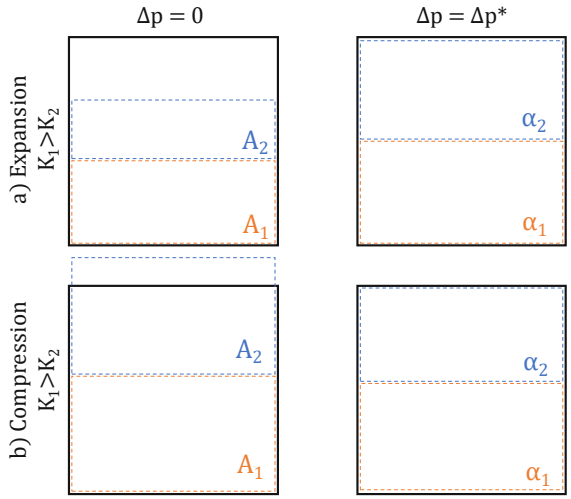

Figure 5: Schematic illustration of phase-norming within the MoF method for the example of two phases of different bulk moduli in a control volume (black outline). Depending on the value of $\sum A_i$ within the control volume, we distinguish between expansion (top) and compression (bottom). At a given pressure change Δp, phases with a lower bulk modulus experience a larger volumetric change (and vice versa).

finding the necessary local change in pressure Δp^* to fulfill

$$\sum_{i=1}^{N} A_i = 1, \tag{53}$$

i.e., the amount of expansion or compression required to achieve the given distribution of ρ_i. Using the definition of the bulk modulus, we introduce a relation between α_i and pressure p as

$$\frac{dp}{K_i} = -\frac{d\alpha_i}{\alpha_i}, \tag{54}$$

which is only valid for infinitesimal changes. For arbitrarily large changes we integrate over the isothermal change from state S_0 to state S_1,

$$\int_{S_0}^{S_1} \frac{dp}{K_i} = -\int_{S_0}^{S_1} \frac{d\alpha_i}{\alpha_i}. \tag{55}$$

To solve Eq. (55), we utilize the Tait equation, Eq. (15), yielding

$$\alpha_{i,1} = \frac{\alpha_{i,0}}{\sqrt[\gamma_i]{\frac{\Delta p}{B_{i,0}} + 1}}, \tag{56}$$

where $\alpha_{i,0}$ and $\alpha_{i,1}$ denote the volume fraction at states S_0 and S_1, respectively, where an isothermal change in pressure, Δp, was applied. We now utilize Eq. (56) to find

Δp^* which is the necessary local change in pressure required to fulfill Eq. (53), as

$$\alpha_i = A_i \forall \left(\sum_{i=1}^{N} A_i = 1 \right). \tag{57}$$

We hence consider $\alpha_{i,0} = A_i$ and $\alpha_{i,1} = \alpha_i$, and aim at minimizing the term

$$\left(\sum_{i=1}^{N} \alpha_i \right) - 1 = \left(\sum_{i=1}^{N} \frac{A_i}{\sqrt[\gamma_i]{\frac{\Delta p}{B_i} + 1}} \right) - 1, \tag{58}$$

which can be directly computed for $N = 1$, but requires an iterative solution procedure for the general case of $N > 1$ with $K_i \neq K_j \; \forall i \neq j$. As the function in Eq. (58) is monotonic, we employ a bisection algorithm to find its minimum. Though showing slower convergence than, e.g., the Newton-Raphson method, it comes with the advantage of guaranteed convergence, independent of the starting value. The process of phase-norming is finished once the iterative root-finding of Eq. (58) has converged, i.e., $\left| \left(\sum_{i=1}^{N} \alpha_i \right) - 1 \right| \leq \delta$, with δ being a sufficiently small convergence tolerance. Then, $\Delta p = \Delta p^*$ and after finding Δp^*, we calculate a new value for the density-normed mixture compressibility, Ψ, as

$$\Psi = \frac{\psi}{\rho} = \frac{1}{K_{mixture}}, \tag{59}$$

where $K_{mixture}$ is not yet known, and for which we use the definition of the bulk modulus, as

$$\Psi = -\frac{d\left(\sum_i^N \alpha_i \right)}{\sum_i^N \alpha_i \cdot dp}, \tag{60}$$

and utilizing Eq. (56) yields

$$\Psi = -\frac{d\left(\sum_i^N \frac{A_i}{\sqrt[\gamma_i]{\frac{\Delta p \gamma_i}{K_i} + 1}} \right)}{\sum_i^N \alpha_i \cdot dp}. \tag{61}$$

Differentiation at $\Delta p = \Delta p^*$ leads to

$$\Psi^* = \Psi(\Delta p^*) = \sum_i^N \frac{\alpha_i}{\gamma_i (\Delta p^* + K_i/\gamma_i)}. \tag{62}$$

After phase-norming, we know the values of α_i (i.e., the volume fractions fulfilling Eq. (53)) which are used for tracking phase interfaces, e.g., as utilized in Eqs. (39)-(40) or Eq. (47), and for calculating volume-weighted material property values for the mixture of phases via Eq. (14). Furthermore, the value of $p^* = p_{ref} + \Delta p^*$ is used for pressure-based evaporation and condensation (cf. Section 3.4) and Ψ^* is used in the pressure equation within the PISO-loop (cf. Section 3.5).

3.4 Phase Changes

The change of ρ_i due to the RHS terms in Eq. (9) is accounted for by explicitly updating ρ_i via

$$\rho_i^k = \rho_{i,conv}^k + \Delta\rho_{i,m}^k + \Delta\rho_{i,s}^k + \Delta\rho_{i,e}^k + \Delta\rho_{i,c}^k. \tag{63}$$

For melting and solidification, the propagation time τ_{prop} occurring in Eqs. (23) and (24) is simply taken as

$$\tau_{prop} = \frac{\Delta x_{LS}}{c_{sound}}, \tag{64}$$

with c_{sound} denoting the speed of sound and Δx_{LS} being the local Finite Volume cell length normal to the solid-liquid interface. The amount of mass molten or solidified within a time step is then calculated for any liquid-solid phase pair l, s undergoing phase change as

$$\Delta\rho_{l,m}^k = -\Delta\rho_{s,m}^k = \Delta t^k \rho_s^k \frac{\Delta E_{melt}}{L_{fus}} \frac{1}{\tau_{prop}}, \tag{65}$$

$$\Delta\rho_{s,s}^k = -\Delta\rho_{l,s}^k = \Delta t^k \rho_l^k \frac{\Delta E_{solidif}}{L_{fus}} \frac{1}{\tau_{prop}}, \tag{66}$$

and $\Delta\rho_{i,m}$ and $\Delta\rho_{i,s}$ are zero for all other phases. The amount of mass evaporated or condensed within a time step is calculated for any liquid-vapor phase pair l, v undergoing phase change as

$$\Delta\rho_{v,e}^k = -\Delta\rho_{l,e}^k = \rho_l^k \left(1 - \exp\left(-\frac{\Delta t^k c_1 (p_{sat} - p_{ext})}{1 + \frac{|c_1|\Delta t^k}{\tilde{\Psi}^*}}\right)\right), \tag{67}$$

$$\Delta\rho_{l,c}^k = -\Delta\rho_{v,c}^k = \rho_v^k \left(1 - \exp\left(-\frac{\Delta t^k c_1 (p_{sat} - p_{ext})}{1 + \frac{|c_1|\Delta t^k}{\tilde{\Psi}^*}}\right)\right), \tag{68}$$

where c_1 is calculated according to Eq. (28), with ξ simply taken as the local Finite Volume cell length normal to the liquid-vapor interface. To account for the possibility of newly created vapor to escape into the vicinity, due to the pressure level surrounding the liquid-vapor interface, we employ a time step- dependent limiter in the above term using a locally averaged compressibility, $\tilde{\Psi}$, calculated within a computational cell j as

$$\tilde{\Psi}_j = \frac{\sum_{m \in U(j)} V_m \Psi_m}{\sum_{m \in U(j)} V_m}, \tag{69}$$

with $U(j)$ denoting all cells that share a face with cell j.
When updating the values of ρ_i following phase change, we also transfer the respective fraction of energy H_i associated with $\Delta\rho_i$ between the phases involved in the phase change process via

$$H_i^k = H_{i,conduct}^k + \Delta H_{i,m}^k + \Delta H_{i,s}^k + \Delta H_{i,e}^k + \Delta H_{i,c}^k, \tag{70}$$

where

$$\Delta H^k_{i,m} = \Delta \rho^k_{i,m}\ h_i(T^k_{conduct}), \tag{71}$$
$$\Delta H^k_{i,s} = \Delta \rho^k_{i,s}\ h_i(T^k_{conduct}), \tag{72}$$
$$\Delta H^k_{i,e} = \Delta \rho^k_{i,e}\ h_i(T^k_{conduct}), \tag{73}$$
$$\Delta H^k_{i,c} = \Delta \rho^k_{i,c}\ h_i(T^k_{conduct}). \tag{74}$$

3.5 PISO-Loop

To establish pressure-velocity coupling we employ a PISO algorithm (Pressure Implicit with Splitting of Operators, cf. [45] for a detailed description), where we use a typical decomposition of the matrix form of the momentum equation (2) as

$$\boldsymbol{A}\boldsymbol{u} - \boldsymbol{H} \equiv \frac{\partial(\rho \boldsymbol{u})}{\partial t} + \nabla \cdot (\rho \boldsymbol{u}\boldsymbol{u}) - \nabla \cdot \boldsymbol{\tau} - \boldsymbol{S_D} + \boldsymbol{S_B} - \boldsymbol{S_S}, \tag{75}$$

and thus,

$$\boldsymbol{A}\boldsymbol{u} - \boldsymbol{H} = -\nabla p. \tag{76}$$

A pressure equation is constructed following the approach of [50], making use of the continuity equation (1), as

$$\begin{aligned} &\underbrace{\nabla \cdot \left(\boldsymbol{A}^{-1}\boldsymbol{H}\right) - \nabla \cdot \left(\boldsymbol{A}^{-1}\nabla p\right)}_{\nabla \cdot \boldsymbol{u}} = \\ &\frac{\partial(\Psi^* p)}{\partial t} + \nabla \cdot (\Psi^* \boldsymbol{u} p) - p \nabla \cdot (\Psi^* \boldsymbol{u}), \end{aligned} \tag{77}$$

where we utilize the fact that

$$\frac{1}{\rho}\frac{\partial \rho}{\partial p} = \Psi. \tag{78}$$

4 Results

To assess the accuracy and universality of the model, test cases of increasing complexity are simulated, starting with academic problems and moving on to more complex problems of laser material processing. It is worth noting that, for solving the problems presented hereafter, the exact same model is used, only changing input properties such as the number of phases and their respective thermophysical properties, the domain geometry and its discretization, and initial and boundary conditions. Spatial discretization is, in all subsequent cases (except Case 3), achieved through meshing with a conformal, purely hexahedral mesh of unitary aspect ratio. In two cases (Sections 4.4 and 4.5) mesh refinement is employed, by iteratively splitting a hexahedral Finite Volume into eight smaller volumes of equal size.

4.1 Case 1: Single-Phase Shock Tube

Sod's one-dimensional shock tube problem [51] is simulated and compared to the results obtained with the density-based compressible flow solver `rhoCentralFoam`

[52], in its native `OpenFOAM-6` version [47], which is dedicated to this exact type of problem. Initial conditions, material properties, geometry and spatial and temporal discretization are listed in Table 2 and are identical for both the simulations with this work's model and `rhoCentralFoam`. The constant time step was kept identical for both the fine and coarse mesh, leading to a very low Courant number for the coarse mesh, but the emphasis was put on keeping all parameters unchanged when comparing the coarse and fine solution. Initial values in the left and right part of the domain are denoted by subscripts 1 and 2, respectively. The simulation is performed on a coarse mesh and a fine mesh. No-slip conditions for u, and zero gradient conditions for T, p and ρ_i are employed at the domain boundaries.
The spatial distributions of u, T, p and ρ at time $t = 0.07$ s are shown in Figure 6, where reasonable agreement between the two solvers is achieved on the coarse mesh, and almost perfect agreement is reached on the fine mesh.

property	value	unit
initial conditions		
pressure p_1	$1{\cdot}10^5$	Pa
pressure p_2	$0.1{\cdot}10^5$	Pa
temperature T_1	348.432	K
temperature T_2	278.746	K
velocity $u_1 = u_2$	0	$\mathrm{m{\cdot}s^{-1}}$
material properties		
specific heat capacity c_p	1004.5	$\mathrm{m^2{\cdot}s^{-2}{\cdot}K^{-1}}$
molar mass M	$28.96{\cdot}10^{-3}$	$\mathrm{kg{\cdot}mol^{-1}}$
thermal conductivity λ	0	$\mathrm{kg{\cdot}m{\cdot}s^{-3}{\cdot}K^{-1}}$
dynamic viscosity μ	0	Pa·s
density ρ	*ideal gas law*	$\mathrm{kg{\cdot}m^{-3}}$
heat capacity ratio c_p/c_v	1.4	-
bulk modulus K	$1{\cdot}10^5$	Pa
domain and discretization		
domain length l	10	m
cell size Δx_c (coarse)	0.1	m
cell size Δx_f (fine)	0.01	m
time step Δt	$1{\cdot}10^{-6}$	s

Table 2: Single-Phase Shock Tube: Initial conditions, material properties and discretization.

4.2 Case 2: Two-Phase Shock Tube

A one-dimensional two-phase shock tube (filled with pressurized air and water) is simulated, in the configuration as investigated by Koch et al. [36], which can be seen as a one-dimensional model for cavitation bubble expansion. The purpose of this test case is to validate the model's ability of resolving compressible flow scenarios involving two fluids of different density and compressibility, where discontinuities need to be resolved and a segregated interface needs to be accurately captured. Initial conditions, material properties, geometry and spatial and temporal discretization are listed in

Table 3. It is noted that the initial temperature values are chosen to match the initial density of air used by [36] via the ideal gas law, and is set equal in both sides of the domain as the liquid's density is modeled constant with respect to temperature (the liquid density's dependence on pressure follows the Tait equation, cf. Section 2.2). The results obtained at $t = 0.8$ µs are compared to the exact solution of [36] and provided in Figure 7, exhibiting very good agreement.

property	value	unit
initial conditions		
pressure p_1	$1.5{\cdot}10^{8}$	Pa
pressure p_2	$1{\cdot}10^{5}$	Pa
temperature $T_1 = T_2$	2374.8	K
velocity $u_1 = u_2$	0	$m{\cdot}s^{-1}$
volume fraction $\alpha_{water,1}$	0	-
volume fraction $\alpha_{water,2}$	1	-
volume fraction $\alpha_{air,1}$	1	-
volume fraction $\alpha_{air,2}$	0	-
material properties (water)		
density ρ	998.2061	$kg{\cdot}m^{-3}$
specific heat capacity c_p	4184	$m^2{\cdot}s^{-2}{\cdot}K^{-1}$
thermal conductivity λ	0	$kg{\cdot}m{\cdot}s^{-3}{\cdot}K^{-1}$
kinematic viscosity ν	$3.645{\cdot}10^{-7}$	$m^2{\cdot}s^{-1}$
surface energy σ	0	$N{\cdot}m^{-1}$
bulk modulus K	$2.178{\cdot}10^{9}$	Pa
material properties (air)		
density ρ	*ideal gas law*	$kg{\cdot}m^{-3}$
heat capacity ratio c_p/c_v	1.4	-
molar mass M	$28.96{\cdot}10^{-3}$	$kg{\cdot}mol^{-1}$
specific heat capacity c_p	1004.5	$m^2{\cdot}s^{-2}{\cdot}K^{-1}$
thermal conductivity λ	0	$kg{\cdot}m{\cdot}s^{-3}{\cdot}K^{-1}$
kinematic viscosity ν	0	$m^2{\cdot}s^{-1}$
surface energy σ	0	$N{\cdot}m^{-1}$
bulk modulus K	$1{\cdot}10^{5}$	Pa
domain and discretization		
domain length l	$3{\cdot}10^{-3}$	m
cell size Δx_c (coarse)	$2{\cdot}10^{-6}$	m
cell size Δx_f (fine)	$2{\cdot}10^{-7}$	m
time step Δt	$1{\cdot}10^{-10}$	s

Table 3: Two-Phase Shock Tube: Initial conditions, material properties and discretization.

4.3 Case 3: Converging-Diverging Nozzle

In the context of laser material processing, supersonic flows and their interaction with liquid material are often encountered. One example for such a process is continuous fiberizing by laser melting and supersonic dragging, where continuous glass

nanofibers are produced [53]. Instabilities in the supersonic gas jet, such as shock waves, can cause oscillations of the filament. Another example is the widely employed process of laser cutting, where a supersonic jet is used to remove liquid metal during the process of cutting, and interactions between the jet and the material have a great influence on the resulting process outcome [54]. Thus, to accurately model such processes, the simulation model must be able to accurately predict real-world gas flows including shock waves. Quintero et al. [55] experimentally investigated the supersonic jet produced by a converging-diverging nozzle that is used in a continuous fiberizing process and simulated the jet using different `OpenFOAM` solvers dedicated to single-phase supersonic flow simulations. The problem is simulated with this work's model, and compared to the experimental results of [55]. A sketch of the nozzle used in experiment, and the meshed geometry of the model are shown in Figure 8. The diameter of the nozzle throat and nozzle exit are $D_t = 5$ mm and $D_e = 5.5$ mm, respectively. As turbulence plays a significant role, we include turbulence effects by including a turbulent viscosity μ_t in the viscous stress tensor of Eq. (2), which we calculate from the standard k-ε model. The mesh is equivalent to that reported in [55] (axisymmetric wedge type covering 2.5° of the three-dimensional physical domain, $\Delta x = 50\mu$m). The material is treated as an ideal gas with a molar mass of $M = 28.9$ g·mol^{-1} and a heat capacity ratio of $c_p/c_v = 1.4$. Thermophysical properties, initial conditions and boundary conditions used in the simulation are also equivalent to those reported in detail in [55], and therefore not repeated here.
The results in terms of density, ρ, and its gradient, grad(ρ) are compared to experimental observations in Figure 9, showing good agreement in terms of shock wave structures and locations. The experimental results were obtained through digital holographic interferometry, utilizing the proportional correlation of optical phase and air density. For visualization in Figure 9, the values are normalized by mapping to greyscale values through $[\min, \max] \rightarrow [0, 1]$.

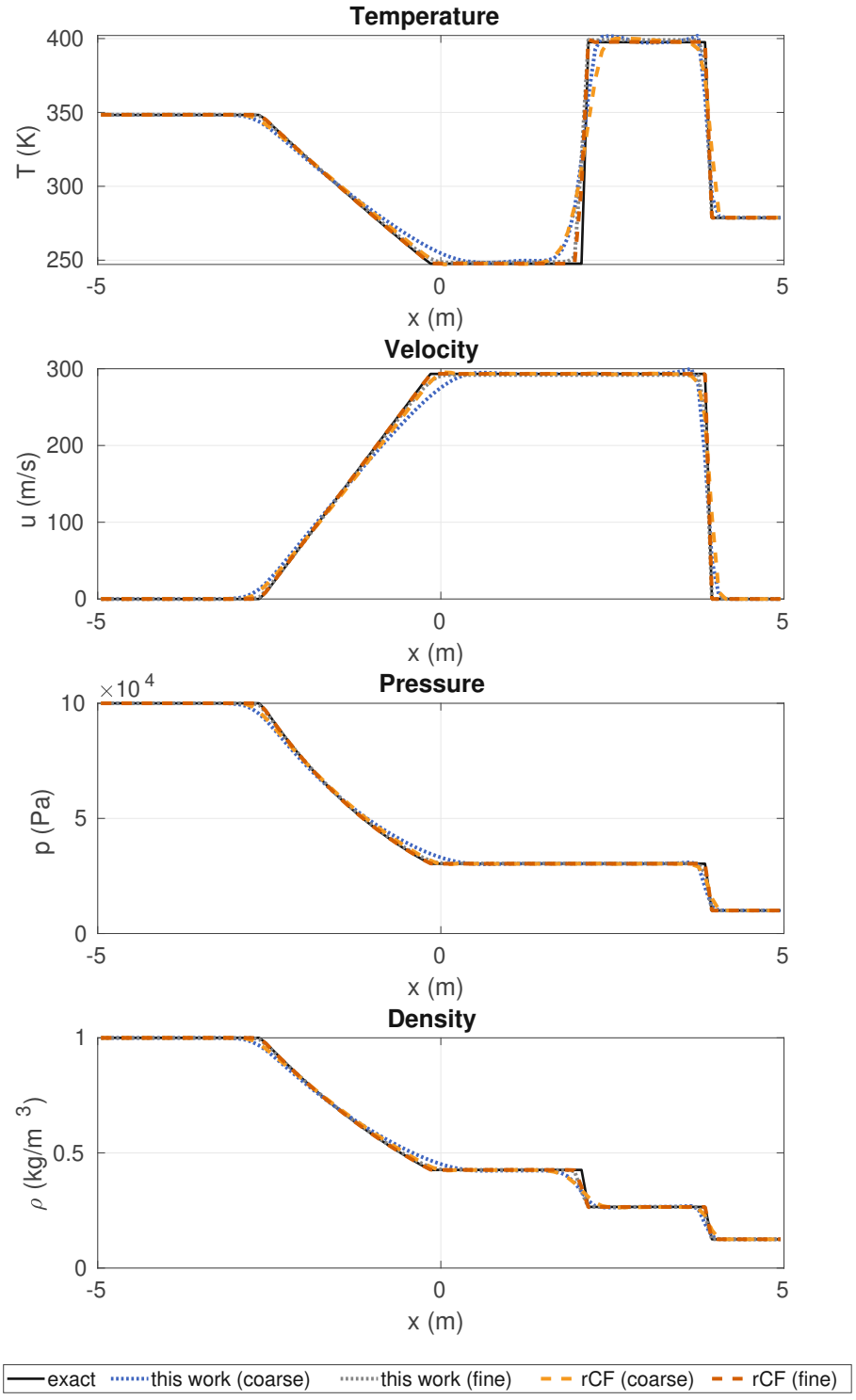

Figure 6: Shock Tube: Comparison of exact solution and simulation results at $t = 0.007$ s on coarse and fine mesh, obtained with this work's model and with `rhoCentralFoam` (denoted rCF), respectively.

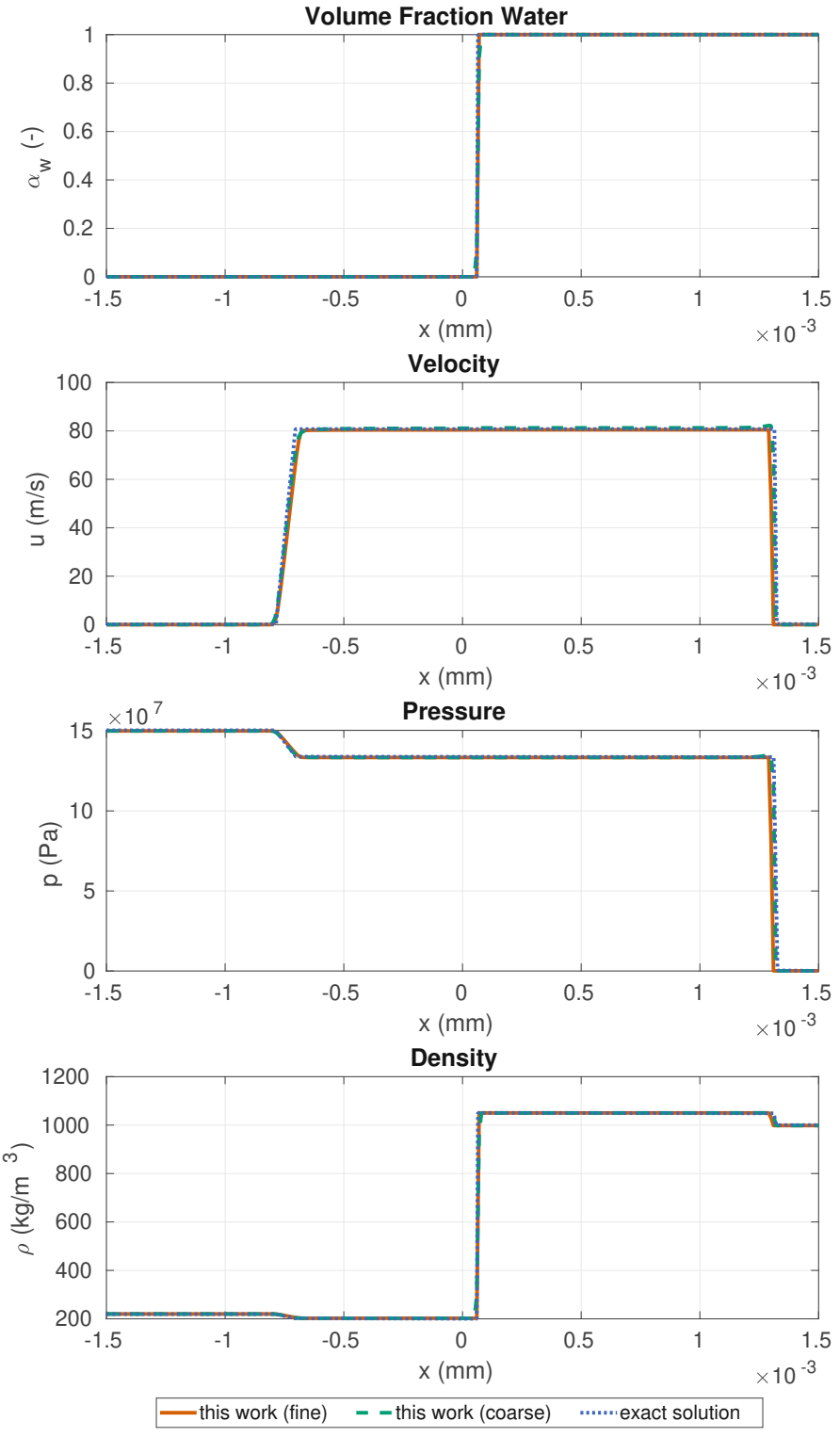

Figure 7: Two-Phase Shock Tube: Comparison of simulation results at $t = 0.8$ µs obtained with this work's model and the exact result reported by Koch et al. [36].

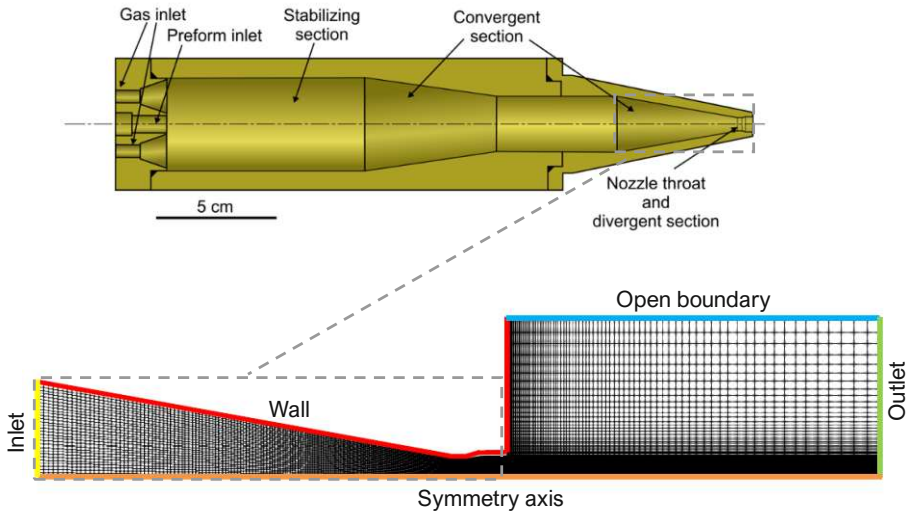

Figure 8: Converging-Diverging Nozzle: Schematic drawing of nozzle geometry used in experiment (Reprinted from [53].) and two-dimensional view of axisymmetrical wedge-type mesh employed in the region of interest.

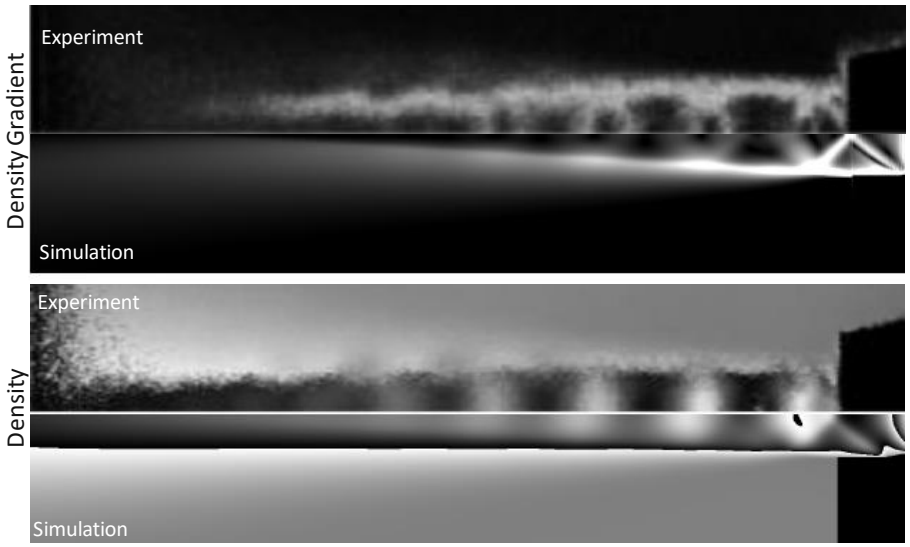

Figure 9: Converging-Diverging Nozzle: Comparison of grad(ρ) (top) and ρ (bottom) between simulation and experiment of Quintero et al. [55] for inlet pressure of p_{in}=3.5 bar. Experimental ρ is calculated from measured optical density.

4.4 Case 4: Stationary illumination of Ti-6Al-4V bare plate

The stationary laser illumination experiment of Cunningham et al. [56] is simulated. In this experiment, in-situ x-ray tomography was used to observe stationary laser beam melting and evaporation on a Ti-6Al-4V bare plate. This experiment has previously been used for validating simulation models by, e.g., Wang et al. [12], Yu and Zhao [10], and Flint et al. [16] as it is particularly suited for this type of validation due to the high spatial and temporal resolution of the reported data. The problem is also interesting per se, as it features conditions (material, laser power and spot size) encountered in industrial additive manufacturing processes, where an understanding of the onset and evolution of a vapor depression and subsequently a keyhole (deep vapor depression of high aspect ratio), as well as its periodic growth and collapse, is important.

Although a Gaussian intensity distribution was provided by the laser source in the experiments of [56], an optical fiber was used to transport the laser light to the scanning head, which due to multiple reflections within the fiber transforms the beam profile into a tophat-like distribution [57]. As no intensity distribution measurements were available, a distribution following measurements conducted by Kaplan [57] was used and scaled to achieve the 140 µm and 95 µm beam diameters (using the $1/e^2$-diameter definition) reported by [56]. The use of a perfect Gaussian intensity distribution leads to higher drill rates and an earlier onset of fluctuations, as observed, e.g., in the simulations of Wang et al. [12]. The used computational domain and mesh are shown in Figure 10. The mesh consists of 462 016 hexahedral cells, with the largest cell size (at the domain bottom) being Δx_{coarse}=25 µm, and the smallest cell size (in the zone of interest, where beam propagation, melting, evaporation, etc. occur) being Δx_{fine}=6.25 µm. The experimental setup is reproduced, using a domain width of 400 µm in $\vec{e}_x$-direction, with a zero gradient thermal boundary condition at the domain boundaries initialized with metal below a height ($\vec{e}_y$-direction) of -0.4 mm, and a fixed value (T=300K) thermal boundary condition at the lower domain boundaries, to model the clamping setup used in the experiment. Domain boundaries initialized with ambient gas are modeled as inlet/outlet. The used material properties are provided in Appendix A.

Following the approach of [12], we shifted the time values reported by [56] in Figures 11 and 12 such that the first evolution of a vapor depression is matched between experiment and simulation, to account for a non-synchronization between switching on the laser and starting the recording.

Figure 11 shows the evolution of keyhole depth over time for two different laser spot sizes, where especially with the larger spot size two distinct regimes can be identified, i.e., the initial steady growth of the keyhole, followed by a sudden onset of violent fluctuations, accompanied by an increase in drill rate. The initial fluctuations deviating from the mean drill rate in the first part of the process (at t <0.75 ms) are within the size of the computational cells, and can therefore be neglected. At a distinct point, the evaporation-induced recoil pressure suddenly outweighs the surface tension force at the liquid-vapor interface, resulting in a sudden increase in keyhole depth, reaching towards the bottom of the meltpool. The drilling process thus gains efficiency, as the melt pool also increases in depth, associated with a change in melt pool shape from hemispherical to conical. In Figure 12, the transition from steady

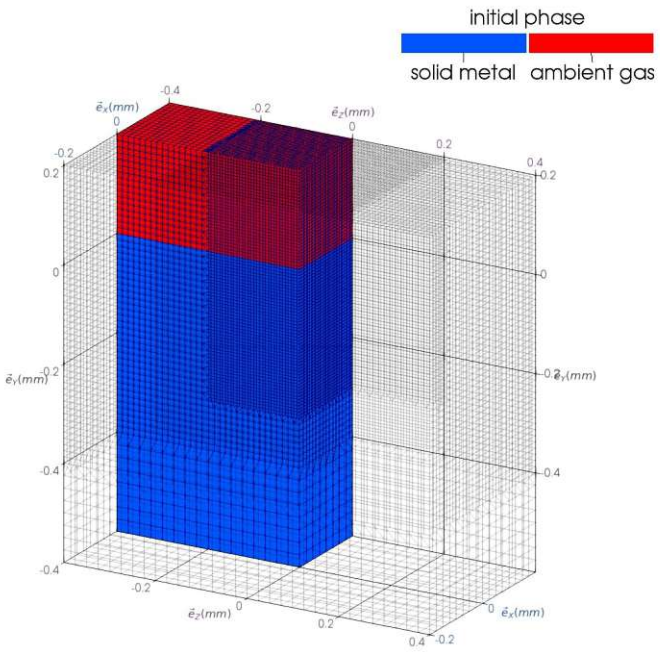

Figure 10: Stationary Illumination of Ti6Al4V bare plate: Computational domain, mesh and initial phase distribution. To show the mesh refinement, the domain is cut in this image along the $\vec{e}_x$- and $\vec{e}_z$-direction, showing only a quarter of the initialized fields.

keyhole growth to deep fluctuations, and keyhole shape irregularities and keyhole collapse at a later stage are compared to the experimental images of [56], showing good agreement. In Figure 13, the process using a smaller spot size is shown at three different stages, i.e., initial onset and steady growth of vapor depression, and violent keyhole fluctuations involving keyhole collapse at two different stages. For this used spot size, no experimental footage was available, but the good agreement of keyhole depth evolution shown in Figure 11 suggests that the results in Figure 13 are correct. Figure 14 provides a detailed view of the result of the 95 µm spot size case at $t =$ 260 µs, where the keyhole tip has just collapsed, and the remaining bubble is partly within the solid and within the melt pool, while collapsing. In the left view of Figure 14, the bubble collapse can be seen through the low pressure at the bubble wall, and the liquid flow velocity vectors being oriented towards the bubble. Meanwhile, the evaporation-induced recoil pressure can be seen in the form of high pressure regions at the keyhole wall, with velocity vector at the upper part of the keyhole being oriented upwards, which is due to entrainment by the metal vapor escaping the keyhole. In the right view of Figure 14, the flow structures of metal vapor escaping the keyhole, with a recirculation zone on the side (vortex structure). Furthermore, $\sum A_i$ is plotted, which can be seen as a measure of compression (cf. Section 3.3), where the bubble at the melt pool bottom is characterized by $\sum A_i < 1$, as most metal vapor has already condensed (cf. Figure 13), and thus the remaining gas is expanded, resulting in a low pressure. Vice versa, the lower part of the keyhole, where new metal vapor is created through evaporation, but cannot escape freely, $\sum A_i > 1$ due to the additional volume of (compressed) metal vapor. The phenomena shown in Figure 14 shall merely serve as an example of the various insights that can be gained from the here-presented model.

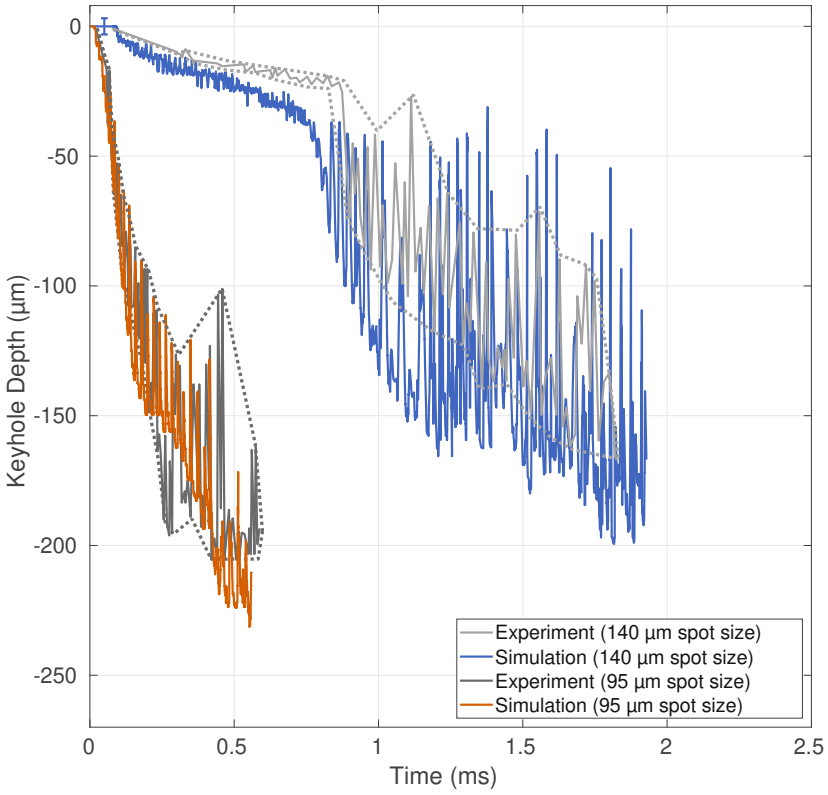

Figure 11: Stationary Illumination of Ti6Al4V bare plate: Comparison of vapor depression (keyhole) depth obtained with this work's model and in experiment by Cunningham et al. [56], respectively. P_{Laser} = 156 W, d_{Laser} = [95 µm, 140 µm]. The cell size used in the simulations is given in the form of an errorbar in the initial flat part of the 140 µm spot size line.

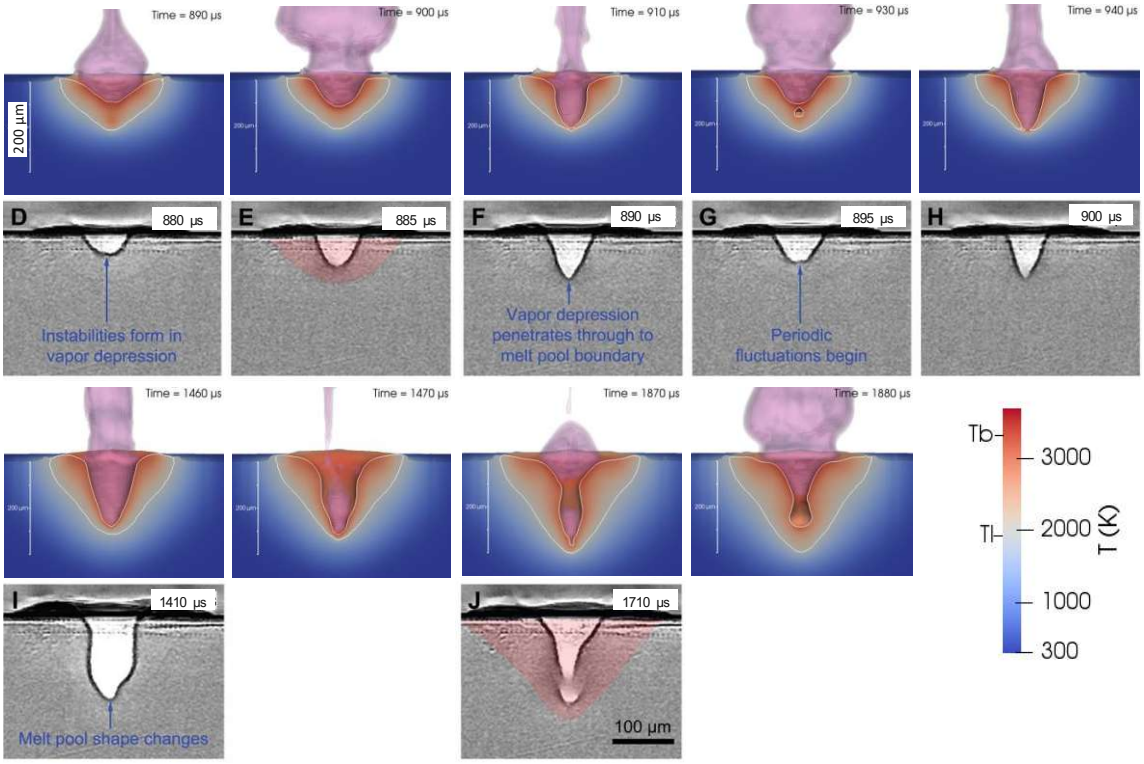

Figure 12: Stationary Illumination of Ti6Al4V bare plate: $P_{Laser} = 156$ W, $d_{Laser} = 140$ µm. Simulation compared to experiment, showing transition from steady keyhole growth to violent fluctuations (experimental frames D-H) and keyhole collapse at later stage (experimental frames I-J). Cut through domain half, showing condensed matter coloured by temperature, and contour surfaces of metal vapor (purple) at different α_{vap}-iso-values within $0.5 < \alpha_{vap} < 1$, white line denotes $\alpha_{liquid} = 0.5$. Experimental images are from Cunningham et al. [56]. Reprinted with permission from AAAS.

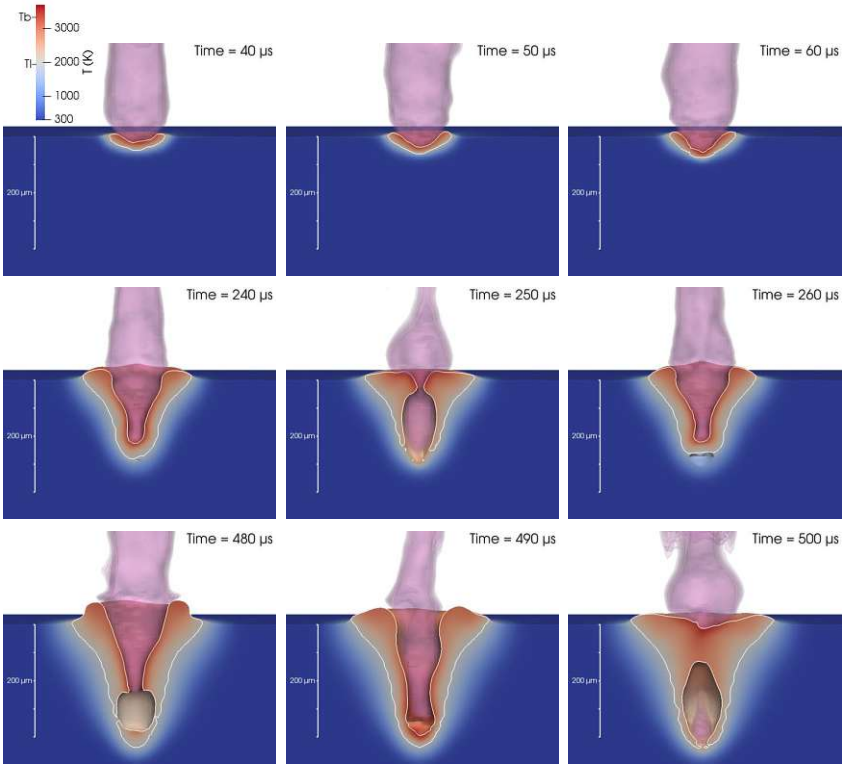

Figure 13: Stationary Illumination of Ti6Al4V bare plate: $P_{Laser} = 156$ W, $d_{Laser} = 95$ µm. Temporal evolution of keyhole at three different stages, showing keyhole growth and collapse. Cut through domain half, showing condensed matter coloured by temperature, and contour surfaces of metal vapor (purple) at different α_{vap}-iso-values within $0.5 < \alpha_{vap} < 1$, white line denotes $\alpha_{liquid} = 0.5$.

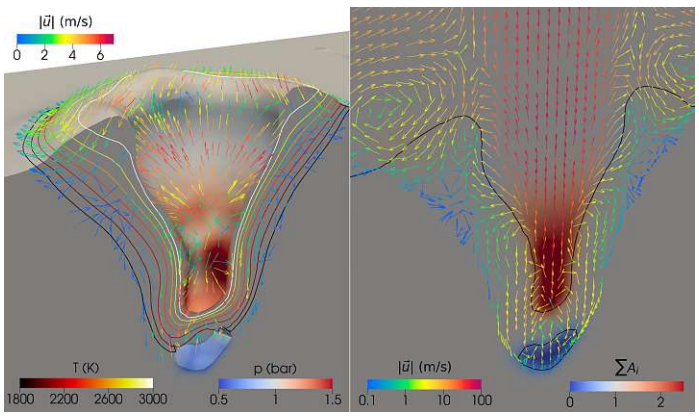

Figure 14: Stationary Illumination of Ti6Al4V bare plate: $P_{Laser} = 156$ W, $d_{Laser} = 95$ µm. Result at $t = 260$ µs, cut through domain half, showing condensed matter colored by pressure with velocity vectors in liquid and temperature contour lines (left) and entire domain colored by $\sum A_i$, showing velocity vectors in liquid and gaseous phases (right).

4.5 Case 5: Keyhole welding of Copper

Keyhole welding of Cu-ETP is simulated and the results are compared to the corresponding in-situ synchrotron X-ray observations at high spatial and temporal resolution conducted by Schricker et al. [58]. The problem is well suited as a validation case because it features a process of high industrial relevance, e.g., for the manufacturing of electric vehicle components. Another benefit of this comparison results from the high resolution of reported experimental data, which allows to test the sensitivity of the laser-fluid interaction of the model and the coupling between different forces. The problem is also interesting per se, as it gives insight into the high dynamicity of the process and aids in gaining process understanding. Within this case, the laser power is 3.5 kW, with a spot size of 90 µm and a feedrate of 10 m/min. The used material properties are provided in Appendix A. The computational domain and mesh are shown in Figure 15, where initially, hexahedral cells of cell size $\Delta x_{initial} = 200$ µm are used, which are dynamically refined up to 3 times during the simulation, depending on the presence of laser energy and liquid, leading to a local minimum cell size of $\Delta x_{fine} = 25$ µm.
In agreement with the experiment, the keyhole is in general quite narrow, but with increasing depth, irregularities increase (mainly in the form of bulges and waves). Although these are much more pronounced at the keyhole back wall, slight irregularities can also be seen on the keyhole front wall. Different forms of bulges can be observed at the keyhole back wall, of which the largest bulges form at the bottom and in the upper part of the keyhole. Some process snapshots showing extreme cases of lower, upper and minimum bulging are compared to the respective experimental observations of [58] in Figure 16. To also enable a quantitative comparison, the keyhole shape is characterized by t_a and t_d, referring to the depth position of the largest bulge and the keyhole depth, respectively, and a and d referring to the size of the bulge and the keyhole aperture at the top surface, respectively. The thus obtained dimensionless geometry parameters show good agreement, except for a/d in the bottom bulge scenario, where the keyhole aperture size is slightly larger in the simulation, most likely due to the wave at the upper keyhole back wall having already traveled further upwards in the simulation than in the respective experimental image. The occurrence of the maximum upper bulge (at $t = 11.35$ ms in simulation) is linked to a large wave of liquid being expelled backwards at the top of the rear keyhole wall in both simulation and experiment. The various dynamic processes reported in [58] can also be seen in the simulation. In Figure 17, the ejection of spatter, associated with a subsequent increase in keyhole aperture is shown. Interestingly, the formation of a pore through pinch-off of the upper bulge can be seen in experiment and simulation (at $t = 6.85$ ms). The pore later re-attaches to the keyhole and is thus not preserved both in simulation and experiment. Another interesting dynamic process that is observed both in simulation and experiment is shown in Figure 18, where, following a spatter ejection event, a wave on the keyhole rear wall travels upwards, but then is not ejected but stays attached to the melt pool and travels backwards.
This case provides many more possibilities for qualitative and quantitative comparison, and the simulation can be effectively used to explain the physical cause-effect relationships leading to the experimentally observed phenomena, which is outside the scope of this work. Currently ongoing work is dedicated to in-depth analysis of

copper welding using the here-presented model, and the results will be presented in a forthcoming publication.

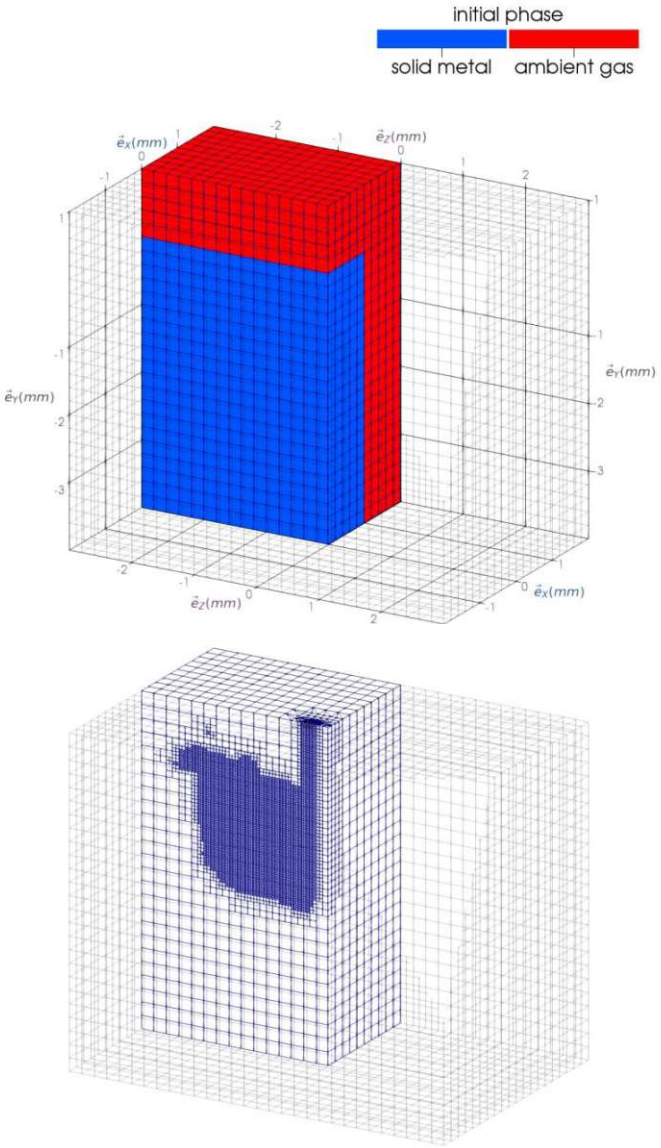

Figure 15: Keyhole welding of copper: Computational domain, showing initial mesh and initial phase distribution (top), as well as dynamically refined mesh during simulation (bottom). To show the mesh refinement, the domain is cut in this image along the $\vec{e}_x$- and $\vec{e}_z$-direction, showing only a quarter of the initialized fields.

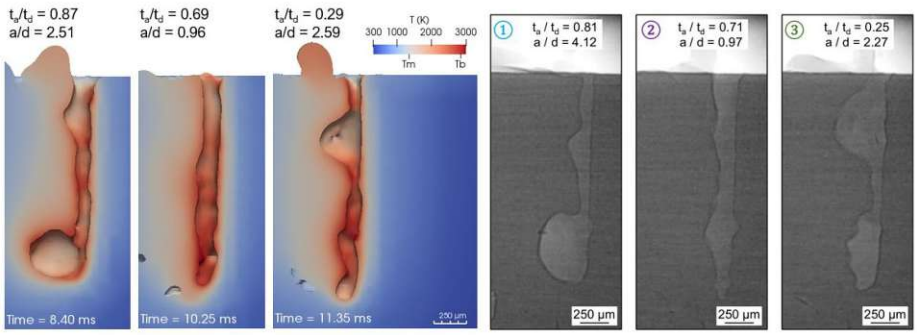

Figure 16: Keyhole welding of copper: Comparison of maximum bulging positions observed in simulation (left) and experiment by Schricker et al. [58] (right).

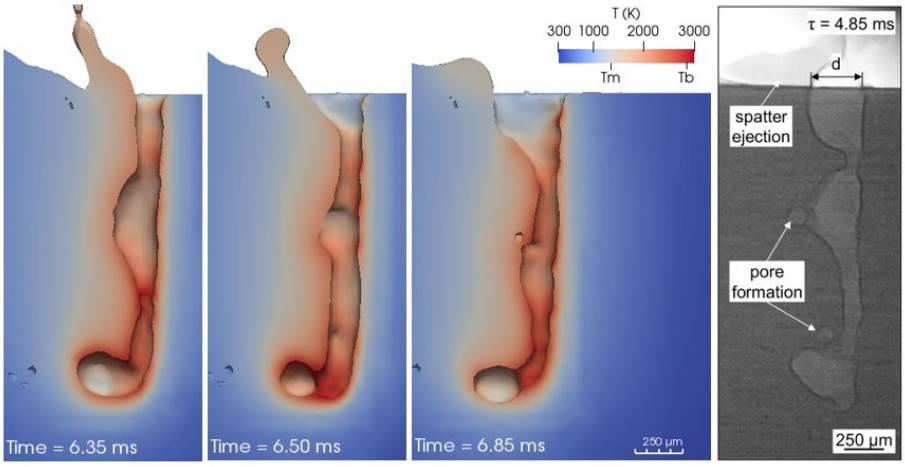

Figure 17: Keyhole welding of copper: Comparison of spatter ejection and associated keyhole aperture increase, as well as pore formation due to pinch-off of upper bulge observed in simulation (left) and experiment by Schricker et al. [58] (right).

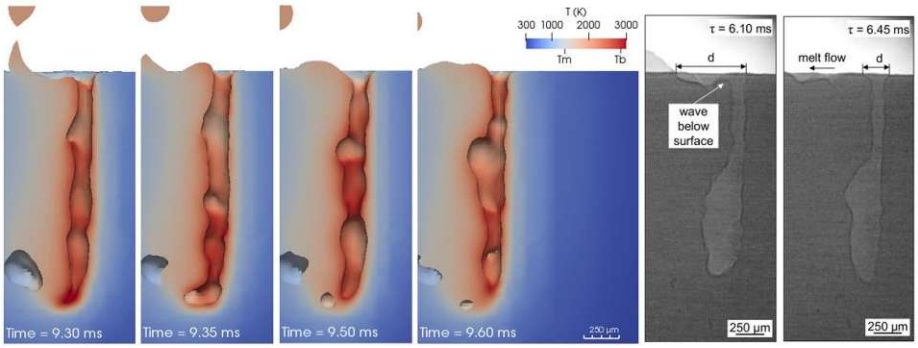

Figure 18: Keyhole welding of copper: Comparison of backwards travelling surface wave following a large spatter event observed in simulation (left) and experiment by Schricker et al. [58] (right).

5 Discussion

The main novelty of the MoF approach is, that instead of advecting a marker function to calculate mass distributions from this marker, like in the VoF approach, we directly advect the conserved quantities of mass and energy, making the approach mass- and energy-conservative. Furthermore, this enables an intuitive inclusion of compressibility in the model, and makes the handling of phase changes straightforward. The approach, however, suffers from the problem that an artificial flux-based interface sharpening method needs to be employed in Eq. (9), because we do not advect a bounded volume fraction, but a local mass density. Typical VoF solvers can easily (at least for two phases) adopt novel interface sharpening methods such as `isoAdvector` [59], which is based on geometric interface reconstruction. Apart from this drawback, the framework proves to be well-suited to handle compressible segregated multiphase scenarios involving phase change. Especially when considering processes involving evaporation, and the thus induced recoil pressure acting on the liquid (which is the case even for low-power processes such as additive manufacturing by laser-based powder bed fusion, as shown by [56]), the recoil pressure does not need to be explicitly modeled. Therefore, no model fine tuning to a specific application through, e.g., a recoil pressure scaling constant is needed. The sudden change from a steadily growing vapor depression to violent fluctuations seen in Figure 11 happens as soon as the recoil pressure is outweighing the surface tension force at the liquid-vapor interface. Here, the recoil pressure does not only depend on the degree of superheating of the liquid, but also on the geometry of the vapor depression and how well the newly produced vapor can escape the depression. Therefore, including the vapor phases and their compressibility in the model enhances the possibilities of drawing conclusions regarding the physical cause-effect relations at play and thus gain process understanding. The same holds true for the copper welding case investigated in Section 4.5. The chaotic nature of the underlying coupled multi-physical process leads to a broad range of irregularities, in a seemingly steady-state process.
The physics-based approach used in this work furthermore highlights the need for accurate temperature-dependent thermophysical and optical material properties in the liquid and gaseous state, as their influence on the process outcome can be high, but data in the literature is scarce and scattered, especially at the high temperatures encountered in laser-material processing.
The simulations presented in Section 4.4 took approximately 24 hours (for the large spot size configuration) on 10 cores (Intel® Xeon™ E5-2690 processor). The use of dynamic mesh refinement would speed up the calculations, but was omitted in this case to allow for easier reproducibility of the results. The simulation presented in Section 4.5 took approximately 20 hours per 1 mm of simulated weld bead length on 20 cores (Intel® Xeon™ E5-2690 processor). While the spatial resolution (and thus also the required temporal resolution) employed in the here-presented cases is very high to capture the highly dynamic phenomena observed experimentally, many practical applications of the here-presented framework allow for lower resolution. As an example, the here-presented model was used in [26] to simulate 30 mm of overlap welding of two 1 mm steel sheets (in good agreement with experimental results), where one simulation took approximately 12 hours on an eight-core desktop computer.

6 Conclusion

A novel multiphase mixture model for laser-based material processing was presented. It is capable of accurately predicting compressible multiphase flows involving phase changes. The main difference over the Volume-of-Fluid method is that, instead of a marker function, the conserved physical quantities of mass and energy are tracked. An evaporation and condensation model that considers the created vapor and the arising pressure is derived, omitting the need of explicit recoil pressure calculation and model parameters for evaporation efficiency. The accuracy of the model and its numerical implementation was tested on one- and two phase shock tube scenarios, yielding very good results when compared to the respective analytical solutions or that of a state-of-the-art dedicated solver. The model's versatility and applicability to real-world laser material processing scenarios was showcased by simulating two different experiments where fine spatial and temporal data on the dynamic process is available. The results show excellent agreement with experimental observations and give detailed insight into the physical phenomena at play in additive manufacturing and welding processes.
Ongoing and future work focuses on the inclusion of further multiphysical aspects to the here-presented framework, such as solid mechanics and crystallographic grain growth, as well as a highly parallelizable Lagrangian particle-based implementation of the laser beam propagation and laser-material interaction model.

CRediT authorship contribution statement

C. Zenz: Conceptualization, Methodology, Software, Validation, Investigation, Visualization, Writing- Original Draft, Writing - Review & Editing. **M. Buttazzoni:** Methodology, Software, Validation, Writing - Review & Editing. **T. Florian:** Validation, Investigation, Writing - Review & Editing. **K.E. Crespo Armijos:** Investigation, Visualization, Writing - Review & Editing. **R. Gómez Vázquez:** Methodology, Software, Supervision, Writing - Review & Editing. **G. Liedl:** Supervision, Writing - Review & Editing. **A. Otto:** Conceptualization, Methodology, Supervision, Resources, Project administration, Funding acquisition, Writing - Review & Editing.

Declaration of Competing Interest

The authors declare that they have no known competing financial interests or personal relationships that could have appeared to influence the work reported in this paper.

Acknowledgements

C. Zenz gratefully acknowledges funding through the TU Wien Doctoral School, within the Doctoral College "DigiPhot". The authors acknowledge TU Wien Bibliothek for financial support through its Open Access Funding Programme.

Appendix A Material Properties

The material properties of Ti6Al4V, Cu-ETP and ambient gas, used in the simulations presented in Section 4.4 and Section 4.5 are provided here in detail. State-independent properties of Ti6Al4V, and properties of the material's solid, liquid and vapor state are listed in Table 4, Table 5, Table 6 and Table 7, respectively. State-independent properties of Cu-ETP, and properties of the material's solid, liquid and vapor state are listed in Table 8, Table 9, Table 10 and Table 11, respectively. The properties of ambient gas are provided in Table 12. Temperature-dependent properties are linearly interpolated between the data points listed in the respective Tables. The surface energy values of solid Ti6Al4V are chosen so that neither hydrophobic nor hydrophilic behaviour is present, but approaching hydrophilic (wetting) conditions between solid and liquid at the melting point. The surface energy values of solid Cu-ETP are chosen so that hydrophobic behaviour is present, as observed in the corresponding experiment of [58], but approaching the value of the liquid at the melting point, as there is no discontinuity across the melting point of Cu, as reported by [60]. The surface energy values of liquid Cu-ETP have been slightly reduced from those for pure Cu to account for the oxygen content of Cu-ETP [61].
Calculation of the viscosity using the kinetic theory is done following the approach of [62] via $\nu(T) = \nu_0(\rho_0/\rho)(T/T_0)^{0.5}$. Calculation of the viscosity using the ideal gas law follows the approach of [63].
The thermal conductivity values of metal vapor have been extrapolated from ambient gas values, as no data was available in literature, and the influence on the results is small. Values for the complex refractive index of solid Ti6Al4V were calculated to reproduce the experimentally observed bare plate absorptivity reported by [64]. As no values for the complex refractive index of liquid Cu-ETP was available in literature, the values were fitted to reproduce the experimentally obtained penetration depth reported by [58].

property	T (K)	value	unit	Ref.
Ti6Al4V (general)				
molar mass M	-	$46.77{\cdot}10^{-3}$	$kg{\cdot}mol^{-1}$	[65]
solidus temperature $T_{solidus}$	-	1878	K	[65]
liquidus temperature $T_{liquidus}$	-	1928	K	[65]
boiling temperature $T_{boiling}$	-	3315	K	[65]
latent heat (fusion) L_{fusion}	-	$2.9{\cdot}10^{5}$	$m^2{\cdot}s^{-2}$	[65]
latent heat (vaporization) L_{vap}	-	$9.82{\cdot}10^{6}$	$m^2{\cdot}s^{-2}$	[65]

Table 4: Material properties of Ti6Al4V: State-independent properties.

property	T (K)	value	unit	Ref.
	Ti6Al4V (solid)			
density ρ	293	4457	$kg \cdot m^{-3}$	[65]
	973	4350	$kg \cdot m^{-3}$	[66]
	1873	4150	$kg \cdot m^{-3}$	[66]
bulk modulus K	293	$119.2 \cdot 10^9$	$kg \cdot s^{-2} \cdot m^{-1}$	[67]
	773	$90 \cdot 10^9$	$kg \cdot s^{-2} \cdot m^{-1}$	[67]
	1928	$40 \cdot 10^9$	$kg \cdot s^{-2} \cdot m^{-1}$	[68]
specific heat capacity c_p	293	580	$m^2 \cdot s^{-2} \cdot K^{-1}$	[67]
	873	668	$m^2 \cdot s^{-2} \cdot K^{-1}$	[69]
	1073	691	$m^2 \cdot s^{-2} \cdot K^{-1}$	[69]
	1278	643	$m^2 \cdot s^{-2} \cdot K^{-1}$	[69]
	1373	660	$m^2 \cdot s^{-2} \cdot K^{-1}$	[69]
	1923	759	$m^2 \cdot s^{-2} \cdot K^{-1}$	[69]
thermal conductivity λ	430	5.957	$kg \cdot m \cdot s^{-3} \cdot K^{-1}$	[70]
	1270	17	$kg \cdot m \cdot s^{-3} \cdot K^{-1}$	[70]
	1383	19.87	$kg \cdot m \cdot s^{-3} \cdot K^{-1}$	[70]
	1888	27	$kg \cdot m \cdot s^{-3} \cdot K^{-1}$	[70]
surface energy σ	300	0.375	$kg \cdot s^{-2}$	
	1500	1.0	$kg \cdot s^{-2}$	
	1878	1.505	$kg \cdot s^{-2}$	[71]
refractive index n	-	3.86	-	[64]
extinction coefficient κ	-	6.1	-	[64]

Table 5: Material properties of Ti6Al4V: Solid state.

property	T (K)	value	unit	Ref.
	Ti6Al4V (liquid)			
density ρ	1923	4100	$kg{\cdot}m^{-3}$	[66]
	2073	4025	$kg{\cdot}m^{-3}$	[66]
	2573	3800	$kg{\cdot}m^{-3}$	[66]
bulk modulus K	1928	$40{\cdot}10^{9}$	$kg{\cdot}s^{-2}{\cdot}m^{-1}$	[68]
	3315	$1{\cdot}10^{9}$	$kg{\cdot}s^{-2}{\cdot}m^{-1}$	
kinematic viscosity ν	1732	$3.9{\cdot}10^{-6}$	$m^{2}{\cdot}s^{-1}$	[71]
	1931	$2.53{\cdot}10^{-6}$	$m^{2}{\cdot}s^{-1}$	[71]
	2045	$2.14{\cdot}10^{-6}$	$m^{2}{\cdot}s^{-1}$	[71]
surface energy σ	1928	1.505	$kg{\cdot}s^{-2}$	[71]
	3315	1.1	$kg{\cdot}s^{-2}$	[71]
specific heat capacity c_p	-	1126	$m^{2}{\cdot}s^{-1}{\cdot}K^{-2}{\cdot}K^{-1}$	[70]
thermal conductivity λ	1913	28.8	$kg{\cdot}m{\cdot}s^{-3}{\cdot}K^{-1}$	[70]
	2666	42.2	$kg{\cdot}m{\cdot}s^{-3}{\cdot}K^{-1}$	[70]
refractive index n	1901	4.01	-	[65]
	2603	4.08	-	[65]
extinction coefficient κ	1901	4.7	-	[65]
	2603	4.83	-	[65]

Table 6: Material properties of Ti6Al4V: Liquid state.

property	T (K)	value	unit	Ref.
	Ti6Al4V (vapor)			
density ρ	-	*ideal gas law*		
bulk modulus K	-	$1{\cdot}10^{5}$	$kg{\cdot}s^{-2}{\cdot}m^{-1}$	
surface energy σ	-	0	$kg{\cdot}s^{-2}$	
specific heat capacity c_p	3631	732	$m^{2}{\cdot}s^{-2}{\cdot}K^{-1}$	[72]
	4000	774	$m^{2}{\cdot}s^{-2}{\cdot}K^{-1}$	[72]
	4800	853	$m^{2}{\cdot}s^{-2}{\cdot}K^{-1}$	[72]
thermal conductivity λ	3315	0.1281	$kg{\cdot}m{\cdot}s^{-3}{\cdot}K^{-1}$	
	5000	0.1588	$kg{\cdot}m{\cdot}s^{-3}{\cdot}K^{-1}$	
kinematic viscosity ν	-	*ideal gas law*		
refractive index n	-	1	-	
extinction coefficient κ	-	0	-	

Table 7: Material properties of Ti6Al4V: Vapor state.

property	T (K)	value	unit	Ref.
Cu-ETP (general)				
molar mass M	-	$63.546 \cdot 10^{-3}$	$kg \cdot mol^{-1}$	[73]
solidus temperature $T_{solidus}$	-	1347	K	[74]
liquidus temperature $T_{liquidus}$	-	1347	K	[74]
boiling temperature $T_{boiling}$	-	2854	K	
latent heat (fusion) L_{fusion}	-	$2.056 \cdot 10^{5}$	$m^2 \cdot s^{-2}$	
latent heat (vaporization) L_{vap}	-	$4.75 \cdot 10^{6}$	$m^2 \cdot s^{-2}$	

Table 8: Material properties of Cu-ETP: State-independent properties.

property	T (K)	value	unit	Ref.
Cu-ETP (solid)				
density ρ	1347	8320	$kg \cdot m^{-3}$	[74]
bulk modulus K	300	$100 \cdot 10^{9}$	$kg \cdot s^{-2} \cdot m^{-1}$	
specific heat capacity c_p	300	385	$m^2 \cdot s^{-2} \cdot K^{-1}$	[72]
	973	440	$m^2 \cdot s^{-2} \cdot K^{-1}$	[72]
thermal conductivity λ	273	390	$kg \cdot m \cdot s^{-3} \cdot K^{-1}$	[74]
	973	300	$kg \cdot m \cdot s^{-3} \cdot K^{-1}$	[74]
	1347	250	$kg \cdot m \cdot s^{-3} \cdot K^{-1}$	
surface energy σ	300	0.1	$kg \cdot s^{-2}$	
	1339	0.1	$kg \cdot s^{-2}$	
	1340	1.135	$kg \cdot s^{-2}$	[61]
refractive index n	-	0.35	-	[75]
extinction coefficient κ	-	7.0	-	[75]

Table 9: Material properties of Cu-ETP: Solid state.

property	T (K)	value	unit	Ref.
		Cu-ETP (liquid)		
density ρ	1350	7970.8	$kg \cdot m^{-3}$	[76]
	1700	7724.1	$kg \cdot m^{-3}$	[76]
bulk modulus K	-	$1 \cdot 10^{9}$	$kg \cdot s^{-2} \cdot m^{-1}$	
kinematic viscosity ν	1356	$5.04 \cdot 10^{-7}$	$m^2 \cdot s^{-1}$	[77]
	1500	$4.07 \cdot 10^{-7}$	$m^2 \cdot s^{-1}$	[77]
	1700	$3.24 \cdot 10^{-7}$	$m^2 \cdot s^{-1}$	[77]
	1950	$2.61 \cdot 10^{-7}$	$m^2 \cdot s^{-1}$	[77]
surface energy σ	1347	1.135	$kg \cdot s^{-2}$	[61]
	2868	0.898	$kg \cdot s^{-2}$	[61]
specific heat capacity c_p	-	516.86	$m^2 \cdot s^{-1} \cdot K^{-2} \cdot K^{-1}$	[72]
thermal conductivity λ	1347	142	$kg \cdot m \cdot s^{-3} \cdot K^{-1}$	[78]
	2854	185	$kg \cdot m \cdot s^{-3} \cdot K^{-1}$	[78]
refractive index n	-	0.96	-	
extinction coefficient κ	-	6.2	-	

Table 10: Material properties of Cu-ETP: Liquid state.

property	T (K)	value	unit	Ref.
		Cu-ETP (vapor)		
density ρ	-	*ideal gas law*		
bulk modulus K	-	$1 \cdot 10^{5}$	$kg \cdot s^{-2} \cdot m^{-1}$	
surface energy σ	-	0	$kg \cdot s^{-2}$	
specific heat capacity c_p	2900	387.9	$m^2 \cdot s^{-2} \cdot K^{-1}$	[72]
	3500	435.7	$m^2 \cdot s^{-2} \cdot K^{-1}$	[72]
	4500	498.2	$m^2 \cdot s^{-2} \cdot K^{-1}$	[72]
thermal conductivity λ	3000	0.15	$kg \cdot m \cdot s^{-3} \cdot K^{-1}$	
	5000	0.24	$kg \cdot m \cdot s^{-3} \cdot K^{-1}$	
kinematic viscosity ν	-	*ideal gas law*		
refractive index n	-	1	-	
extinction coefficient κ	-	0	-	

Table 11: Material properties of Cu-ETP: Vapor state.

property	T (K)	value	unit	Ref.
ambient gas				
molar mass M	-	$28.014 \cdot 10^{-3}$	$kg \cdot mol^{-1}$	
density ρ	-	*ideal gas law*		
bulk modulus K	-	$1 \cdot 10^{5}$	$kg \cdot s^{-2} \cdot m^{-1}$	
surface energy σ	-	0	$kg \cdot s^{-2}$	
specific heat capacity c_p	300	1041.3	$m^2 \cdot s^{-2} \cdot K^{-1}$	[72]
	1800	1270.8	$m^2 \cdot s^{-2} \cdot K^{-1}$	[72]
thermal conductivity λ	300	$2.597 \cdot 10^{-2}$	$kg \cdot m \cdot s^{-3} \cdot K^{-1}$	[72]
	900	$6.052 \cdot 10^{-2}$	$kg \cdot m \cdot s^{-3} \cdot K^{-1}$	[72]
	1800	$10.088 \cdot 10^{-2}$	$kg \cdot m \cdot s^{-3} \cdot K^{-1}$	[72]
kinematic viscosity ν	-	*kinetic theory*		
		$\nu_0 = 1.593 \cdot 10^{-5}$	$m^2 \cdot s^{-1}$	[72]
		$\rho_0 = 1.1233$	$kg \cdot m^{-3}$	[72]
		$T_0 = 300$	K	
refractive index n	-	1	-	
extinction coefficient κ	-	0	-	

Table 12: Material properties of ambient gas.

References

[1] W. Steen. "Laser material processing—an overview". In: *Journal of Optics A: Pure and Applied Optics* 5, 2003. DOI: https://doi.org/10.1088/1464-4258/5/4/351.

[2] Y. C. Shin, B. Wu, S. Lei, G. J. Cheng, and Y. Lawrence Yao. "Overview of laser applications in manufacturing and materials processing in recent years". In: *Journal of Manufacturing Science and Engineering* 142, 2020, p. 110818. DOI: https://doi.org/10.1115/1.4048397.

[3] A. Otto, H. Koch, K.-H. Leitz, and M. Schmidt. "Numerical simulations-a versatile approach for better understanding dynamics in laser material processing". In: *Physics Procedia* 12, 2011, pp. 11–20. DOI: https://doi.org/10.1016/j.phpro.2011.03.003.

[4] J. Zhao and P. Cheng. "A lattice Boltzmann method for simulating laser cutting of thin metal plates". In: *International Journal of Heat and Mass Transfer* 110, 2017, pp. 94–103. DOI: https://doi.org/10.1016/j.ijheatmasstransfer.2017.02.091.

[5] J.-H. Cho and S.-J. Na. "Implementation of real-time multiple reflection and Fresnel absorption of laser beam in keyhole". In: *Journal of Physics D: Applied Physics* 39, 2006, p. 5372. DOI: https://doi.org/10.1088/0022-3727/39/24/039.

[6] M. Courtois, M. Carin, P. Le Masson, S. Gaied, and M. Balabane. "A new approach to compute multi-reflections of laser beam in a keyhole for heat transfer and fluid flow modelling in laser welding". In: *Journal of Physics D: Applied Physics* 46, 2013, p. 505305. DOI: https://doi.org/10.1088/0022-3727/46/50/505305.

[7] W. Tan and Y. C. Shin. "Analysis of multi-phase interaction and its effects on keyhole dynamics with a multi-physics numerical model". In: *Journal of Physics D: Applied Physics* 47, 2014, p. 345501. DOI: https://doi.org/10.1088/0022-3727/47/34/345501.

[8] Y. Ai, P. Jiang, X. Shao, P. Li, and C. Wang. "A three-dimensional numerical simulation model for weld characteristics analysis in fiber laser keyhole welding". In: *International Journal of Heat and Mass Transfer* 108, 2017, pp. 614–626. DOI: https://doi.org/10.1016/j.ijheatmasstransfer.2016.12.034.

[9] Y. Ai, P. Jiang, X. Shao, P. Li, C. Wang, G. Mi, S. Geng, Y. Liu, and W. Liu. "The prediction of the whole weld in fiber laser keyhole welding based on numerical simulation". In: *Applied Thermal Engineering* 113, 2017, pp. 980–993. DOI: https://doi.org/10.1016/j.applthermaleng.2016.11.050.

[10] T. Yu and J. Zhao. "Quantitative simulation of selective laser melting of metals enabled by new high-fidelity multiphase, multiphysics computational tool". In: *Computer Methods in Applied Mechanics and Engineering* 399, 2022, p. 115422. DOI: https://doi.org/10.1016/j.cma.2022.115422.

[11] D. Wu, X. Hua, L. Huang, and J. Zhao. "Numerical simulation of spatter formation during fiber laser welding of 5083 aluminum alloy at full penetration condition". In: *Optics & Laser Technology* 100, 2018, pp. 157–164. DOI: https://doi.org/10.1016/j.optlastec.2017.10.010.

[12] L. Wang, Y. Zhang, and W. Yan. "Evaporation Model for Keyhole Dynamics during Additive Manufacturing of Metal". In: *Physical Review Applied* 14, 2020, p. 064039. DOI: https://doi.org/10.1103/PhysRevApplied.14.064039.

[13] P. S. Cook and D. J. Ritchie. "Determining the laser absorptivity of Ti-6Al-4V during laser powder bed fusion by calibrated melt pool simulation". In: *Optics & Laser Technology* 162, 2023, p. 109247. DOI: https://doi.org/10.1016/j.optlastec.2023.109247.

[14] Y. Feng, X. Gao, Y. Zhang, C. Peng, X. Gui, Y. Sun, and X. Xiao. "Simulation and experiment for dynamics of laser welding keyhole and molten pool at different penetration status". In: *The International Journal of Advanced Manufacturing Technology* 112, 2021, pp. 2301–2312. DOI: https://doi.org/10.1007/s00170-020-06489-y.

[15] T. F. Flint, L. Scotti, H. C. Basoalto, and M. C. Smith. "A thermal fluid dynamics framework applied to multi-component substrates experiencing fusion and vaporisation state transitions". In: *Communications Physics* 3, 2020, p. 196. DOI: https://doi.org/10.1038/s42005-020-00462-7.

[16] T. F. Flint, J. D. Robson, G. Parivendhan, and P. Cardiff. "laserbeamFoam: Laser ray-tracing and thermally induced state transition simulation toolkit". In: *SoftwareX* 21, 2023, p. 101299. DOI: https://doi.org/10.1016/j.softx.2022.101299.

[17] M. Dal and R. Fabbro. "An overview of the state of art in laser welding simulation". In: *Optics & Laser Technology* 78, 2016, pp. 2–14. DOI: https://doi.org/10.1016/j.optlastec.2015.09.015.

[18] P. S. Cook and A. B. Murphy. "Simulation of melt pool behaviour during additive manufacturing: Underlying physics and progress". In: *Additive Manufacturing* 31, 2020, p. 100909. DOI: https://doi.org/10.1016/j.addma.2019.100909.

[19] Y. Shu, D. Galles, O. A. Tertuliano, B. A. McWilliams, N. Yang, W. Cai, and A. J. Lew. "A critical look at the prediction of the temperature field around a laser-induced melt pool on metallic substrates". In: *Scientific Reports* 11, 2021, p. 12224. DOI: https://doi.org/10.1038/s41598-021-91039-z.

[20] A. Otto, H. Koch, and R. Gómez Vázquez. "Multiphysical Simulation of Laser Material Processing". In: *Physics Procedia* 39, 2012, pp. 843–852. DOI: https://doi.org/10.1016/j.phpro.2012.10.109.

[21] R. Gómez Vázquez, H. Koch, and A. Otto. "Multi-Physical Simulation of Laser Welding". In: *Physics Procedia* 56, 2014, pp. 1334–1342. DOI: https://doi.org/10.1016/j.phpro.2014.08.059.

[22] A. Otto, A. Patschger, and M. Seiler. "Numerical and Experimental Investigations of Humping Phenomena in Laser Micro Welding". In: *Physics Procedia* 83, 2016, pp. 1415–1423. DOI: https://doi.org/10.1016/j.phpro.2016.09.004.

[23] A. Otto and R. Gómez Vázquez. "Fluid dynamical simulation of high speed micro welding". In: *J. Laser Appl.* 30, 2018, p. 032411. DOI: https://doi.org/10.2351/1.5040652.

[24] A. Otto, R. Gómez Vázquez, U. Hartel, and S. Mosbah. "Numerical analysis of process dynamics in laser welding of Al and Cu". In: *Procedia CIRP* 74, 2018, pp. 691–695. DOI: https://doi.org/10.1016/j.procir.2018.08.040.

[25] P. Drobniak, A. Otto, R. Gómez Vázquez, R. M. Arias, and J. L. Arias. "Simulation of keyhole laser welding of stainless steel plates with a gap". In: *Procedia CIRP* 94, 2020, pp. 731–736. DOI: https://doi.org/10.1016/j.procir.2020.09.134.

[26] M. Buttazzoni, C. Zenz, A. Otto, R. Gómez Vázquez, G. Liedl, and J. L. Arias. "A Numerical Investigation of Laser Beam Welding of Stainless Steel Sheets with a Gap". In: *Appl. Sci.* 11, 2021, p. 2549. DOI: https://doi.org/10.3390/app11062549.

[27] C. Zenz, M. Buttazzoni, M. Martínez Ceniceros, R. Gómez Vázquez, J. R. Blasco Puchades, L. Portolés Griñán, and A. Otto. "Simulation-based process optimization of laser-based powder bed fusion by means of beam shaping". In: *Additive Manufacturing* 77, 2023, p. 103793. DOI: https://doi.org/10.1016/j.addma.2023.103793.

[28] A. Otto, H. Koch, R. Gómez Vázquez, Z. Lin, and B. Hainsey. "Multiphysical Simulation of ns-Laser Ablation of Multi-Material LED-Structures". In: *Physics Procedia* 56, 2014, pp. 1315–1324. DOI: https://doi.org/10.1016/j.phpro.2014.08.057.

[29] S. Tatra, R. Gómez Vázquez, C. Stiglbrunner, and A. Otto. "Numerical Simulation of Laser Ablation with Short and Ultra-short Pulses for Metals and Semiconductors". In: *Physics Procedia* 83, 2016, pp. 1339–1346. DOI: https://doi.org/10.1016/j.phpro.2016.08.141.

[30] H. Matsumoto, Z. Lin, J. N. Schrauben, J. Kleinert, R. Gómez Vázquez, M. Buttazzoni, and A. Otto. "Rapid formation of high aspect ratio through holes in thin glass substrates using an engineered, QCW laser approach". In: *Applied Physics A* 128, 2022, pp. 1–10. DOI: https://doi.org/10.1007/s00339-022-05404-4.

[31] S. Whitaker. "Flow in porous media I: A theoretical derivation of Darcy's law". In: *Transport in Porous Media* 1, 1986, pp. 3–25. DOI: https://doi.org/10.1007/BF01036523.

[32] F. Rösler and D. Brüggemann. "Shell-and-tube type latent heat thermal energy storage: numerical analysis and comparison with experiments". In: *Heat and Mass Transfer* 47, 2011, pp. 1027–1033. DOI: https://doi.org/10.1007/s00231-011-0866-9.

[33] M. Ruths. "Surface Forces, Surface Tension, and Adhesion". In: *Encyclopedia of Tribology*. Ed. by Q. J. Wang and Y.-W. Chung. Boston, MA: Springer US, 2013, pp. 3435–3443. ISBN: 978-0-387-92897-5. DOI: https://doi.org/10.1007/978-0-387-92897-5_463.

[34] J. U. Brackbill, D. B. Kothe, and C. Zemach. "A continuum method for modeling surface tension". In: *Journal of computational physics* 100, 1992, pp. 335–354. DOI: https://doi.org/10.1016/0021-9991(92)90240-Y.

[35] C. W. Hirt and B. D. Nichols. "Volume of fluid (VOF) method for the dynamics of free boundaries". In: *Journal of Computational Physics* 39, 1981, pp. 201–225. DOI: https://doi.org/10.1016/0021-9991(81)90145-5.

[36] M. Koch, C. Lechner, F. Reuter, K. Köhler, R. Mettin, and W. Lauterborn. "Numerical modeling of laser generated cavitation bubbles with the finite volume and volume of fluid method, using OpenFOAM". In: *Computers & Fluids* 126, 2016, pp. 71–90. DOI: https://doi.org/10.1016/j.compfluid.2015.11.008.

[37] A. Stein. *Simulation rotordynamischer Problemstellungen mit der Smoothed Particle Hydrodynamics Methode*. kassel university press GmbH, 2016. DOI: https://doi.org/doi:10.19211/KUP9783737602211.

[38] V. R. Voller and C. Prakash. "A fixed grid numerical modelling methodology for convection-diffusion mushy region phase-change problems". In: *International Journal of Heat and Mass Transfer* 30, 1987, pp. 1709–1719. DOI: https://doi.org/10.1016/0017-9310(87)90317-6.

[39] J. A. Dantzig and M. Rappaz. *Solidification: -Revised & Expanded*. EPFL press, 2016. ISBN: 978-0-84938-238-3.

[40] K. M. Watson. "Thermodynamics of the liquid state". In: *Industrial & Engineering Chemistry* 35, 1943, pp. 398–406. DOI: https://doi.org/10.1021/ie50400a004.

[41] H. Hügel and T. Graf. *Laser in der Fertigung*. 2nd ed. Springer, 2009. DOI: https://doi.org/10.1007/978-3-8348-9570-7.

[42] E. Beyer. *Schweißen mit Laser*. Springer: Berlin/Heidelberg, Germany, 1995. DOI: https://doi.org/10.1007/978-3-642-75759-4.

[43] H. Jasak. "Error analysis and estimation for the finite volume method with applications to fluid flows". PhD thesis. Imperial College London, 1996.

[44] H. G. Weller, G. Tabor, H. Jasak, and C. Fureby. "A tensorial approach to computational continuum mechanics using object-oriented techniques". In: *Computers in physics* 12, 1998, pp. 620–631. DOI: https://doi.org/10.1063/1.168744.

[45] H. Rusche. "Computational fluid dynamics of dispersed two-phase flows at high phase fractions". PhD thesis. Imperial College London, 2003. URL: http://hdl.handle.net/10044/1/8110.

[46] C. Greenshields and H. Weller. *Notes on Computational Fluid Dynamics: General Principles*. Reading, UK: CFD Direct Ltd, 2022. ISBN: 978-1-3999-2078-0.

[47] *The OpenFOAM Foundation: OpenFOAM 6 Source Code*. accessed: 11.07.2022. URL: https://github.com/OpenFOAM/OpenFOAM-6.

[48] C. Dritselis and G. Karapetsas. "Open-source finite volume solvers for multiphase (n-phase) flows involving either Newtonian or non-Newtonian complex fluids". In: *Computers & Fluids* 245, 2022, p. 105590. DOI: https://doi.org/10.1016/j.compfluid.2022.105590.

[49] S. S. Deshpande, L. Anumolu, and M. F. Trujillo. "Evaluating the performance of the two-phase flow solver interFoam". In: *Computational science & discovery* 5, 2012, p. 014016. DOI: https://doi.org/10.1088/1749-4699/5/1/014016.

[50] S. T. Miller, H. Jasak, D. A. Boger, E. G. Paterson, and A. Nedungadi. "A pressure-based, compressible, two-phase flow finite volume method for underwater explosions". In: *Computers & Fluids* 87, 2013. USNCCM Moving Boundaries, pp. 132–143. DOI: https://doi.org/10.1016/j.compfluid.2013.04.002.

[51] G. A. Sod. "A survey of several finite difference methods for systems of nonlinear hyperbolic conservation laws". In: *Journal of Computational Physics* 27, 1978, pp. 1–31. DOI: https://doi.org/10.1016/0021-9991(78)90023-2.

[52] C. J. Greenshields, H. G. Weller, L. Gasparini, and J. M. Reese. "Implementation of semi-discrete, non-staggered central schemes in a colocated, polyhedral, finite volume framework, for high-speed viscous flows". In: *International Journal for Numerical Methods in Fluids* 63, 2010, pp. 1–21. DOI: https://doi.org/10.1002/fld.2069.

[53] F. Quintero, J. Penide, A. Riveiro, J. Del Val, R. Comesaña, F. Lusquiños, and J. Pou. "Continuous fiberizing by laser melting (Cofiblas): Production of highly flexible glass nanofibers with effectively unlimited length". In: *Science Advances* 6, 2020, eaax7210. DOI: https://doi.org/10.1126/sciadv.aax7210.

[54] A. Riveiro, F. Quintero, M. Boutinguiza, J. Del Val, R. Comesaña, F. Lusquiños, and J. Pou. "Laser cutting: A review on the influence of assist gas". In: *Materials* 12, 2019, p. 157. DOI: https://doi.org/10.3390/ma12010157.

[55] F. Quintero, A. F. Doval, A. Goitia, R. Gómez Vázquez, K. Crespo, R. Barciela, M. Fernández-Arias, F. Lusquiños, A. Otto, and J. Pou. "Analysis of the oscillations induced by a supersonic jet applied to produce nanofibers". In: *International Journal of Mechanical Sciences* 238, 2023, p. 107826. DOI: https://doi.org/10.1016/j.ijmecsci.2022.107826.

[56] R. Cunningham, C. Zhao, N. Parab, C. Kantzos, J. Pauza, K. Fezzaa, T. Sun, and A. D. Rollett. "Keyhole threshold and morphology in laser melting revealed by ultrahigh-speed x-ray imaging". In: *Science* 363, 2019, pp. 849–852. DOI: https://doi.org/10.1126/science.aav4687.

[57] A. F. Kaplan. "Analysis and modeling of a high-power Yb: fiber laser beam profile". In: *Optical Engineering* 50, 2011, pp. 054201–054201. DOI: https://doi.org/10.1117/1.3580660.

[58] K. Schricker, L. Schmidt, H. Friedmann, C. Diegel, M. Seibold, P. Hellwig, F. Fröhlich, J.-P. Bergmann, F. Nagel, P. Kallage, A. Rack, H. Requardt, and Y. Chen. "Characterization of keyhole dynamics in laser welding of copper by means of high-speed synchrotron X-ray imaging". In: *Procedia CIRP* 111, 2022, pp. 501–506. DOI: https://doi.org/10.1016/j.procir.2022.08.079.

[59] J. Roenby, H. Bredmose, and H. Jasak. "A computational method for sharp interface advection". In: *Royal Society Open Science* 3, 2016, p. 160405. DOI: https://doi.org/10.1098/rsos.160405.

[60] H. Udin. "Surface tension of solid copper". PhD thesis. Massachusetts Institute of Technology, 1949.

[61] D. A. Harrison, D. Yan, and S. Blairs. "The surface tension of liquid copper". In: *The Journal of Chemical Thermodynamics* 9, 1977, pp. 1111–1119. DOI: https://doi.org/10.1016/0021-9614(77)90112-4.

[62] P. T. Bauman, B. S. Kirk, T. A. Oliver, S. Plessis, and R. H. Stogner. *Antioch: C++ Chemical Kinetics, Thermodynamics, and Transport Library*. accessed: 05.05.2023. URL: https://github.com/libantioch/antioch.

[63] R. B. Bird, W. E. Stewart, and E. N. Lightfoot. *Transport Phenomena*. Wiley & Sons, 2007.

[64] B. J. Simonds, J. Tanner, A. Artusio-Glimpse, P. A. Williams, N. Parab, C. Zhao, and T. Sun. "The causal relationship between melt pool geometry and energy absorption measured in real time during laser-based manufacturing". In: *Applied Materials Today* 23, 2021, p. 101049. DOI: https://doi.org/10.1016/j.apmt.2021.101049.

[65] Z. Yang, A. Bauereiß, M. Markl, and C. Körner. "Modeling Laser Beam Absorption of Metal Alloys at High Temperatures for Selective Laser Melting". In: *Advanced Engineering Materials* 23, 2021, p. 2100137. DOI: https://doi.org/10.1002/adem.202100137.

[66] A. Schmon, K. Aziz, and G. Pottlacher. "Density of liquid Ti-6Al-4V". In: *EPJ Web Conf.* 151, 2017, p. 04003. DOI: https://doi.org/10.1051/epjconf/201715104003.

[67] G. Welsch, R. Boyer, and E. W. Collings. *Materials properties handbook: titanium alloys*. ASM international, 1993.

[68] Y. N. Starodubtsev and V. S. Tsepelev. "Effect of Atomic Size on the Isothermal Bulk Modulus and Surface Tension of Liquid Metals". In: *Metallurgical and Materials Transactions B* 53, 2022, pp. 2547–2552. DOI: https://doi.org/10.1007/s11663-022-02550-1.

[69] X. Zhao, C. Reilly, L. Yao, D. M. Maijer, S. L. Cockcroft, and J. Zhu. "A three-dimensional steady state thermal fluid model of jumbo ingot casting during electron beam re-melting of Ti–6Al–4V". In: *Applied Mathematical Modelling* 38, 2014, pp. 3607–3623. DOI: https://doi.org/10.1016/j.apm.2013.11.063.

[70] M. Boivineau, C. Cagran, D. Doytier, V. Eyraud, M.-H. Nadal, B. Wilthan, and G. Pottlacher. "Thermophysical Properties of Solid and Liquid Ti-6Al-4V (TA6V) Alloy". In: *International Journal of Thermophysics* 27, 2006, pp. 507–529. DOI: https://doi.org/10.1007/PL00021868.

[71] R. K. Wunderlich. "Surface Tension and Viscosity of Industrial Ti-Alloys measured by the Oscillating Drop Method on Board Parabolic Flights". In: *High Temperature Materials and Processes* 27, 2008, pp. 401–412. DOI: https://doi.org/10.1515/HTMP.2008.27.6.401.

[72] E. W. Lemmon, I. H. Bell, M. L. Huber, and M. O. McLinden. "Thermophysical properties of fluid systems". In: *NIST chemistry WebBook, NIST Standard Reference Database 69*. Ed. by P. Linstrom and W. Mallard. National Institute of Standards and Technology. DOI: https://doi.org/10.18434/T4D303.

[73] M. E. Wieser. "Atomic weights of the elements 2005 (IUPAC Technical Report)". In: *Pure and Applied Chemistry* 78, 2006, pp. 2051–2066. DOI: https://doi.org/10.1351/pac200678112051.

[74] *Matweb Cu-ETP data sheet*. accessed: 12.05.2023. URL: https://www.matweb.com/.

[75] P. B. Johnson and R. W. Christy. "Optical Constants of the Noble Metals". In: *Physical Review B* 6, 1972, p. 4370. DOI: https://doi.org/10.1103/PhysRevB.6.4370.

[76] A. R. Kurochkin, P. S. Popel', D. A. Yagodin, A. V. Borisenko, and A. V. Okhapkin. "Density of copper-aluminum alloys at temperatures up to 1400 C determined by the gamma-ray technique". In: *High Temperature* 51, 2013, pp. 197–205. DOI: https://doi.org/10.1134/S0018151X13020120.

[77] M. J. Assael, A. E. Kalyva, K. D. Antoniadis, R. Michael Banish, I. Egry, J. Wu, E. Kaschnitz, and W. A. Wakeham. "Reference Data for the Density and Viscosity of Liquid Copper and Liquid Tin". In: *Journal of Physical and Chemical Reference Data* 39, 2010, p. 033105. DOI: https://doi.org/10.1063/1.3467496.

[78] L. Alter, A. Heider, and J.-P. Bergmann. "Investigations on copper welding using a frequency-doubled disk laser and high welding speeds". In: *Procedia CIRP* 74, 2018, pp. 12–16. DOI: https://doi.org/10.1016/j.procir.2018.08.003.

Simulation-Based Process Optimization of Laser-Based Powder Bed Fusion by Means of Beam Shaping

Constantin Zenz[a,1,*], Michele Buttazzoni[a,1], Mario Martínez Ceniceros[b], Rodrigo Gómez Vázquez[a], Jose Ramón Blasco Puchades[b], Luis Portolés Griñán[b], Andreas Otto[a]

[a]Institute of Production Engineering and Photonic Technologies, TU Wien, Getreidemarkt 9, 1060, Vienna, Austria

[b]AIDIMME, Leonardo da Vinci 38, 46980, Paterna, Spain

[1]These authors contributed equally to the work

[*]Corresponding author

This version of the article has been accepted for publication, after peer review, but is not the Version of Record. The Version of Record is available online at: https://doi.org/10.1016/j.addma.2023.103793

Abstract: Laser powder bed fusion (PBF-LB/M) is an additive manufacturing technique which has recently been growing in popularity in industrial use cases. However, several challenges persist, including the issue of solidification cracking observed in widely used Ni-based superalloys. Through retrofitting an existing PBF - machine with a dual beam system capable of dynamic beam shaping, it is possible to overcome this issue. Beforehand it is crucial to determine the appropriate process parameters for the laser beam need to be determined prior to manufacturing the system. In this regard we propose a methodology that utilizes a numerical simulation tool to identify optimized parameters. To demonstrate the effectiveness of this approach, two example processes are presented. Initially the numerical model is validated by comparing its results against experimental data obtained from single track scans of two metal powders: CM247LC and IN713LC. Subsequently, an optimization study is conducted to identify optimal combinations of differently shaped and sized primary and secondary beams. The goal is to reduce the cooling rates within certain critical temperature ranges, thus mitigating the likelihood of solidification cracking, while avoiding the occurrence of other process defects such as balling, porosity, or lack of fusion. The effectiveness of these beam shapes is then verified through the production of physical samples. Through this example, a methodology for leveraging physics-based, model-driven process optimization is presented. Additionally, we provide insights into the potential application of the same model for large-scale simulations.

Keywords: Laser Powder Bed Fusion; Process Optimization; Ni-based Superalloys; Multiphysical Simulation; Beam Shaping

1 Introduction

Additive manufacturing (AM) has revolutionized production by allowing the creation of complex shapes directly from three-dimensional CAD models. Initially utilized primarily for non-functional design prototypes (rapid prototyping), the numerous advantages of AM over conventional processes, have led to its rapid adoption across various industries, including aerospace, automotive, medical and energy [1]. These benefits encompass the ability to fabricate customised parts, minimize material waste and manufacture shapes, that were previously unattainable using conventional manufacturing techniques [2]. The industry's adoption of AM has been made possible by advancements in high-power industrial lasers and the development of new metal powders over the past two decades. [1].

PBF-LB/M is a manufacturing process that involves dividing a three-dimensional geometry into multiple layers, each with a predetermined layer height, which are subsequently manufactured. To build each layer a metal powder is evenly spread across a substrate, which can be either a plate or a previously processed powder layer. Utilizing a laser beam, the powder is selectively melted to construct the geometry of a single layer. Subsequent re-solidification of the molten metal gives the required shape. This process is repeated for each layer, with the build plate being lowered and a new layer of powder applied afterward [2]. While AM techniques are applied to various types of materials, most research and development has been concentrated in the domain of metal AM. Recent research efforts are focused on the development of new materials, as well as process optimization, including the development of scanning strategies for the reduction of residual stresses and improvement of part properties [2]. As noted by DebRoy et al. [3], most research published on metal AM covers fundamentals and lacks direct relevance for practical applications, whereas industrially exploitable research activities are mostly performed by corporations and therefore remain unpublished. This leaves a research gap in the area of applied research on AM.

During the project CUSTODIAN [4], funded by the European Union, a novel methodology enhancing established industrial processes through laser beam shaping was developed. Within this approach, new or existing machines are equipped with a laser head containing a passive optical element, facilitating dynamic freeform beam shaping on the basis of Multi Plane Light Conversion (MPLC) [5]. The main advantages of this technology are the complete freedom of beam shape design and the possibility of retrofitting any existing machine. However, one limitation of this technology is that the desired beam shape, which can be dynamically modulated to a certain extent, must be known prior to manufacturing the device. Therefore, the beam shapes cannot be found experimentally and physics-based simulations are used instead. A similar use case for the optimization of beam shapes in a laser beam welding process has previously been presented by Buttazzoni et al. [6].

This work showcases the applicability of this method to PBF-LB/M processes. It demonstrates the utilization of an MPLC device to add a secondary laser beam to a process where crack-free parts cannot be achieved using a single Gaussian laser beam. Two widely used nickel-based alloys, CM247LC and IN713LC, were selected as suitable materials for this optimization study based on their industrial significance and

inherent susceptibility to cracking. The simulation model is used to obtain preliminary beam shapes with the aim of reducing cooling rates and thus crack susceptibility, while avoiding the occurrence of other process defects.
In contrast to welding, where information on weldability and suitable process parameters for various alloys is widely available, information on printability and suitable parameter spaces for AM processes is scarce and correct process parameters are often obtained through trial-and-error experiments [1]. This lack of process understanding calls for accurate, physics-based, models to gain a better understanding and to use these models as process optimization tools [7, 8].
Many transient phenomena occurring in PBF-LB/M processes are only directly observable, when using very elaborate experimental setups [7]. For example, Cunningham et al. recently used high speed x-ray imaging techniques to perform in-situ observations of keyhole dynamics in PBF-LB/M [9]. While such methods are crucial in understanding and developing process models, they often fall short when it comes to industrial application, particularly in tasks like process optimization, where parameter studies have to be completed within a given time frame.
A recent study conducted by Shu et al. [10] emphasized the importance of accurately incorporating convective heat- and mass transfer needs in a PBF-LB/M model. It was demonstrated that neglecting these factors can lead to inaccurate three-dimensional weld bead shape, even when a model has been validated by comparing two-dimensional cross sections to experiments. Hence, when employing a calibrated and validated model for straightforward optimization tasks that do not necessitate gaining further process insights, it is imperative to incorporate a certain level of complexity. Specifically it should always account for convective transport, considering the influence of surface tension-, recoil pressure- and buoyancy-induced forces.
Simulation models can be characterized by the length scale on which they are applicable [7]. The model applied within this study is of the meso-scale type, where the fluid flow within the melt pool of each single process track is fully resolved, while also allowing the simulation of several layers, each consisting of several tracks, within reasonable amount of computing time (in the order of days on a desktop computer). Details on the model are presented in Section 2. In Section 3, the methodology of optimizing a beam shape using the FVM model is presented. The possibility of using the here-presented method on larger scales than single scan tracks is demonstrated in a brief outlook in Section 4 and finally, a conclusion and an outlook are provided in Section 5.

2 Simulation Model

2.1 Model overview

The model utilized in this study was originally developed over a decade ago [11] to simulate the multiphysical problem of laser beam welding. Since then, it has been significantly expanded to encompass various laser-assisted manufacturing processes. The model has been used in various application, such as simulating humping and the transition to cutting in laser beam welding of thin stainless steel foils [12], investi-

gating spiking and pore formation in welding of copper and aluminum [13], exploring welding of dissimilar materials [14] and optimizing overlap welding of stainless steel sheets with a gap using MPLC technology [6]. Furthermore, laser cutting [15], and laser-based direct energy deposition [16] have been simulated. Additionally, the model is applicable to processes involving short pulsed lasers, such as ablation of multi-material structures using ns-pulses [17], and the processing of semiconductor materials [18] and dielectric materials [19] using ps- to fs-pulses.
The model is implemented using the open source C++ library OpenFOAM [20] and is based on the solver `multiphaseInterFoam`, an extension of the two-phase Volume-of-Fluid solver `interFoam` [21], capable of handling an arbitrary number of phases. Details on the model can be found in the aforementioned publications, especially [12] and [6], as well as in [22]. A more in-depth description of the modeling approach is the topic of a forthcoming publication. Therefore, only a brief overview will be given here, with emphasis on process-specific details relevant for the simulation of PBF-LB/M. The steps performed within each time step of the simulation model are provided in Figure 1 in the form of a flow chart and described below.
Caustic-aware laser beam propagation is modeled through a radiative transfer equa-

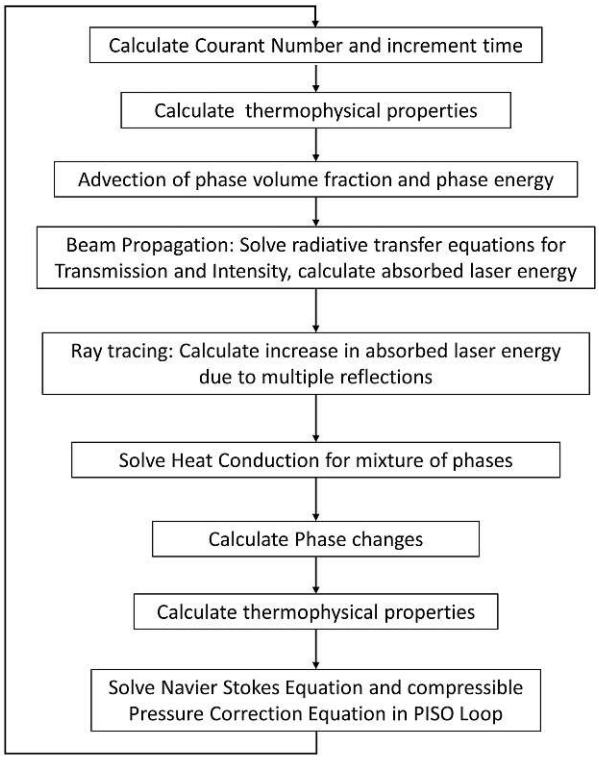

Figure 1: Basic overview of calculation steps performed by the solver during each simulation time step.

tion in combination with a ray tracing algorithm to account for multiple reflections.

Reflectivity, R, is modeled through the Fresnel equations,

$$R_S = \left| \frac{cos(\beta) - \underline{n}\sqrt{1 - sin^2(\beta)/\underline{n}^2}}{cos(\beta) + \underline{n}\sqrt{1 - sin^2(\beta)/\underline{n}^2}} \right|, \tag{1}$$

$$R_P = \left| \frac{\underline{n}cos(\beta) - \sqrt{1 - sin^2(\beta)/\underline{n}^2}}{\underline{n}cos(\beta) + \sqrt{1 - sin^2(\beta)/\underline{n}^2}} \right|, \tag{2}$$

$$R = \frac{R_S + R_P}{2}, \tag{3}$$

where β is the local angle of incidence and $\underline{n}$ is the material's complex refractive index. Absorption of laser intensity I along its optical path, z, is modeled via Beer's law [23],

$$I(z) = I(0)\exp(-\kappa z), \tag{4}$$

with κ denoting the imaginary part of the material's complex refractive index, i.e., its extinction coefficient. Phase changes issue mass- and energy transfer between the respective phases. While melting and solidification are calculated through an enthalpy-porosity method [24], evaporation and condensation are modeled through the Hertz-Knudsen equation [25],

$$\frac{d\rho_{vap}}{dt} = \frac{1}{\Delta x}\sqrt{\frac{M}{2\pi RT}}\left(p_{sat} - p\right), \tag{5}$$

with ρ_{vap} denoting the mass density of the vapour phase, and p and T denoting pressure and temperature, respectively. Furthermore, R, M, and Δx denote the universal gas constant, the phase's molar mass and the local cell length, respectively. The local saturation pressure, p_{sat}, is calculated according to the Clausius-Clapeyron equation [26] as

$$p_{sat}(T) = p_{ref}\exp\left(\frac{ML}{T_b R}\left(1 - \frac{T_b}{T}\right)\right), \tag{6}$$

with T_b and L denoting the phase's boiling temperature and latent heat of vaporization, respectively. Fluid flow is modeled through the Navier-Stokes equations in a homogeneous equilibrium mixture formulation as

$$\frac{\partial\left(\rho\boldsymbol{u}\right)}{\partial t} + \nabla\cdot\left(\rho\boldsymbol{u}\boldsymbol{u}\right) = -\nabla p + \nabla\cdot\boldsymbol{\tau} - \boldsymbol{S_B} + \boldsymbol{S_S} + \boldsymbol{S_D}, \tag{7}$$

where $\boldsymbol{u}$ is the velocity of the mixture of phases, and $\boldsymbol{\tau}$ is the viscous stress tensor, assuming laminar flow. The last three source terms on the right hand side of Eq. (7) contain body forces due to gravity, surface forces due to surface tension, and a source term for movement restriction in solid regions following Darcy's law, respectively. The Darcy term, $\boldsymbol{S_D}$, is modeled following the Carman-Kozeny equation [27] in the form

$$\boldsymbol{S_D} = -\frac{\mu}{A_{perm}}\frac{\left(\alpha_{solid}\right)^2}{\left(1 - \alpha_{solid}\right)^3 + 10^{-6}}\boldsymbol{u}, \tag{8}$$

where α_{solid} is the volume fraction of solid material and μ is the dynamic viscosity of the mixture. The permeability area is set to $A_{perm} = 10^{-12}$ m^2. Temperature-

dependent surface tension forces are explicitly included through $\boldsymbol{S_S}$, which is calculated as

$$\boldsymbol{S_S} = \sum_{i,j \forall i \neq j} \nabla \cdot \left[\sigma_{i,j} \left(\alpha_j \nabla \alpha_i - \alpha_i \nabla \alpha_j \right) \right], \tag{9}$$

with surface energies $\sigma_{i,j}$ at interfaces between phase i and phase j, are calculated from the individual phase surface energies σ_i and σ_j, as [28]

$$\sigma_{i,j} = \sigma_i + \sigma_j - 2\sqrt{\sigma_i \sigma_j}. \tag{10}$$

Forces resulting from recoil pressure due to evaporation are taken into account implicitly, as both liquid as well as vapour phases are treated as compressible fluids and a phase change from liquid to vapour issues a corresponding change in density resulting in expansion of the evaporating material, which in turn issues the recoil pressure.

To avoid the computational costs of modeling individual powder particles, the powder is modeled as a continuum, by introducing an additional, distinct Volume-of-Fluid phase for the powder. The characteristics of powder (low density, low thermal conductivity, high laser beam absorptivity) are considered through the respective material properties of the powder phase. It has been modeled as having 50% of the density of the bulk material, in accordance with conducted measurements, and its thermal conductivity was calculated in accordance with the model of Sih and Barlow [29], yielding a value of $\approx 2\%$ of the bulk material's conductivity.

The simulation domain and phase distribution at the start of a simulation is shown in Figure 2. Mesh refinement was kept constant throughout the simulation and each subsequent run for consistency, where the cell size ranges from 25 µm up to 100 µm. At the boundaries different boundary conditions are applied. The boundary of the region depicted as solely containing surrounding phase in Figure 2 is treated as an open boundary, facilitating the in- and outflow. Conversely, the remaining regions are treated as closed boundaries, eliminating the transfer of heat and mass across those boundaries. Heat accumulation effects were negligible as earlier tests showed.

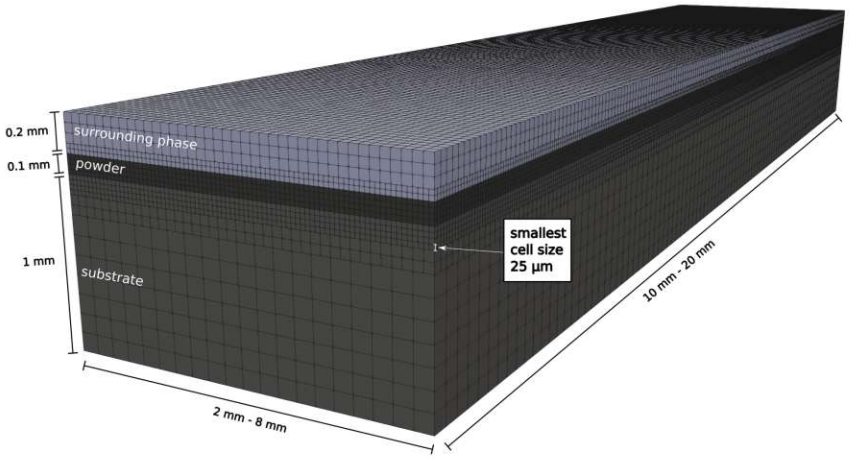

Figure 2: Sketch of simulation domain used. Length and width are varied according to secondary beam size (the smallest domain is shown)

2.2 Model validation

Experimental validation of mechanistic models is important as through each physical model, as well as through spatial and temporal discretization, some degree of uncertainty is introduced [7]. In order to gain physically accurate and practically relevant results, basic material properties were obtained from literature [30]. Data about the complex refractive index and the surface energies of all phases at high temperatures is scarce, due to the difficulty related to their measurement. Values for surface energies for instance are highly temperature-dependant as well as a function of physical state (solid, liquid, vapour) and alloy composition. These values are furthermore very sensitive to impurities. As these parameters have a great influence on the process outcome, great care was taken by properly calibrating it against experimental data. A summary of the properties for both investigated materials is provided in A, in Figure 24 and Figure 25, respectively, and their chemical composition is listed in Table 4.

Due to the fast convergence to a quasi-steady state process and the high computational cost associated with multi-track and multi-layer simulations, a single track was compared against experimental results in the calibration phase. The experiments used for the validation were performed at the facilities of AIDIMME, where the samples were also processed to produce cross sectional images that could then be compared against simulation results. All the tests presented in this publication have been conducted on a Concept Laser M3 PBF-LB/M machine, which has been modified with a high power laser (4000W) and a custom scanning head housing the MPLC. This modification was required to deliver sufficient energy for both melting the scan tracks with a primary beam and heating the surrounding area with a secondary beam. A track of approx. 9.5 mm in length was scanned on a substrate immersed in powder with a layer height of 100 µm. A summary of the process parameters is presented in Table 1 for both materials. These were chosen after extensive experimental testing,

where scanning speed and lasing power was varied between 300-800 mm/s and 200-600 W respectively. The chosen reference condition presents the highest part density and lowest crack appearance for each material. Samples presented in Figures 3 and 4 were carried out with a standard Gaussian distribution beam shape. The validated simulation results can be seen in Figure 3 for CM247LC and in Figure 4 for IN713LC, respectively.

	CM247LC	**IN713LC**
scanning speed (mm/s)	750	750
laser power (W)	452	520
laser wavelength (nm)	1070	1070
laser M^2	1	1
laser focus position	on surface	on surface
laser radius on substrate (µm)	176	176
scan track length (mm)	9.5	9.5
powder bed height (µm)	100	100

Table 1: Single-beam process conditions for both investigated alloys used for validation of the simulation model

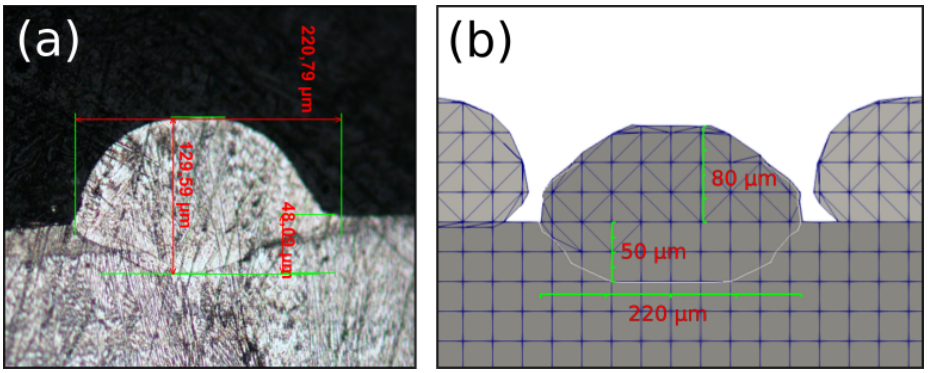

Figure 3: Validation against experiment for CM247LC: (a) Experimental cross section. (b) Cross section resulting from the simulation.

The decision to employ such a detailed and complex multiphysical model as an optimization tool was not only driven by the need to investigate the beam configuration's influence on cooling rates, but to also simultaneously identify (and avoid) any unwanted printing errors during the optimization process. This capability is shown here by example of the so-called balling defect. A first round of testing was carried out using the same laser power of 452 W for both investigated alloys. The experimental results of three single tracks produced side-by-side by scanning IN713LC powder can be seen in Figure 5 and Figure 6, where three exemplary cross sectional views and a top view are provided respectively. It is noticeable, that balling occurred, where the liquid metal tends to agglomerate rather than to wet the underlying substrate, leading to the formation of melt spheres with high contact angles, exhibiting poor penetration of the substrate and a weld of unconnected sphere-like beads [31].

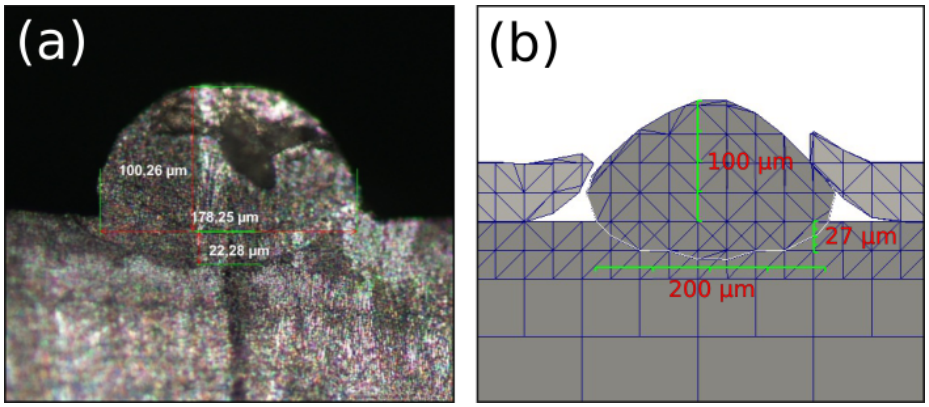

Figure 4: Validation against experiment for IN713LC: (a) Experimental cross section. (b) Cross section resulting from the simulation.

This surface tension force-driven phenomenon is usually associated with the Plateau-Rayleigh capillary instability [32]. Further proofing the adaptability and accuracy of the here presented model, a simulation of this process condition was carried out and is provided in Figure 7. The calculation and material properties used are the same as in the validation case (cf. Table 1), except for the lower input laser power. The formation mechanism behind the characteristic weld beads of unconnected, spherical structures shown in Figure 6 and Figure 7 can also be observed in the simulation, which is shown in Figure 8, where the effect of evaporation-induced recoil pressure was deliberately excluded from the simulation to clearly show that this is a purely surface-tension driven phenomenon (as opposed to the humping mechanism, which could lead to a similar weld bead). The melt pool at the beginning of the process is very shallow and has a flat interface to the underlying colder substrate. Due to the low thermal conductivity of the surrounding inert gas and powder, most of the heat is dissipated downwards into the bulk material. Due to the larger temperature gradient at the bottom of the melt pool, more cooling takes place in this region and thus the top remains liquid for longer time and heat accumulates in this region. Because of the inverse relationship between surface tension and temperature, the resulting force will cause a contraction (inwards-pointing force) of the melt pool, pushing it into the characteristic spherical shapes. The phenomenon is further amplified, as the formation of spherical melt structures inhibits cooling and promotes heat accumulation (a). The surface tension force holding together the melt agglomeration, drags the liquid along with the moving heat source (b). After some time, the sphere solidifies from below, slowly halting the movement of the bead (c) and causing the first sphere to separate from the remaining melt pool (d). Its surface tension is now providing a force acting across the liquid bridge between the first and second sphere (d), also preventing the second sphere from moving. After complete separation has occurred and with increased accumulated heat input, the laser effectively penetrates the substrate, resulting in a larger shared interface between the melt pool and the substrate. Thus, in turn, creating a multidirectional (as opposed to only vertical) heat sink, mitigating the heat accumulation at the top of the weld bead that leads to the aforementioned phenomenon (e-f). The process now reaches a steady state with subsequently forming spheres not being dragged along and remaining smaller than the first one, leading to

a periodic distribution of spherical structures (cf. top view in Figure 7). The steady state exhibits the typical (idealized) phenomenon associated with Plateau-Rayleigh capillary instability [32].
In a similar way, other process defects could potentially be identified, e.g., the model was recently used to simulate pore formation [6].

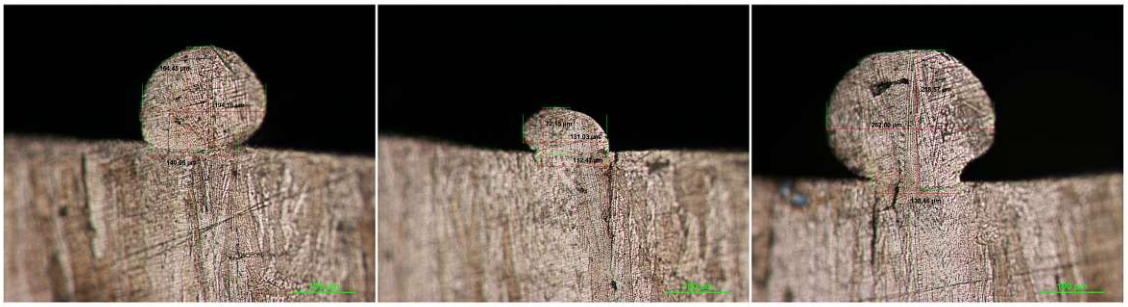

Figure 5: Cross sectional views of single track experiments with IN713LC, laser power P = 452W, scanning velocity $v_s = 750\ \frac{mm}{s}$, hatch distance $d_h = 100$ µm and powder thickness $t_p = 50$ µm

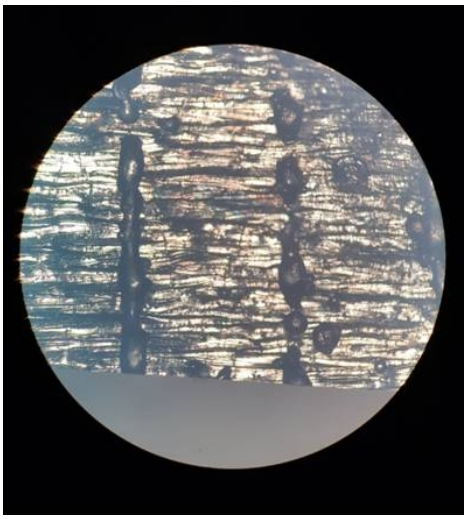

Figure 6: Top view of the single track experiments seen also in Figure 5

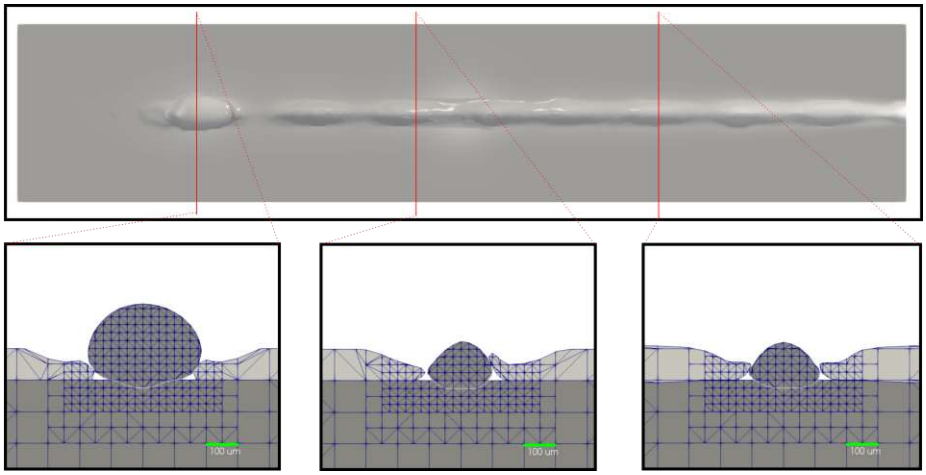

Figure 7: Single track simulation: Top view and exemplary cross sections with IN713LC, P = 452W

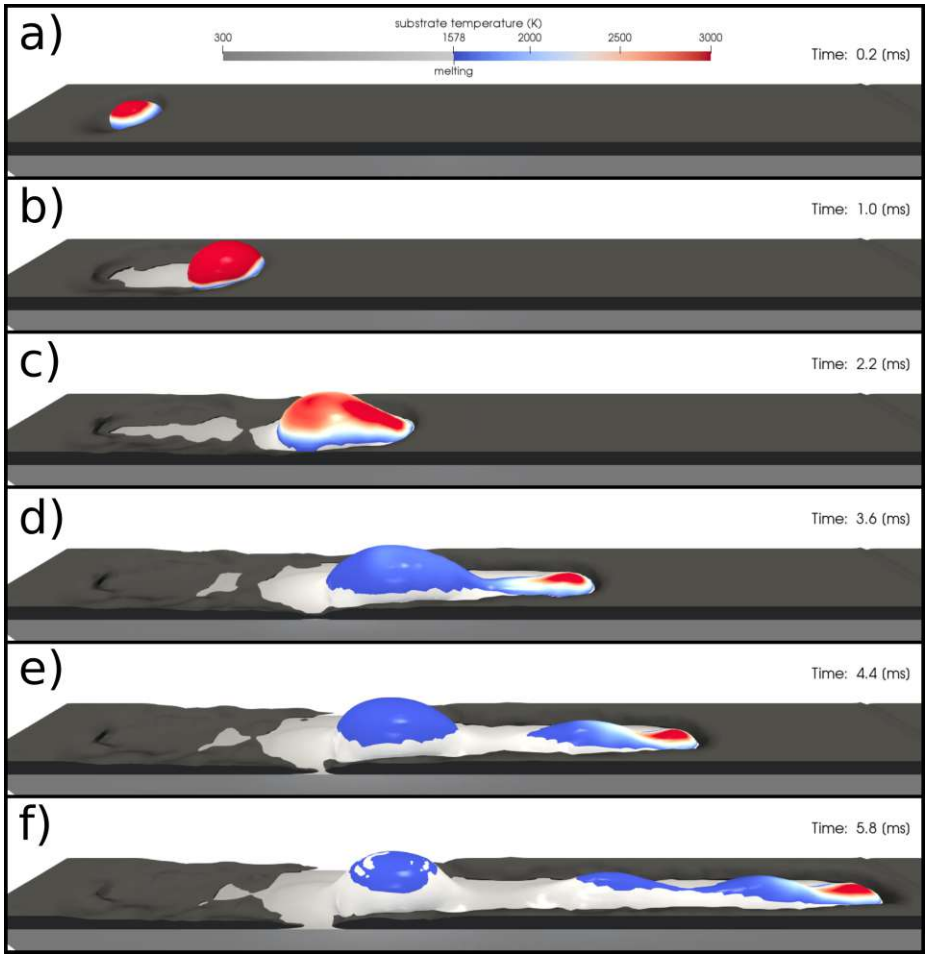

Figure 8: Single track simulation of PBF-LB/M of IN713LC, P = 452W: a) - c) Formation of first spherical agglomeration. d) - f) Formation of subsequent agglomerations.

3 Parameter study and beam shape optimization

A major issue in additive manufacturing of nickel-based superalloys is the appearance of cracks induced by thermal stresses during solidification in the final part. The high susceptibility to solidification cracking is associated with the high amount of Al and Ti within the alloys. According to [33], Ni-based superalloys are classified as non-weldable when exhibiting concentrations of Al and Ti above 6 % wt., as is the case with both CM247LC and IN713LC. Non-weldability can be taken as a measure of non-printability in this context [34]. A reduction of these defects was sought after in the course of the EU-funded CUSTODIAN [4] project through appropriate beam shaping using MPLC technology. As a result of conducting metallurgical investigations in a preceding study within the CUSTODIAN project [35], it was identified that the defect density increases drastically, when the material is cooled down rapidly from its melted state. More specifically a rapid cooling inside a well-defined temperature range, known as the brittle temperature region (where the alloy's phases coexist in a so-called mushy zone), contributes greatly to crack formation. The nucleation and crystalline growth at different locations inside this region results in a morphology where growing crystals are surrounded by a liquid melt at the grain boundaries. This temperature range usually lies a few hundred degrees below the liquidus temperature. By rapidly cooling the melt, the liquid melt does not have time to back-fill all of the intermittent spaces created by tensile stresses caused by contraction of the material [33].
Following the validation of the simulation model in Section 2.2, a parameter study was carried out in order to obtain appropriate beam shapes for a dual beam setup for each of the investigated materials in Section 3.3 and Section 3.4.

3.1 Optimization methodology

In order to avoid micro-structural damage to the final part, an approach to reduce the cooling rates, $\frac{dT}{dt}$, in the most susceptible temperature range, by means of laser beam shaping, was pursued. More details on the calculation of the cooling rates and their usage is presented in Section 3.2.
A secondary goal was to achieve a welded cross section with a high width-to-depth ratio, as this was also found to reduce the probability of cracking. The crack susceptibility is greater in a deep and narrow melt pool [36], because in this case the thermal gradients are oriented parallel to the free surface, where the movement of the material is restricted. In the case of a shallow melt pool, the surface of the mushy zone can move freely when experiencing tensile stresses and thus help reduce their concentration in the solidified substrate.
The scanning speed in Section 3.3 and Section 3.4 is not varied from the value of v_s = 750 $\frac{mm}{s}$ used in Section 2.2 for the validation against experiments.

3.2 Calculation of cooling rates for comparative study

The cooling rates are calculated at run-time at every point (cell-center) where material has previously been molten and its temperature is passing the brittle temperature range [35] during the course of the simulation. To limit the amount of data to be

stored, only the maximum value of $\frac{dT}{dt}$ during the entire simulation is stored. Furthermore, to enable a quick quantitative comparison between simulated processes with differing melt pool sizes, the cooling rates are discretized in bins and the volume of material being cooled within these bins, $V(\frac{dT}{dt})$, is summed up and plotted. The bin size was carefully chosen to find a compromise between spurious data smoothing and noise. The resulting curves are then compared to each other, as is shown for example for different sized laser spots in Figure 9. A certain beam combination is regarded as superior in terms of cracking susceptibility, if the geometric center of its plot curve is shifted towards the origin of the graphs relative to other process conditions.

3.3 Beam shape optimization on CM247LC

Before adding a secondary beam to the process, the influence of changing primary beam size and power was investigated. Two larger spot sizes were investigated (see Table 2), while adjusting the power to keep the penetration depth similar. The resulting cooling rates in the brittle temperature region from 1523K to 1673K [35] were plotted and then compared to the reference condition. This is shown in Figure 9 and the respective cross sections in Figure 10.

Spot diameter on work-piece surface d (µm)	Laser power P (W)
176	452
352	800
528	1000

Table 2: Configurations for investigations on primary beam influence on CM247LC

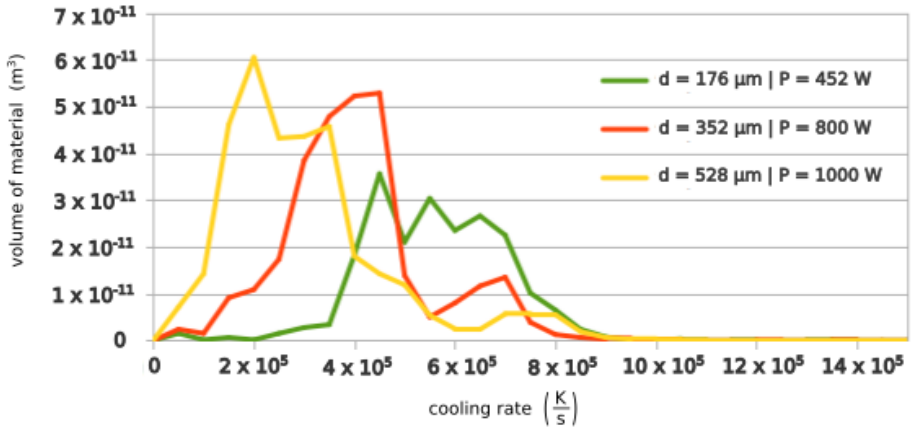

Figure 9: Cooling rate curves using different primary beam

An investigation of even larger spot sizes was deemed unnecessary due to the limitations in power of real-world laser systems, the inaccuracy introduced by larger spots and the clear trend that was observed. These trends led to the conclusion that larger illuminated areas at similar intensities lead to lower cooling rates and more favorable cross sections (enforced by the condition of keeping the penetration depth

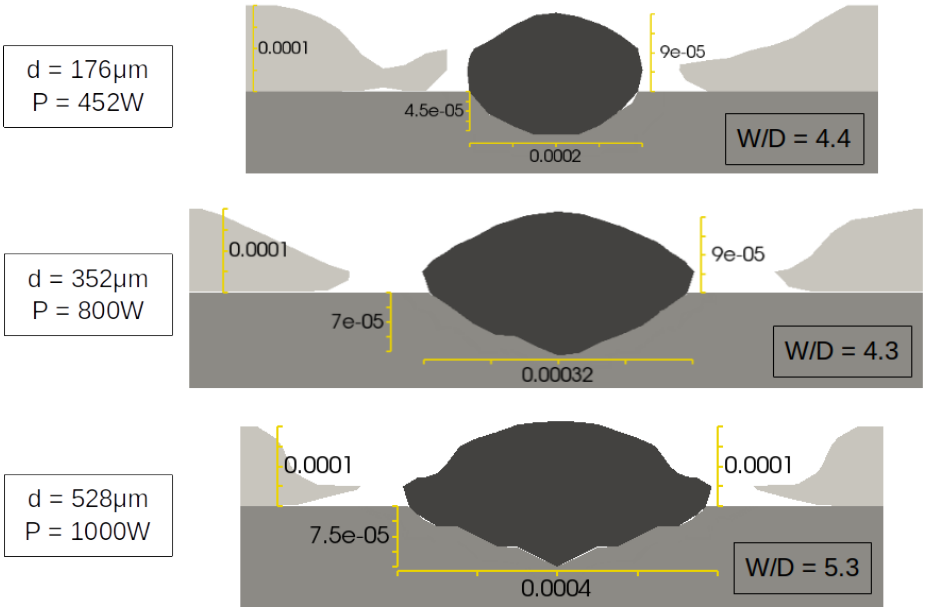

Figure 10: Cross sections using different primary beams used for width-to-depth ratio (W/D) comparison

similar).
A main strategy followed during CUSTODIAN consists of pre- and/or post-heating the powder and/or substrate to further reduce the risk of solidification crack appearance. Due to the high scanning speeds necessary in PBF-LB/M and the utilization of random scan patterns, there was a need for a beam geometry that is rotationally symmetric. This requirement aimed to avoid the rotation of the laser head, which was beyond the scope of the project.
Several experiments were conducted, which determined that a unidirectional scanning strategy cannot be used and therefore asymmetrical shapes are not possible. As shown in Figure 11,when employing a unidirectional scanning direction without rotation between layers, noticeable swelling occurs in the topmost layers, leading to an intensified cracking phenomenon. Avoiding rotation between layers leads to a cracking tendency along the build direction. For this reason, the secondary beam was chosen to be circular, concentric to the primary beam and of tophat energy distribution as depicted in Figure 12.

The pairings of primary and secondary beams are summarized in Table 3. These values resulted from careful evaluation of efficiency and restrictions in form of maximum available power, recyclability of the powder, surface area of the samples, as well as accuracy. After a few test runs, it became evident that a large secondary spot with enough intensity to preheat the powder and substrate, without actually melting the powder, is favorable in terms of avoiding high cooling rates. That is why secondary spots with large radii and higher power than their coupled primary spots were used. The results of the simulations using the aforementioned laser beam pairings are presented in Figures 13 - 18, where cooling rate plots and cross sections are shown.
In conclusion, it can be inferred that the size of the secondary beam has an impact on the extent of pre- and post-heating during the process, and it is advisable to select

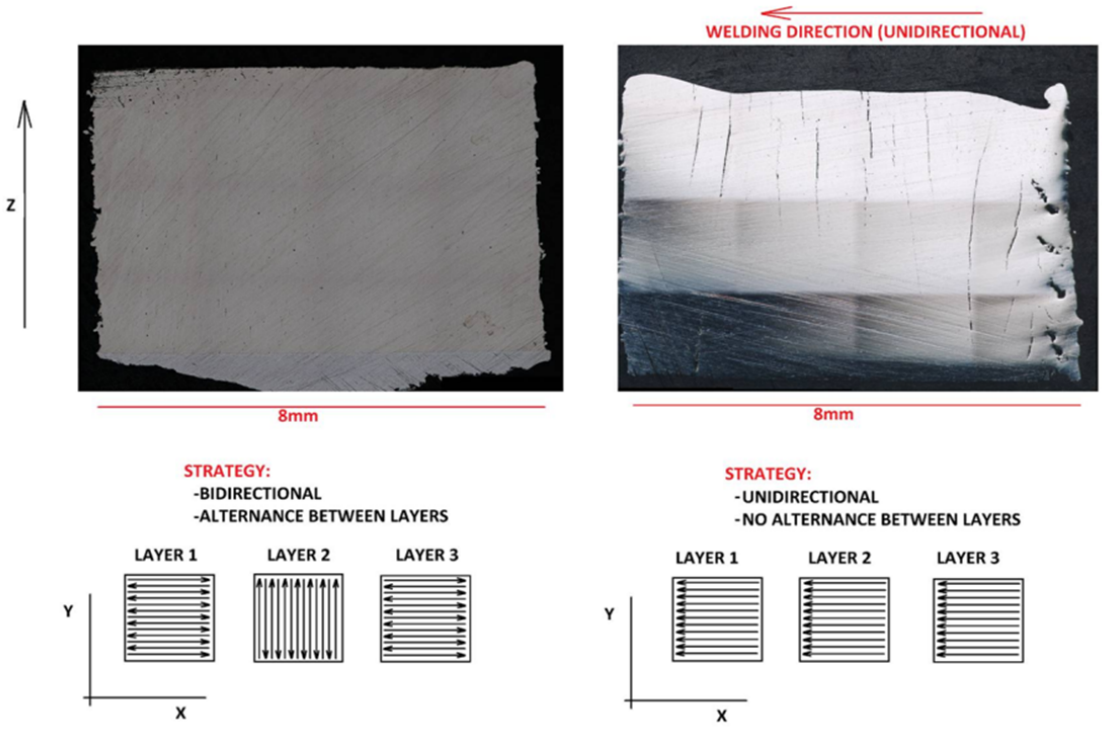

Figure 11: Cross section analysis of CM247LC processed by different scanning strategies; bidirectional + alternated (LEFT), and unidirectional + no alternance between layers (RIGHT). Process parameters: laser power P = 452W, scanning velocity $v_s = 750\ \frac{mm}{s}$, hatch distance $d_h = 100$ µm and powder thickness $t_p = 50$ µm

a larger size within the limits of the available power. This increase in energy input results in a larger portion of the melted volume experiencing lower cooling rates, provided that the intensity of the secondary beam is appropriately selected. However, it was found that the influence of the secondary beam, despite requiring more power, is not as pronounced as the size and power of the primary beam.
The optimal beam combination, considering technological and other limitations, that results in reduced cooling rates and an optimized cross sectional shape, is highlighted in bold lettering in Table 3.

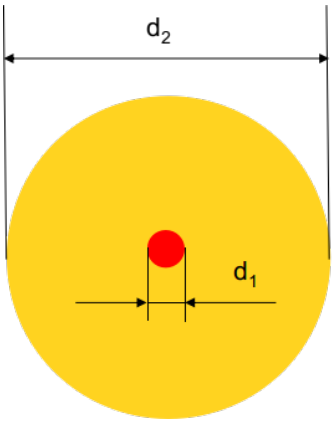

Figure 12: Sketch of primary and secondary beam combination layout

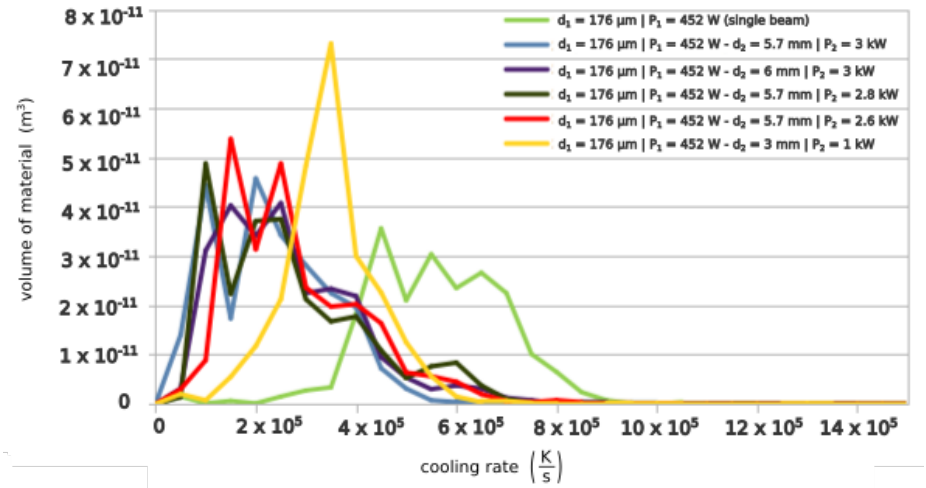

Figure 13: Cooling rate curves different secondary beams paired with a 176 µm primary beam

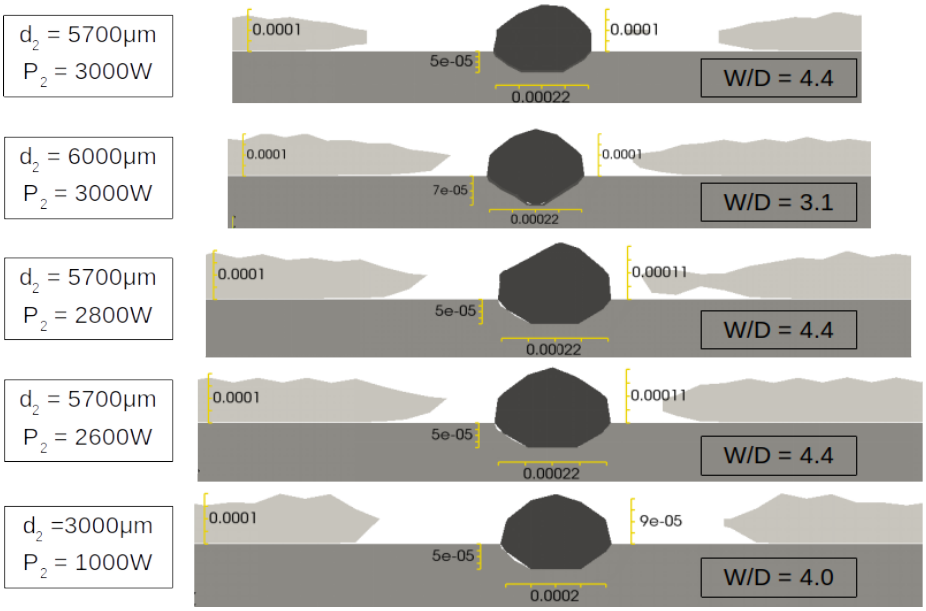

Figure 14: Cross sections related to conditions in Figure 13

Primary spot diameter on work-piece surface d_1 (µm)	**Primary laser beam power P_1 (W)**	**Secondary spot diameter on work-piece surface d_2 (µm)**	**Secondary laser beam power P_2 (W)**
176	452	5700	3000
176	452	6000	3000
176	452	5700	2800
176	452	5700	2600
176	452	3000	1000
352	800	5400	2300
352	800	5400	2700
528	1000	1000	100
528	1000	2000	400
528	1000	3000	900
528	1000	4000	1600
528	1000	5000	2500
528	**1000**	**4500**	**2500**

Table 3: Parameter combinations investigated on CM247LC (best beam combination highlighted in the last row)

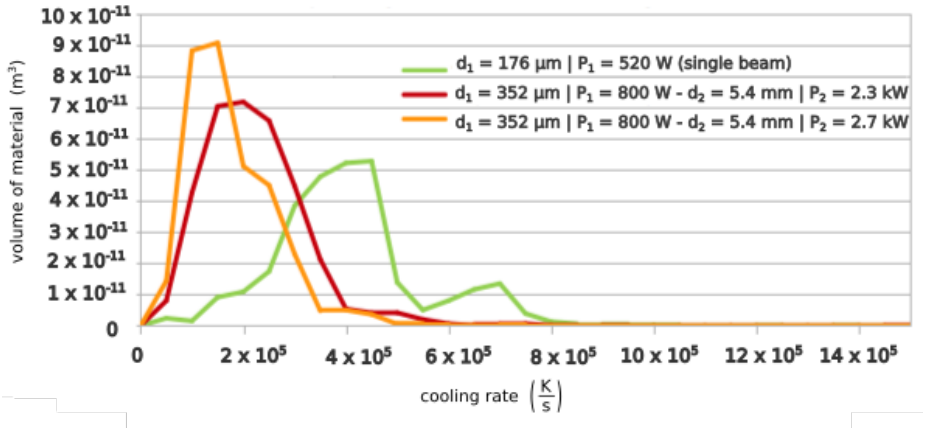

Figure 15: Cooling rate curves different secondary beams paired with a 352 µm primary beam

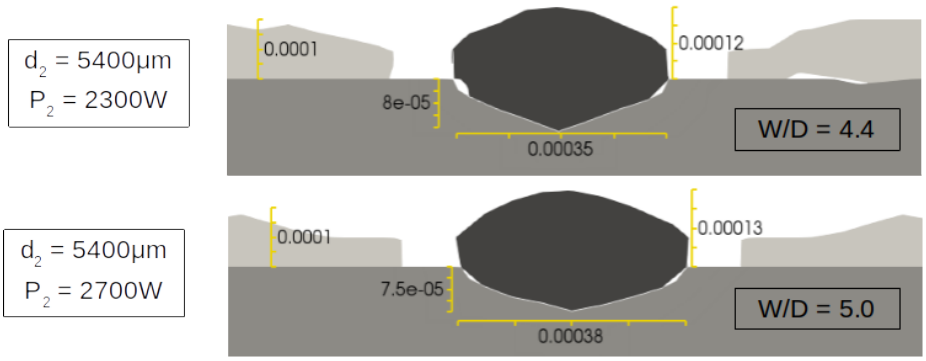

Figure 16: Cross sections related to conditions in Figure 15

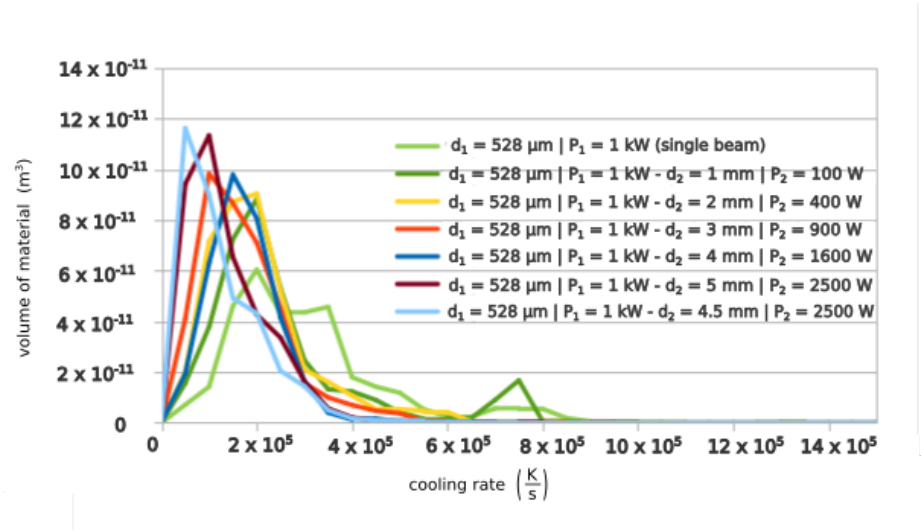

Figure 17: Cooling rate curves of different secondary beams paired with a 528 µm primary beam

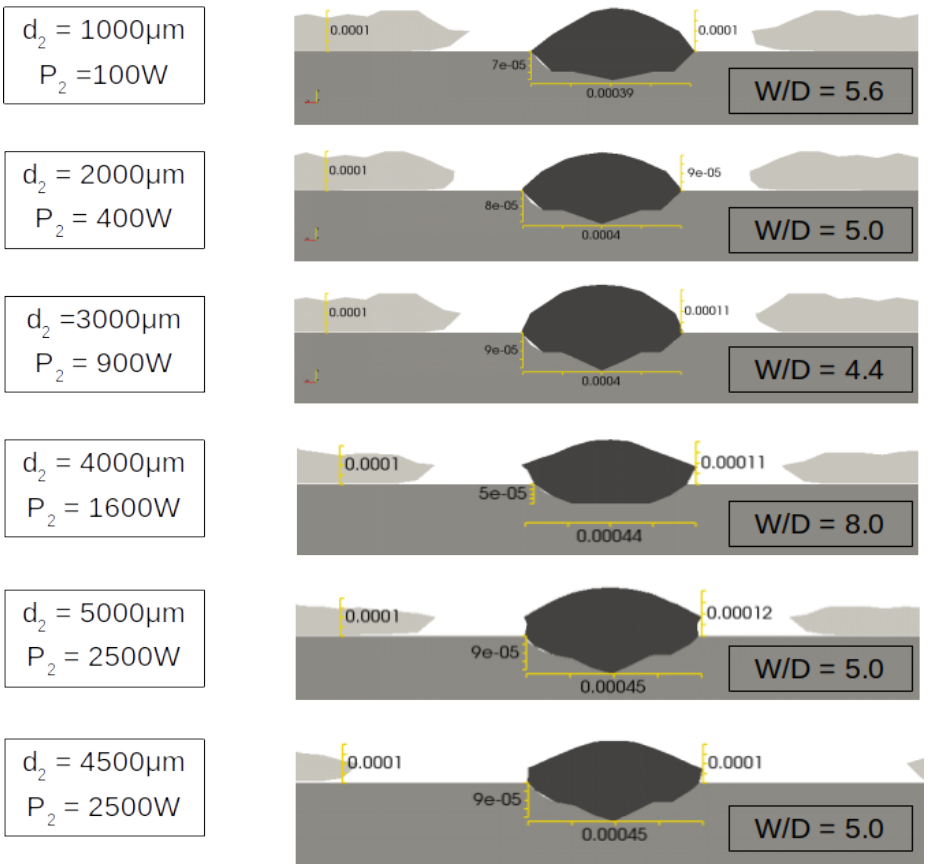

Figure 18: Cross sections related to conditions in Figure 17

3.4 Beam shape optimization on IN713LC

Using the same simulation tool and appropriately changed material properties (see Figure 25) a further parameter study has been conducted on the nickel based superalloy IN713LC. Its chemical composition is summarized in Table 4.
The simulated domain's geometry and meshing, as well as the general laser parameters, remained unchanged, as shown in Table 1 (note the modification in primary beam power to prevent balling in the reference condition).
As this alloy presents comparable material properties to CM247LC, a similar trend in the parameter study was expected, which was validated by simulating the process using one larger primary spot size and two different secondary beam pairings. The higher power needed for the primary beam however implies less power was available for the secondary beam. The larger primary beam has a spot size of 528 µm and uses 1100 W of power.
The resulting cooling rate plot is shown in comparison to the respective reference condition in Figure 19. For this material the brittle temperature range is defined from 1213K to 1571K [35]. The resulting cooling rate plots for the tested dual beam

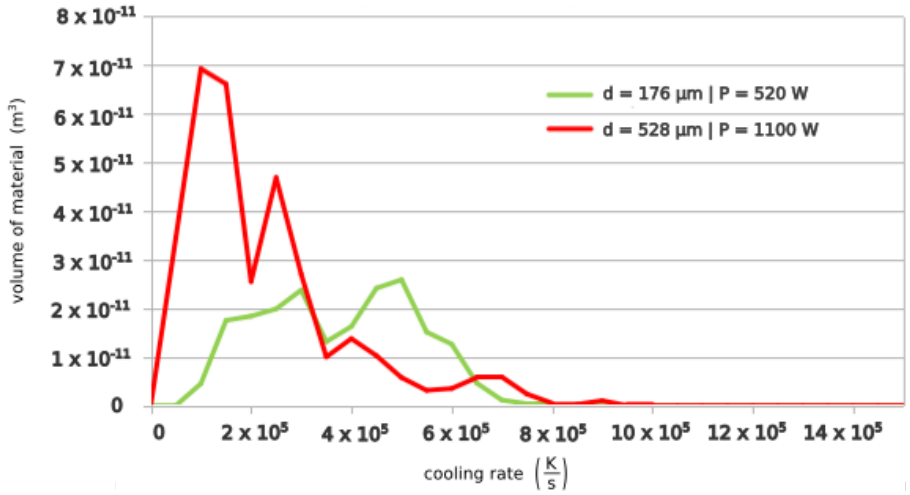

Figure 19: Cooling rate plot of a larger primary beam compared to the reference condition.

configurations can be found in Figure 20. In conclusion, the trends for cooling rate reduction and minimizing the risk of solidification cracking remain consistent for IN713LC, similar to CM247LC. The optimal values differ slightly due to a higher primary beam power requirement for IN7LC, as explained in Section 2.2.

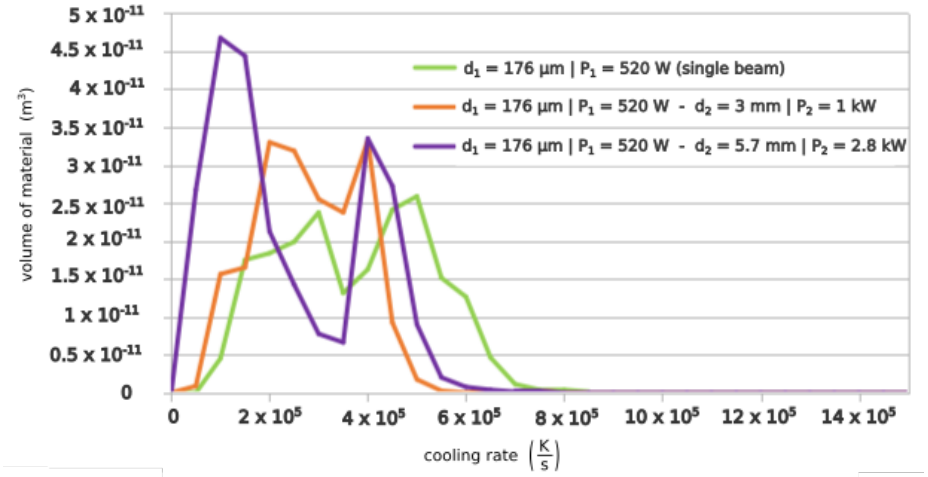

Figure 20: Cooling rate plot of selected dual beam configurations.

3.5 Validation of the cracking phenomenon improvement through 3D printing tests

In order to verify the optimized results obtained from the simulations, using beam shapes defined within CUSTODIAN, 3D printing tests were carried out at part scale. A custom optical bench (MPLC) was developed and installed in the PBF-LB/M machine, enabling the modification of the beam shapes. This setup was installed and tested in the above mentioned laboratory facilities. A process parameter mapping was carried out over both materials (CM247LC and IN713LC) by varying scanning speed, laser power, line offset, layer height, scanning strategy, and primary and secondary beam power ratio. Cross section were then produced and analyzed. Figures 21 and 22 display the best results obtained in the process parameter mapping of both materials. However, it was observed that cracks were still evident specifically on the bottom and top areas of the sample. Nevertheless, a fairly dense structure was observed at mid-thickness with the number of cracks greatly reduced in comparison to the material processed under a standard single beam setup. In conclusion, significant

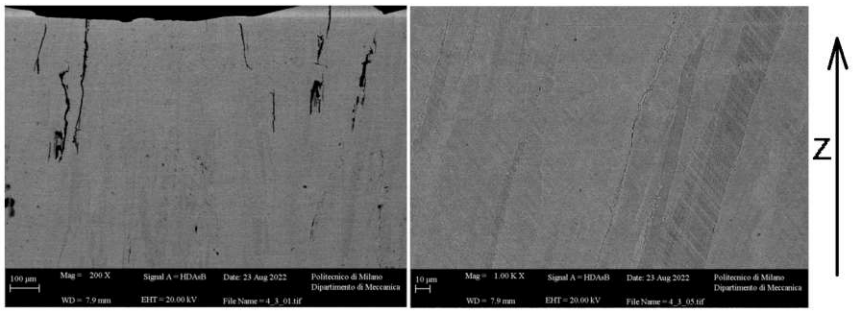

Figure 21: IN713LC sample produced by one of the tailored beam shapes.

improvement in the cracking behavior has been achieved, especially in the mid-part region of the processed samples where large cracks with open faces are less frequent. However, further studies must be conducted to reduce crack formation on the top and bottom areas of the sample. To further decrease crack occurrence, the here-

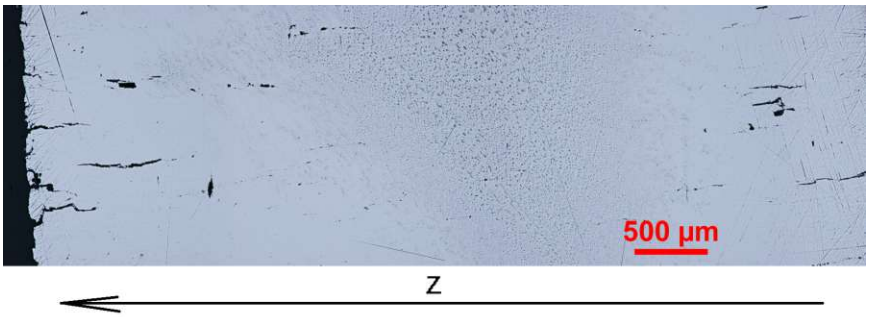

Figure 22: CM247LC sample produced by one of the tailored beam shapes.

presented methodology should be applied to explore more advanced, asymmetrical beam shapes in subsequent studies, once the limitations regarding laser head rotation are overcome.

4 Outlook: Simulation of multi track process

To demonstrate the suitability of the above-presented simulation model to simulate large-scale processes, processing of a 5x5 mm layer of CM247LC consisting of 49 tracks of alternating direction is simulated. The process parameters (velocity, power, powder bed height) are unchanged from those listed in Table 1. Figure 23 shows the results of this simulation and the corresponding experiment. To the best knowledge of the authors, no process of this scale has ever been simulated taking into account fluid flow phenomena such as evaporation and vapour plume movement and compressible fluid flow. Due to the FVM approach and an adaptive meshing strategy, the simulation was completed within approximately 130 hours on an eight core AMD Ryzen 7 2700 CPU. Considering that defects, such as the above-discussed balling defect, are the result of fluid flow phenomena, where effects such as surface tension, evaporation, etc. cannot be neglected, it is important to bring multiphysical models, which are currently at most used for the simulation of single scan tracks, towards the part scale.

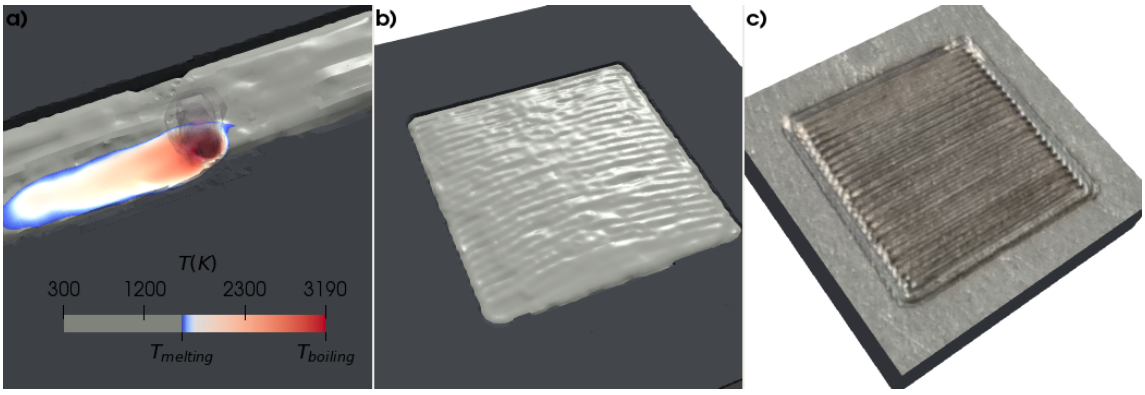

Figure 23: Processing of 5x5mm of CM247LC: a) Melt pool top surface coloured by temperature, vapour depression and vapour plume during track 6 of 49. b) Final, solidified top surface of 5x5mm sample (after 49 scan tracks). c) Top surface of corresponding experiment.

5 Conclusion

The present paper provides a methodology to improve an existing PBF-LB/M process through beam shaping using a passive optical element based on MPLC technology. The methodology carries great potential for retrofitting existing PBF-LB/M machines, as the MPLC device can be paired with any existing laser system. Within this approach, an experimental optimization loop to find suitable beam shapes is unfeasible, and therefore a multiphysical simulation model is used to carry out parameter studies and find appropriate beam shape combinations. To demonstrate this approach, a PBF-LB/M process was optimized with the aim of reducing solidification cracking susceptibility, through the introduction of a secondary, low-intensity heat source aimed at reducing cooling rates. A trend was observed, that larger spot sizes at appropriate intensities used as a working or secondary beam can contribute to a reduced probability of crack formation, mostly at the expense of accuracy. The effectiveness of the optimized beam shapes was proven in experiments, where crack density was reduced to near-zero, which was not possible using only a single Gaussian laser beam.

While optimizing the process, the occurrence of defects must be avoided. The capability of the multiphysical process simulation to identify process defects is highlighted at the example of the balling defect, which is identified both in simulation and experiment at insufficient energy input.

Additionally, an outlook over the capabilities and possible uses of the model in terms of part-scale simulation are presented. In a reasonable amount of time, it was possible to simulate multiple scan tracks, while considering the same physical phenomena as in single track simulations. This shows the adaptability, flexibility and efficiency of this generically programmed multiphysical simulation tool to be used for process optimization in laser based processes.

CRediT authorship contribution statement

C. Zenz: Methodology, Software, Validation, Formal analysis, Investigation, Data curation, Writing- Original Draft, Writing - Review & Editing, Visualization. **M. Buttazzoni:** Methodology, Software, Validation, Formal analysis, Investigation, Data curation, Writing- Original Draft, Writing - Review & Editing, Visualization. **M. Martínez Ceniceros:** Methodology, Validation, Formal analysis, Investigation, Writing- Original Draft, Writing - Review & Editing, Visualization. **R. Gómez Vázquez:** Conceptualization, Methodology, Software, Writing - Review & Editing. **J.R. Blasco Puchades:** Formal analysis, Investigation, Data curation, Writing - Review & Editing. **L. Portolés Griñán:** Conceptualization, Writing - Review & Editing, Supervision, Resources, Project administration, Funding acquisition. **A. Otto:** Conceptualization, Writing - Review & Editing, Supervision, Resources, Project administration, Funding acquisition.

Declaration of Competing Interest

The authors declare that they have no known competing financial interests or personal relationships that could have appeared to influence the work reported in this paper

Funding Acknowledgement

This work has received funding from the European Union's Horizon 2020 research and innovation programme within the project CUSTODIAN, under grant agreement number 825103. CUSTODIAN project is an initiative of the Photonics Public Private Partnership. Furthermore, the work of C. Zenz was partly funded through the TU Wien Doctoral School, within the Doctoral College "DigiPhot".

Appendix A Material Properties

	C	Cr	Co	Mo	W	Ta	Nb	Al	Ti	Hf	Zr	B	Ni
CM247LC	0.07	8.0	9.3	0.5	9.5	3.2		5.6	0.7	1.4	0.010	0.015	bal.
IN713LC	0.05	12.0		4.5			2.0	5.9	0.6		0.1	0.01	bal.

Table 4: Chemical composition of investigated alloys [35]

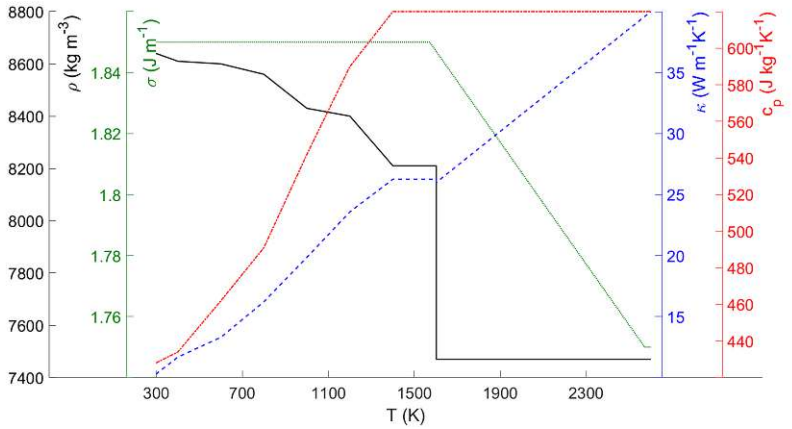

Figure 24: Temperature-dependent values for density, ρ, specific heat capacity, c_p, and thermal conductivity, κ, [30, 37] and surface energy, σ [38–40], of CM247LC.

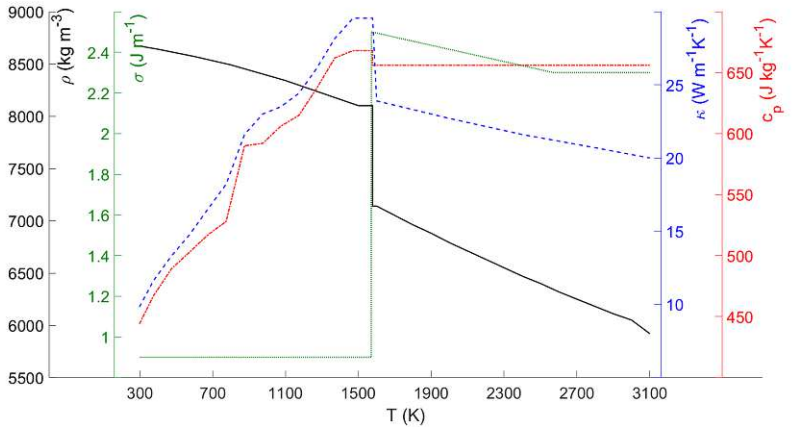

Figure 25: Temperature-dependent values for density, ρ [40], specific heat capacity, c_p, thermal conductivity, κ, [41] and surface energy, σ [38–40], of IN713LC.

References

[1] T. DebRoy, H. Wei, J. Zuback, T. Mukherjee, J. Elmer, J. Milewski, A. Beese, A. Wilson-Heid, A. De, and W. Zhang. "Additive manufacturing of metallic components – Process, structure and properties". In: *Progress in Materials Science* 92, 2018, pp. 112–224. DOI: https://doi.org/10.1016/j.pmatsci.2017.10.001.

[2] S. Sing and W. Yeong. "Laser powder bed fusion for metal additive manufacturing: perspectives on recent developments". In: *Virtual and Physical Prototyping* 15, 2020, pp. 359–370. DOI: https://doi.org/10.1080/17452759.2020.1779999.

[3] T. DebRoy, T. Mukherjee, J. Milewski, J. Elmer, B. Ribic, J. Blecher, and W. Zhang. "Scientific, technological and economic issues in metal printing and their solutions". In: *Nature Materials* 18, 2019, pp. 1026–1032. DOI: https://doi.org/10.1038/s41563-019-0408-2.

[4] URL: https://shapeyourlaser.eu. (accessed: 20.06.2022).

[5] M. Meunier, A. Otto, R. Gómez Vázquez, J. Arias, R. Fernández, G. Pallier, P. Jian, O. Pinel, and G. Labroille. "Freeform beam shaping with multi-plane light conversion for 1.07 µm ultra-high throughput laser-based material macro-processing". In: *Proceedings of ICALEO 2019* (Oct. 7–10, 2019). Laser Institute of America (LIA). 2019.

[6] M. Buttazzoni, C. Zenz, A. Otto, R. Gómez Vázquez, G. Liedl, and J. Arias. "A Numerical Investigation of Laser Beam Welding of Stainless Steel Sheets with a Gap". In: *Appl. Sci.* 11, 2021, p. 2549. DOI: https://doi.org/10.3390/app11062549.

[7] H. Wei, T. Mukherjee, W. Zhang, J. Zuback, G. Knapp, A. De, and T. DebRoy. "Mechanistic models for additive manufacturing of metallic components". In: *Progress in Materials Science* 116, 2021, p. 100703. DOI: https://doi.org/10.1016/j.pmatsci.2020.100703.

[8] V. T. Nguyen, A. B. Murphy, G. W. Delaney, S. J. Cummins, P. W. Cleary, P. S. Cook, D. R. Gunasegaram, M. J. Styles, and M. D. Sinnott. "Progress towards a Complete Model of Metal Additive Manufacturing". In: *Materials Science Forum*. Vol. 1016. Trans Tech Publ. 2021, pp. 1031–1038. DOI: https://doi.org/10.4028/www.scientific.net/MSF.1016.1031.

[9] R. Cunningham, C. Zhao, N. Parab, C. Kantzos, J. Pauza, K. Fezzaa, T. Sun, and A. D. Rollett. "Keyhole threshold and morphology in laser melting revealed by ultrahigh-speed x-ray imaging". In: *Science* 363, 2019, pp. 849–852. DOI: https://doi.org/10.1126/science.aav4687.

[10] Y. Shu, D. Galles, O. A. Tertuliano, B. A. McWilliams, N. Yang, W. Cai, and A. J. Lew. "A critical look at the prediction of the temperature field around a laser-induced melt pool on metallic substrates". In: *Scientific Reports* 11, 2021, p. 12224. DOI: https://doi.org/10.1038/s41598-021-91039-z.

[11] M. Geiger, K.-H. Leitz, H. Koch, and A. Otto. "A 3D transient model of keyhole and melt pool dynamics in laser beam welding applied to the joining of zinc coated sheets". In: *Prod. Eng. Res. Devel.* 3, 2009, pp. 127–136. DOI: https://doi.org/10.1007/s11740-008-0148-7.

[12] A. Otto and R. Gómez Vázquez. "Fluid dynamical simulation of high speed micro welding". In: *J. Laser Appl.* 30, 2018, p. 032411. DOI: https://doi.org/10.2351/1.5040652.

[13] A. Otto, R. Gómez Vázquez, U. Hartel, and S. Mosbah. "Numerical analysis of process dynamics in laser welding of Al and Cu". In: *Procedia CIRP* 74, 2018, pp. 691–695. DOI: https://doi.org/10.1016/j.procir.2018.08.040.

[14] R. Gómez Vázquez, H. Koch, and A. Otto. "Multi-Physical Simulation of Laser Welding". In: *Physics Procedia* 56, 2014, pp. 1334–1342. DOI: https://doi.org/10.1016/j.phpro.2014.08.059.

[15] H. Koch, R. Gómez Vázquez, and A. Otto. "A multiphysical simulation model for laser based manufacturing". In: *European Congress on Computational Methods in Applied Sciences and Engineering (ECCOMAS 2012)* (Vienna, Austria, Sept. 10–14, 2012). Ed. by J. E. et al. 2012, pp. 6709–6722.

[16] M. Buttazzoni. *Multiphysical numerical simulation of laser based additive manufacturing processes: Direct Energy Deposition*. Master's thesis, TU Wien, 2020.

[17] A. Otto, H. Koch, R. Gómez Vázquez, Z. Lin, and B. Hainsey. "Multiphysical Simulation of ns-Laser Ablation of Multi-Material LED-Structures". In: *Physics Procedia* 56, 2014, pp. 1315–1324. DOI: https://doi.org/10.1016/j.phpro.2014.08.057.

[18] S. Tatra, R. Gómez Vázquez, C. Stiglbrunner, and A. Otto. "Numerical simulation of laser ablation with short and ultra-short pulses for metals and semiconductors". In: *Physics Procedia* 83, 2016, pp. 1339–1346. DOI: https://doi.org/10.1016/j.phpro.2016.08.141.

[19] H. Matsumoto, Z. Lin, J. N. Schrauben, J. Kleinert, R. Gómez Vázquez, M. Buttazzoni, and A. Otto. "Rapid formation of high aspect ratio through holes in thin glass substrates using an engineered, QCW laser approach". In: *Applied Physics A* 128, 2022, pp. 1–10. DOI: https://doi.org/10.1007/s00339-022-05404-4.

[20] H. Weller, G. Tabor, H. Jasak, and C. Fureby. "A tensorial approach to computational continuum mechanics using object-oriented techniques". In: *Computers in Physics* 12, 1998, pp. 620–631. DOI: https://doi.org/10.1063/1.168744.

[21] S. Deshpande, L. Anumolu, and M. Trujillo. "Evaluating the performance of the two-phase flow solver interFoam". In: *Comput. Sci. Discov.* 5, 2012, p. 014016. DOI: https://doi.org/10.1088/1749-4699/5/1/014016.

[22] A. Otto, H. Koch, and R. Gómez Vázquez. "Multiphysical simulation of laser material processing". In: *Physics Procedia* 39, 2012, pp. 843–852. DOI: https://doi.org/10.1016/j.phpro.2012.10.109.

[23] H. Hügel and T. Graf. *Laser in der Fertigung*. Vol. 2. Springer, 2009.

[24] V. R. Voller and C. Prakash. "A fixed grid numerical modelling methodology for convection-diffusion mushy region phase-change problems". In: *International Journal of Heat and Mass Transfer* 30, 1987, pp. 1709–1719. DOI: https://doi.org/10.1016/0017-9310(87)90317-6.

[25] K. W. Kolasinski. *Surface science: foundations of catalysis and nanoscience*. John Wiley & Sons, 2012. DOI: https://doi.org/10.1002/9781119941798.

[26] L. Wang, Y. Zhang, and W. Yan. "Evaporation model for keyhole dynamics during additive manufacturing of metal". In: *Physical Review Applied* 14, 2020, p. 064039. DOI: https://doi.org/10.1103/PhysRevApplied.14.064039.

[27] F. Rösler and D. Brüggemann. "Shell-and-tube type latent heat thermal energy storage: numerical analysis and comparison with experiments". In: *Heat and Mass Transfer* 47, 2011, pp. 1027–1033. DOI: https://doi.org/10.1007/s00231-011-0866-9.

[28] M. Ruths. "Surface Forces, Surface Tension, and Adhesion". In: *Encyclopedia of Tribology*. Ed. by Q. J. Wang and Y.-W. Chung. Boston, MA: Springer US, 2013, pp. 3435–3443. ISBN: 978-0-387-92897-5. DOI: https://doi.org/10.1007/978-0-387-92897-5_463.

[29] S. Sih and J. Barlow. "The Prediction of the Emissivity and Thermal Conductivity of Powder Beds". In: *Particulate Science and Technology* 22, 2004, pp. 427–440. DOI: https://doi.org/10.1080/02726350490501682.

[30] L. Avala, M. Bheema, P. Singh, R. Rai, and S. Srivastava. "Measurement of Thermo Physical Properties of Nickel Based Superalloys". In: *International Journal on Mechanical Engineering and Robotics* 1, 2013, pp. 108–112.

[31] J. P. Kruth, L. Froyen, J. V. Vaerenbergh, P. Mercelis, M. Rombouts, and B. Lauwers. "Selective laser melting of iron-based powder". In: *Journal of Materials Processing Technology* 149, 2004, pp. 611–622. DOI: doi:10.1016/j.jmatprotec.2003.11.051.

[32] I. Yadroitsev, A. Gusarov, I. Yadroitsava, and I. Smurov. "Single track formation in selective laser melting of metal powders". In: *Journal of Materials Processing Technology* 210, 2010, pp. 1624–1631. DOI: dx.doi.org/10.1016/j.jmatprotec.2010.05.010.

[33] M. Henderson, D. Arrell, R. Larsson, M. Heobel, and G. Marchant. "Nickel based superalloy welding practices for industrial gas turbine applications". In: *Science and Technology of Welding and Joining* 9, 2004, pp. 13–21. DOI: https://doi.org/10.1179/136217104225017099.

[34] M. Raza and Y.-L. Lo. "Experimental investigation into microstructure, mechanical properties, and cracking mechanism of IN713LC processed by laser powder bed fusion". In: *Materials Science and Engineering: A* 819, 2021, p. 141527. DOI: https://doi.org/10.1016/j.msea.2021.141527.

[35] M. Vedani. *Handbook on metallurgical defects and their genesis*. Tech. rep. Politecnico di Milano, 2019.

[36] E. Hallberg. "Investigation of hot cracking in additive manufactured nickel-based superalloys; Process optimization and crack removal with hot isostatic pressing". MA thesis. Chalmers University of Technology, 2018.

[37] M. Rahimian. "Physical simulation of investment casting of Mar-M247 Ni-based superalloy". PhD thesis. Carlos III University of Madrid, 2015.

[38] P. Sahoo, T. Debroy, and M. McNallan. "Surface Tension of Binary Metal - Surface Active Solute Systems under Conditions Relevant to Welding Metallurgy". In: *Metallurgical Transactions B* 19, 1988, pp. 483–491. DOI: https://doi.org/10.1007/BF02657748.

[39] Y. Su, K. Mills, and A. Dinsdale. "A model to calculate surface tension of commercial alloys". In: *Journal of Materials Science* 40, 2005, pp. 2185–2190. DOI: https://doi.org/10.1007/s10853-005-1930-y.

[40] K. Mills, Y. Youssef, Z. Li, and Y. Su. "Calculation of Thermophysical Properties of Ni-based Superalloys". In: *ISIJ International* 46, 2006, pp. 623–6321. DOI: https://doi.org/10.2355/isijinternational.46.623.

[41] M. Zieliñska, M. Yavorska, M. Porêba, and J. Sieniawski. “Thermal properties of cast nickel based superalloys”. In: *Archives of Materials Science and Engineering* 44, 2010, pp. 35–38.

Multi-Scale Simulation of PBF-LB/M

Constantin Zenz[a]

Excerpt from

Universal Numerical Simulation Model for Laser Material Processing

Andreas Otto[a], Michele Buttazzoni[a] Carlos Durán[a], Tobias Florian[a], Constantin Zenz[a]

[a]Institute of Production Engineering and Photonic Technologies, TU Wien, Getreidemarkt 9, 1060, Vienna, Austria

This version has been accepted for publication, after peer review, but is not the Version of Record. The final authenticated version of Record will be available online in the Springer Series in Optical Sciences: `https://link.springer.com/book/9783032171320`

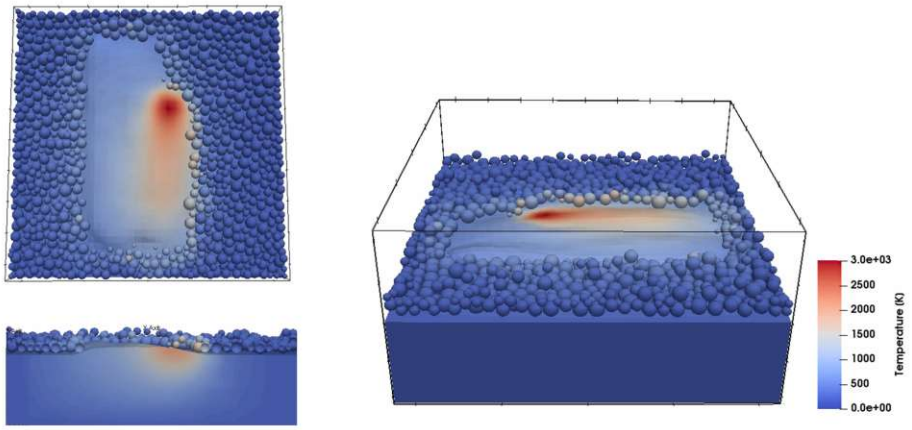

Figure 1: Single-layer simulation of PBF-LB/M using coupled FVM-DEM model: Realistic representation of powder particle distribution is achieved via modeling individual particles as discrete elements, which are coupled to the CFD domain and exchange mass and energy when undergoing melting. This comes at a trade-off with higher computational costs

PBF-LB/M poses a very complex simulation and modeling challenge due to its multi-scale aspect. An overview of the state of the art and emerging trends of PBF-LB/M among other laser-based additive manufacturing processes is provided in Chap. 23 (Lasagni et al.) of [1]. In principle, PBF-LB/M can be seen as a series of small scale welds involving powder material. One possible modeling strategy consists of resolving individual powder particles via the discrete element method (DEM) and coupling these elements with the remaining continuum mechanical problem through a mass- and energy transfer once the particles melt, yielding a coupled FVM-DEM model. An example of such a simulation is given in Figure 1, where multiple adjacent tracks of a PBF-LB/M process are simulated. While such an approach provides advanced predictive capabilities regarding the influence of particle distributions on process outcomes, and enables the simulation of particle-related phenomena such

as denudation, the computational costs involved with resolving individual particles become prohibitive when surpassing the scale of several short tracks. While the timescales of interest at the single track level are in the microsecond to millisecond regime, the entire process spans much larger timescales, with processing of entire parts usually taking many hours. Therefore, often, the smallest building block of a PBF-LB/M process is considered when simulating this process: A single scan track. However, it is often needed to go beyond the single track or even single layer scale. To facilitate simulations at a larger scale, a viable alternative to CFD-DEM approaches involves modeling the powder as a continuum with average powder-like properties [2, 3]. Consequently, it is possible to simulate several layers of many scan tracks each, where each track bares the entire multiphysical complexity of any welding process.

Figure 2 highlights an example of the multi-scale nature of the problem: Process parameter combinations that work well on the level of a single track can lead to unwanted defects at the level of an entire part. Figure 2a shows the top surface of a 5 mm x 5 mm layer of a solidification crack-prone nickel-based-superalloy, fabricated using a conventional PBF-LB/M process. Nickel-based superalloys are particularly interesting for many applications due to their high strength at high temperatures, making them a widely used class of materials for turbine blades, as an example. However, many of these alloys are classified as "non-weldable" as they exhibit high crack susceptibility when processed with a laser [4]. To avoid the formation of cracks, a new process was designed where a large, low-intensity secondary laser beam was added to provide sufficient pre- and post heating to the process zone in order to lower cooling rates [2]. Figure 2b-d show exemplary results using different secondary beams (that lead to good results in both experiments and simulations of a single track), where the scan speed and/or hatching distance was already increased to compensate for the additional heat input of the secondary beam. However, both experiments and simulations in b-d exhibit unwanted heat accumulation- and surface tension-driven defects that only develop after multiple tracks. Towards the end of the processed layer in b and c we see a region where melt accumulated, that did not fully solidify between processing of individual scan tracks, and accumulated driven by Marangoni currents, even reaching over the defined area to be processed. In d the hatch spacing was increased. While heat accumulation poses a less significant problem here, the structure of the scan tracks can easily be seen, where the melt tracks clearly agglomerated to tube-like structures, yielding unwanted surface finish and inhomogeneous part density. Furthermore, we can see the onset of heat accumulation-driven defects in the form of two slightly elevated regions, on both sides of the center. In the case study presented here, the secondary beams were introduced via MPLC technology [5–7], where the approximate shape needs to be defined prior to manufacturing the beam shaping device. Hence, experiments cannot be conducted at the stage of optics design and simulations are essential. However, a PBF-LB/M process leading to good results at the level of a single track might not work at larger scales.

In Figure 3, the model scale is further increased, by simulating multiple layers of the entire PBF-LB/M printing process, while still resolving all relevant fluid mechanical phenomena, such as evaporation, gas dynamics, and surface tension. The shown simulation results feature the thermal history of a point at the center of the rectangular part that is being built, over the course of four printing layers, comparing

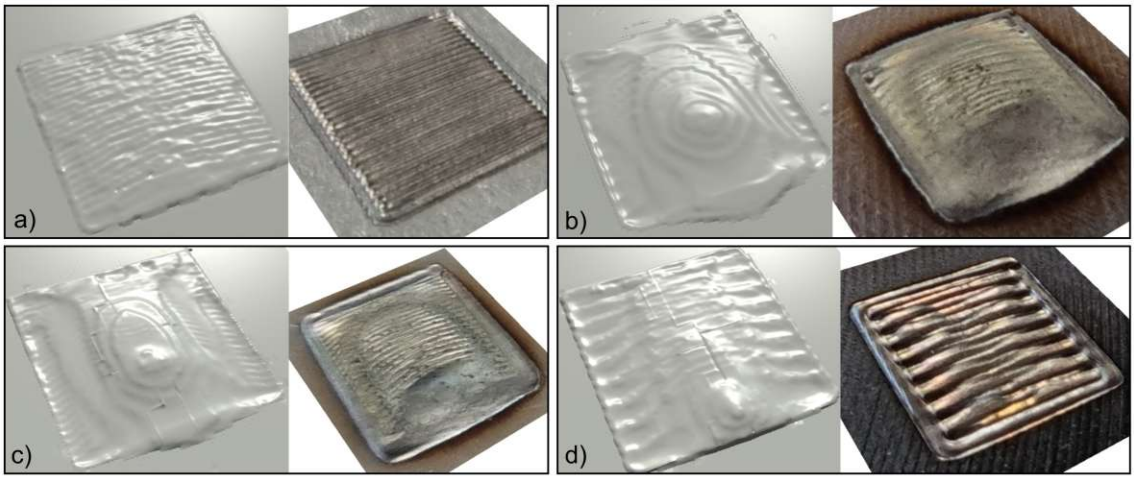

Figure 2: Single-layer simulations (left) of PBF-LB/M using continuum powder model: Solidified layer (powder removed) compared to corresponding experiments (right) for different dual beam approaches: a) Single beam reference result, b) – d): Addition of various secondary large diameter tophat beams and variation of scan speed and hatching distance, all of which lead to unwanted heat accumulation- and surface tension-driven defects. Experimental images courtesy of AIDIMME, Spain

three different scanning strategies, which are illustrated in Figure 4. Interestingly, depending on the strategy, the point of interest will be fully melted either two or three times, and the cooling rates at which the point solidifies in each layer differ strongly between strategies. Moreover, intuition would tell us that scanning "inwards" will lead to more heat accumulation in the center (where the thermal history is plotted), which should lead to lower cooling rates (favorable in terms of crack susceptibility). However, the cooling rates after each melting cycle are much higher for this strategy. While these simulations are certainly not at the scale of an entire built part, they represent a unit cell of a part (i.e., one simple geometrical element, many of which make up a part, such as a thin wall), and encompass the scales at which accurate representation of phase change and fluid flow are relevant. In Figure 5, the thermal histories of three different positions in the sample are shown, all for the "left to right" strategy: at the center of the rectangle forming the layer geometry in the plane normal to build direction, and respectively at the middle of the long and short edge of the rectangle, each at the height of the first layer. It becomes obvious that, for a given part geometry and scan strategy, thermal histories drastically differ from location to location, calling for geometry-specific parameter optimization.

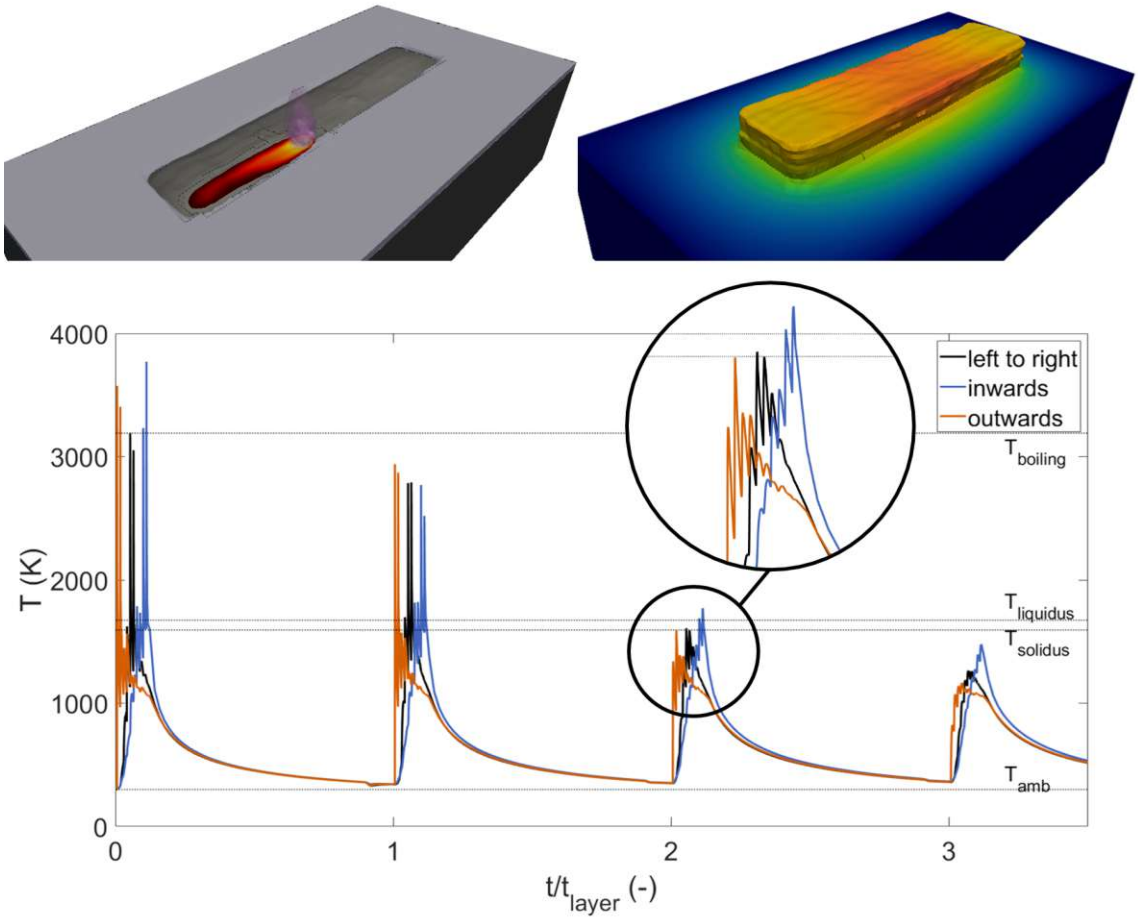

Figure 3: Multi-layer simulation of PBF-LB/M using continuum powder model. Top: Snapshot during process (left) and final part after processing six layers of ten tracks each, colored by temperature during cool down (right). Bottom: Thermal histories of one location during the first four layers of the process for three different scanning strategies (bottom), time normalized by printing time of one layer, t_{layer}

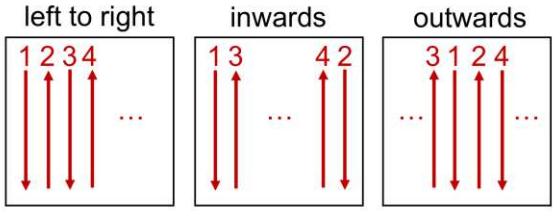

Figure 4: Illustration of different exemplary layer scan strategies as referred to in Figure 3

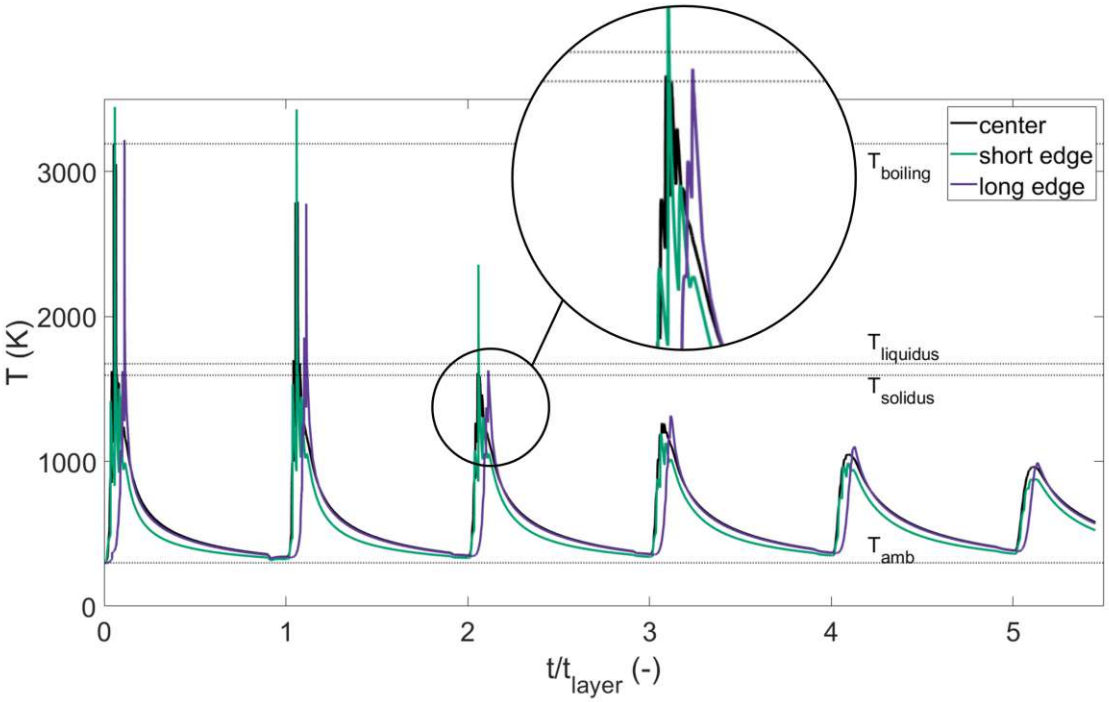

Figure 5: Multi-layer simulation of PBF-LB/M using continuum powder model. Thermal histories of three different locations for "left to right" scan strategy, time normalized by printing time of one layer, t_{layer}

References

[1] J. Bonse and A. F. Lasagni, eds. *Scaling of Laser Processing – Making Light Matter*. Cham, Switzerland: Springer, 2026. The final authenticated version will be available online in the Springer Series in Optical Sciences: https://link.springer.com/book/9783032171320.

[2] C. Zenz, M. Buttazzoni, M. Martínez Ceniceros, R. Gómez Vázquez, J. R. Blasco Puchades, L. Portolés Griñán, and A. Otto. "Simulation-based process optimization of laser-based powder bed fusion by means of beam shaping". In: *Additive Manufacturing* 77, 2023, p. 103793. DOI: https://doi.org/10.1016/j.addma.2023.103793.

[3] C. Zenz, C. Duran, T. Florian, R. Bielak, and A. Otto. "Multiphysical simulation of hot cracking in Laser-Based Powder Bed Fusion". In: *Procedia CIRP* 124, 2024, pp. 341–346. DOI: https://doi.org/10.1016/j.procir.2024.08.130.

[4] S. Sanchez, P. Smith, Z. Xu, G. Gaspard, C. J. Hyde, W. W. Wits, I. A. Ashcroft, H. Chen, and A. T. Clare. "Powder Bed Fusion of nickel-based superalloys: A review". In: *International Journal of Machine Tools and Manufacture* 165, 2021, p. 103729. DOI: https://doi.org/10.1016/j.ijmachtools.2021.103729.

[5] J.-F. Morizur, H. Bachor, and N. Treps. "Method and system for configuring a device for correcting the effect of a medium on a light signal, method, device and system for correcting said effect". AU2011347385. Dec. 2011. URL: https://patents.google.com/patent/AU2011347385B2/en.

[6] J.-F. Morizur, L. Nicholls, P. Jian, S. Armstrong, N. Treps, B. Hage, M. Hsu, W. Bowen, J. Janousek, and H.-A. Bachor. "Programmable unitary spatial mode manipulation". In: *J. Opt. Soc. Am. A* 27, Nov. 2010, pp. 2524–2531. DOI: https://doi.org/10.1364/JOSAA.27.002524.

[7] J. Bayol and G. Pallier. "Advances in laser powder bed fusion thanks to beam shaping: Beam shaper based on multi-plane light conversion enables new forms of material processing". In: *PhotonicsViews* 19, 2022, pp. 52–55. DOI: https://doi.org/10.1002/phvs.202200045.

Multiphysical Simulation of Hot Cracking in Laser-Based Powder Bed Fusion

Constantin Zenz[a,*], Carlos Durán[a], Tobias Florian[a], Robert Bielak[a], Andreas Otto[a]

[a]Institute of Production Engineering and Photonic Technologies, TU Wien, Getreidemarkt 9, 1060, Vienna, Austria

*Corresponding author

This version of the article has been accepted for publication, after peer review, but is not the Version of Record. The Version of Record is available online at: https://doi.org/10.1016/j.procir.2024.08.130

Abstract: This study extends an existing comprehensive computational framework to gain insight on hot cracking in the simulation of laser-based additive manufacturing via powder bed fusion. A novel approach to predict hot crack susceptibility based on vapor cavitation, building on a conceptual model akin to the Rappaz-Drezet-Gremaud criterion is introduced. Unlike conventional practices involving ex-situ evaluation of a criterion, the proposed model emerges implicitly from the underlying multiphysical modeling framework. The model exhibits sensitivity to variations in both material attributes (e.g., alloy composition) and processing conditions (e.g., laser beam shape or scanning strategy). Furthermore, non-equilibrium solidification is incorporated in the underlying Mass-of-Fluid framework, and a model for multi-layer printing is introduced to extend the length and time scale, enabling the derivation of detailed thermal histories on near-part-scale level. Consequently, the framework proves pivotal in optimizing process parameters, transcending the limitations inherent in conventional single melt track computational experiments.

Keywords: Additive Manufacturing; Laser Powder Bed Fusion; Hot Cracking; Multiphysical Simulation; Gulliver-Scheil

1 Introduction

Hot cracking is an unwanted phenomenon commonly encountered in laser-based manufacturing. The underlying physical problem is complex, involving thermal, fluid-mechanical, solid-mechanical, and metallurgical aspects, and although many explanations for the occurrence of such cracks have been proposed, and even more criteria exist that aim at predicting the susceptibility of a given material to exhibit hot cracks under given conditions, no general theory has been proposed to fully explain this phenomenon [1]. Although many types of cracks can be encountered in laser-based material processing, we refer to those that form within the mushy zone, close to the end of solidification, which are typically divided into solidification and liquation cracks. Throughout this work, we focus on solidification cracks. Many materials that

are of interest for manufacturing via laser-based powder bed fusion of metals (PBF-LB/M) are prone to hot cracking. The large parameter space in PBF-LB/M calls for process optimization towards lower hot cracking susceptibilities (HCS). Examples for such strategies are alloy modification through adding additional elements [2] which can be done through powder blending, or the optimization of scanning strategies or laser intensity profiles (beam shaping) [3]. To better understand the relationship between process parameters and the resulting occurrence of hot cracks, and to optimize processes, numerical simulations have proven as powerful tool. Depending on the nature of a given simulation model, different hot cracking criteria can be easily applied in a post-processing manner, evaluating, e.g., the thermal gradients, cooling rates, stress- or strain rates, etc. A recent example is the study by Wimmer et al. [2], who have coupled a thermo-fluid simulation of the PBF-LB/M process with the well-established Rappaz-Drezet-Gremaud (RDG) criterion for hot cracking [4], utilizing the thermal gradients obtained within the simulation for evaluating the RDG criterion for given alloy compositions.
Within the present work, we extend an existing multiphysical simulation model for laser-based material processing [5] by implementing several aspects that will help analyzing the crack susceptibility of PBF-LB/M processes, such as non-equilibrium solidification, thermo-mechanics, and multi-layer powder modeling, and we show that cavitation in the mushy zone during the late stage of solidification can be used as an indicator for hot crack initiation, which is similar to the assumptions underlying the RDG criterion [4]. In the following Sections, the additional model developments are outlined and validated. Then, exemplary applications of the simulation model to PBF-LB/M processes are demonstrated and discussed, and an outlook on ongoing and future work is provided.

2 Model description and validation

The coupled multiphysical problem of laser-based powder bed fusion is modeled via the Mass-of-Fluid (MoF) model in the form previously presented by Zenz et al. [5], where the mathematical model and numerical methods are outlined in detail. Hereafter, only additional model developments specifically related to simulating hot cracking and the process of laser powder bed fusion are laid out, and the reader is referred to [3] for additional information about the model itself, and a series of detailed benchmark simulations for validation.

2.1 Non-equilibrium alloy solidification

As laser-based manufacturing involves high cooling rates, solidification typically takes place under non-equilibrium conditions. To account for this, we implement the Gulliver-Scheil model of microsegregation [6] in the MoF framework. Transport of energy and phase transformations are energy-based in the MoF model, therefore we cannot simply use, e.g., precalculated lookup tables for temperature - solid fraction pairs, but need to embed the Gulliver-Scheil equation directly in the phase change model. Conservation of the mass density of phases, ρ_i (subscript i denotes a phase,

for example liquid metal), is ensured via:

$$\frac{\partial \rho_i}{\partial t} + \nabla \cdot (\boldsymbol{u}\rho_i) = \dot{\rho}_{i,m} + \dot{\rho}_{i,s} + \dot{\rho}_{i,e} + \dot{\rho}_{i,c} \tag{1}$$

Here, $\boldsymbol{u}$ denotes velocity and the four terms on the right-hand side of Eq. (1) refer to changes in mass density of phase i due to melting, solidification, evaporation, and condensation, respectively. For the sake of simplicity, we now consider a binary alloy, bearing in mind that an extension to multicomponent alloys is possible analogously. With c_0, m_L and m_S denoting initial (bulk) alloy element concentration, liquidus slope and solidus slope, respectively, we calculate the local liquidus and solidus temperature, T_L and T_S through the local interface concentration as given by the Gulliver-Scheil equation [6] via:

$$T_L = \max\left(T_M + m_L c_0 \alpha_l^{k-1}, T_E\right) \tag{2}$$

$$T_S = \max\left(T_M + m_S c_0 \alpha_l^{k-1}, T_E\right) \tag{3}$$

Here, $k = m_L/m_S$ is the partition coefficient and T_E denotes the eutectic temperature, at which solidus and liquidus line meet in the phase diagram and isothermal solidification is assumed. Furthermore, α_l is the volume fraction of liquid, which we norm by the sum of liquid and solid volume fractions to avoid spurious influence of low values at liquid-vapor interfaces. We then calculate the local latent heat of solidification, L_S, as:

$$L_S = \rho_l \left(h_l(T_L) - h_s(T_S)\right) \tag{4}$$

n Eq. (4), the terms $h_l(T_L)$ and $h_s(T_S)$ denote the specific heat of the liquid phase at liquidus temperature, and specific heat of the solid phase at solidus temperature, respectively, which are separated by the latent heat required for isothermal solidification at the melting temperature. The amount of liquid that will solidify, i.e., the mass (and associated energy) that is transferred from the liquid to the solid phase is calculated as:

$$\Delta\rho_{l,s} = -\Delta\rho_{s,s} = -\rho_l \frac{\rho_l h_l(T_L) - H_l}{L_S} \tag{5}$$

Here, H_l denotes the energy of the liquid phase, hence the fraction on the right-hand side of Eq. (5) represents energy deficit of the liquid phase with respect to the latent heat. The quantities $\Delta\rho_{i,s}$ are then used to explicitly update the phase mass densities within the numerical solution algorithm. Melting is treated analogously but utilizing constant liquidus and solidus temperatures at bulk concentration, c_0.

To validate the here-presented solidification model, a one-dimensional Stefan problem is solved, where a liquid Al-Cu alloy is solidified by cooling one domain boundary. The solid fraction over temperature for different Cu concentrations as predicted by the MoF simulations is compared to solidification curves obtained using the Gulliver-Scheil model within the software MatCalc [7]. The results are presented in Figure 1. The deviation between the MoF and MatCalc results can be attributed to the constant values of liquidus and solidus slope used in the MoF simulations, that were chosen to match T_L. As m_L and m_S are usually not constant (and non-constant within MatCalc), there is a deviation increasing with the solid fraction. Choosing a different value of m_L leads to matching the results at the other end of the solidification curve, cf. the curves for Al-4wt.%Cu.

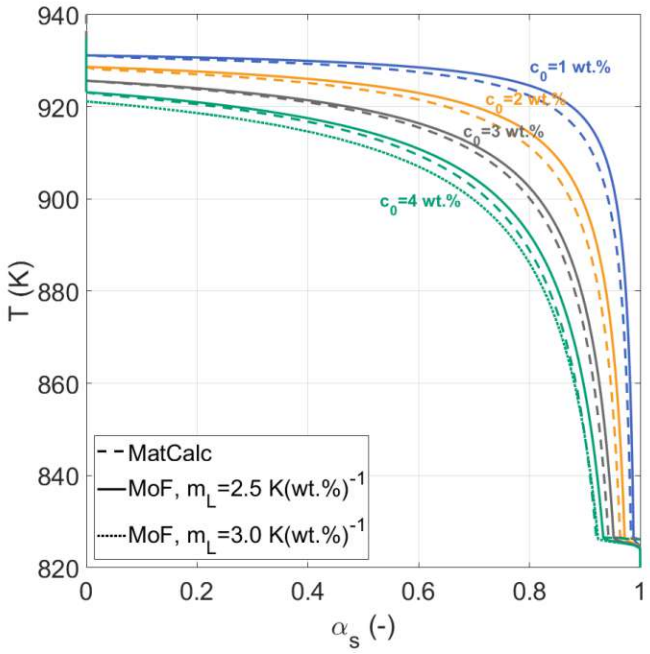

Figure 1: Solid fraction as function of temperature for different Al-Cu alloys, comparing the results of Gulliver-Scheil calculations using MatCalc and a one-dimensional Stefan problem using the here-presented MoF model.

2.2 Solid body thermo-mechanics

To obtain information on the deformation and stress development of the solidified material close to the melt pool, we incorporate a weakly coupled solid stress model similarly to the approach taken by Zhang et al. [8]. We model solid body deformation $\boldsymbol{D}$, ignoring inertia effects, as follows:

$$\nabla \cdot \boldsymbol{\sigma} = 0 \tag{6}$$

$$\boldsymbol{\sigma} = G\nabla \boldsymbol{D} + G\nabla \boldsymbol{D}^T + \lambda tr(\boldsymbol{D})\boldsymbol{I} - (2G + 3\lambda)\beta(T - T_{ref})\boldsymbol{I} \tag{7}$$

Here, λ and G are the first and second Lamé constant, respectively, and T_{ref} is the reference temperature of the undeformed solid, which we set to the material's initial temperature for regions that have not undergone melting, and to the coherency temperature (i.e., where the solid fraction $\alpha_s \approx 0.6$ during solidification) for previously molten material. Analogously to the "Quiet Element Method" in Finite Element methods, we set λ and G to very small, non-zero values outside the solid domain. Eq. (7) represents perfect thermoelastic behavior, which is for sure not close to reality on the scale of the entire process, where plasticity will play a role. However, in the vicinity of the melt pool and within the mushy zone, we argue that excessively large deformation will be taken up by the remaining liquid within the mushy zone, leading either to compensation via liquid backfill or to cavitation, liquid film rupture, and hence crack initiation, before the solid material undergoes plastic deformation. The above formulation can be extended to account for plasticity in the future if information on part deformation and residual stresses are of interest.

We solve the steady-state problem of Eq. (6) in each time step of the transient solution algorithm using the Finite Volume Method in a pseudo-Lagrangian manner, i.e., assuming small deformations that are locally stored at discretization points. Although the time steps used in the transient solution algorithm of the multiphysical simulation are usually very small, due to the large thermal gradients involved, a significant number of iterations is necessary in each time step to obtain a converged solution for Eq. (6), leading to the larger part of overall CPU time being spent on solving the thermomechanical problem. Furthermore, to achieve a strong coupling between solid body deformation and the fluid mechanical problem, the deformation needs to be accounted for in the advection of phases, i.e., Eq. (1), which in turn requires advection of the deformation vector itself. For the problem of hot cracking, the main quantity of interest stemming from the thermo-mechanical problem is the deformation rate of the solid skeleton within the mushy zone, cf. Section 2.3. To avoid the excessive computational costs associated with the above-described, fairly simple model, especially when going towards larger computational domains, we use a local estimation for the deformation rate following linear thermal expansion which we introduce in Section 2.3.

2.3 Crack initiation via cavitation in the mushy zone

During solidification, both shrinkage due to the difference in liquid and solid density, and deformation due to the contracting solid skeleton need to be compensated for via liquid feeding, which becomes increasingly difficult with ongoing solidification. As a result, the pressure in the remaining liquid film drops below the cavitation pressure of the liquid and hence a pore forms. These considerations yield the widely used RDG criterion [4]. In the present MoF framework most of these physical phenomena are already present. The permeability of the mushy zone and the associated pressure change is accounted for via a Darcy porosity term in the momentum equations which has the same form as in the RDG model:

$$\boldsymbol{S}_D = -\frac{\mu \alpha_s^2}{A(1-\alpha_s)^3 + \delta}\boldsymbol{u} = -K_D \boldsymbol{u} \tag{8}$$

The permeability area A is a function of the secondary dendrite arm spacing, μ is the dynamic viscosity of the liquid and δ is a small constant preventing division by zero. Furthermore, shrinkage is directly accounted for through the different densities of liquid and solid. Consequently, we often observe cavitation during the last stage of solidification within our model. To further account for the contribution of solid body deformation towards mushy zone cavitation, we include its contribution directly in the evaporation model via:

$$\dot{\alpha}_v = c_e \left(p_{sat} - (p + p_{deform})\right) \tag{9}$$

Here, the vapor generation rate, $\dot{\alpha}_v$, depends on local difference between saturation pressure, p_{sat}, and pressure, p, to which we add the local contribution of solid body deformation, p_{deform}. For details on the evaporation model and the structure of c_e, we refer the reader to [5]. In the case of a weakly coupled thermo-mechanical simulation (cf. Section 2.2), the change in volume due to deformation can be obtained from the

deformation rate, and the respective additional pressure drop will follow Darcy's law. As the approach is computationally expensive, and the gained insight is limited due to the simple nature of the mechanical model, we estimate, for a first proof of concept of our proposed hot cracking model, the deformation following linear thermoelasticity directly from the local thermal gradient within this study. Assuming linear thermoelastic solid body deformation, and utilizing Darcy's law, we arrive at the following additional pressure drop:

$$p_{deform} = -\int_{\alpha_{s,0}}^{\alpha_{s,1}} \frac{3\beta|\nabla T|V_S K_D u_s}{A_{flow}} dx \tag{10}$$

This integral is evaluated over the critical part of the mushy zone, i.e., $\alpha_{s,0} \approx 0.6$ and $\alpha_{s,1} \approx 0.98$, where the solid part of the mush can transmit strain, and liquid films may be deformed by this deformation. V_S, u_S and A_{flow} denote the volume of solid, local velocity of the solid-liquid interface, and the unblocked area of the mush, respectively (the latter is needed to calculate a volumetric flow rate from the Darcy equation). We explicitly integrate Eq. (10) over the length of the mushy zone during solidification within the solution algorithm to update its contribution to Eq. (9). Note that the shrinkage contribution is already implicitly accounted for within the MoF framework, and that we set the solid density to a constant value, as thermal contraction is accounted for via β - otherwise, part of the deformation would also be included in non-zero movement of the solid in regions where the Darcy term is not yet blocking all motion (i.e., most parts of the mush). To validate the sensitivity of

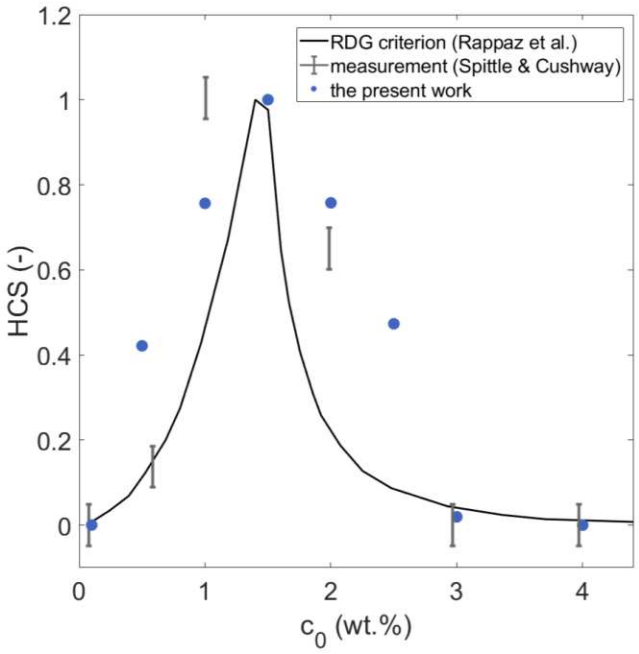

Figure 2: Hot cracking susceptibility (HCS) of different Al-Cu compositions as predicted by the RDG model [4], measured by Spittle and Cushway [9] and predicted by this work's model in a one-dimensional Stefan problem.

mushy zone cavitation towards alloy composition, we again perform simulations of a

one-dimensional Stefan problem of different Al-Cu compositions, where the domain is initialized with liquid metal above its liquidus temperature and then cooled from one side. We compare the normalized (divided by the maximum amount observed across the compared alloys) average amount of metal vapor that cavitated within the mushy zone, denoting this number a dimensionless hot cracking susceptibility (HCS). The results, compared to measurements from [9] and the predictions of the RDG criterion from [4], are presented in Figure 2. Note that all reported data points are normalized, therefore, the maximum observed in the experiments of [9] is only the maximum of the specific concentrations tested (the same holds true for this work), and the curves might shift towards the left or right if more compositions were tested.

2.4 Continuum powder and recoating model

We model the powder as a continuum, with powder-like average properties to avoid the excessive computational costs of resolving individual particles when performing simulations of several tracks and layers. The density and thermal conductivity of the powder are set to 50% and 2% of the bulk values, respectively, as in [3]. While recoating can be straightforwardly modeled in particle-based frameworks, e.g., through a rain-dropping model, special care must be taken when recoating with a continuum, as it is crucial that, e.g., pores that formed during previous layers are not filled with powder. Therefore, we solve a steady-state diffusion equation for an arbitrary marker, ζ, which has the following form:

$$\nabla \cdot \left[\left(c_1 L_{ch}^2 \alpha_g \right) \nabla \zeta \right] - \left(\frac{(1-\alpha_g)}{c_2 \Delta x} \right) \zeta = 0 \tag{11}$$

In Eq. (11), α_g denotes the sum of volume fraction of gaseous phases, L_{ch} is a characteristic length (approx. height of simulation domain), Δx is the cell size and c_1 and c_2 are constants. The boundary condition at the top boundary of the simulation domain is set to $\zeta = 1$, and to $\nabla \zeta = 0$ elsewhere. By solving the above equation, we essentially "mark" all gaseous cells directly connected to the top boundary (i.e., all regions that can be filled with powder during recoating). Recoating itself then only involves exchanging mass density and energy of gaseous phases with those of the newly added powder in marked regions (below the new powder bed height). The approach is demonstrated on a simple artificial mock part with surface structures and porosity, shown in Figure 3.

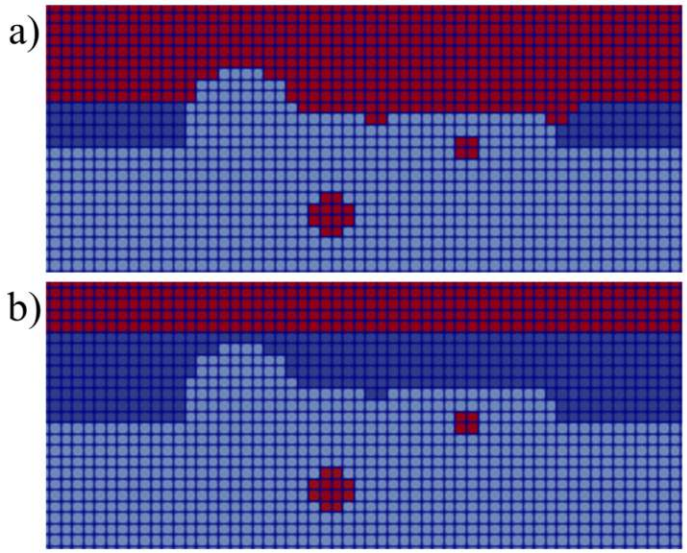

Figure 3: Demonstration of continuum powder recoating on artificial two-dimensional test structure, colored by phase: Powder (dark blue), bulk material (light blue) and gas (red): (a) before recoating, (b) after recoating.

3 Results and Discussion

We now apply the above-described simulation model to "real" PBF-LB/M (as opposed to the preceding simple test cases). We use Al-2wt.%-Cu, which exhibits a relatively high HCS (cf. Figure 2), a Gaussian laser beam with 100 µm spot size and 300 W power, and 1000 mm/s scan speed. The powder layer height is 30 µm. In Figure 4, a single scan track is shown (the liquid melt pool is colored by temperature), and locations where a significant amount of vapor cavitated within the mushy zone are colored with the normalized vapor amount (relative to the maximum observed within the simulations of Figure 4). In Figure 4(b), the same conditions are used, but the substrate and powder are preheated to 600 K as initial conditions. Intuitively, we expect much lower HCS for such high preheating, and indeed, only in the very beginning of the scan track two locations exhibit low amounts of cavitated vapor, while the rest of the scan track is free of cavitation, indicating a low hot cracking risk. Therefore, the model is not only sensitive to alloy composition (cf. Section 2.3), but also to local processing conditions, opening possibilities for process parameter optimization (in addition to optimized alloy design).

Figure 5 shows deformation and solid body stress along a transverse line across the weld bead, at the rear tip of the melt pool, close to the end of solidification (denoted 0), and 100 µm behind that position (denoted 1). D_X is the component of the deformation vector in transverse direction (normal to the scan direction), which poses the most critical deformation with respect to cracking, and D_Z is the component in scan direction, where possibly the effect of shrinkage is larger. The stress values at time 1 are probably incorrect as here plasticity needs to be accounted for, but at time 0, elasticity is arguably a valid assumption as any excessive deformation should result in liquid film rupture and hence crack initiation, rather than plastic deformation of the solid. The presence of compressive stresses due to expansion of the solid on the

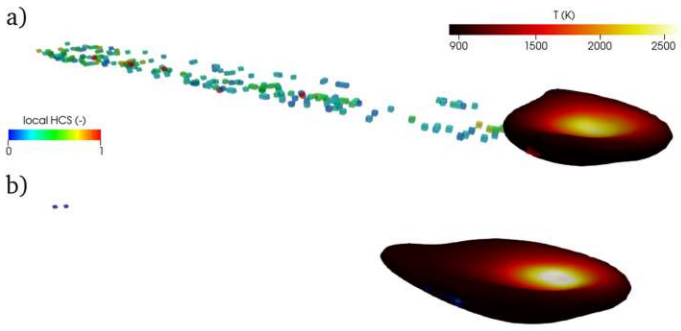

Figure 4: Simulation of single-track PBF process (a) without preheating, and (b) with substrate preheated to 600 K, showing melt pool, colored by temperature, and the volume fraction of vapor cavitated within the mushy zone, normalized by the maximum amount encountered to form a local HCS.

side of the weld bead opens up potential optimization strategies for compensating critical deformations within the mushy zone by further expanding the bulk material on the sides through suitable beam shapes. Such (highly speculative) ideas could be further tested and refined using the here presented multiphysical framework.

Figure 6 shows the result of a multi-track simulation, with the same parameters as in the previous example, and a hatching distance of 100 µm, with a meandering scanning pattern. As expected, we also see potential crack initiation sites across the solidified weld bead. Some additional information can be gathered by looking at the contribution of deformation towards mushy zone cavitation, p_{deform}: While the contribution of shrinkage is mainly due to the ratio of solid and liquid densities, and the solidification curve of the given alloy, the deformation contribution is mainly a result of processing conditions. In Figure 6(b), we see that p_{deform} is largest in the first few scan tracks, and then decreases throughout the processing of consecutive tracks, with increasing heat accumulation and hence lower thermal gradients and deformation.

Using the here-presented recoating approach, it is possible to simulate multiple layers, up to the scale of small unit cells of a real part, which is demonstrated in Figure 7, where exemplarily four layers of each ten tracks are simulated, including wait times. Given the level of detail in the used model, including non-equilibrium solidification, convective heat transport in condensed and gaseous phases, evaporation, etc., this method gives the possibility to produce very accurate thermal histories – even considering scanning strategies and consecutive melting and heating cycles across several layers. Notably, the simulation shown here took a total of only 12 hours on a standard desktop computer.

It is important, that the here-presented way of obtaining information on HCS from the amount of vapor that cavitated in a critical part of the mushy zone is only a model for the likelihood of a crack initiation site being present, and no information on crack propagation is associated with this metric. Furthermore, the possibility of homogeneous pore nucleation from within the liquid film has been questioned, and other mechanisms like heterogeneous nucleation and growth from preexisting nuclei and dissolved gas have been proposed, cf. [1] for a discussion. However, we argue that the interdendritic liquid will contain sufficient disturbances in the form of heterogeneous nucleation sites and small amounts of dissolved gas or microporosity so

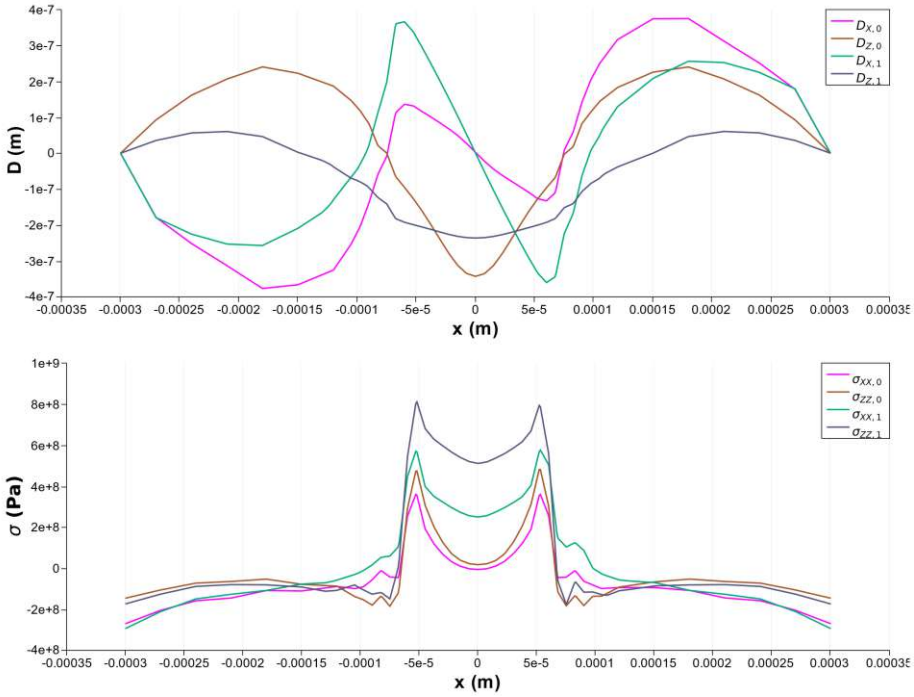

Figure 5: Single track PBF process without preheating: Deformation and principal stress components (transverse and longitudinal direction) along a transverse line near the end of melt pool (0) and 100 µm behind melt pool (1).

that cavitation occurs if the pressure is sufficiently low. To further increase the quantitative predictive power of the model, additional effects such as the surface tension counteracting growth of a pore forming through cavitation, or some information on the presence of preexisting micropores or dissolved gas could be included. So far, the here-presented measure for HCS is a relative metric: A higher value means the associated location is more likely to exhibit crack formation compared to one with a lower HCS - but this does not imply that any location will exhibit a crack at all. When comparing results from different simulations, the same mesh resolution should be used (especially for large domains, where it is challenging to properly resolve the mushy zone).
Finally, different values for the critical range of the mushy zone have been proposed in literature, and the choice of cutoff solid fraction threshold, above which it is believed that liquid film fracture through cavitation is not possible anymore is crucial (reported values vary between 0.90 and 0.99), and it might be necessary to calibrate this value with experimental results for a given process to obtain reliable HCS data.

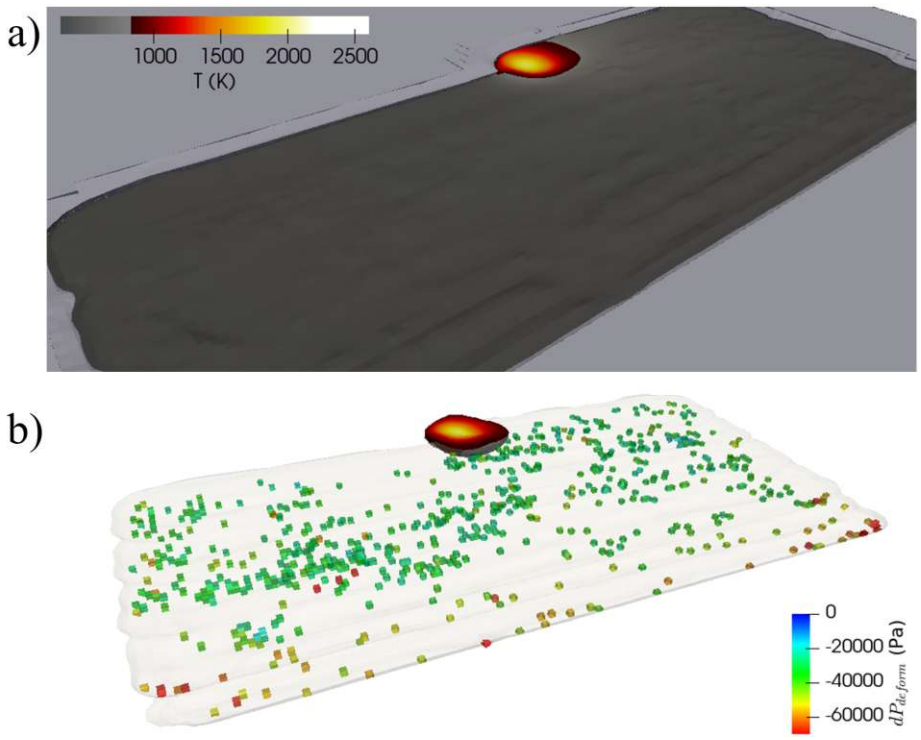

Figure 6: Simulation of multi-track PBF process, showing (a) consolidated material (dark grey) and powder (light grey), and (b) locations with significant values of vapor cavitated within the mushy zone, colored by peak values of p_{deform} encountered.

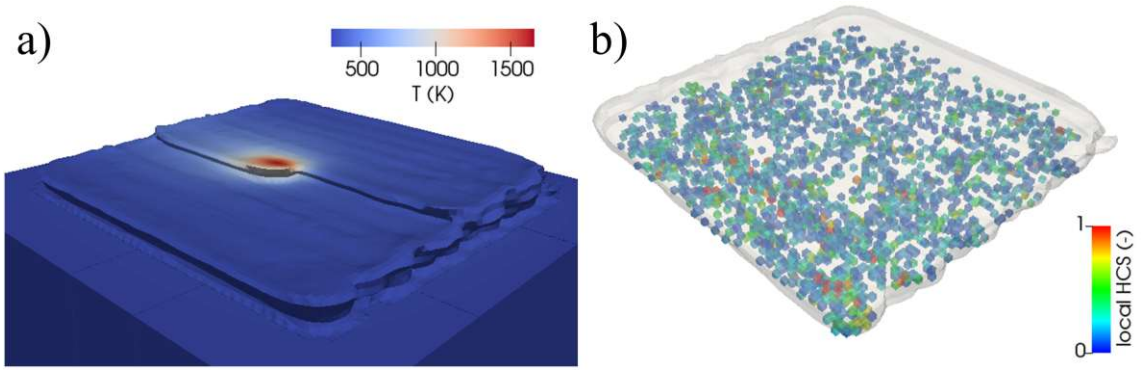

Figure 7: Simulation of multi-layer PBF process, showing (a) temperature distribution on consolidated material (powder not shown) during fourth layer, and (b) local HCS distribution after processing 4 layers of 10 tracks each.

4 Conclusion and Outlook

We presented and discussed several developments with respect to facilitating the prediction of hot cracking in PBF-LB/M processes within an existing physics-based simulation model for laser-material processing. These include non-equilibrium solidification, weakly coupled thermo-mechanics, recoating with continuum powder and the possibility of utilizing the amount of vapor that cavitates within a critical part of the mushy zone as an indicator for crack initiation. We have validated the approach successfully and demonstrated the use of the hot cracking model on PBF processes of different scales (from single scan tracks to multiple printing layers).
Ongoing and future work includes the incorporation of additional physical aspects such as the role of surface tension in the formation of a cavitation bubble within the mushy zone, and a two-way coupling of solid skeleton deformation with the liquid, to increase the quantitative predictive power of the model. Further possibilities to enhance the model include coupling with a grain growth model, or the inclusion of a species diffusion model to account for local changes in alloy composition (and thus solidification curves) in the case of dissimilar metal applications.

Acknowledgements

C. Zenz gratefully acknowledges funding through the TU Wien Doctoral School, within the Doctoral College *DigiPhot*.

References

[1] N. Coniglio and C. Cross. “Initiation and growth mechanisms for weld solidification cracking”. In: *International Materials Reviews* 58, 2013, pp. 375–397. DOI: https://doi.org/10.1179/1743280413Y.0000000020.

[2] A. Wimmer, H. Panzer, C. Zoeller, S. Adami, N. A. Adams, and M. F. Zaeh. “Experimental and numerical investigations of the hot cracking susceptibility during the powder bed fusion of AA 7075 using a laser beam”. In: *Progress in Additive Manufacturing* 9, 2024, pp. 1589–1603. DOI: https://doi.org/10.1007/s40964-023-00523-7.

[3] C. Zenz, M. Buttazzoni, M. Martínez Ceniceros, R. Gómez Vázquez, J. R. Blasco Puchades, L. Portolés Griñán, and A. Otto. “Simulation-based process optimization of laser-based powder bed fusion by means of beam shaping”. In: *Additive Manufacturing* 77, 2023, p. 103793. DOI: https://doi.org/10.1016/j.addma.2023.103793.

[4] M. Rappaz, J.-M. Drezet, and M. Gremaud. “A new hot-tearing criterion”. In: *Metallurgical and Materials Transactions A* 30, 1999, pp. 449–455. DOI: https://doi.org/10.1007/s11661-999-0334-z.

[5] C. Zenz, M. Buttazzoni, T. Florian, K. E. Crespo Armijos, R. Gómez Vázquez, G. Liedl, and A. Otto. "A compressible multiphase Mass-of-Fluid model for the simulation of laser-based manufacturing processes". In: *Computers & Fluids* 268, 2024, p. 106109. DOI: https://doi.org/10.1016/j.compfluid.2023.106109.

[6] J. A. Dantzig and M. Rappaz. *Solidification: -Revised & Expanded*. EPFL press, 2016. ISBN: 978-0-84938-238-3.

[7] E. Kozeschnik. "Mean-Field Microstructure Kinetics Modeling". In: *Encyclopedia of Materials: Metals and Alloys*. Ed. by F. G. Caballero. Oxford: Elsevier, 2022, pp. 521–526. ISBN: 978-0-12-819733-2. DOI: https://doi.org/10.1016/B978-0-12-819726-4.00055-7.

[8] Y. Zhang, Q. Chen, G. Guillemot, C.-A. Gandin, and M. Bellet. "Numerical modelling of fluid and solid thermomechanics in additive manufacturing by powder-bed fusion: Continuum and level set formulation applied to track- and part-scale simulations". In: *Comptes Rendus Mécanique* 346, 2018, pp. 1055–1071. DOI: https://doi.org/10.1016/j.crme.2018.08.008.

[9] J. Spittle and A. Cushway. "Influences of superheat and grain structure on hot-tearing susceptibilities of AI-Cu alloy castings". In: *Metals Technology* 10, 1983, pp. 6–13. DOI: https://doi.org/10.1179/030716983803291226.

A particle-based approach for the prediction of grain microstructures in solidification processes

Salem Mosbah[a,*], Rodrigo Gómez Vázquez[b,c], Constantin Zenz[b], Damien Tourret[d], Andreas Otto[b]

[a]SOLIDIFICATION SAS, Sophia Antipolis, France
[b]Institute of Production Engineering and Photonic Technologies, TU Wien, Getreidemarkt 9, 1060, Vienna, Austria
[c]LKR Light Metals Technologies, Austrian Institute of Technology, Giefinggasse 2, Vienna, Austria
[d]IMDEA Materials, 28906, Madrid, Spain
[*]Corresponding author

This version of the article has been accepted for publication, after peer review, but is not the Version of Record. The Version of Record is available online at: https://doi.org/10.1016/j.commatsci.2025.113918

Abstract: Grain microstructures are crucial to the mechanical properties, performance, and often lifetime of metallic components. Hence, the prediction of grain microstructures emerging from solidification processes at relevant macroscopic scale is essential to the design or optimization of new alloys and processing conditions. Yet, despite the broad range of multi-scale models proposed so far, all of them suffer from computational limitations, such that advances from computational and algorithm perspectives remain needed. Here, we present a novel approach for tracking crystallographic solidification grain envelopes capable of predicting competitive growth scenarios and columnar-to-equiaxed transitions for stationary grains. The model relies on classical assumptions and equations in use in several broadly used and thoroughly validated approaches (e.g. cellular automata). Yet, our approach defines the grain envelope using Lagrangian particles and tracks their evolution using an algorithm and an implementation relying on scalable libraries and using modern CPU/GPU architectures. The model is used to simulate several benchmarks of increasing complexity, and the results are compared to analytical, experimental, and numerical results from literature for the purpose of model validation. To highlight the applicability to real-world processes and the possibility of coupling the model with existing physics-based simulation tools, the model is also (one-way) coupled with a multiphysics laser-material-interaction model to simulate competitive grain growth during laser beam welding of steel.

Keywords: Solidification; Polycrystalline Microstructures; Dendritic Growth; Computational Modeling

1 Introduction

Microstructures in metallic alloys occupy a pivotal point within the process–structure–property–performance paradigm [1–4]. Hence, the prediction of grain structures resulting from solidification processes – often the starting point of microstructure emergence – is essential to leverage Integrated Computational Materials Engineering [1–3] approaches. In this context, accurate yet fast numerical models incorporating all underlying phenomena at microstructure scale – namely transport of heat, mass, and solute species, as well as solid-liquid interface stability and growth kinetics – are key to a computationally-guided design strategy for achieving application-specific properties and performance [4].

Solidification models cover a broad range of length and time scales [5, 6]. At the lowest scales (∼nm), first principles may be used to calculate phase diagrams [7], and atomistic models allow studying the structure and properties of solid-liquid interfaces (e.g. anisotropic excess free energy and kinetic coefficient) [8], but their computational cost remains prohibitive for simulations at the scale of a representative polycrystalline structure. At a slightly higher scale (∼µm), the phase-field (PF) method is the most efficient and versatile method to simulate the evolution of complex interface patterns, such as dendrites, eutectics, and more [9–11]. However, the need for an accurate discretization of the interface morphology (e.g. the local curvature of every single dendrite tip) imposes stringent scale limitations, even when using advanced algorithms – including parallelization [12–15], adaptive remeshing [14, 15], or spectral solvers [16–19]. On the other end of the scale range, macroscopic scale models applicable at the scale of entire ingots (∼m) are most often based on volume-averaged balances of heat, solute, and momentum, coupled with fields representing the volume fraction of one or several phases [20–23], but they do not capture details of the polycrystalline structure. Therefore, a variety of intermediate-scale models have been proposed, for instance based on dendritic needle network [24, 25], grain envelope [26, 27], Monte Carlo (Potts) [28], phase-field [29], or cellular automaton (CA) [30–37] approaches.

Among these models, the CA approach stands out as a mature method, incorporating all essential underlying physics (i.e. nucleation, growth kinetics, alloy-specific solidification path, microstructure length scales), validated against a range of experimental conditions [32–36]. In a CA model, within a spatial grid of cubic cells, nucleation is addressed statistically via explicit seeding of nuclei with random orientations, and their growth proceeds by the progressive transitions of cells over liquid, mushy (i.e. a mixture of solid and interdendritic liquid within the grain envelope), and solid states. The grain envelope, i.e. the fictitious surface joining actively growing dendrite arms, is represented as polyhedral building blocks – e.g. octahedrons for cubic (fcc, bcc) crystals, whose vertices correspond to ⟨100⟩ preferred growth directions. The coupling with the macroscopic transport of mass, species, and heat is typically achieved by coupling with a Finite Element (FE) solver. CA-based models are applicable in three dimensions at macroscopic scale [33–36]. However, the exponential storage and computation requirements with the number of cells require strategies for the dynamical allocation of active (below liquidus temperature) and inactive (fully solid or liquid) cells. Indeed, the inherent algorithm complexity of the CA model, where a cell state

depends upon its neighboring cells, scales as $\mathcal{O}(n^2)$, where n is the number of cells. Moreover, post processing cost, e.g. for recovering the predicted grain structure, also increases dramatically with the number of cells.
Here, we present an alternative approach that can be applied to predict the grain structure during solidification processes, e.g. casting, welding, or additive manufacturing (AM). The model tracks the evolution of the theoretical envelope for each grain without solving the inner evolution of the dendritic features. We introduce a new point-based grain envelope tracking scheme, implemented using libraries optimized for modern computing CPU/GPU architectures to enable large scale industrially relevant simulations. The model is presented in Section 2 Section 3 provides an extensive review of benchmark results to validate the proposed approach. Section 4 showcases a couple of original applications, including laser beam welding, where the model is coupled with an existing multiphysics laser processing solver. The results and their implications are directly discussed within each subsection of Sections 3 and 4. Finally, a brief summary and some perspectives are provided in Section 5.

2 Solidification model

The main objective of the model is to predict polycrystalline grain microstructure formation during solidification of a metallic alloy, and the resulting heterogeneities, e.g. solute segregation at grain boundaries (GBs), and texture, which critically affect the potentially heterogeneous mechanical properties of cast parts [38, 39]. To do so, we need to build a model that incorporates and couples the relevant underlying physics of (a) solid nucleation (Section 2.1.1), (b) crystal growth (Section 2.1.2), and (c) interactions between growing crystallites and the transport (e.g. flow) of heat and species (Section 2.2.). The model itself relies on well-accepted assumptions and equations common to several "mesoscale" modeling approaches (e.g. [24–27, 30–37]). In its current version, the model remains limited to the nucleation and growth of stationary grains (i.e. excluding the potential floatation or sedimentation of grains). The main novelty is the introduction of a particle-based grain envelope tracking scheme, presented in Section 2.1.2, which allows an efficient data handling and the use of existing scalable libraries. The resulting scheme is generic and can be coupled with any model for the complementary thermo-fluid problem. In this section, we present the main underlying assumptions and equations of the model, which we later test against benchmark cases from the literature (Section 3) and later illustrate original applications to melting and welding (Section 4).

2.1 Particle-based tracking of solidification and melting

2.1.1 Nucleation

Since nucleation is a rare event that occurs at the scale of small clusters of atoms, macroscopic approaches cannot be fully predictive, which is why stochastic phenomenological models are typically used in phase-field [40] or cellular automaton [30, 31] models. As homogeneous nucleation is irrelevant in practical applications, where heterogeneous nucleation is the main mechanism at play [38, 39], we only consider

heterogeneous nucleation. We use a nucleation model similar to that in the seminal CA model of [30]. Therein, random distributions of locations and associated nucleation undercooling are initially generated, typically following normal distributions throughout the whole domain, including boundaries. While the statistical distribution of nucleation undercoolings and the nuclei density are treated as calibration parameters, this method allows a direct correlation to available experimental measurements of cast ingot grain densities [39].

2.1.2 Growth

A meshless grain envelope tracking approach is used based on the hierarchical nature of dendritic structures. Each point within the grain envelope is ascribed a velocity corresponding to that of a dendrite tip in the crystal preferred growth directions. In a Cartesian coordinate system $(\vec{e}_x, \vec{e}_y, \vec{e}_z)$, for a cubic crystal (e.g. face centered cubic, fcc, or body centered cubic, bcc) these correspond to $\langle 100 \rangle$ directions, i.e., $[100]$, $[010]$, $[001]$, $[\bar{1}00]$, $[0\bar{1}0]$ and $[00\bar{1}]$. For the sake of simplicity, here we limit the presentation to such crystal systems, but the same approach could be extended to other crystal systems, e.g. hexagonal close packed (hcp). An isolated stagnant equiaxed grain growing into a homogeneously undercooled and supersaturated melt grows isotropically in its six $\langle 110 \rangle$ directions. During its growth, the grain shape evolution is equivalent to an isotropic re-scaling of its envelope approximated by an encapsulating octahedron. The scaling factor can be computed via a kinetic law relating the dendrite tip velocity to the undercooling computed at the farthest dendritic tips (i.e. the octahedron vertices). In this configuration, only six points are required to define the grain envelope, as depicted in Figure 1(a). In an inhomogeneous ther-

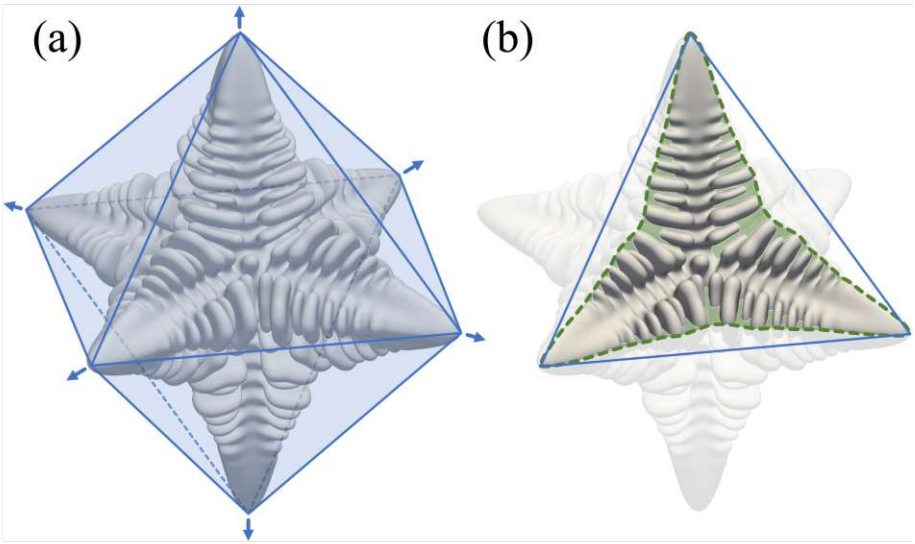

Figure 1: Approximations of an equiaxed grain envelope: (a) octahedron represented with six tracking point growing along directions (blue arrows); (b) comparison between schematic grain envelope (green shaded area and dashed line) joining the active secondary dendrite and its octahedral approximation (blue solid lines).

mal and solute field, potentially in the presence of fluid flow, the grain envelope is

still defined as the imaginary surface connecting the "active" dendrite tips. Active secondary (or n-ary) tips are usually defined as the tips of branches that are longer than any other secondary (n-ary) branch rooted closer to the tip of their common primary ($(n-1)$-ary) parent branch [26, 27] as illustrated in Figure 1(b). Each envelope active dendrite tip, i.e. each tracking point, is expected to evolve following different growth kinetics based on its surrounding temperature and solute concentration. Under these conditions, the overall envelope can no longer be approximated by a simple polyhedron. Nevertheless, the actual grain envelope can be estimated by tracking the evolution of all the active dendrite tips. Therefore, an important consideration to accurately predict the shape of the grain envelope is the position of the outer primary, secondary and, if applicable, tertiary and higher-order dendritic tips. An optimal positioning of the tracking points is achieved when the distance between successive tracking points, denoted λ_0, represents a microstructural length scale of the dendritic pattern. A natural choice for λ_0 is the secondary dendrite arm spacing (SDAS), λ_2. Hence, in most cases we can use $\lambda_0 = \lambda_2$, but in practice the value of the numerical parameter λ_0 may be increased well above λ_2 in order to speed up the calculations, provided a convergence analysis on λ_0 (see, e.g., Section 3.3). Using existing scalable libraries (see Section 2.3), we implemented an algorithm to dynamically allocate the tracking points of the grain envelope.
The approach and implementation presented here are three-dimensional. For the sake of simplicity, we schematize a 2D growth case in Figure 2(a) and a generalized 3D case in Figure 2(b). Upon nucleation (Step 0), we can define an initial nucleus envelope from the nucleation center with six unique tracking points in 3D, or four tracking points in 2D (three of which are represented in Figure 2(a) illustrating only one half of a grain). These tracking points (smaller solid-filled points) are tracked up to a predefined target position (hatched points in Figure 2(a)), i.e. up to a distance λ_0. Once a tracking point reaches its target position, a new six/four points-based pattern is generated, and all points are initialized at the target position of the parent tracking point. The newly created points are each assigned a growth direction, initially forming an infinitesimal octahedral shape (or square in 2D). Only outer points, i.e. points growing in a direction that increases the overall grain volume, are considered. Hence, except for the initial nucleation event, the number of generated tracking points during growth is actually lower than six (lower than four in 2D). The position of each tracking point is then updated following the growth direction and the chosen kinetic law accounting from both local temperature and solute concentration fields. The process is repeated for each point resulting in a dynamically allocated, locally determined grain envelope.

Importantly, while Figure 2 illustrates the simplified case of symmetric (nearly-isotropic) equiaxed grains, since the growth of each tracking point depends on its local temperature and solute concentration fields, the approach naturally captures heterogeneous conditions, as shown later in Section 3.1. This contrasts with the simplest (early) CA algorithms where the growth of all vertices depends upon the driving force (undercooling or supersaturation) at the center of the cell [30, 31, 36], which was later addressed with slightly more advanced CA algorithms where the growth of each vertex can be calculated from its own surrounding driving force [32, 37].
The resulting model, in a similar manner as a CA model, is thus capable of tracking

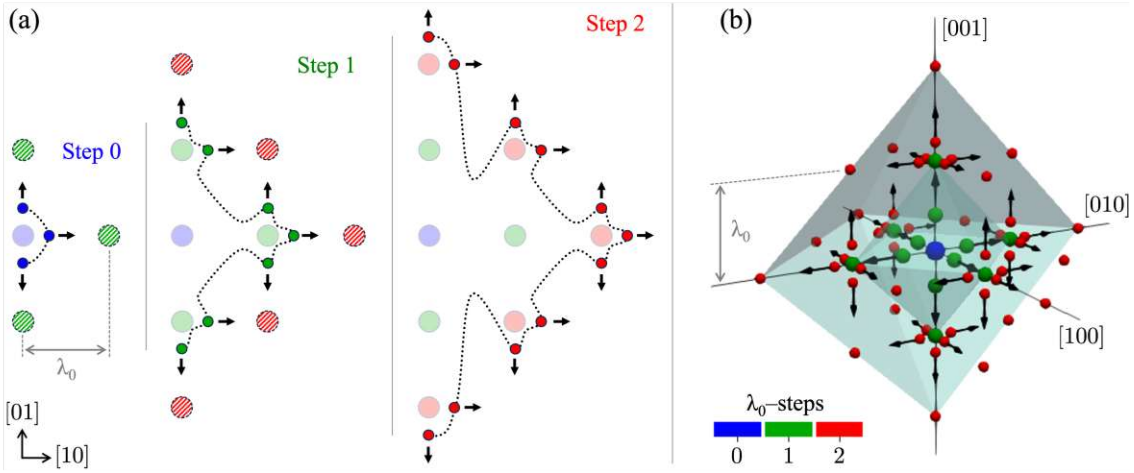

Figure 2: Particle-based grain envelope tracking algorithm illustrated in 2D (a) and 3D (b) for an equiaxed grain growing into a homogeneously undercooled/supersaturated melt. At nucleation, active particles are initialized in each ⟨100⟩ direction. They grow following dendrite tip kinetics until they reach the next target position (hatched points in (a)), after which a new set of active tracking points is generated in outer ⟨100⟩ directions (arrows).

the growth (and growth competition) of dendritic grains at macroscopic scale. In the case of polycrystalline growth competition, the advance of particles is naturally stopped when two particles from different grains meet, thus forming a GB. Since these envelope-based models do not explicitly account for individual dendritic branches, they cannot capture detailed mechanisms of dendrite impingement at converging GBs or sidebranching at diverging GBs, resulting in a simplified (nearly linear) morphology of resulting GBs [41]. However, in spite of their inability to accurately model the complex (rough) morphologies of GBs, once averaged over a sufficient population of grains (i.e. hundreds or more), such models nonetheless result in realistic statistical grain distributions in polycrystalline microstructures, as recently discussed based on a quantitative comparison between CA and PF simulations [41]. Morphological transitions, such as the columnar-to-equiaxed transition, hence emerge naturally from the applied nucleation and growth laws. Equiaxed grains appear whenever the nucleation criterion is fulfilled, their growth follows a similar kinetic law as the columnar grains that they compete with, and GBs are formed whenever two grain envelopes meet (regardless of whether they belong to columnar or equiaxed grains).

A key advantage of the particle-based approach over a traditional CA method is that it does not require to track the "capture" of neighboring cells (i.e. locating whether a grid point is located within a polyhedral shape) nor to calculate a new center for the new polyhedron associated with a newly captured cell [31, 36]. Indeed, here we just track particles that essentially multiply when they reach a given distance λ_0.

The next missing component to the growth model is the correlation between the growth velocity, v, and local conditions, such as temperature, T, and/or local solute concentration, w. In practice, the particle-based approach can work with any expression of $v(T, w)$. Here, we simply use a classical KGT-type model [42, 43], combining a local solute diffusion balance around the tip together with a tip selection criterion incorporating capillarity/curvature effect. For the solute transport, which may be assumed mostly diffusive in the immediate vicinity of the tip, we use the classical

Ivantsov equation [44]. We consider a total undercooling $\Delta T = T_L - T$ below the Liquidus temperature T_L of the alloy at its nominal concentration. Kinetic undercooling is not considered here, since we focus on applications at moderate cooling rate (i.e. moderate growth velocity $1 \ll m/s$). As we aim for simplicity for a first demonstration of the particle-based approach, we chose a relatively simple set of equations for the growth kinetics model similar to the well-known KGT model for binary alloys [42, 43] with two unknowns, namely the tip radius, r, and tip velocity, v. For its multicomponent extension, we use a simple additive contribution of the different solute species, as proposed and used in various models [35, 45, 46]. In practice, for the sake of computational efficiency, we use a power law $v(\Delta T)$ fitted to the KGT prediction of $v(\Delta T)$ for the given alloy, of the form

$$v = a\Delta T^b \tag{1}$$

or alternatively

$$v = a_1\Delta T^{b_1} + a_2\Delta T^{b_2} \tag{2}$$

with fitted coefficients (a, b) or (a_1, b_1, a_2, b_2).

2.1.3 Melting

Melting or re-melting can result from a local temperature increase beyond the Liquidus temperature of the alloy, due to melt flow, latent heat release during solidification, or an external energy source (e.g. a laser or electron beam). The present model handles melting by re-computing the new envelope with a "walk back" approach: i.e., the solid/liquid interface is redefined by seeking among each of the previously defined tracking points those which result in a null undercooling. It is achieved via a search algorithm identifying the tracking points closest (within a predefined distance) to the iso-surface satisfying $\Delta T = 0$. The distance threshold is typically set as $2\lambda_0$. Lower values lead to a faster search, but at the risk of a partially reconstructed discontinuous interface if chosen too low. The model hence re-activates tracking points that are at the edge between positively and negatively undercooled liquid. Results presented here consider the Liquidus temperature of the alloy at its nominal concentration, but it would be relatively straightforward to extend it to a local composition-dependent Liquidus temperature. Melting is thus assumed here to result in a well-mixed interdendritic liquid, hence only requiring the value of the average composition, directly provided by the phase diagram. When an entire grain is melted, the original nucleation seed is kept in case of possible later re-solidification, however it is not allowed to interact with the grain structure until it reaches again the nucleation undercooling. This approach for melting and its implementation are tested and validated in Section 4.1.

2.2 Thermomechanical coupling

The particle-based grain growth model may be coupled with nearly any macroscopic thermo-mechanical model using a classical volume-averaging approach [20–23]. Here, we use a classical volume-averaged model and a coupling strategy similar to CA coupling schemes (see [33, 34]). Below we briefly summarize the volume-averaged

conservation equations (Section 2.2.1) as well as the coupling strategy (Section 2.2.2) used to obtain the results presented later in Section 3. Note that all mathematical symbols are summarized in Table S10 of the joint Supplementary Data.

2.2.1 Conservation equations

The conservation of mass is ensured with

$$\frac{\partial \rho}{\partial t} + \nabla \cdot (\rho \boldsymbol{U}) = 0, \tag{3}$$

where $\boldsymbol{U} = g^l \boldsymbol{U}^l + g^s \boldsymbol{U}^s$ is the volume-averaged flow velocity and $\rho = \rho(T)$ is the density of the mixture of solid and liquid. The liquid fraction, g^l, is defined as the sum of extra- and intra-dendritic liquid within a mushy zone of volume fraction, g^m, as

$$g^l = 1 - g^m g^{si} = 1 - g^s \tag{4}$$

Like in classical CA [30–37] models, the mushy zone is defined as a mixture of dendritic solid and interdendritic liquid. The mushy zone corresponds to the volume within the envelope of a grain, here delimited by the convex hull of the tracking particles for a grain. The internal solid volume fraction in the mushy zone, g^{si}, is expressed as a function of the local temperature, T, and concentration w_i in solute species i as

$$g^{si} = f(T, w_i) \tag{5}$$

which can be tabulated using different solidification path such as lever rule or Gulliver-Scheil model, either analytically or computationally using the CalPhaD method. Here, we used the lever rule, except for the simple scenarios in Sections 3.1, 3.3 and 4.1, where a linear variation of solid fraction with temperature was assumed and microsegregation was not accounted for.
The conservation of momentum follows the volume-averaged Navier-Stokes equations

$$\frac{\partial (\rho \boldsymbol{U})}{\partial t} + \nabla \cdot \left(\frac{\rho}{g^l} \boldsymbol{U}\boldsymbol{U} \right) = \nabla \cdot (\mu \nabla \boldsymbol{U}) - g^l \nabla p + g^l \rho \boldsymbol{g} - \frac{\mu}{K} g^l \boldsymbol{U} + \boldsymbol{S}_M \tag{6}$$

The mixture density ρ and viscosity μ are temperature-dependent, and the term $\boldsymbol{S}_M$ is the sum of source terms. The penultimate term represents the volumetric friction force where K is the mushy zone permeability, here using the Carman–Kozeny relation:

$$K = \frac{\lambda_2^2 {g^l}^3}{180(1 - g^l)^2} \tag{7}$$

derived based on the assumption of an isotropic porous mushy zone. Density gradients driven by species concentration are assumed to be dominant against temperature-induced density changes, such that the source term, $\boldsymbol{S}_M$, can be considered using the Boussinesq approximation:

$$\boldsymbol{S}_M = \rho_{T=T_L} \boldsymbol{g} \sum_{i=1}^{n} \left\{ b_{w_i} (w_i^l - w_{i,0}^l) \right\} \tag{8}$$

where b_{w_i} are solute expansion coefficients for each species i.
The conservation of energy follows a classical diffusion-advection equation:

$$\frac{\partial \rho H}{\partial t} + \boldsymbol{U} \cdot \nabla \rho H - \nabla \cdot (\kappa \nabla T) = 0 \tag{9}$$

The mixture enthalpy, H, is defined as

$$H = H^s + g^l (H^l - H^s) \tag{10}$$

with

$$H^s = \int_{T_{ref}}^{T} c_p(T) dT \tag{11}$$

and

$$H^l = H^s + \Delta H_f \tag{12}$$

where $c_p(T)$ is the heat capacity and ΔH_f is the enthalpy (latent heat) of fusion.
Species transport via convection and diffusion is modeled through

$$\frac{\partial w_i}{\partial t} + \boldsymbol{U} \cdot \nabla w_i^l - \nabla \cdot (D_i^l g^l \nabla w_i^l) - \nabla \cdot (D_i^s g^s \nabla w_i^s) = 0 \tag{13}$$

with the average composition, w_i, defined as

$$w_i = g^s w_i^s + g^l w_i^l \tag{14}$$

In most simulations presented here (i.e. all except the one in Section 4.2), the equations above are solved using a custom-built volume-averaged finite volume (FV) Navier-Stokes (NS) solver. Note that, in Section 3, we intentionally selected test cases that do not involve convection, so as to discard potential discrepancies expected from the resolution of the volume-averaged NS equation with different solvers [47], hence simply solving diffusion equations for enthalpy and solute concentration(s), when relevant. Furthermore, some test cases in Section 3 use a given temperature field as an imposed condition (namely Sections 3.2, 3.3 and 3.4). Material parameters (e.g. D_i^s, D_i^l, c_p, κ) may be phase- and temperature-dependent (in spite of their simplified notation here).

2.2.2 Coupling between macroscopic and microstructure model

Conservation Eqs. (9) to (14) require an additional set of assumptions to compute the evolution of all fields. The heat conservation equation includes three unknowns, namely: the average temperature (T), the enthalpy (H), and the liquid fraction (g^l) fields. We use a classical enthalpy method [48] to solve the enthalpy as the primary unknown. We eliminate the temperature as an unknown using:

$$H^t - H^{t_0} = \frac{dH^*}{dT}(T^t - T^{t_0}) \tag{15}$$

with

$$\frac{dH^*}{dT} = c_p + \Delta H_f \frac{dg^{l^*}}{dT} \tag{16}$$

where the superscripts t_0 and $*$ denote the previous time step and the previous iteration variable values, respectively. The term dg^{l^*}/dT in the mushy zone is nonlinear and can be computed numerically or expressed analytically assuming a Gulliver-Scheil model or lever rule with a simplified phase diagram (e.g. with constant partition coefficient, k, and Liquidus slope, m_L).
A similar approach is used to isolate the average composition, w_i, for each species i and solve the mass conservation equation as follows:

$$w_i^t - w_i^{t_0} \approx \frac{dw_i^*}{dw_i^l}[w_i^{l_t} - w_i^{l_{t_0}}] \tag{17}$$

with dw_i^*/dw_i^l as the key term which is nonlinear in the mushy zone and can be derived from the considered solidification path (e.g. Gulliver-Scheil or lever rule). Equation (17), which is used to estimate w_i^l in Eq. (13), relies on the fact that a local change of concentration in a finite volume comes from a change in liquid concentration, since the solid is here immobile.
In summary, the two-way coupling between the volume-averaged finite volume solver and the particle-based envelope tracking solver proceeds as follows. The evolution of the enthalpy (H), pressure (p), velocity ($\boldsymbol{U}$), and average concentration (w_i) fields are solved via the FV solver from the system of Eqs. (3), (6), (9) and (13). After the growth of the grain envelopes, i.e. the advance of the tracking particles following Eq. (1) or (2), the value of the mushy zone fraction (g^m) in each FV element is calculated from the location of the envelope. The mushy zone fraction is thus used in the FV solver to compute the solid fraction g^s and liquid equilibrium concentration via Eqs. (4) and (14), accounting for a given solidification path (5), e.g. lever rule of Gulliver-Scheil model. These are subsequently combined to calculate the temperature field T via Eq. (10).
Up to this point, we have only addressed the growth of a single solid phase within an undercooled/supersaturated liquid. Yet, in most alloys, secondary reactions (e.g. eutectic, peritectic) are expected. In such cases, the considered solidification path, Eq. (5), could be substituted by a more advanced microsegregation model (e.g., [49, 50]). Here, we use a simple approach whereby, once a given eutectic temperature T_{eut} is reached, all the enthalpy change is converted into a eutectic (solid) fraction, which does not directly affect the envelope growth model.
As already mentioned, the particle-based approach can be integrated with nearly any solver of arbitrary complexity. To illustrate this, in the final application (Section 4.2), it is (one-way) coupled to a multiphase model for the simulation of laser processing [51]. The solver accounts for fluid flow in both liquid and gas phases. It relies on a *mass-of-fluid* approach, which allows better mass conservation than the usual *volume-of-fluid* method in the case of compressible phases and phase change. Details on the governing equations, the numerical algorithm, and a series of results for validation purposes were recently presented elsewhere [51] and are therefore not repeated here.

2.3 Numerical resolution

Transport equations presented above are solved using the open-source C++-based finite volume (FV) solver `OpenFOAM` [52]. To couple the grain structure model with

the continuum volume-averaged model, an accurate estimation of g_l, dH/dT, and w^l is essential. These quantities are calculated based on the value of the mushy zone fraction, which is estimated at the particle positions from the cell centers of the FV mesh. While the FV solver calculates quantities (e.g. fields) at the center of cells, the local undercooling used to calculate the growth velocity for each particle point uses the local value of temperature and solute concentration(s) interpolated between cell centers (here using the `OpenFOAM` built-in interpolation scheme `cellPointFace`), which ensure continuity of undercooling across cell boundaries. We show later (Section 3) that this approach is adequate and accurate enough for a correct coupling while minimizing expensive interpolation operations.

For the particle-based grain growth model, we designed an algorithm that takes advantage of modern computer architectures and the use of scalable libraries. Namely, we use `OpenVDB` [53] space-partitioning acceleration structure, where active points are partitioned into voxels to accelerate search steps for particles within a given spatial range or for nearest neighbors. The resulting dynamic allocation strategy reduces the dendritic structure evolution problem to the computation of the evolution of a point cloud, where each point only carries essential information about grain properties (namely orientation and nucleation origin). Grain boundaries are naturally computed from serial, multi-threaded, and/or GPU-accelerated collision detection. Information about the grain inner volume is only necessary in case of re-melting and is stored using `OpenVDB` volumetric, dynamic grid that shares several characteristics with B-trees [53]. The result is a compact encoded data and grid topology representation of the solidification grain structure that requires minor overhead of CPU/GPU clock cycle and dynamic/persistent storage.

In essence, the model predicts the grain envelopes as a cloud of points. In order to render the grain structure, a Voronoi kernel-based interpolation can be used to recover the closest tracking point grain orientation at any given point. The Voronoi interpolation allows recovering spatial data within the empty shell-like point cloud for each grain, therefore allowing efficient data storage compared to CA-based models.

In summary, the underlying assumptions and equations of the model are somewhat standard, e.g. providing a grain growth description comparable to that in the popular CA method [30–36]. However, the particle-based description of the grain envelope and the choice of scalable tools and libraries results in a lighter data structure. The computational efficiency and a detailed scalability analysis will be discussed in a separate article (see preliminary results in [54]). First, in the present paper, we focus on the verification and validation of our model and numerical implementation against relevant existing benchmark cases from the literature (Section 3) and then illustrate the potential of the fully coupled model (Section 4).

3 Verification & validation against benchmark cases

In this section, we simulate different benchmark cases from the literature, quantitatively comparing the results to experimental data, analytical solutions, or numerical results, in order to verify and validate the proposed model and its numerical implementation. The cases are selected to test individually the capabilities of the model to simulate different key physical phenomena, with an increasing level of coupling

and complexity, up to real-word applicable scenarios. For the sake of reproducibility, while maintaining the relative brevity and hence clarity of the main text, all input parameters such as material properties, initial and boundary conditions, and numerical discretization, are gathered in tables provided as Supplementary Material.

3.1 Single grain envelope in a temperature gradient

First, we verify the accurate prediction of three-dimensional grain envelopes in a heterogeneous thermal field, by simulating the growth of a single grain in the presence of a temperature gradient, where an analytical solution exists [30]. Here, the simulation is only testing the particle growth algorithm, as it involves no solute field, and the temperature field is imposed. The grain orientation is defined by the Euler angles $(20°, 20°, 20°)$ and the growth kinetics model follows Eq. (1) with $a = 10^{-4}$ m s^{-1} K^2 and $b = 2$. The initial undercooling is set to $\Delta T = 2$ K, the cooling rate is $\dot{T} = -0.1$ K/s, with a thermal gradient of $G = 250$ K/m in the $\vec{e}_z$-direction. The microstructure length scale is set to $\lambda_0 = 200$ µm and the time step is $\Delta t = 0.01$ s. In Figure 3, we compare the model prediction at a time $t = 5$ s with the analytical solution provided in [30], showing a perfect match of the two solutions. Although the test case is very simple, it provides a valuable benchmark to verify the particle-based approach and its implementation in terms of accounting for the combined effect of the surrounding thermal field and crystal orientation.

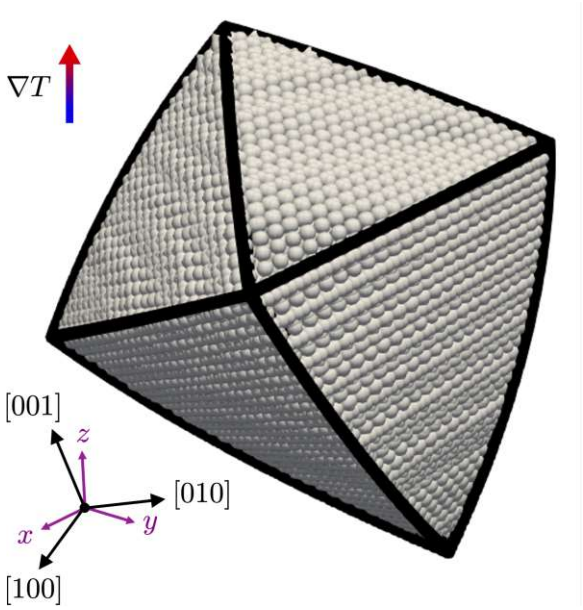

Figure 3: Particle-based envelope tracking for a tilted grain within a temperature gradient. Comparison of the model prediction (spheres) and the analytical solution (black outline) provided by Gandin and Rappaz [30] of the grain envelope at $t = 5$ s after nucleation with an initial undercooling $\Delta T = 2$ K, a grain misorientation $(\psi, \theta, \varphi) = (20°, 20°, 20°)$, a cooling rate of 0.1 K/s, and a thermal gradient $G = 250$ K/m in the $\vec{e}_z$-direction.

3.2 Unidirectional solidification of an Al-Si alloy

Next, we test the model in the case of a one-dimensional (1D) unidirectional solidification of an Al-7wt.%-Si alloy and compare our results to that of Carozzani et al. [33]. In this case, the calculation involves only the diffusive thermal field coupled with the particle-based solidification model. One domain boundary obeys a heat flux boundary condition defined by a heat transfer coefficient and an outside temperature, while the other boundary is adiabatic. As our model is inherently three-dimensional, we simulate a 5 mm × 5 mm × 100 mm domain with adiabatic boundary conditions on the lateral (short dimension) directions. The material parameters, initial and boundary conditions, and discretization used in this simulation are provided in Table S1 of the joint supplementary document.
In Figure 4, we plot the time evolution of temperature and solid fraction at several probe locations, compared to the CA-FE model results presented in [33]. For consistency, we use as reference the non-iterative CA-FE algorithm described in [33]. Our results show an excellent agreement with these reference results. Discrepancies are of the same order as those observed between CA-FE and front tracking models (see Fig. 5 in [33]). As discussed in [33], the small oscillations and steps observed in the vicinity of Liquidus and eutectic temperatures (also observed in CA-FE results) are due to a change of slope in the enthalpy-temperature conversion, and they can be reduced with a finer spatiotemporal numerical discretization [33]. As also discussed in [33], while an iterative coupling scheme would allow a more accurate matching to front tracking models, the faster non-iterative algorithm leads to acceptable deviations (< 0.5°C in this case), which are reduced even further in 3D compared to 1D and 2D simulations. These results show that the present model leads to predictions that are very close to those from a CA-based approach (even up to similar numerical oscillations).

3.3 Directional solidification of a quasi-2D thin sample

Next, we test the model for a simulation of grain growth competition in a simple, two-dimensional case. The selection of grain boundary (GB) orientation during dendritic grain growth competition, even in 2D within a simple one-dimensional temperature gradient, is stochastic (due to the origin of sidebranches in the selective amplification of noise) [38, 39, 55]. However, models based on a CA or the model presented here are inherently deterministic. Here, we focus on one specific case in which the CA was previously shown to closely approach experimental measurements as the grid spacing is refined [30]. Namely, this corresponds to the pioneering experiment on a transparent succinonitrile-acetone alloy by Esaka et al. [56].
Here, the problem consists of a diffusive thermal field coupled with the particle-based solidification solver (no solute field). As the experiment contains three grains, we initialize our simulation by seeding 15 nuclei at the bottom of the domain at locations $(x, y) = (w/2 + i \times 360, 0.15)$ µm with w the width of the domain in the y-direction and $-7 \leq i \leq +7$. The three leftmost nuclei ($i \leq -5$) are initialized with a tilt angle $\psi = 4°$, the three rightmost nuclei ($i \leq 5$) with $\psi = 11°$, and the remaining central nuclei ($|i| \leq 4$) with $\psi = 30°$, according to experimental observation (and reference CA-based simulation), with all other Euler angles being $\varphi = \theta = 0°$. The boundary

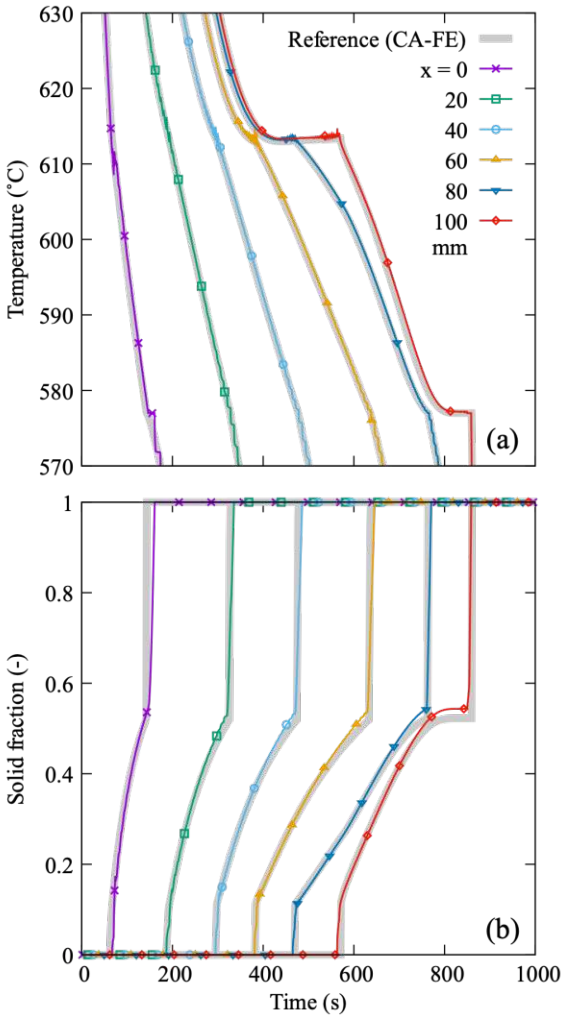

Figure 4: One-dimensional simulation of Al-7wt.%Si solidification: (a) Temperature and (b) solid fraction at $x = 0$, 20, 40, 60, 80, and 100 mm, computed with the present model (foreground thin color lines with symbols) compared to the CA-FE results from [33] (background thick gray lines).

conditions are chosen to result in a constant thermal gradient and cooling rate, and a pulling velocity of $v_{pull} = 86$ µm s^{-1}. Following [30], the kinetic model was set as Eq. (2) with $a_1 = 8.26 \times 10^{-6}$ m s^{-1} K^{-2}, $b_1 = 2$, $a_2 = 8.18 \times 10^{-5}$ m s^{-1} K^{-3}, $b_2 = 3$. Further details on the domain, discretization, thermophysical properties, initial and boundary conditions are given in Table S2 of the joint Supplementary Material.
Focusing on the right-hand-side GB between the central grain at $\psi = 30°$ and the right grain with $\psi = 11°$, Figure 5 compares the predicted GB angle by the current model and the CA results from [30] as a function of the microscopic growth model spatial discretization (i.e. λ_0 in the present model, and the CA grid element size in [30]). The convergence trends exhibited by the CA and the particle-based approach are similar, with the current model overall resulting in a GB angle closer to the fully converged result, which is close to the experimentally measured angle $\approx 19°$. The present model appears reasonably converged for any $\lambda_0 \leq 48$ µm, which is higher than the experimentally measured SDAS $\lambda_2 = 8.4 \pm 0.4$ µm [56]. It should be noted that, the uncertainty on the measurement of the GB angle is of order $\pm 1°$ to $\pm 2°$ for coarser grids ($\lambda_0 > 55$ µm), while it is a vanishingly small fraction of a degree for finer grids ($\lambda_0 < 55$ µm). (This is mostly due to the selection of exact locations for GB start and end points between laterally adjacent yet increasingly far-apart particles.)
Even though the optimal choice of cell size in CA (and, by extension, the choice

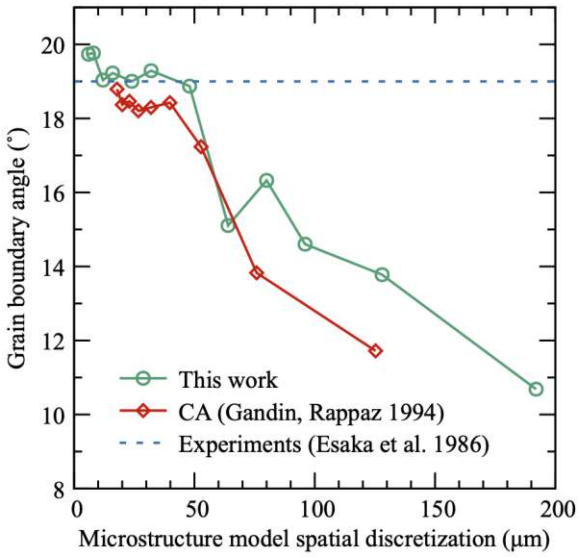

Figure 5: Average orientation of the grain boundary between grains titled by 30° and 11° predicted by the current particle-based model compared to published CA-FE results [30] and experimental results by Esaka et al. [56].

of λ_0 in our particle-based approach) in the context of grain growth competition is still debated [37, 41, 57], these results suggest that similar convergence trends might be expected from the present model. In the next subsections, we move on to more complex 3D polycrystalline cases, without (Section 3.4) and with (Section 3.5) nucleation.

3.4 Directional solidification of three-dimensional polycrystal

In the next test of our model and implementation, we simulate the polycrystalline competitive growth of dendritic grains in a three dimensional (3D) configuration, and compare our results with phase-field results published by Takaki et al. [58]. The simulations correspond to the directional solidification of an Al-3wt.%Cu alloy in the z-direction at a velocity $v_{pull} = 100$ µm s^{-1} under various temperature gradients and initial grain distributions (referred to as cases 1, 2, and 3 in [58]). Here, the temperature field is imposed using the classical "frozen temperature approximation" (i.e. using homogeneous and constant temperature gradient and cooling rate), and the diffusive solute concentration field is coupled to the particle-based solidification solver. We focus on cases 1 and 3 for $G = 10$ K mm^{-1} and 100 K mm^{-1}. Periodic boundary conditions were applied on domain boundaries normal to the x and y directions. For the growth kinetics, we used Eq. (1) with $b = 2.282$ and $a = 1.834 \times 10^{-4}$ m s^{-1} K^{-b}. The spatial distribution and grain orientation of the initial nuclei for cases 1 and 3 are as given in the Supplementary Materials of Ref. [58]. Further details on input parameters including spatial and temporal discretization and thermophysical properties are provided in Table S3 of the attached Supplementary Materials.

Figure 6 shows a top-view (i.e. with the main growth direction, z, oriented towards the reader) of the solidification front, colored by the angle between the z-axis and the [100] crystalline direction, at three different time steps $t \approx 8$, 27 and 133 s ($\pm$ 1 s), for each of the four cases, comparing our results to published PF results [58] using the same color palette. While the results of the two models do not exhibit an exact match, the overall trends are qualitatively well reproduced, in terms of grain elimination rates (Figure 7). Indeed, even though their precise spatial distribution is not exactly similar, results of the particle-based approach show similar color shades within proportions comparable to PF results. As already discussed in previous articles (e.g. [41]), discrepancies are expected between PF and coarse-grained envelope-based approaches. PF results tend to be stochastic in nature, due to the fact that dendritic side-branches have their origin in the selective amplification of fluctuations. (Whether or not PF simulations are performed with noise, minor changes in initial conditions or numerical resolution may lead to noticeable differences at diverging GBs.) Diverging GBs thus exhibit a high lateral mobility since their morphology results from side-branching competition [59, 60]. The use of growth kinetics based on steady-state assumptions (e.g. Ivantsov) also leads to discrepancies with PF results that numerically resolve the transient diffusion of species ahead of each dendrite tip. Another source of discrepancy comes from the fact that dendrites do not always grow perfectly aligned with their ⟨100⟩ directions [59, 61–63], while they are assumed to do so in coarse-grained models. This is particularly important for higher temperature gradient, which may lead to an intermediate cellular-dendritic regime where the cells/dendrites grow more closely aligned to the temperature gradient direction, hence resulting in significantly different growth competition mechanisms [58, 64].

In these specific simulations, the temperature field is imposed, and the grain growth competition occurs through the solute field, just like in PF simulations, as the local undercooling entering the growth kinetics is estimated with respect to the local solute

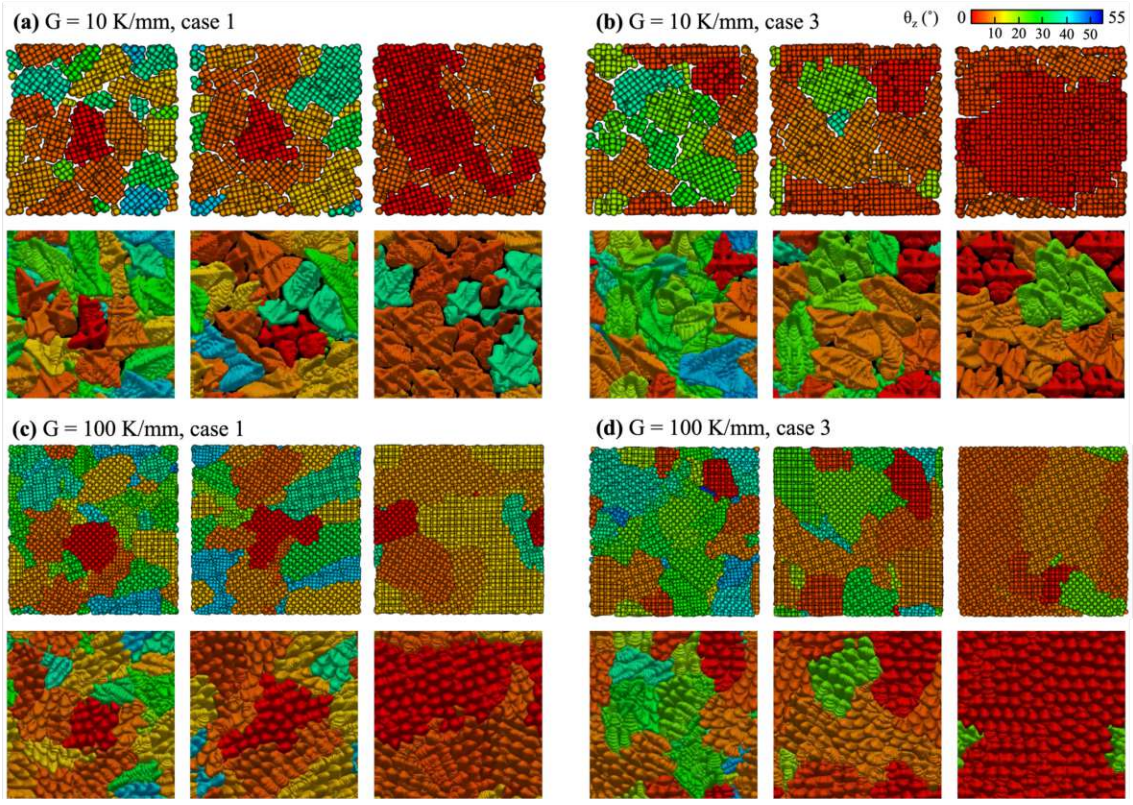

Figure 6: Top view of the solid-liquid interface for a temperature gradient $G = 10$ K mm^{-1} (a,b) and 100 K mm^{-1} (c,d) for initial grain distributions corresponding to case 1 (a,c) and 3 (b,d). For each case, we compare the results of the particle-based approach (top) and phase field model [58] (bottom), for $t \approx 8$, 27 and 133 s ($\pm$ 1 s)(left to right). Lateral dimensions are both 768 µm.

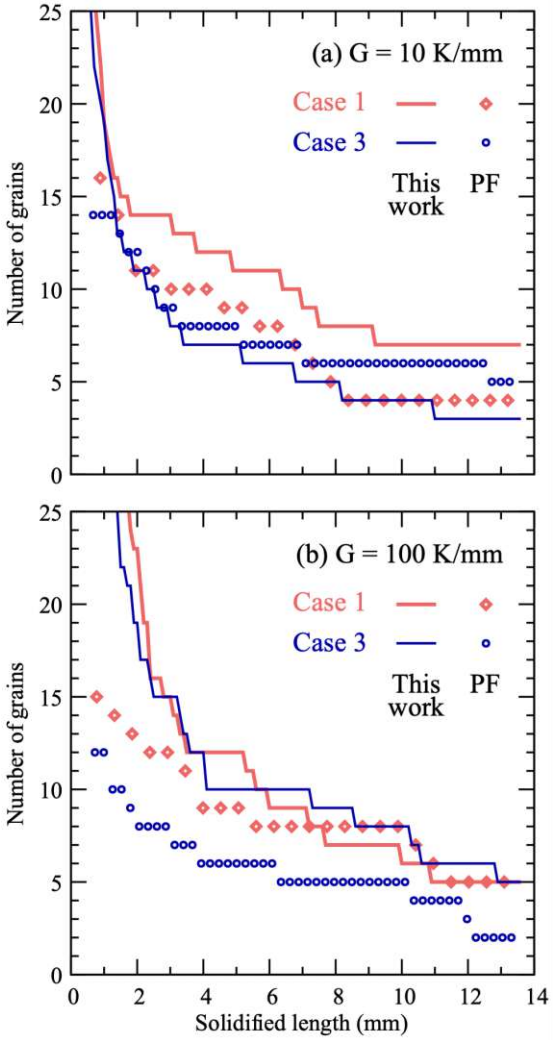

Figure 7: Number of surviving grains as a function of the solidified length for cases 1 and 3 predicted by the particle-based model (lines), compared to PF result by Takaki et al. [58] (symbols) for a thermal gradient of = 10 K mm^{-1} (a) and 100 K mm^{-1} (b).

concentration. This allows calculating the solute concentration map within the solidified domain, as illustrated in Figure 8 for the two simulations with = 10 K mm^{-1}. The cross sections (a,b) and longitudinal sections (c,d) of the solute concentration field clearly highlight interdendritic segregation patterns within the grains, as well as along grain boundaries. Still, it is worth noting that, in order to obtain this level of detail, both the grid element size Δx and the microstructural length scale λ_0 need to be taken relatively small compared to the primary dendrite arm spacing, which may be inconvenient for computational purposes.

In spite of the inability of coarse-grained envelope-based models to reproduce fine

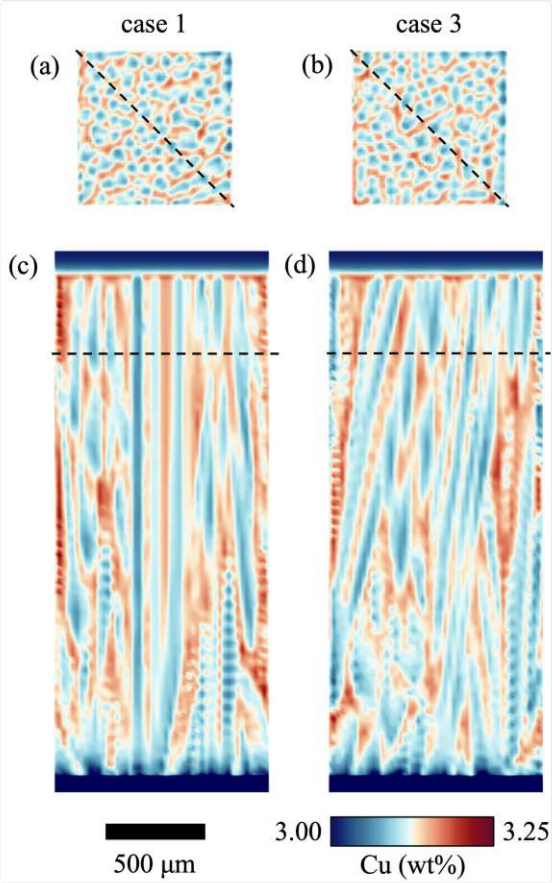

Figure 8: Solute concentration maps for the two cases at $G = 10$ K mm^{-1}, within a cross section (a,b) and a longitudinal section (c,d) marked with dashed lines, pictured at $t = 27$ s.

details of grain growth competition, it was previously shown that, when focusing on average distributions over a statistically representative number of grains, a reasonable agreement with PF results can be achieved if the microstructural model discretization is fine enough [41]. Here, the total number of grains is not sufficient to extract meaningful orientation distribution histograms. However, a quantitative and averaged comparison can still be drawn by comparing the number of grains as a function of the grown length, as in Figure 7. These plots show that, despite some expected deviation, the predicted grain coarsening/elimination rate is close to PF results. The elimination rate from the particle-based model appears slightly slower (i.e. higher number of grains), but not by a significant amount. Figure 7 also shows the increas-

ing discrepancy expected with a higher temperature gradient due to the transition toward an intermediate cellular-dendritic regime. These results are satisfactory, given that the benchmark is applied with a much more accurate yet much more demanding phase-field model.
In terms of computational cost, our model can afford a FV spatial discretization step of 16 µm with a microstructural scale $\lambda_0 = 24$ µm (for $G = 10$ K mm^{-1}) or 10 µm (100 K mm^{-1}), compared to the fine grid element size of 0.75 µm required for well-converged PF simulations. Each simulation was performed in between 15.7 h (for $G = 10$ K mm^{-1}) and 22.5 h ($G = 100$ K mm^{-1}) of wall clock time using 24 CPU cores of an AMD EPYC 7713 Processor, while the PF model requires about 5 days on 144 GPUs [58].

3.5 Columnar-to-equiaxed transition in an Al-Si alloy

As a final verification, we simulate the solidification and resulting columnar-to-equiaxed transition in a cylindrical Al-7wt.%Si ingot, corresponding to experiments by Gandin [65]. The problem involves a diffusive thermal field coupled with the particle-based solidification solver (no solute field). While the grain distribution and orientation are randomized, initial and boundary conditions are taken according to subsequent CA-FE simulations performed by Carozzani et al. [33]. Nuclei of uniform random orientation distribution and location are initialized across the cooled lower domain boundary and within the volume at a given nuclei density. The nucleation undercooling of the boundary nuclei is set to zero, whereas it exhibits a normal distribution for nuclei in the bulk with $\Delta T_{min} = 0$ K, $\Delta T_{min} = 10$ K, $\Delta T_{\mu} = 5.19$ K and $\Delta T_{\sigma} = 0.25$ K. The thermal boundary condition at the lower domain boundary is identical to Ref. [33], where the experimentally obtained temperature values of [65] are extrapolated to $z = 0$ (see Figure 10). Following [33], a heat flux of 3000 W m^{-2} is applied to the top boundary for $t \leq 900$ s, in order to account for heat losses at the liquid-gas interface resulting from the air gap forming due to solidification shrinkage. The full list of material parameters, initial and boundary conditions and numerical parameters used in this simulation are provided in Table S4 of the attached Supplementary Materials, with temperature-dependent density and thermal conductivity listed in Tables S5 and S6.
Figure 9 shows the resulting evolution of the grain structure, and Figure 10 shows the evolution of temperature in the ingot measured at different heights z within the ingot (measured along its central axis). The predicted grain structure exhibits a clear columnar-to-equiaxed transition (CET), with elongated columnar grains at the bottom and equiaxed grains at the top, which is consistent with experiments [65] and CA simulations [33]. The CET occurs progressively between approximately 100 and 110 mm in height, compared to $\approx$ 118 mm in the experiment and $\approx$ 108 mm in the CA-based simulation. The temperature evolution at the $z = 140$ mm probe clearly exhibits a recalescence just below the alloy liquidus temperature ($\approx$ 618 °C), which can only be reproduced using a model accounting for undercooled nucleation and grain growth. Like in Ref.[33], discrepancies between experiments and simulations can be attributed to several effects that are not included in the model, such as sedimentation, fragmentation, shrinkage, and macrosegregation driven by fluid flow. The

CA-FE simulation in [33] required a CA cell size of 250 µm resulting in 43 × 106 cells. In comparison, the number of active tracking points in the present particle-based approach resulted in a peak in active particles of 413 766 at $t = 906$ s, with an average number of about 206 000 active particles over the entire simulation. The main conclusion from these results (like those previously presented in this section) is that the current approach allows simulations with a similar accuracy as reference grain-scale simulations methods, such as CA, yet with a more data- and computation-efficient particle-based approach.

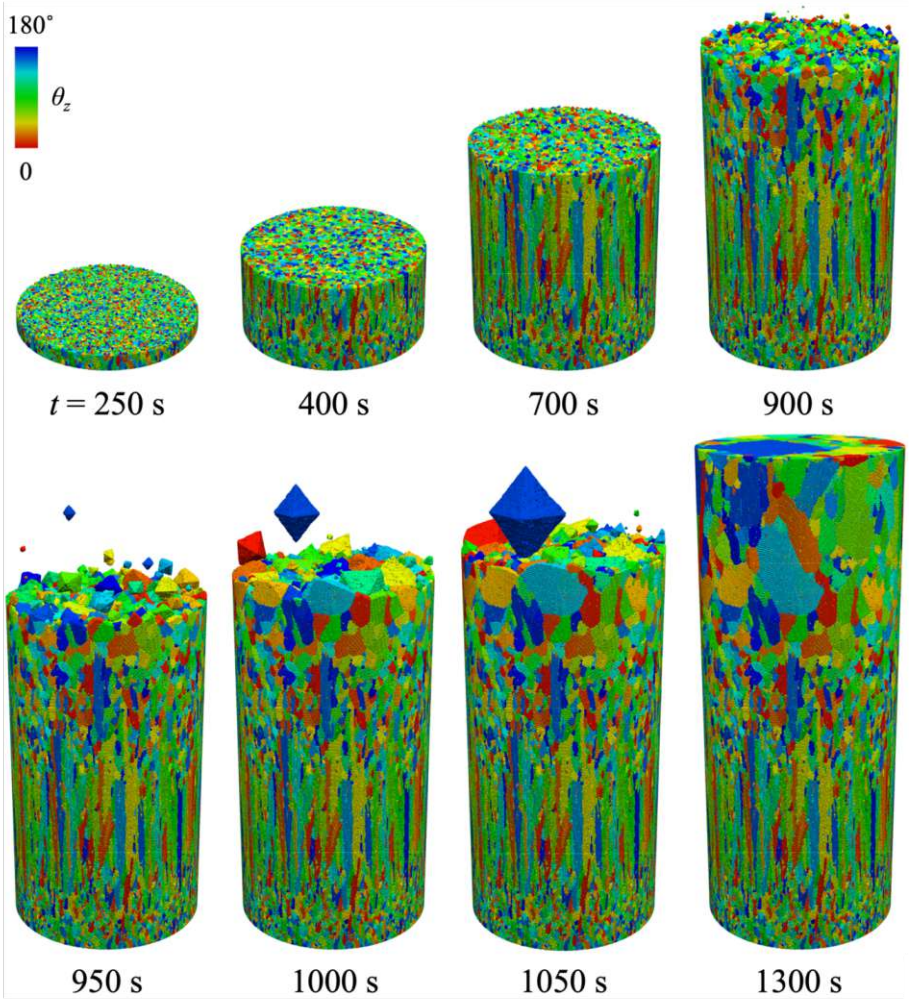

Figure 9: Grain structure evolution during 3D simulation of columnar-to-equiaxed transition in Al-7wt.%Si ingot of height 173 mm and diameter 70 mm.

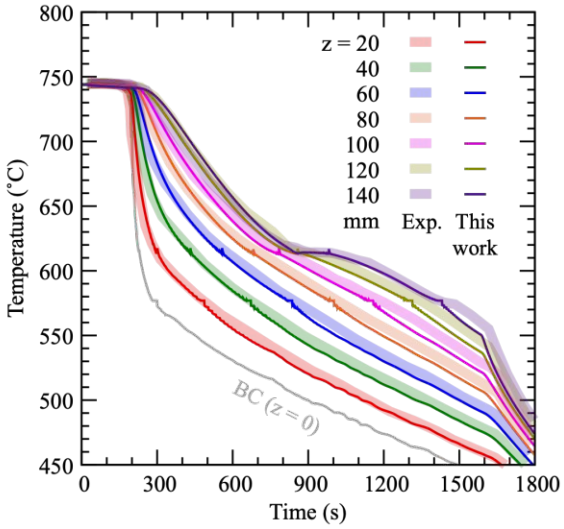

Figure 10: Temperature evolution at different locations in the ingot, comparing experimental measurements from [65] (thick pale lines) with predictions of the FV model coupled with the particle-based grain nucleation growth (thin darker lines), also showing the imposed BC at the lower end ($z = 0$) of the ingot (gray line).

4 Original applications

4.1 Melting test case

Before applying our solver to a laser welding case (Section 4.2), we test the implementation of melting described in Section 2.1.3. To do so, we set up a simple, quasi-two-dimensional case, where the initial random Voronoi-based grain structure is partially melted and re-solidified under a steep thermal gradient relevant to industrial processes, such as laser-beam melting.

The considered quasi-2D domain (with dimensions $L_x \gg L_z$ and $L_y \gg L_z$) is sketched in the inset of Figure 11. Two different Dirichlet boundary conditions (BCs) are used, denoted as isothermal on the bottom ($y-$) and right ($x+$) boundaries and constrained on the top ($y+$) and left ($x-$) boundaries. Boundary conditions imposed on the front and back boundaries along the short z direction are Neumann (no-flux) BCs (i.e. so-called `empty` BCs in OpenFOAM). The constrained boundary serves as simplified model for a high-energy beam (e.g., laser) melting process, i.e. with a steep temperature increase followed by a slower decrease in temperature. The imposed Dirichlet BCs are plotted in Figure 11. Initially, nuclei are seeded with a density of $\rho_{nuc} = 10^{13}$ m^{-3} throughout the domain, and random three-dimensional (ψ, θ, φ) orientation. From these nuclei, an initial grain structure develops from the cooling of the domain below the liquidus temperature in the first 2.5 ms of the simulation. Then, a steep rise in temperature at the constrained boundary serves as simple model for a high-energy beam heat input, followed by a linear cooldown at constant cooling rate, $dT/dt = 2 \times 10^4$ K s^{-1}, representative of laser-based processing. For the growth kinetics model, we use Eq. (2) with coefficients $a_1 = 8.315 \times 10^{-6}$ m s^{-1} K$^{-2.49}$, $b_1 = 2.49$, $a_2 = 9.628 \times 10^{-7}$ m s^{-1} K$^{-3.622}$, and $b_2 = 3.622$, which corresponds to a stainless steel [35]. All case-specific parameters, such as thermophysical properties, initial conditions, and

domain size, are summarized in Table S7 of the joint supplementary material.
The resulting grain structure evolution is illustrated in Figure 12, where the grains

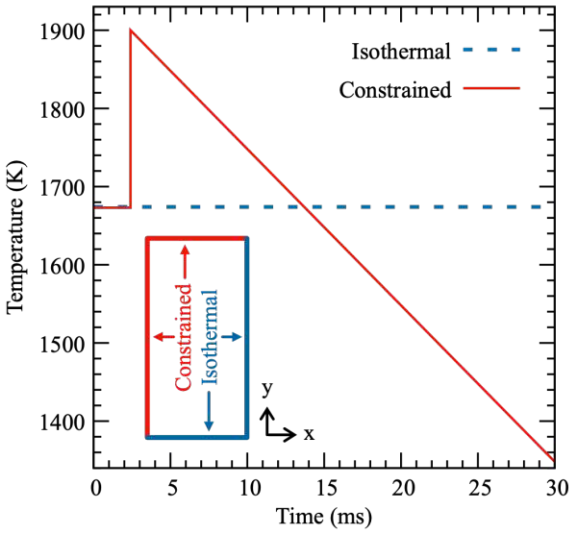

Figure 11: Temperature evolution profiles imposed as Dirichlet conditions on the x- and y-direction boundaries. The inset schematics illustrates the location of "isothermal" and "constrained" conditions in the (x, y) plane.

are colored by their [100] orientation with respect to the $\vec{e}_y$-axis. These results show that the considered approach and algorithm for melting (Section2.1.3), i.e. tracing back the particles up to the nominal liquidus temperature, qualitatively reproduces the expected behavior for a melted and (re)solidified structure.

4.2 Laser beam welding of 316L stainless steel

Now that the solidification and melting model and its implementation have been validated, we illustrate an industrially relevant application. At the same time, we also illustrate that the particle-based approach can be coupled with nearly any custom CFD solver. To do so, we focus on keyhole-mode laser beam welding (LBW) of a stainless steel. The particle-based model (referred to as the solidification solver) was coupled with a multiphysics laser-based manufacturing solver (referred to as the CFD solver) [66].
The `OpenFOAM`-based CFD solver was described in detail in [51]. Its capability for predicting real-world processes was demonstrated for a broad range of processes, such as the humping phenomenon and transition to cutting in welding of steel [67], dissimilar metal welding [68], overlap welding with beam shaping under the presence of an interfacial gap [69], or additive manufacturing via powder bed fusion [70]. A detailed description of the solver, its underlying mathematical framework and numerical implementation, including multiple validation cases including laser beam welding, was recently published elsewhere [51].
While in Section 3, the particle-based solver and transport FV solver are coupled in both directions (even though not iteratively), here we use a simplified coupling scheme. The coupling between the CFD and solidification solvers is of a one-way nature (weak coupling): the solidification solver receives information on the distribution

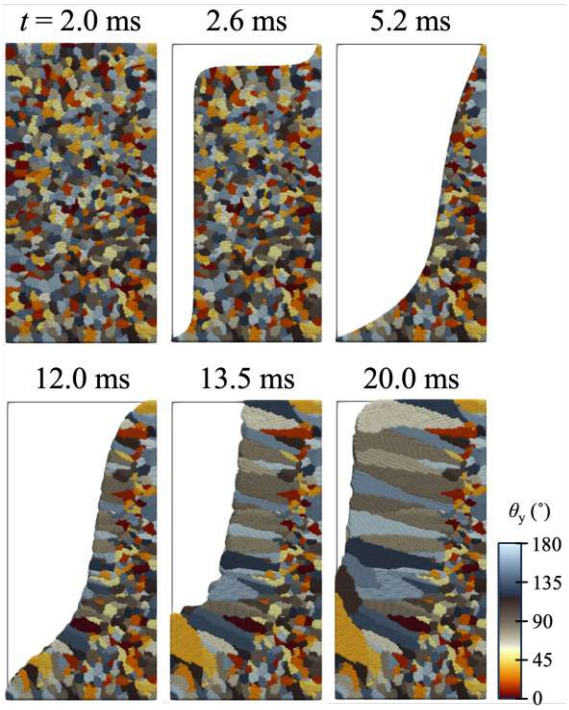

Figure 12: Grain structure at different time steps of the melting and solidification simulation, with grains colored by their crystal orientation within the (x, y) plane, θ_y. (Since grains have random three-dimensional orientations, the chosen color scale is mostly illustrative.)

of phases (solid, liquid, and gaseous metal, as well as ambient gas) and temperature distribution at each CFD simulation time step to calculate the resulting grain structure evolution. A two-way coupling, with information feedback from the solidification solver to the CFD solver is also feasible, but here we simply illustrate that the approach can also be applied as a post-processing tool to any complex multiphysics solver.

In welding, the solid base metal acts as seed for epitaxial grain growth. In spite of some variability, the resulting grain growth competition typically favors grains oriented normal to the liquid-solid interface, i.e. along the main temperature gradient direction [41, 60]. Keyhole mode welding, as opposed to conduction mode welding, is characterized by high temperatures, locally reaching the boiling point. This leads to evaporation, with the recoil pressure forming a capillary, which eventually reaches a keyhole shape, in which the laser beam is reflected multiple times, increasing the amount of laser power further absorbed by the material. The resulting melt pool and final weld seam have a high depth-to-width ratio [71]. The microstructure obtained through laser beam welding is typically determined by the high peak temperatures, a moving solidification front, and negligible constitutional and kinetic undercoolings [72].

The simulated configuration features a 2 mm sheet of 316L stainless steel welded in total penetration mode, as investigated experimentally and analytically by Artinov et al. [73]. The material properties of 316L stainless steel are set using the values reported in [74] and [75]. An initial structure is established in the base material with randomly distributed seeds (see Figure 13). The initial grain structure is only placed

within a small portion of the entire domain, where the process is expected to be in steady-state mode, to avoid computational costs associated with computing the grain structure within the entire domain. This initial structure is then locally "erased" by melting during the welding process (see Section 4.1), allowing for re-growth under the thermal gradients and cooling rates determined by the CFD simulation. The computational domain, FV mesh and initially generated grain structure are illustrated in Figure 13. Full details on the initialization parameters, kinetic model, process and numerical parameters are provided in Table S8, with temperature-dependent material properties listed in Table S9 of the Supplementary Material.

Figure 14 shows an image of the simulated melt pool and surrounding temperature

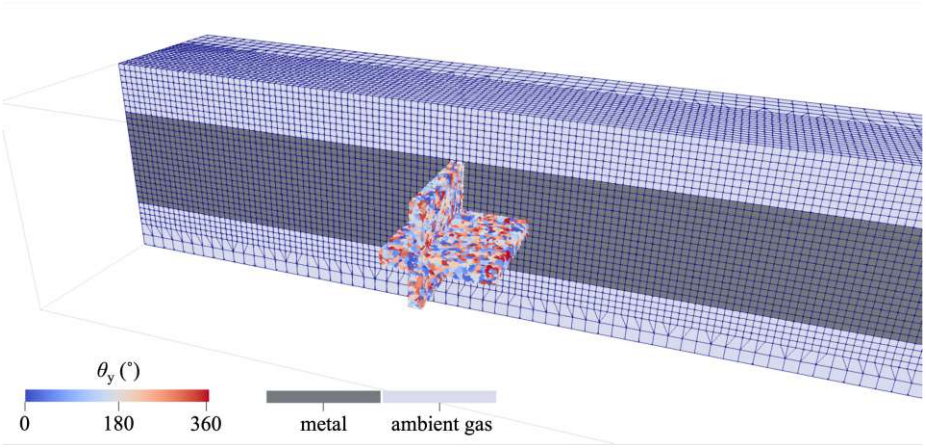

Figure 13: Computational domain showing mesh and initial phase distribution (cut along longitudinal section, showing only half of domain), and initial grain structure generated from randomly seeded nuclei, placed in a horizontal and transverse section.

field once it has reached a steady state (i.e. when the melt pool length is not changing anymore). The resulting grain structure evolution is illustrated in horizontal and transverse sections in Figure 15. As expected, a structure develops with elongated grains roughly oriented normal to the solidification front. The horizontal section also shows a slight tendency of favoring grains oriented following the welding direction, due to the shape of the melt pool tail. The solid-liquid interface formed by the grain envelopes remains located within the mushy zone (i.e. the region with a liquid fraction between zero and one).

Although qualitative, these results illustrate that our particle-based solidification solver can be integrated within any CFD solver. The entire coupled simulation took approximately 80 h to complete on 8 CPU cores of a standard desktop computer. Notably, during the peak in computational load (competitive re-growth in solidifying melt pool), nearly 25% of overall CPU time was consumed by the grain growth tracking algorithm, therefore not standing out as a severe bottleneck even in a non-optimized "proof-of-concept" simulation that did not rely on GPU acceleration.

5 Summary and Outlook

We presented an original approach for the modeling of solidification applicable at the scale of three-dimensional grain structures (i.e. microstructure representative volume

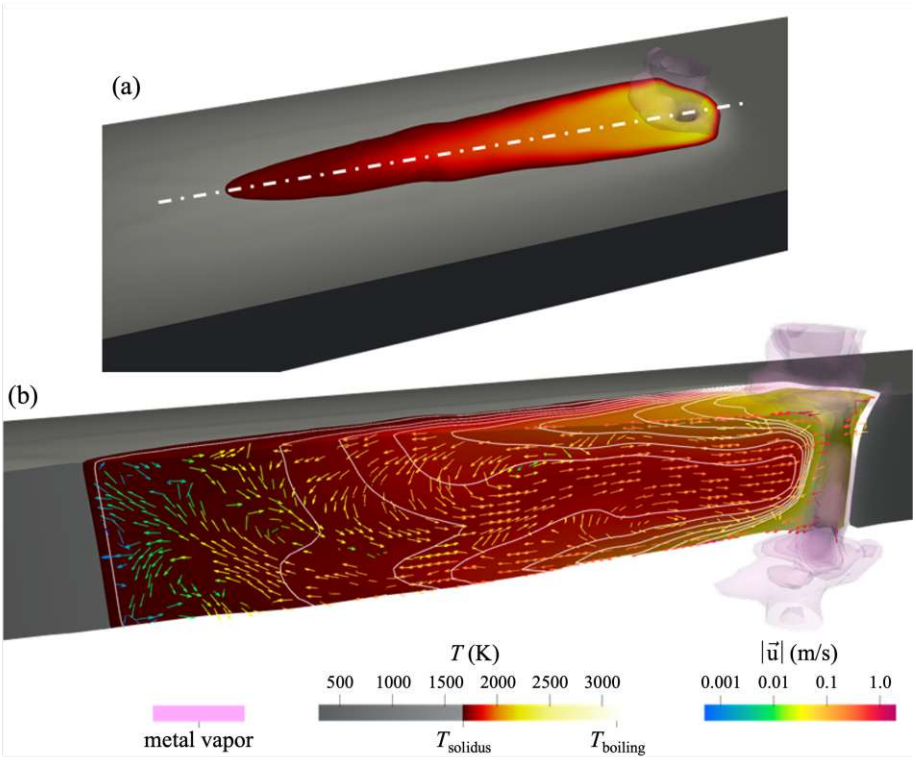

Figure 14: Top view (a) and longitudinal section (b) along the laser path (white dash-dotted line) during the welding simulation, showing temperature field as color map with contour lines at steps of 50 K between 1700 K and 2100 K, as well melt flow (arrows) and evaporated metal (translucent pink shading).

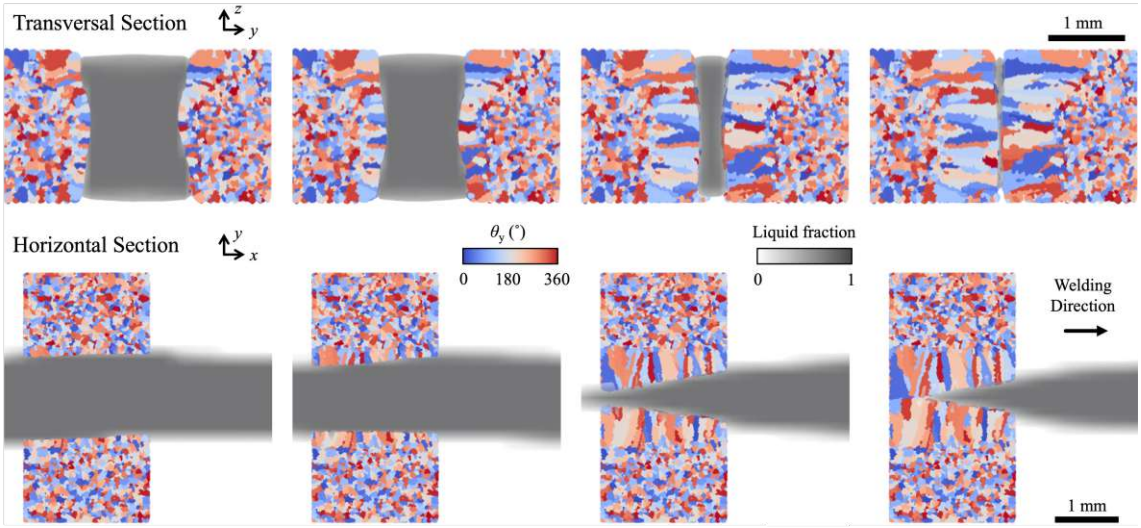

Figure 15: Transversal and horizontal sections at different times during solidification, showing grains (colored by orientation) and liquid metal (grayscale).

elements). In terms of underlying physics and assumptions, the model relies on classical equations common to state-of-the-art "mesoscale" models, in particular those considered for cellular automaton models.
The key novelty is the use of a grain envelope tracking scheme using a Lagrangian point-based discretization. The evolution of the tracking points is inspired by the self-similar hierarchical pattern of dendritic crystals. The computational task of nearest neighbor search for grain "collision" detection between particles in competitive growth scenarios (i.e. the formation of grain boundaries) is implemented in a way that leverages CPU/GPU-parallelization using C++ libraries, e.g. `OpenVDB`. The VDB data structure is hierarchically designed and provides $\mathcal{O}(1)$ random stencil data access [53], thus making it well suited for nearest neighbor search and collision detection of narrow band level sets (computationally challenging in competitive grain growth scenarios). Hence, we expect both one-way and two-way coupled solvers to be highly scalable [53, 54, 76], which will be fully addressed in a follow-up article. Hence, the approach is suitable for both small-scale scenarios encountered in laser-based manufacturing as well as large-scale scenarios such as ingot casting.
We validated the model against various benchmark cases, including single crystal growth where an analytical solution is available, two- and three-dimensional competitive grain growth scenarios, as well as columnar-to-equiaxed transition in three dimensions. Agreement with analytical, experimental, and numerical (CA) solutions is satisfactory. Finally, we illustrated the potential of the approach to be coupled with a multiphysics laser-processing simulation model. This last example showcases the straightforward inclusion of three-dimensional competitive grain growth in a thermo-fluid-mechanical model. It should be noted that the results of the particle-based approach – like these of a CA model – are strongly dependent on the choice of the underlying volume-averaged model, and on its appropriateness to tackle the problem at hand.
Ongoing and future work includes a thorough study of the approach scalability including massive parallelization of the tracking algorithm on large GPU architectures, which has shown promising results but remains to be quantified in a more systematic basis [54]. The most important extensions foreseen include the incorporation of the movement of solid grains, and/or solid-state microstructure evolution (e.g. grain growth or formation of secondary phases in the heat affected zone adjacent to a laser path). We expect the present approach to constitute a valuable alternative to existing models, hence applicable to large scale relevant to industrial cases (e.g., industrial parts manufactured by laser-based powder bed fusion).

CRediT authorship contribution statement

S. Mosbah: Conceptualization, Methodology, Software, Formal Analysis, Resources, Supervision, Writing- Original Draft. **R. Gómez Vázquez:** Methodology, Software, Validation, Formal Analysis, Investigation, Visualization, Writing - Original Draft. **C. Zenz:** Methodology, Software, Validation, Formal Analysis, Investigation, Visualization, Writing - Original Draft. **D. Tourret:** Formal Analysis, Visualization, Writing - Review & Editing. **A. Otto:** Supervision, Resources, Funding Acquisition, Writing - Review & Editing.

Data availability

Data will be made available on request.

Acknowledgements

The authors wish to thank Charles-André Gandin and Tomohiro Takaki for kindly providing data of their original simulations to compare with our results. This work was funded in part by the European Union Horizon 2020 research and innovation program under grant agreement number 825103. CZ was supported by TU Wien Doctoral School, within the Doctoral College DigiPhot. DT gratefully acknowledges support from the Spanish Ministry of Science through a Ramón y Cajal Fellowship (Ref. RYC2019-028233-I).

Appendix A Supplementary Data

A.1 Unidirectional solidification of an Al-Si alloy

Parameter	Symbol	Value	Unit
Domain size $\vec{e}_x$ direction	L_x	100	mm
Domain size $\vec{e}_y$ direction	L_y	5	mm
Domain size $\vec{e}_z$ direction	L_z	5	mm
Finite Volume cell size	$\Delta x = \Delta y = \Delta z$	1	mm
Microstructure length scale (SDAS)	λ_0	50	µm
Density	ρ	2600	$kg{\cdot}m^{-3}$
Thermal conductivity	κ	70	$J{\cdot}s^{-1}{\cdot}m^{-1}{\cdot}K^{-1}$
Dynamic viscosity	μ	0.001	$kg{\cdot}m{\cdot}s^{-1}$
Latent heat of fusion	ΔH_f	365384.62	$J{\cdot}kg^{-1}$
Melting temperature of pure Al	T_m	936.65	K
Liquidus slope	m_L	-6.5	K^{-1}
Initial concentration of Si	w_0	7.0	wt.%
Eutectic concentration of Si	w_{eut}	13.31	wt.%
Partition coefficient	k	0.13	–
Diffusion coefficient in liquid	D_l	$4.37{\cdot}10^{-9}$	$m^2{\cdot}s^{-1}$
Diffusion coefficient in solid	D_s	$10.0{\cdot}10^{-13}$	$m^2{\cdot}s^{-1}$
Initial nucleus position	$(r_{i,x}, r_{i,y}, r_{i,z})$	(0, 2.5, 2.5)	mm
Initial nucleus orientation	$(\psi_i, \theta_i, \varphi_i)$	(0, 0, 0,)	°
Lower boundary external temperature	T_{ext}	373.15	K
Lower boundary heat transfer coefficient	α	500	$W{\cdot}m^{-2}{\cdot}K^{-1}$
Initial temperature in domain	T_0	1073.15	K
Kinetic model coefficient	a	$2.9{\cdot}10^{-6}$	$m{\cdot}s^{-1}{\cdot}K^{-b}$
Kinetic model exponent	b	2.7	–
Time step	Δt	0.5	s

Table 1: Domain size, discretization, thermophysical properties, initial conditions, boundary conditions, kinetic model for the 1D Al-7wt.%Si solidification case (Section 3.2 of the main text).

A.2 Directional solidification of a quasi-2D thin sample

Parameter	Symbol	Value	Unit
Domain size $\vec{e}_x$ direction	L_x	4	mm
Domain size $\vec{e}_y$ direction	L_y	3	mm
Domain size $\vec{e}_z$ direction	L_z	400	µm
Finite Volume cell size	$\Delta x = \Delta y = \Delta z$	400	µm
Microstructure length scale (SDAS)	λ_0	192 ... 12	µm
Time step	Δt	0.1	s
Liquidus temperature	T_l	937.65	K
Solidus temperature	T_s	800.00	K
Initial temperature	T_0	938.65	K
Thermal gradient	∇T	1900	$K{\cdot}m^{-1}$
Pulling velocity	v_{pull}	86	$\mu m{\cdot}s^{-1}$
Cooling rate	dT/dt	-0.1634	$K{\cdot}s^{-1}$
Lower boundary temperature	T_{lower}	$937.65{+}t \cdot dT/dt$	K
Upper boundary temperature	T_{upper}	$952.85{+}t \cdot dT/dt$	K
Kinetic model coefficient 1	a_1	$8.26{\cdot}10^{-6}$	$m{\cdot}s^{-1}{\cdot}K^{-2}$
Kinetic model exponent 1	b_1	2	–
Kinetic model coefficient 2	a_2	$8.18{\cdot}10^{-5}$	$m{\cdot}s^{-1}{\cdot}K^{-3}$
Kinetic model exponent 2	b_2	3	–

Table 2: Domain size, discretization, thermophysical properties, initial conditions, boundary conditions, kinetic model for the 2D grain growth competition case (Section 3.3 of the main text).

A.3 Directional solidification of three-dimensional polycrystal

Parameter	Symbol	Value	Unit
Domain size $\vec{e}_x$ direction	L_x	768	µm
Domain size $\vec{e}_y$ direction	L_y	768	µm
Domain size $\vec{e}_z$ direction	L_z	13.824	mm
Finite Volume cell size	$\Delta x = \Delta y = \Delta z$	16	µm
Microstructure length scale (SDAS)	λ_0	24, 10	µm
Macro time step	Δt	0.001	s
Pulling velocity	v_{pull}	100	$\mu m{\cdot}s^{-1}$
Thermal gradient	G	10, 100	$K{\cdot}mm^{-1}$
Melting temperature of pure Al	T_m	933.25	K
Liquidus slope	m_L	-2.668	$K{\cdot}wt.\%^{-1}$
Initial concentration of Cu	w_0	3.01	wt.%
Partition coefficient	k	0.14	–
Gibbs-Thomson coefficient	Γ	$0.24{\cdot}10^{-6}$	K·m
Interface energy anisotropy strength	ε	0.02	–
Diffusion coefficient in liquid	D_l	$3.0{\cdot}10^{-9}$	$m^2{\cdot}s^{-1}$
Diffusion coefficient in solid	D_s	$3.0{\cdot}10^{-13}$	$m^2{\cdot}s^{-1}$
Kinetic model coefficient	a	$1.834{\cdot}10^{-4}$	$m{\cdot}s^{-1}{\cdot}K^{-b}$
Kinetic model exponent	b	2.282	–

Table 3: Domain size, discretization, thermophysical properties, initial conditions, boundary conditions, kinetic model for the 3D grain growth competition case (Section 3.4 of the main text)

A.4 Columnar-to-equiaxed transition in an Al-Si alloy

Parameter	Symbol	Value	Unit
Domain height $\vec{e}_z$ direction	L_z	173	mm
Domain diameter ($\vec{e}_x$-$\vec{e}_y$ direction	L_{xy}	70	mm
Number of Finite Volume cells $\vec{e}_z$	n_z	100	–
Number of Finite Volume cells $\vec{e}_x$-$\vec{e}_y$	$n_x = n_y$	15	–
Microstructure length scale (SDAS)	λ_0	250	µm
Density of Al	ρ_{Al}	Table 5	
Specific heat capacity	c_p	1070	$J{\cdot}kg^{-1}{\cdot}K^{-1}$
Thermal conductivity	κ	Table 6	
Dynamic viscosity	μ	0.001	$kg{\cdot}m{\cdot}s^{-1}$
Latent heat of fusion	ΔH_m	400844	$J{\cdot}kg^{-1}$
Melting temperature of pure Al	T_m	936.65	K
Liquidus slope	m_L	-6.5	$K{\cdot}wt.\%^{-1}$
Initial concentration of Si	w_0	7.0	wt.%
Eutectic concentration of Si	w_{eut}	13.32	wt.%
Density of Si	ρ_{Si}	2370	$kg{\cdot}m^{-3}$
Partition coefficient	k	0.13	–
Diffusion coefficient in liquid	D_l	$4.37{\cdot}10^{-9}$	$m^2{\cdot}s^{-1}$
Diffusion coefficient in solid	D_s	$10.0{\cdot}10^{-13}$	$m^2{\cdot}s^{-1}$
Nuclei density lower boundary	$\rho_{Nuc}(z=0)$	$5{\cdot}10^5$	m^{-2}
Nuclei density volume	$\rho_{Nuc}(z>0)$	$1{\cdot}10^9$	m^{-3}
Lower boundary external temperature	$T(z=0)$	Carrozzani et al. [33]	
Upper boundary heat flux (for $t \leq 900$ s)	Q	3000	$W{\cdot}m^{-2}$
Initial temperature in domain	T_0	1017.1	K
Kinetic model coefficient	a	$2.9{\cdot}10^{-6}$	$m{\cdot}s^{-1}{\cdot}K^{-b}$
Kinetic model exponent	b	2.7	–
Time step	Δt	0.5	s

Table 4: Domain size, discretization, thermophysical properties, initial conditions, boundary conditions, kinetic model for the 3D simulation of columnar-to-equiaxed transition in a cylindrical Al-Si ingot (Section 3.5 of the main text).

T (K)	850	850.15	855.15	860.15	865.15	...
ρ ($kg{\cdot}m^{-3}$)	2535	2456	2451	2444	2437	...
...	870.15	875.15	880.15	885.15	890	891.15
...	2428	2418	2406	2392	2375	2370

Table 5: Tabulated temperature-dependent values for density.

T (K)	573.15	673.15	773.15	823.15	850.15	855.15	860.15	...
κ ($J{\cdot}s^{-1}{\cdot}m^{-1}{\cdot}K^{-1}$)	170	165	155	145	102.04	99.38	96.34	...
...	865.15	870.15	875.15	880.15	885.15	890	891.15	1073.15
...	92.85	88.79	84.01	78.32	71.43	63.22	61	66

Table 6: Tabulated temperature-dependent values for thermal conductivity.

A.5 Melting test case

Parameter	Symbol	Value	Unit
Domain size $\vec{e}_x$ direction	L_x	1	mm
Domain size $\vec{e}_y$ direction	L_y	2	mm
Domain size $\vec{e}_z$ direction	L_z	0.1	mm
Finite Volume cell size	$\Delta x = \Delta y = \Delta z$	25	µm
Microstructure length scale (SDAS)	λ_0	10	µm
Liquidus temperature	T_l	1723.15	K
Solidus temperature	T_s	1673.15	K
Density	ρ	7873	$kg{\cdot}m^{-3}$
Specific heat capacity	c_p	450	$J{\cdot}kg^{-1}{\cdot}K^{-1}$
Thermal conductivity	κ	300	$J{\cdot}s^{-1}{\cdot}m^{-1}{\cdot}K^{-1}$
Latent heat of fusion	ΔH_m	1	$J{\cdot}kg^{-1}$
Initial temperature in domain	T_0	1674	K
Cooling rate	dT/dt	$2{\cdot}10^{4}$	$K{\cdot}s^{-1}$
Nuclei density	ρ_{Nuc}	$1{\cdot}10^{13}$	m^{-3}
Kinetic model coefficient 1	a_1	$8.315{\cdot}10^{-6}$	$m{\cdot}s^{-1}{\cdot}K^{-b_1}$
Kinetic model exponent 1	b_1	2.490	–
Kinetic model coefficient 2	a_2	$9.628{\cdot}10^{-7}$	$m{\cdot}s^{-1}{\cdot}K^{-b_2}$
Kinetic model exponent 2	b_2	3.622	–

Table 7: Domain size, discretization, thermophysical properties, initial conditions, boundary conditions, kinetic model for the quasi-2D remelting test case (Section 4.1 of the main text)

A.6 Laser beam welding of 316L stainless steel

Parameter	Symbol	Value	Unit
Domain width	L_y	6	mm
Domain length	L_x	40	mm
Domain height	L_z	4	mm
Finite Volume cell size	$\Delta x = \Delta y = \Delta z$	125	µm
Microstructure length scale (SDAS)	λ_0	20	µm
Steel sheet thickness	t_{sheet}	2	mm
Laser power	P	2.3	kW
Welding speed	$v_{welding}$	20	$mm{\cdot}s^{-1}$
Laser spot size	d_{Laser}	420	µm
Initial grain structure undercooling	ΔT_{init}	100	K
Initial nuclei density	$\rho_{Nuc,init}$	$5{\cdot}10^{12}$	m^{-3}
Kinetic model coefficient 1	a_1	$8.315{\cdot}10^{-6}$	$m{\cdot}s^{-1}{\cdot}K^{-b_1}$
Kinetic model exponent 1	b_1	2.490	–
Kinetic model coefficient 2	a_2	$9.628{\cdot}10^{-7}$	$m{\cdot}s^{-1}{\cdot}K^{-b_2}$
Kinetic model exponent 2	b_2	3.622	–
Liquidus temperature	T_l	1708	K
Solidus temperature	T_s	1675	K
Boiling temperature	T_b	3134	K
Latent heat of fusion	ΔH_m	$247.1{\cdot}10^{3}$	$J{\cdot}kg^{-1}$
Latent heat of vaporization	ΔH_v	$6.21{\cdot}10^{6}$	$J{\cdot}kg^{-1}$
Density (solid)	ρ_s	8000	$kg{\cdot}m^{-3}$
Density (liquid)	ρ_l	6936	$kg{\cdot}m^{-3}$

Table 8: Simulations parameters (growth kinetics coefficients, material parameters, process parameters, domain size and discretization) for the 3D welding case (Section 4.2 of the main text).

Parameter	Symbol	T(K)	Value	Unit
Specific heat capacity (solid)	$c_{p,s}$	300	483.5	$J{\cdot}kg^{-1}{\cdot}K^{-1}$
		1708	684.0	$J{\cdot}kg^{-1}{\cdot}K^{-1}$
Specific heat capacity (liquid)	$c_{p,l}$	–	800.0	$J{\cdot}kg^{-1}{\cdot}K^{-1}$
Thermal conductivity (solid)	κ_s	300	13.58	$W{\cdot}m^{-1}{\cdot}K^{-1}$
		1708	32.6	$W{\cdot}m^{-1}{\cdot}K^{-1}$
Thermal conductivity (liquid)	κ_l	1708	27	$W{\cdot}m^{-1}{\cdot}K^{-1}$
		3134	42	$W{\cdot}m^{-1}{\cdot}K^{-1}$
Surface energy (liquid)	γ_l	1708	1.802	$N{\cdot}m^{-1}$
	$d\gamma_l/dT$	–	$3.66{\cdot}10^{-4}$	$N{\cdot}m^{-1}{\cdot}K^{-1}$
Kinematic viscosity (liquid), Arrhenius pre-exponential factor	ν_0	–	$4.48{\cdot}10^{-8}$	$m^2{\cdot}s^{-1}$
Kinematic viscosity (liquid), Arrhenius activation energy	E_a	–	$45.5{\cdot}10^{-3}$	$J{\cdot}mol^{-1}$

Table 9: Temperature-dependent material properties for stainless steel 316L (linearly interpolated between data points).

References

[1] J. Allison, D. Backman, and L. Christodoulou. "Integrated computational materials engineering: a new paradigm for the global materials profession". In: *JOM* 58, 2006, pp. 25–27. DOI: https://doi.org/10.1007/s11837-006-0223-5.

[2] J. Panchal, S. Kalidindi, and D. McDowell. "Key computational modeling issues in integrated computational materials engineering". In: *Computer-Aided Design* 45, 2013, pp. 4–25. DOI: https://doi.org/10.1016/j.cad.2012.06.006.

[3] W. Wang, J. Li, W. Liu, and Z. Liu. "Integrated computational materials engineering for advanced materials: A brief review". In: *Computational Materials Science* 158, 2019, pp. 42–48. DOI: https://doi.org/10.1016/j.commatsci.2018.11.001.

[4] W. Xiong and G. Olson. "ybermaterials: materials by design and accelerated insertion of materials". In: *npj Computational Materials* 2, 2016, p. 15009. DOI: https://doi.org/10.1038/npjcompumats.2015.9.

[5] A. Karma and D. Tourret. "Atomistic to continuum modeling of solidification microstructures". In: *Current Opinion in Solid State and Materials Science* 20, 2016, pp. 25–36. DOI: https://doi.org/10.1016/j.cossms.2015.09.001.

[6] M. Rappaz. "Modeling and characterization of grain structures and defects in solidification". In: *Current Opinion in Solid State and Materials Science* 20, 2016, pp. 37–45. DOI: https://doi.org/10.1016/j.cossms.2015.07.002.

[7] W. Shao, J. Guevara-Vela, A. Fernández-Caballero, S. Liu, and J. LLorca. "Accurate prediction of the solid-state region of the Ni-Al phase diagram including configurational and vibrational entropy and magnetic effects". In: *Acta Materialia* 253, 2023, p. 118962. DOI: https://doi.org/10.1016/j.actamat.2023.118962.

[8] J. Hoyt, M. Asta, and A. Karma. "Atomistic and continuum modeling of dendritic solidification". In: *Materials Science and Engineering: R: Reports* 41, 2003, pp. 121–163. DOI: https://doi.org/10.1016/S0927-796X(03)00036-6.

[9] W. Boettinger, J. Warren, C. Beckermann, and A. Karma. "Phase-field simulation of solidification". In: *Annual Review of Materials Research* 32, 2003, pp. 163–194. DOI: https://doi.org/10.1146/annurev.matsci.32.101901.155803.

[10] N. Provatas and K. Elder. *Phase-field methods in materials science and engineering*. John Wiley & Sons, 2011.

[11] D. Tourret, H. Liu, and J. LLorca. "Phase-field modeling of microstructure evolution: Recent applications, perspectives and challenges". In: *Progress in Materials Science* 123, 2022, p. 100810. DOI: https://doi.org/10.1016/j.pmatsci.2021.100810.

[12] T. Shimokawabe, T. Aoki, T. Takaki, T. Endo, A. Yamanaka, N. Maruyama, A. Nukada, and S. Matsuoka. "Peta-scale phase-field simulation for dendritic solidification on the TSUBAME 2.0 supercomputer". In: *Proceedings of 2011 International Conference for High Performance Computing, Networking, Storage and Analysis*. 2011, pp. 1–11.

[13] J. Hötzer, A. Reiter, H. Hierl, P. Steinmetz, M. Selzer, and B. Nestler. "The parallel multi-physics phase-field framework Pace3D". In: *Journal of Computational Science* 26, 2018, pp. 1–12. DOI: https://doi.org/10.1016/j.jocs.2018.02.011.

[14] S.Sakane, T. Takaki, and T. Aoki. "Parallel-GPU-accelerated adaptive mesh refinement for three-dimensional phase-field simulation of dendritic growth during solidification of binary alloy". In: *Materials Theory* 6, 2022, p. 3. DOI: https://doi.org/10.1186/s41313-021-00033-5.

[15] M. Greenwood, K. Shampur, N. Ofori-Opoku, T. Pinomaa, L. Wang, S. Gurevich, and N. Provatas. "Quantitative 3D phase field modelling of solidification using next-generation adaptive mesh refinement". In: *Computational Materials Science* 142, 2018, pp. 153–171. DOI: https://doi.org/10.1016/j.commatsci.2017.09.029.

[16] W. Feng, P. Yu, S. Hu, Z. Liu, Q. Du, and L. Chen. "Spectral implementation of an adaptive moving mesh method for phase-field equations". In: *Journal of Computational Physics* 220, 2006, pp. 498–510. DOI: https://doi.org/10.1016/j.jcp.2006.07.013.

[17] L. Chen and J. Shen. "Applications of semi-implicit Fourier-spectral method to phase field equations". In: *Computer Physics Communications* 108, 1998, pp. 147–158. DOI: https://doi.org/10.1016/S0010-4655(97)00115-X.

[18] J. Zhu, L.-Q. Chen, J. Shen, and V. Tikare. "Coarsening kinetics from a variable mobility Cahn–Hilliard equation: Application of a semi-implicit Fourier spectral method". In: *Physical Review E* 60, 1999, p. 3564. DOI: https://doi.org/10.1103/PhysRevE.60.3564.

[19] A. Boccardo, M. Tong, S. Leen, D. Tourret, and J. Segurado. "Efficiency and accuracy of GPU-parallelized Fourier spectral methods for solving phase-field models". In: *Computational Materials Science* 228, 2023, p. 112313. DOI: https://doi.org/10.1016/j.commatsci.2023.112313.

[20] J. Ni and C. Beckermann. "A volume-averaged two-phase model for transport phenomena during solidification". In: *Metallurgical Transactions B* 22, 1991, pp. 349–361. DOI: https://doi.org/10.1007/BF02651234.

[21] C. Wang and C. Beckermann. "A multiphase solute diffusion model for dendritic alloy solidification". In: *Metallurgical and Materials Transactions A* 24, 1993, pp. 2787–2802. DOI: https://doi.org/10.1007/BF02659502.

[22] H. Combeau, M. Založnik, S. Hans, and P. Richy. "Prediction of macrosegregation in steel ingots: Influence of the motion and the morphology of equiaxed grains". In: *Metallurgical and Materials Transactions B* 40, 2009, pp. 289–304. DOI: https://doi.org/10.1007/s11663-008-9178-y.

[23] J. Li, M. Wu, A. Ludwig, and A. Kharicha. "Simulation of macrosegregation in a 2.45-ton steel ingot using a three-phase mixed columnar-equiaxed model". In: *International Journal of Heat and Mass Transfer* 72, 2014, pp. 668–679. DOI: https://doi.org/10.1016/j.ijheatmasstransfer.2013.08.079.

[24] D. Tourret and A. Karma. "Three-dimensional dendritic needle network model for alloy solidification". In: *Acta Materialia* 120, 2016, pp. 240–254. DOI: https://doi.org/10.1016/j.actamat.2016.08.041.

[25] T. Isensee and D. Tourret. "Convective effects on columnar dendritic solidification–A multiscale dendritic needle network study". In: *Acta Materialia* 234, 2022, p. 118035. DOI: https://doi.org/10.1016/j.actamat.2022.118035.

[26] I. Steinbach, C. Beckermann, B. Kauerauf, Q. Li, and J. Guo. "Three-dimensional modeling of equiaxed dendritic growth on a mesoscopic scale". In: *Acta Materialia*, 1999, pp. 971–982. DOI: https://doi.org/10.1016/S1359-6454(98)00380-2.

[27] Y. Souhar, V. D. Felice, C. Beckermann, H. Combeau, and M. Založnik. "Three-dimensional mesoscopic modeling of equiaxed dendritic solidification of a binary alloy". In: *Computational Materials Science* 112, 2016, pp. 304–317. DOI: https://doi.org/10.1016/j.commatsci.2015.10.028.

[28] T. Rodgers, J. Madison, and V. Tikare. "Simulation of metal additive manufacturing microstructures using kinetic Monte Carlo". In: *Computational Materials Science* 135, 2017, pp. 78–89. DOI: https://doi.org/10.1016/j.commatsci.2017.03.053.

[29] A. Chadwick and P. Voorhees. "The development of grain structure during additive manufacturing". In: *Acta Materialia* 211, 2021, p. 116862. DOI: https://doi.org/10.1016/j.actamat.2021.116862.

[30] C.-A. Gandin and M. Rappaz. "A coupled finite element-cellular automaton model for the prediction of dendritic grain structures in solidification processes". In: *Acta Metallurgica et Materialia* 42, 1994, pp. 2233–2246. DOI: https://doi.org/10.1016/0956-7151(94)90302-6.

[31] C.-A. Gandin and M. Rappaz. "A 3D Cellular Automaton algorithm for the prediction of dendritic grain growth". In: *Acta Materialia* 45, 1997, pp. 2187–2195. DOI: https://doi.org/10.1016/S1359-6454(96)00303-5.

[32] H. Takatani, C.-A. Gandin, and M. Rappaz. "EBSD Characterisation and Modeling of Columnar Dendritic Grains Growing in the Presence of Fluid Flow". In: *Acta Materialia* 48, 2000, pp. 675–688. DOI: https://doi.org/10.1016/S1359-6454(99)00413-9.

[33] T. Carozzani, H. Digonnet, and C.-A. Gandin. "3D CAFE modeling of grain structures: application to primary dendritic and secondary eutectic solidification". In: *Modelling and Simulation in Materials Science and Engineering* 20, 2012, p. 015010. DOI: https://doi.org/10.1088/0965-0393/20/1/015010.

[34] T. Carozzani, C.-A. Gandin, H. Digonnet, M. Bellet, K. Zaidat, and Y. Fautrelle. "Direct simulation of a solidification benchmark experiment". In: *Metallurgical and Materials Transactions A* 44, 2013, pp. 873–887. DOI: https://doi.org/10.1007/s11661-012-1465-1.

[35] S. Chen, G. Guillemot, and C.-A. Gandin. "Three-dimensional cellular automaton-finite element modeling of solidification grain structures for arc-welding processes". In: *Acta Materialia* 115, 2016, pp. 448–467. DOI: https://doi.org/10.1016/j.actamat.2016.05.011.

[36] A. Rai, M. Markl, and C. Körner. "A coupled Cellular Automaton–Lattice Boltzmann model for grain structure simulation during additive manufacturing". In: *Computational Materials Science* 124, 2016, pp. 37–48. DOI: https://doi.org/10.1016/j.commatsci.2016.07.005.

[37] A. Pineau, G. Guillemot, D. Tourret, A. Karma, and C.-A. Gandin. "Growth competition between columnar dendritic grains–Cellular automaton versus phase field modeling". In: *Acta Materialia* 155, 2018, pp. 286–301. DOI: https://doi.org/10.1016/j.actamat.2018.05.032.

[38] J. A. Dantzig and M. Rappaz. *Solidification*. EPFL press, 2009.

[39] W. Kurz, D. Fisher, and M. Rappaz. *Fundamentals of solidification (5th edition)*. EPFL press, 2023.

[40] L. Gránásy, G. Tóth, J. Warren, F. Podmaniczky, G. Tegze, L. Rátkai, and T. Pusztai. "Phase-field modeling of crystal nucleation in undercooled liquids – A review". In: *Progress in Materials Science* 106, 2019, p. 100569. DOI: https://doi.org/10.1016/j.pmatsci.2019.05.002.

[41] S. Elahi, R. Tavakoli, I. Romero, and D. Tourret. "Grain growth competition during melt pool solidification — Comparing phase-field and cellular automaton models". In: *Computational Materials Science* 216, 2023, p. 111882. DOI: https://doi.org/10.1016/j.commatsci.2022.111882.

[42] W. Kurz, B. Giovanola, and R. Trivedi. "Theory of microstructural development during rapid solidification". In: *Acta Metallurgica* 34, 1986, pp. 823–830. DOI: https://doi.org/10.1016/0001-6160(86)90056-8.

[43] M. Rappaz, S. David, J. Vitek, and L. Boatner. "Analysis of solidification microstructures in Fe-Ni-Cr single-crystal welds". In: *Metallurgical Transactions A* 21, 1990, pp. 1767–1782. DOI: https://doi.org/10.1007/BF02672593.

[44] G. P. Ivantsov. "Temperature field around a spherical, cylindrical, and needle-shaped crystal, growing in a pre-cooled melt". In: *Doklady, Akademiya Nauk SSR* 58, 1947, pp. 567–569.

[45] M. Bobadilla, J. Lacaze, and G. Lesoult. "Influence des conditions de solidification sur le déroulement de la solidification des aciers inoxydables austénitiques". In: *Journal of Crystal Growth* 89, 1988, pp. 531–544. DOI: https://doi.org/10.1016/0022-0248(88)90216-3.

[46] M. Rappaz and W. Boettinger. "On dendritic solidification of multicomponent alloys with unequal liquid diffusion coefficients". In: *Acta Materialia* 47, 19999, pp. 3205–3219. DOI: https://doi.org/10.1016/S1359-6454(99)00188-3.

[47] H. Combeau, M. Bellet, Y. Fautrelle, D. Gobin, E. Arquis, O. Budenkova, B. Dussoubs, Y. D. Terrail, A. Kumar, C.-A. Gandin, B. Goyeau, S. Mosbah, T. Quatravaux, M. Rady, and M. Založnik. "Analysis of a numerical benchmark for columnar solidification of binary alloys". In: *IOP Conference Series: Materials Science and Engineering* 33, 2012, p. 012086. DOI: https://doi.org/10.1088/1757-899X/33/1/012086.

[48] V. Voller and C. Prakash. "A fixed grid numerical modelling methodology for convection-diffusion mushy region phase-change problems". In: *International Journal of Heat and Mass Transfer* 30, 1987, pp. 1709–1719. DOI: https://doi.org/10.1016/0017-9310(87)90317-6.

[49] C.-A. Gandin, S. Mosbah, T. Volkmann, and D. Herlach. "Experimental and numerical modeling of equiaxed solidification in metallic alloys". In: *Acta Materialia* 56, 2008, pp. 3023–3035. DOI: https://doi.org/10.1016/j.actamat.2008.02.041.

[50] D. Tourret, C.-A. Gandin, T. Volkmann, and D. Herlach. "Multiple non-equilibrium phase transformations: Modeling versus electro-magnetic levitation experiment". In: *Acta Materialia* 59, 2011, pp. 4665–4677. DOI: https://doi.org/10.1016/j.actamat.2011.04.013.

[51] C. Zenz, M. Buttazzoni, T. Florian, K. E. Crespo Armijos, R. Gómez Vázquez, G. Liedl, and A. Otto. "A compressible multiphase Mass-of-Fluid model for the simulation of laser-based manufacturing processes". In: *Computers & Fluids* 268, 2024, p. 106109. DOI: https://doi.org/10.1016/j.compfluid.2023.106109.

[52] H. Jasak, A. Jemcov, and Z. Tukovic. "OpenFOAM: A C++ library for complex physics simulations". In: *International workshop on coupled methods in numerical dynamics*. Vol. 1000. 2007, pp. 1–20.

[53] K. Museth. "VDB: High-Resolution Sparse Volumes with Dynamic Topology". In: *ACM Transactions on Graphics* 32, 2012, pp. 1–22. DOI: https://doi.org/10.1145/2487228.2487235.

[54] D. B. Cañás. “Evaluación del potencial de aceleración de un código profesional de simulación de estructuras de solidificación en aleaciones metálicas por medio de paralelización en CPU y/o GPU”. MA thesis. Universidade da Coruña, 2024.

[55] J. Langer. “Instabilities and pattern formation in crystal growth”. In: *Reviews of Modern Physics* 52, 1980, p. 1. DOI: https://doi.org/10.1103/RevModPhys.52.1.

[56] H. Esaka. “Dendrite growth and spacing in succinonitrile-acetone alloys”. PhD thesis. Ecole Polytechnique Fédérale de Lausanne, 1986.

[57] E. Dorari, K. Ji, G. Guillemot, C.-A. Gandin, and A. Karma. “Growth competition between columnar dendritic grains–The role of microstructural length scales”. In: *Acta Materialia* 223, 2022, p. 117395. DOI: https://doi.org/10.1016/j.actamat.2021.117395.

[58] T. Takaki, S. Sakane, M. Ohno, Y. Shibuta, T. Aoki, and C.-A. Gandin. “Competitive grain growth during directional solidification of a polycrystalline binary alloy: Three-dimensional large-scale phase-field study”. In: *Materialia* 1, 2018, pp. 104–113. DOI: https://doi.org/10.1016/j.mtla.2018.05.002.

[59] D. Tourret and A. Karma. “Growth competition of columnar dendritic grains: A phase-field study”. In: *Acta Materialia* 82, 2015, pp. 64–83. DOI: https://doi.org/10.1016/j.actamat.2014.08.049.

[60] D. Tourret, Y. Song, A. Clarke, and A. Karma. “Grain growth competition during thin-sample directional solidification of dendritic microstructures: A phase-field study”. In: *Acta Materialia* 122, 2017, pp. 220–235. DOI: https://doi.org/10.1016/j.actamat.2016.09.055.

[61] S. Akamatsu and T. Ihle. “Similarity law for the tilt angle of dendrites in directional solidification of non-axially-oriented crystals”. In: *Physical Review E* 56, 1997, p. 4479. DOI: https://doi.org/10.1103/PhysRevE.56.4479.

[62] J. Deschamps, M. Georgelin, and A. Pocheau. “Growth directions of microstructures in directional solidification of crystalline materials”. In: *Physical Review E* 78, 2008, p. 011605. DOI: https://doi.org/10.1103/PhysRevE.78.011605.

[63] Y. Song, F. Mota, D. Tourret, K. Ji, B. Billia, R. Trivedi, N. Bergeon, and A. Karma. “Cell invasion during competitive growth of polycrystalline solidification patterns”. In: *Nature Communications* 14, 2023, p. 2244. DOI: https://doi.org/10.1038/s41467-023-37458-0.

[64] T. Takaki, M. Ohno, Y. Shibuta, S. Sakane, T. Shimokawabe, and T. Aoki. “Two-dimensional phase-field study of competitive grain growth during directional solidification of polycrystalline binary alloy”. In: *Journal of Crystal Growth* 442, 2016, pp. 14–24. DOI: https://doi.org/10.1016/j.jcrysgro.2016.01.036.

[65] C.-A. Gandin. “Experimental Study of the Transition from Constrained to Unconstrained Growth during Directional Solidification”. In: *ISIJ International* 40, 2000, pp. 971–979. DOI: https://doi.org/10.2355/isijinternational.40.971.

[66] A. Otto, R. Gómez Vázquez, U. Hartel, and S. Mosbah. "Numerical analysis of process dynamics in laser welding of Al and Cu". In: *Procedia CIRP* 74, 2018, pp. 691–695. DOI: https://doi.org/10.1016/j.procir.2018.08.040.

[67] A. Otto and R. Gómez Vázquez. "Fluid dynamical simulation of high speed micro welding". In: *Journal of Laser Applications* 30, 2018, p. 032411. DOI: https://doi.org/10.2351/1.5040652.

[68] R. Gómez Vázquez, H. Koch, and A. Otto. "Multi-physical simulation of laser welding". In: *Physics Procedia* 56, 2014, pp. 1334–1342. DOI: https://doi.org/10.1016/j.phpro.2014.08.059.

[69] M. Buttazzoni, C. Zenz, A. Otto, R. Gómez Vázquez, G. Liedl, and J. L. Arias. "A Numerical Investigation of the Laser Beam Welding of Stainless Steel Sheets with a Gap". In: *Applied Sciences* 11, 2021, p. 2549. DOI: https://doi.org/10.3390/app11062549.

[70] C. Zenz, M. Buttazzoni, M. Martínez Ceniceros, R. Gómez Vázquez, J. R. Blasco Puchades, L. Portolés Griñán, and A. Otto. "Simulation-based process optimization of laser-based powder bed fusion by means of beam shaping". In: *Additive Manufacturing* 77, 2023, p. 103793. DOI: https://doi.org/10.1016/j.addma.2023.103793.

[71] E. Beyer. *Schweißen mit Laser*. Springer, 1995.

[72] H. Wie, J. Elmer, and T. DebRoy. "Crystal growth during keyhole mode laser welding". In: *Acta Materialia* 133, 2017, pp. 10–20. DOI: https://doi.org/10.1016/j.actamat.2017.04.074.

[73] A. Artinov, V. Karkhin, X. Meng, M. Bachmann, and M. Rethmeier. "A General Analytical Solution for Two-Dimensional Columnar Crystal Growth during Laser Beam Welding of Thin Steel Sheets". In: *Applied Sciences* 13, 2023, p. 6249. DOI: https://doi.org/10.3390/app13106249.

[74] Y. Miyata, M. Okugawa, Y. Koizumi, and T. Nakano. "Inverse columnar-equiaxed transition (CET) in 304 and 316L stainless steels melt by electron beam for additive manufacturing (AM)". In: *Crystals* 11, 2021, p. 856. DOI: https://doi.org/10.3390/cryst11080856.

[75] Z. Yang, A. Bauereiß, M. Markl, and C. Körner. "Modeling laser beam absorption of metal alloys at high temperatures for selective laser melting". In: *Advanced Engineering Materials* 23, 2021, p. 2100137. DOI: https:/doi.org/10.1002/adem.202100137.

[76] K. Museth. "NanoVDB: A GPU-friendly and portable VDB data structure for real-time rendering and simulation". In: *ACM SIGGRAPH 2021 Talks*. 2021, pp. 1–2. DOI: https://doi.org/10.1145/3450623.3464653.

A critical comparison of one- and two-fluid approaches for the simulation of laser-induced melt pool formation and vaporisation

Constantin Zenz[a,1,*], Peter S. Cook[b,1,*], Laszlo Vörös[a], Andreas Otto[a]

[a]Institute of Production Engineering and Photonic Technologies, TU Wien, Getreidemarkt 9, 1060, Vienna, Austria

[b]CSIRO Manufacturing, Private Bag 10, Clayton, VIC 3169, Australia

[1]These authors contributed equally to the work

[*]Corresponding authors

This version of the article has been accepted for publication, after peer review, but is not the Version of Record. The Version of Record is available online at: https://doi.org/10.1007/s43939-025-00434-0

Abstract: Physics-based simulations are routinely used to understand and optimize laser-based metal additive manufacturing processes. Across the wide range of model predictive capabilities and computational costs, a lack in understanding of the implications of model choice for simulation accuracy persists. We present the first detailed comparison of results between a leading commercial one-fluid model and an advanced two-fluid model. Only condensed matter is included in the one-fluid model domain, with gas effects being incorporated as phenomenological equations. The two-fluid model directly couples gaseous and condensed phases. Solving both analytical benchmarks and increasingly complex cases of laser heating, melting and evaporation, the two approaches are systematically compared. Finally, both models' predictions are compared to experimental data for keyhole development. Model differences become visible even at moderate laser intensities, when only a mild vapor depression occurs. The main sources of divergence are the evaporative mass flux and resulting recoil pressure, and surface tension-driven contact angles at the three-phase line. Reducing the evaporative recoil factor in the one-fluid model by 70% gave the best match to experiment in a deep keyhole scenario. However, such one-fluid calibrations must be repeated when process conditions alter, so their applicability to more complex scenarios remains unclear. On the other hand, the greater predictive capabilities of two-fluid models come with a factor of 10 increase in computational cost. This work provides guidance on the implications of model choice for AM simulations and presents groundwork for the development of multi-fidelity models for more complex scenarios.

Keywords: Laser material processing; additive manufacturing; multiphase modelling; melt pool; vaporisation; CFD

1 Introduction

Laser-assisted manufacturing of metals encompasses a broad range of processes, due to the versatility of the laser tool itself, including conduction- and keyhole mode welding, additive manufacturing (AM) via powder bed fusion or powder- or wire-based directed energy deposition, cutting, surface texturing or bending, among many more. The market for laser material processing, especially for AM, is growing rapidly across various industrial sectors [1]. Most laser-based manufacturing processes involve local melting and evaporation of solid material, with the melt pool behaviour being influenced by many physical phenomena which are nonlinear and coupled. This makes the task of accurate yet efficient modelling very challenging. Even in conduction mode welding or AM scenarios not involving a keyhole, it has been shown that convection-driven phenomena inside the melt pool must be included to obtain accurate three-dimensional melt pool shapes and correct thermal history predictions [2]. Naturally, the problem becomes even more difficult if the incident laser energy density is sufficiently high that vaporisation becomes non-negligible, leading to the onset of a vapour depression and consequently an unstable or metastable keyhole (deep vapour depression of high depth-to-width ratio). Hence, considerable effort has been made to derive suitable simulation models for melt pool formation and evolution.
These approaches are often categorized by the type of discretization scheme used to solve the underlying equations, such as the Finite Volume Method [3] or Finite Element Method [4], usually in combination with an interface capturing method such as the Volume-of-Fluid (VoF) Method [5], or the Level Set method [6, 7]. Other frameworks use the Lattice Boltzmann method [8] or mesh-free approaches such as Smoothed Particle Hydrodynamics [9], or coupled mesh-based and mesh-free approaches particularly suited for processes involving powder, such as coupled VoF-DEM [10]. However, as the chosen discretization method should only be a tool to solve the underlying equations, a more reasonable classification of melt pool modelling approaches is to examine what physical phenomena and assumptions are incorporated in a given framework. With respect to melt pool modelling at the scale of an individual scan track, the main difference between available models is whether gas phases are included within the domain, and whether a distinction between different gas phases (i.e., ambient gas and metal vapor) is made. Furthermore, most differences between models arise from the treatment of vaporisation and the induced recoil pressure. Here a key model characteristic is whether actual mass (or volume) is transferred during evaporation and condensation (also called interface-resolved evaporation models) or none is exchanged (unresolved or phenomenological models) Furthermore, some models include heat loss due to radiation, while others do not. Nearly all published models assume the liquid metal flow to be laminar, which seems to be a reasonable consideration as we discuss later, and the gas flow is also assumed to be laminar within most modelling frameworks.
Most published models have excluded the gaseous phase from the simulation domain and accounted for its effect on condensed matter via boundary conditions. The commercial software FLOW-3D is one of the most widely used frameworks in this category. Example applications of FLOW-3D include the work of Wang et al., who studied pore formation in selective laser melting of a titanium alloy through combin-

ing in situ x-ray observations and simulation [11] and implemented a new evaporation model in FLOW-3D's phenomenological recoil pressure formulation to improve the prediction of keyhole instabilities under stationary illumination [3]. The development of lack-of-fusion defects has been analysed in multi-layer FLOW-3D studies of powder bed fusion [12] and electron beam melting [13]. Other FLOW-3D melt pool simulations have correlated temperature histories with subsequent microstructure [14] and investigated the effects of particle morphology and powder bed depth [15]. Many other software packages have been used to study melt pool CFD and make similar model assumptions for heat transfer, phase change, surface tension and species diffusion to FLOW-3D, most commonly ALE3D, Ansys Fluent, ESI ACE+, COMSOL, in-house codes based on OpenFOAM (refer summary in [16]) and more recently TruchasPBF [17, 18]. Like FLOW-3D, recoil pressure is explicitly calculated and imposed on the liquid's free surface as a boundary condition rather than solving the gas flow.

Many modelling approaches that include the gas phase have been implemented using the Finite Volume C++ library OpenFOAM. One example is the model of Parivendhan et al. [19], which incorporates the coupling between gaseous phases within the domain by imposing phenomenological recoil pressure and heat loss contributions. No actual mass or energy transfer is applied between phases during evaporation or condensation and the authors argue that, although underpredicting vapour velocities compared to higher fidelity approaches, the computational effort can be greatly decreased this way. However, the benefit of including the vapour phase is then not obvious compared to models such as FLOW-3D, where the liquid-gas interface is a boundary and the vapour phase movement is not solved. Other frameworks including the gas phase are the models published by Flint et al. [20–22], who added some features such as selective evaporation and component diffusion, or Yu and Zhao [10], who incorporate a new evaporation model which considers the Knudsen layer to more accurately predict the explicitly calculated recoil pressure term. Flint et al. [23] further extended their framework, employing an interface-resolved evaporation model by implicitly including the recoil pressure through actual expansion of the mass transferred to the gas phase during evaporation, with a local volume dilation term that allows for gas phase compressibility and obviates the need to explicitly calculate recoil pressure. Another recent contribution to interface-resolved evaporation models for laser material processing is the work of Schreter-Fleischhacker et al. [24]. Flint et al. elaborate in [22] that the phenomenological recoil pressure adopted by most studies for its lower computational demand will fail to correctly predict destabilization of a thermocapillary under evaporation- and condensation-driven conditions. Therefore, it is expected that with greater keyhole depth-to-width ratio (e.g., going from selective laser melting towards deep penetration welding), the error induced by applying a phenomenological recoil pressure model will increase, and more in-depth modelling approaches such as that of [23] will be required to avoid needing to re-calibrate recoil for each distinct process regime [25]. The modelling approach recently presented by Zenz et al. [26] resolves both condensed and gaseous phases, treating both as compressible fluids, and transferring mass between phases during phase change. Due to the large difference in density between liquid and gas, this mass transfer is accompanied by a volumetric expansion of the newly created vapour which produces a

recoil pressure. With this method, neither a phenomenological recoil pressure source term nor an evaporation efficiency is needed. The pressure differential with respect to saturation pressure is the controlling factor in the mass transfer rate, and local pressure increase at the evaporation site automatically limits the rate. Consequently, even highly dynamic scenarios such as deep penetration copper welding with different beam shapes can be accurately simulated without process-specific calibration [27]. While approaches such as those of [23] or [26] possess strong predictive capabilities, especially with respect to highly dynamic, evaporation-driven phenomena, they come with the downside of greatly increased computational costs. In practice, it is not clear how all these different modelling approaches compare in terms of accuracy and speed, and which is best suited to a given scenario.

This study aims to compare approaches with and without a vapour phase by applying two of the above-described models, FLOW-3D and the Mass-of-Fluid model of Zenz et al. [26], to a series of well-defined test cases of increasing complexity. A preliminary comparison of similar type was presented by Flint, Parivendhan et al. [28], showing strong differences between phenomenological recoil pressure models and interface-resolved evaporation models. Mayi et al. [29] followed a systematic methodology when they compared Level Set and Arbitrary Lagrangian-Eulerian techniques for front tracking. However, to the best knowledge of the authors, no comprehensive investigation of this type which compares one- and two-fluid approaches for simulating laser melting has yet been published. Therefore, care is taken to ensure to present test cases in sufficient detail to allow reproduction by researchers who wish to benchmark their own models. By increasing case complexity one feature at a time, the goal is to identify regimes where these two very different approaches still deliver essentially identical results, and where they begin to differ. Finally, the two models are benchmarked against a well-known experiment to directly evaluate and compare the accuracy of each approach, while ensuring identical simulation setups to avoid any ambiguity.

2 Modelling Frameworks

In this section we set out the physical equations commonly employed in laser welding and LPBF simulations of the melting and vaporisation behaviour of metals. The differences between the implementations used for one-fluid and two-fluid models are highlighted. By ‘one-fluid’ we refer to models which include only the condensed matter (melt and solid), although an allowance for mass and enthalpy loss by evaporation may be made. Models which explicitly include the vapour phase are termed here ‘two-fluid’ to emphasize the resolution of at least two distinct fluid phases and may include multiple vapour species such as the ambient atmosphere and evaporated metal. Our aim is to examine where the equations required for these two approaches differ. For brevity, the equations in some areas of commonality are just referenced rather than described in detail.

2.1 Common assumptions

Virtually all published simulations have made some simplifying approximations:

- All phases move at a common velocity, termed $\boldsymbol{u}$ here, and locally share a common temperature, T, and pressure, p (i.e., the assumption of a homogeneous equilibrium mixture).
- Solid and liquid phases are usually treated as incompressible. Rare exceptions are the work of Flint et al. [23], where the vapour phase is treated as locally compressible at the liquid-vapour interface, and the work of Zenz et al. [26], where all phases are treated as compressible.
- Flow in the melt and the vapour phase is usually treated as laminar. Turbulence has only rarely been included due to the additional computational time and complexity and is also omitted in the current work. Full melt pool turbulence calculations, e.g. by RANS, have been mostly limited to welding [30] and directed energy deposition [31] processes since turbulence is less common in the smaller melt pools created by laser powder bed fusion [32, 33]. Empirical enhancements of melt viscosity and thermal conductivity to better match measured track cross sections have sometimes been applied instead [34]. Simulations of vapour turbulence during AM have only begun to appear recently, examining interactions between the vapour plume, shielding gas flow, entrained particles and the laser beam [35, 36].
- The viscosity of fluid phases is usually, and throughout this work, treated as Newtonian.

2.2 Continuity equation and interface movement

Movement of the free surface between the melt pool and vapour is closely linked to mass conservation. We start with the standard equation for mass continuity:

$$\frac{\partial \rho}{\partial t} + \nabla \cdot (\rho \boldsymbol{u}) = S_M \tag{1}$$

where ρ is the overall mass density of the mixture of phases, and S_M represents any mass sources. Usually, S_M is zero due to mass conservation, except at domain boundaries where mass may be added as wire or powder in additive manufacturing processes or lost by evaporation in one-fluid models. For two-fluid scenarios, we can introduce a mass concentration ρ_i for each of the N phases i, leading to

$$\frac{\partial \rho_i}{\partial t} + \nabla \cdot (\rho_i \boldsymbol{u}) = S_{Mi} \tag{2}$$

with $\sum \rho_i = \rho$. Here, S_{Mi} is a mass source for phase i, and $S_{Mi} = -S_{Mj}$ for mass sources associated with phase change for a phase pair i, j, such as the liquid and gaseous phase of an evaporating or condensing material. It often proves convenient to introduce phase volume fractions, α_i, which satisfy $\sum \alpha_i = 1$. Then, for mixtures of incompressible phases we have $\rho_i = \alpha_i \langle \rho_i \rangle$, where $\langle \rho_i \rangle$ is the thermodynamic density of phase i, i.e., the density of the pure phase at the same temperature and pressure. In one-fluid models, the evolution of the free surface is tracked by a dimensionless

marker or colour function, F, which is identical to the volume fraction of condensed matter, α_c. Assuming incompressibility, Eq. (1) then simplifies to:

$$\frac{\partial F}{\partial t} + \nabla \cdot (F\boldsymbol{u}) = \dot{F} \tag{3}$$

The melt mass loss by evaporation, expressed in terms of change in volume fraction, $\dot{F}$, is often omitted because the associated melt volume reduction is much smaller than other sources of free surface movement (the recoil effect of escaping vapour is usually applied separately in the momentum equation, as explained below). A prominent class of models using the above formulation is the so-called Volume-of-Fluid (VoF) method, as used here in FLOW-3D. A less common alternative to VoF is the Level Set method, for which distance-to-surface rather than volume fraction is propagated. Examples range from keyhole welding [37] to an adaptive finite element mesh for powder bed fusion [38]. Level Set methods have been shown to be more accurate in their treatment of surface tension with combined VoF-LS schemes being particularly promising [39], as demonstrated by Heeling et al. [40]. Yet another scheme for front-tracking is ALE (Arbitrary Lagrangian-Eulerian) in which the mesh adapts to follow the interface. Mayi et al. [29] conducted a systematic and detailed comparison of LS vs ALE for LPBF benchmark cases.

In two-fluid models, Eq. (3) is usually replaced by a set of N advection equations of identical structure for each volume fraction i. Alternatively, Eq. (2) may be directly solved, like in the Mass-of-Fluid (MOF) method employed in this work. Average thermophysical properties ϕ of the mixture, such as thermal conductivity or viscosity, are then usually obtained via $\phi = \sum \alpha_i \phi_i$.

Within each timestep of the transient analysis, Eq. (3) (or its two-fluid equivalent, e.g. (2) is typically solved in a segregated fashion by first updating F for a fixed velocity field and then solving for velocity using the (newly updated) fixed F. Numerical diffusion can pose a challenge when solving advection equations such as Eq. (2) or (3), causing the conserved quantity to be spuriously smeared out by an amount depending on the alignment of $\boldsymbol{u}$ with the computational grid. Depending on the numerical method employed to solve the above equations, various methods have been developed to counteract numerical diffusion. A simple example of such an interface sharpening method is adding an artificial term, $\boldsymbol{u}_c = c_\alpha \frac{\nabla \alpha_i}{|\nabla \alpha_i|}(\alpha_i(1-\alpha_i)\boldsymbol{u})$, to the velocity field in Eq. (2) (or (3)) which points towards the bulk of phase i and is only active at the interface. The constant c_α is used to set the amount of interface sharpening, with a trade-off between smearing reduction and spurious induced interface movement. Another numerical challenge arises because the low density of the vapour phase means that evaporation usually creates a large velocity in the vapour adjacent to the interface. Much of the numerical difficulty in the two-fluid models stems from the need to handle this evaporative volume expansion while simultaneously ensuring $\sum \alpha_i = 1$. Many two-fluid modelling approaches ignore the effect of evaporation on gaseous matter. More comprehensive approaches, where the effect of evaporation on the vapour side is incorporated, include the work of Flint et al. [23] and Zenz et al. [26].

2.3 Momentum equation

The momentum conservation equation for laser applications has a general form applicable to both one- and two-fluid approaches:

$$\frac{\partial(\rho \boldsymbol{u})}{\partial t} + \nabla \cdot (\rho \boldsymbol{u}\boldsymbol{u}) = -\nabla p + \nabla \cdot \boldsymbol{\tau} + \boldsymbol{S}_B + \boldsymbol{S}_D + \boldsymbol{S}_S + \boldsymbol{S}_R \tag{4}$$

where $\boldsymbol{u}$, p, ρ and $\boldsymbol{\tau}$ denote velocity, pressure, density and the viscous stress tensor of the mixture, respectively. The remaining terms $\boldsymbol{S}_B$, $\boldsymbol{S}_D$, $\boldsymbol{S}_S$ and $\boldsymbol{S}_R$ are momentum sources due to buoyancy, mushy zone drag, surface tension and evaporative recoil, as explained shortly. Two-fluid methods need to approximate effective material properties (e.g. density and viscosity) in cells containing a liquid-vapour interface, usually just a simple average weighted by volume fraction (cf. the preceding subsection). One-fluid models do not require such averaging, but on the other hand need a conservative scheme to adjust cell volumes and areas according to the local filled fraction F. The resultant errors in both methods should approach zero with cell refinement. The buoyancy force associated with fluid density variations and the Darcy drag force on melt next to a solidified boundary create momentum sources $\boldsymbol{S}_B$ and $\boldsymbol{S}_D$ respectively. These are volumetric sources which are calculated in the same way for one- and two-fluid models, as described in many references [16]. Differences between one- and two-fluid approaches arise from the handling of the momentum sources $\boldsymbol{S}_S$ and $\boldsymbol{S}_R$ produced by surface tension and evaporative recoil. In general, a momentum source at a liquid-vapour interface can either be applied as a surface flux (force per unit area, $\boldsymbol{F}$) or as an equivalent volumetric source $\boldsymbol{S}$. The conversion is usually done by the Continuum Surface Force (CSF) approximation of Brackbill et al. [41]. They treat the interface as a band across which some 'colour' marker (e.g. phase fraction α) varies from 0 to 1 and density ρ varies continuously from ρ_c to ρ_g, leading to the following widely-used formulation to obtain a volumetric source:

$$\boldsymbol{S} = \boldsymbol{F}|\nabla \alpha_c| \frac{2\rho}{\rho_c + \rho_g} \tag{5}$$

Note that the phase gradient spreads the force over the interface cells and also creates the required units conversion. Also, the density ratio tends to concentrate the force in cells containing a higher liquid fraction so minimises spurious acceleration of the gaseous phase. In practice, depending on the specific nature of $\boldsymbol{F}$ and other factors, the density weighting term is sometimes omitted, and alternative formulations to $|\nabla \alpha_c|$ are often used. Furthermore, these terms must be calculated on a discretised domain which entails a degree of approximation. With typically only 1 – 3 cells across the interface thickness to limit computation time, developing numerical schemes which are simultaneously stable, conservative and geometrically correct is a challenging task.

Using the CSF method, the volumetric momentum source created by surface tension between a single phase-pair (e.g., condensed and non-condensed matter) can, for example, be written as:

$$\boldsymbol{S}_S = \left((\sigma \kappa \hat{\boldsymbol{n}}) + \frac{d\sigma}{dT}(\nabla T - \hat{\boldsymbol{n}}(\hat{\boldsymbol{n}} \cdot \nabla T)) \right) |\nabla \alpha_c| \frac{2\rho}{\rho_c + \rho_g} \tag{6}$$

The force terms inside the brackets comprise the component normal to the surface, proportional to curvature, κ, and the Marangoni component acting tangentially to the surface in the direction of the temperature gradient. Here, it is assumed that the value of surface tension at the interface, σ, is already known and only dependent on temperature, and $\hat{\boldsymbol{n}}$ is a unit vector normal to this interface. In the more general scenario of multiple phase pairs, $\boldsymbol{S}_S$ is calculated as a sum of terms of the form of Eq. (6) for each phase-pair, as outlined in [26] or [42]. The surface tension at the interface of phase pair i, j can be calculated as $\sigma_{i,j} = \sigma_i + \sigma_j - 2\sqrt{\sigma_i \sigma_j}$, where σ_i is the surface energy of phase i [43]. The one-fluid implementation of Eq. (6) is slightly simpler since the phase gradient becomes ∇F and the average value of the density ratio in Eq. (5) is F. In fact, rather than a volumetric source, most one-fluid models instead apply the force terms within the brackets as a boundary flux, $\boldsymbol{F}_S$.
The last term, $\boldsymbol{S}_R$, in Eq. (4) is the force exerted by escaping vapour on the liquid surface, usually termed recoil pressure. In a one-fluid model, it must be applied by a phenomenological equation since the local vapour conditions are not determined. The contributions of evaporation and condensation are combined, with a coefficient of 0.54 usually adopted, derived for a vacuum but said to be still a good approximation at higher pressures [44]. Following this assumption, a pressure p_R due to evaporative recoil is calculated as:

$$p_R = 0.54 \cdot p_{amb} \cdot \exp\left(L \, \frac{T - T_b}{R T T_b}\right) \tag{7}$$

Many one-fluid models, including the current work, apply Eq. (7) directly as a pressure boundary condition, since the liquid-vapour interface is the domain boundary and the pressure condition is otherwise treated as zero. Others adopt the alternative of adding a volumetric source $\boldsymbol{S}_R$ in Eq. (4) which is calculated from p_R via the CSF approximation as:

$$\boldsymbol{S}_R = p_R \hat{\boldsymbol{n}} |\nabla \alpha_c| \frac{2\rho}{\rho_c + \rho_g} \tag{8}$$

In two-fluid models, an explicit recoil term is not required because mass transfer between two phases of different densities (liquid and vapour in Eq. (2)) is accompanied by a large change in volume which creates a pressure change. However, many two-fluid models [10, 19] still rely on the phenomenological Eq. (8) and omit applying actual mass transfer between different phases to enhance computational speed and numerical stability, at the cost of a loss of predictive power of the model. In the two-fluid model employed within this work, $\boldsymbol{S}_R$ is set to zero, and the mass transfer between liquid and vapour phases during evaporation and condensation is calculated to account for the respective source terms in Eq. (2).
To calculate the mass flux, we start with the Clausius-Clapeyron relation for saturation vapour pressure:

$$p_{sat}(T) = p_{ref} \cdot \exp\left(\frac{ML}{T_b R}\left(1 - \frac{T_b}{T}\right)\right) \tag{9}$$

with T_b, L, M and R denoting the material's boiling temperature, effective latent heat of vaporisation, molar mass and the universal gas constant, respectively. The reference pressure condition, p_{ref}, is usually one atmosphere. In a two-fluid model,

an evaporative mass flux between a liquid-vapour phase pair l, v can be calculated based on the difference between local pressure, p, and saturation pressure, p_{sat}, as:

$$S_{mv,e} = -S_{Ml,e} = (p_{sat} - p)\sqrt{\frac{M}{2\pi RT}}\frac{\varepsilon_e}{\xi}\forall(p_{sat} > p) \tag{10}$$

In Eq. (10), ξ denotes the thickness of the liquid-vapour interface, which is usually of the order of the grid spacing, and (analogously to Brackbill et al.'s CSF formulation) serves to yield a volumetric mass flux from a mass flux per surface area. The evaporation efficiency coefficient, $[\varepsilon_e$, can be used to calibrate the evaporation mass flux, but is taken as $\varepsilon_e = 1$ in the here-employed two-fluid model. Analogously, a condensation mass flux can be calculated as:

$$S_{mv,c} = -S_{Ml,c} = (p_{sat} - p)\sqrt{\frac{M}{2\pi RT}}\frac{\varepsilon_c}{\xi}\forall(p_{sat} < p) \tag{11}$$

In the current study, we set $\varepsilon_c = \alpha_c$ to promote condensation in the vicinity of condensed matter, and to limit spontaneous condensation (as homogeneous nucleation would require substantially more subcooling than heterogeneous nucleation). The appropriate mass flux arising from Eqs. (10) and (11) is then applied in Eq. (2) for two-fluid models.

One-fluid models combine the effects of evaporation and condensation into a single 'evaporation coefficient' whose accurate calculation is complex [45] but in most published simulations, like here, is given a value of 0.82 [16]. Then the nett evaporative mass flux becomes

$$S_{Mv} = 0.82(p_{sat} - p)\sqrt{\frac{M}{2\pi RT}}\forall(p_{sat} > p) \tag{12}$$

When saturation pressure is less than the ambient pressure p, a mass flux of zero is assumed. The equation is broadly similar to the two-fluid versions but with the important distinction that ambient pressure is a fixed value rather than varying with the local evaporation rate. Actually, one-fluid models rarely add the evaporative mass flux to the continuity Eq. (1) since the cumulative increment of the melt surface is less than one computational cell. Also, the associated recoil force is applied separately via Eq. (7). However, the mass flux does figure in the energy equation as explained in the next section.

To numerically solve the above-described set of equations, variants of the PISO (Pressure Implicit with Splitting of Operators) algorithm are commonly employed, in which a pressure correction equation is formulated using Eqs. (1) and (4). This pressure correction equation is then solved iteratively together with the momentum Eq. (4) in each time step of the transient problem, producing a solution for $\boldsymbol{u}$ and p which fulfils both Eq. (1) and Eq. (4). Details of the numerical solution algorithm vary greatly with the specific choice of modelling approach and are therefore not further elaborated here.

2.4 Energy conservation equation

Conservation of energy can be expressed as:

$$\frac{\partial \rho h}{\partial t} + \nabla \cdot (\boldsymbol{u}\rho h) = \nabla \cdot (k\nabla T) + S_H \tag{13}$$

Here, h and k denote the specific energy and thermal conductivity of the mixture of phases in a two-fluid model, or of the single fluid in a one-fluid model. The source term S_H contains energy input from the laser source and, depending on the specific model and its assumptions, also heat loss due to radiation, evaporation and convective cooling. Viscous heating is insignificant and usually neglected.
In two-fluid models, a problem arises from the usual assumption of all mixture phases locally sharing a common temperature. Heat conduction is a temperature gradient-driven process, but in a two-fluid scenario, an energy gradient cannot be straightforwardly converted into a temperature gradient, e.g., an energy gradient across an isothermal phase change front should not lead to heat conduction. One viable approach to overcome this issue is to decouple heat conduction from all remaining terms of Eq. (13) and employ a so-called 'temperature recovery' method [46]. Then, in a two-fluid model, Eq. (13) becomes:

$$\frac{\partial \rho_i h_i}{\partial t} + \nabla \cdot (\boldsymbol{u} \rho_i h_i) = S_{Hi} \tag{14}$$

$$\frac{\partial \rho c_p T}{\partial t} = \nabla \cdot (k \nabla T) \tag{15}$$

Here, Eq. (14) encompasses convective transport of energy for each phase i together with any heat sources, whereas heat conduction within the mixture of phases (all sharing a common temperature, T) is accounted for through Eq. (15). During the transient numerical solution procedure, Eq. (14) is usually solved at the same stage as Eq. (2). A new temperature distribution is then calculated from the given distribution of $\rho_i h_i$ ("recovering" temperature) and is updated at a later stage by solving Eq. (15). Then, h_i is again updated via $h_i = c_{p,i} T$, with $c_{p,i}$ denoting the specific heat capacity of phase i, whereas c_p in Eq. (15) denotes the specific heat capacity of the mixture. Note that S_{Hi} in Eq. (14) includes any energy transfers associated with mass transfer from one phase to another. As an example, in the case of evaporation, the vapour phase, denoted by subscript v, receives the heat source $S_{Hv,e} = S_{Mv,e} h_l$ (and the liquid phase loses the same amount). Note that the specific energy of the liquid phase, denoted by subscript l, is used to calculate the amount of heat transferred with a given mass flux from liquid to vapour. As the energy of liquid and vapour differ by the latent heat, a lower temperature is calculated in the temperature recovery step after a net mass flux towards the vapour phase, i.e. evaporative cooling occurs. In one-fluid models (or those two-fluid models omitting mass transfers and relying on phenomenological evaporation and recoil pressure equations [19]), an evaporative heat loss contribution to the sources S_H in Eq. (13) is made. It is simply the product of the latent heat of evaporation and the mass flux given by Eq. (12):

$$S_{H,e} = L S_{Mv} \tag{16}$$

In two-fluid models, melting and solidification can be handled in the same way as evaporation and condensation, by formulating source terms similar to Eqs. (10) and (11). An example is provided in [47], where non-equilibrium solidification is incorporated in this way. One-fluid models usually employ a solid fraction-temperature relationship (such as the Lever Rule) to determine the volume fraction of solid when needed, such as for updating $\boldsymbol{S}_D$. They incorporate the latent heat of solidification in

the specific energy h, ramping the increment over the solidus-liquidus range as done here in FLOW-3D. Some two-fluid models adopt this one-phase approach to incorporate melting and solidification, and only employ a two-fluid approach to distinguish between condensed matter and vapour [23].

2.5 Laser treatment

Energy absorbed by the material is described by the heat source term S_H in Eq. (13), or S_{Hi} in Eq. (14) for two-fluid models. Depending on the model type and numerical implementation, the source can be applied as a surface heat flux in the form of a boundary condition (for one-fluid models) or as a volumetric heat flux (for two-fluid models). Most published simulations assume the input laser energy exhibits a Gaussian intensity distribution. Adopting cylindrical coordinates and denoting the normal distance to the optical axis of the laser beam as r, and the distance to the focus position along the optical axis as z, a Gaussian intensity distribution $I(r, z)$ can be written as:

$$I(r,z) = I_0 \left(\frac{w_0}{w(z)}\right)^2 \exp\left(\frac{-2r^2}{w(z)^2}\right) \tag{17}$$

In Eq. (17), w is the radius of the laser beam and the subscript 0 denotes values at the focus position, i.e., at $r = 0, z = 0$. Given an input laser power and material absorptivity (i.e., the fraction of incident laser energy absorbed by the material and transformed into heat), a volumetric or surface heat flux can be obtained. Rather than a constant value of absorptivity, the Fresnel Eqs. (18) to (22) can be used to calculate an angle-of-incidence dependent absorptivity, which becomes especially important once a vapour depression or keyhole forms. With β being the local angle of incidence between the laser beam and the illuminated surface, and n_r, κ_r being the refractive index and extinction coefficient of the material, the fraction of absorbed laser energy, A, can be calculated as [48]:

$$A_S = 1 - \frac{a^2 + b^2 - 2a\cos(\beta) + \cos^2(\beta)}{a^2 + b^2 + 2a\cos(\beta) + \cos^2(\beta)} \tag{18}$$

$$A_P = 1 - \frac{a^2 + b^2 - 2(a(n_r^2 - \kappa_r^2) + 2bn_r\kappa_r)\cos(\beta) + (n_r^2 + \kappa_r^2)^2\cos^2(\beta)}{a^2 + b^2 + 2(a(n_r^2 - \kappa_r^2) + 2bn_r\kappa_r)\cos(\beta) + (n_r^2 + \kappa_r^2)^2\cos^2(\beta)} \tag{19}$$

$$a^2 = \frac{1}{2}\left(\sqrt{(n_r^2 - \kappa_r^2 - \sin^2(\beta)) + 4n_r^2\kappa_r^2} + n_r^2 - \kappa_r^2 - \sin^2(\beta)\right) \tag{20}$$

$$b^2 = \frac{1}{2}\left(\sqrt{(n_r^2 - \kappa_r^2 - \sin^2(\beta)) + 4n_r^2\kappa_r^2} - \left(n_r^2 - \kappa_r^2 - \sin^2(\beta)\right)\right) \tag{21}$$

$$A = \frac{A_S + A_P}{2} \tag{22}$$

Furthermore, most models use a ray tracing algorithm to calculate subsequent multiple reflections on the walls of the keyhole, to capture the associated increase in absorbed laser energy. While two-fluid models are capable of calculating laser beam attenuation within the vapour plume, or subsequent plasma ignition and plasma shielding [49], the vapour phases are assumed to be fully transparent to laser light throughout this work to enable the one-fluid comparison.

3 Methodology of investigation

To compare one-fluid and two-fluid approaches, we chose a leading solver from each category. The one-fluid models employed the commercial solver FLOW-3D®WELD[1]. This is a finite difference code which has been used for more than 100 studies of laser welding and laser powder bed fusion. It is normally employed, as here, with an additional WELD module which allows laser multiple reflections, Fresnel absorption, beam caustics, etc. The two-fluid code selected is an extension of the open source OpenFOAM code [50], starting from the VoF solver `multiphaseInterFoam`. It uses a segregated finite volume solution with extensive capabilities, at the forefront of the field, which are described in detail elsewhere [26].
We first applied both solvers to a typical scenario of a laser melting a track across a metal substrate (Section 4). By progressively introducing the key physical features of melting, Marangoni stress, evaporation, multiple laser reflections and angle-dependent (Fresnel) reflection, we sought to identify the sources of any differences in results. We then modelled the case of keyhole development with a stationary laser (Section 5). This case was chosen for both the computational challenges, pushing each solver to the limits of capability, and for the availability of experimental data, enabling the absolute accuracy of each solution approach to be determined. Furthermore, this direct comparison provided the unprecedented opportunity of setting up both solvers with (as far as possible) identical computational grid, boundary conditions, material properties and laser parameters.

3.1 Verification against analytic benchmarks

As will be apparent from the results presented in Sections 4 and 5, the two modelling approaches lead to different results, and the deviations naturally increase with the number and complexity of the contributing physical phenomena. To rule out any fundamental problems with either solver, initial verification tests were first conducted on two cases which have an analytical solution. To check the melt-solidification and thermal accuracy, we simulated a one-dimensional phase change problem (i.e., a Stefan problem). This is a widely used benchmark for problems involving phase change, which can also be used for liquid-vapor interfaces [51]. To verify Marangoni convection, crucial in laser melting, we simulated a standard test case of thermocapillary flow in a cavity.

3.1.1 Phase change verification

We simulated a metal slab undergoing a transition from solid to liquid for the idealised Stefan case of no liquid flow (constant density, same value for liquid and solid) and one-dimensional melting. Physically, we imagine a box filled with solid metal at a uniform temperature T_c for which the wall at $x = 0$ is suddenly heated to a temperature T_h above the melting point T_m. If the hot wall temperature is fixed and the other walls are adiabatic, the location of the melt front $X(t)$ can be determined analytically. The solution is somewhat complex [52] but depends just on

[1]Version 3.0.0.3.4; 2022; `https://www.flow3d.com`; Flow Science, Inc.

the material's thermal properties (refer Table 6) and the three temperatures described above. First, we determine the dimensionless Stefan numbers within the liquid and solid regions:

$$St_L = \frac{c_p(T_h - T_m)}{L} \tag{23}$$

$$St_S = \frac{c_p(T_m - T_c)}{L} \tag{24}$$

Then we solve for λ in Eq. (25), where erf is the error function:

$$\frac{St_L}{\mathrm{erf}(\lambda)} - \frac{St_S}{(1 - \mathrm{erf}(\lambda))} = \lambda \exp(\lambda^2)\sqrt{\pi} \tag{25}$$

Finally, the melt front location is given by:

$$X(t) = 2\lambda\sqrt{\alpha t} \tag{26}$$

where α is the thermal diffusivity, $k/(\rho c_p)$. For the chosen parameters, the analytic solution for the melt front location is $X(t) = 0.001255\sqrt{t}$.
The FLOW-3D and OpenFOAM simulations were set up with the parameters listed in Table 6. They used the same timestep size (fixed at 1.0e-7 secs) and identical 1D domains with 12.5 µm computational cells in the x-direction. The domain length was made sufficiently long, 10 mm, that the far boundary remained at T_c throughout the analyses, to ensure consistency with the adiabatic assumption of the analytic solution. Analyses were run for a period of 1.0 s.
Figure 1 compares the solver results to the analytic solution. There is excellent agreement, with the solver differences to analytic (Figure 1 (b)) being much less than the 12.5 µm cell size. This indicates that the phase transition treatment in both solvers is physically correct. Regular oscillations are visible in the difference results for both solvers whose period matches the time for the melt front to progress from one cell to the next. These fluctuations represent the error from approximating a linear variation of temperature across each cell when interpolating the melt front location. In the OpenFOAM solution, a drift can be observed over time, which likely stems from accumulated errors introduced by decoupling energy transfer associated with phase changes from that due to thermal conduction (cf. the preceding section). However, as the overall error stays within approx. 1/10 cell size, we argue it is insignificant.

3.1.2 Marangoni convection verification

The second verification case tests the accuracy of simulation of the Marangoni effect, since this is a major driver of the fluid flow in the melt pool during AM. Sen and Davis [53] derived an analytical solution for steady-state thermocapillary flow in a simple geometry. They considered an incompressible liquid in a two-dimensional rectangular cavity (i.e. infinite in the third dimension) which is heated at the left wall so that a lateral temperature gradient develops. The top surface of the liquid is free, so the temperature variation along that gas-liquid interface generates liquid flow by the Marangoni effect, which in turn causes a deflection of the free surface.

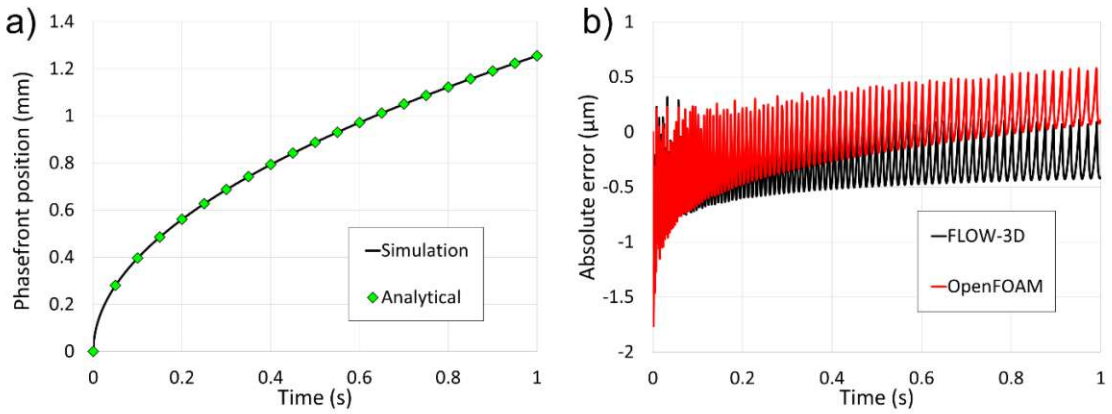

Figure 1: Comparison of numerical and analytic values of melt location for Stefan phase transition case, showing (a) absolute values obtained from both simulation models and from the analytical solution; and (b) absolute difference between analytical solution and results obtained with the respective solvers. As the absolute difference between the FLOW-3D and OpenFOAM results are in the sub-µm range, both simulation results are merged into one curve in the plot in (a).

Sen and Davis determined the asymptotic liquid surface profiles in the limit of a very small liquid aspect ratio A, where A is the depth to width ratio. They calculated the normalised depth $h(x)$ of the liquid as a function of normalised location x, where x varies from -0.5 at the left wall to 0.5 at the right wall. If a contact angle θ is prescribed at each wall, then:

$$h(x) = 1 - \frac{AC_n}{16}\left[x(4x^2 - 3) + \frac{4}{3}m(12x^2 - 1)\right] \tag{27}$$

The parameter C_n is a normalised capillary number:

$$C_n = \frac{\partial\sigma}{\partial T}\frac{(T_h - T_c)}{\sigma_r A^3} \tag{28}$$

where T_h and T_c are the fixed hot and cold wall temperatures, σ_r is the surface tension at a reference temperature T_r (mean of T_h and T_c) and $\frac{\partial\sigma}{\partial T}$ is evaluated at T_r. The parameter m in Eq. (27) defines the wall contact angle θ:

$$\tan\left(\theta - \frac{1}{2}\pi\right) = mA^2C_n \tag{29}$$

The test case conditions are detailed in Table 7, including the derived parameters C_n and m. The cavity was modelled as a 400 mm by 1000 mm rectangle with an initial liquid height of 200 mm and a uniform computational grid of square cells. The left and right wall temperatures were fixed to the values indicated in Table 7. Steady state results were obtained by running transient analyses until stationary surface profiles were attained.

The expected height of the liquid surface calculated from Eq. (27) is 187.5 mm at the left wall and 212.5 mm at the right wall, so the deflection magnitude is 12.5 mm at both walls. An example of the simulation results at steady state (Figure 2 (a)) shows the left-to-right temperature gradient, the liquid circulation pattern and the sloping

top surface. Figure 2 (b) compares the deflection magnitudes predicted by the two solvers at each wall with the analytic result. To check for mesh convergence, analyses were run with four cell sizes, with the finest mesh requiring several days. Both solvers tend to slightly under-estimate the amount of deflection but approach the analytic solution as grid size is reduced, with OpenFOAM being a little more accurate. The errors are of comparable size to those reported in previous simulations of this case, such as Saldi [54] (deflections 13 and 8 mm), Yamamoto et al.[39] (deflections 11 and 11 mm) and Flint et al. [20] (deflections 13 and 10 mm).

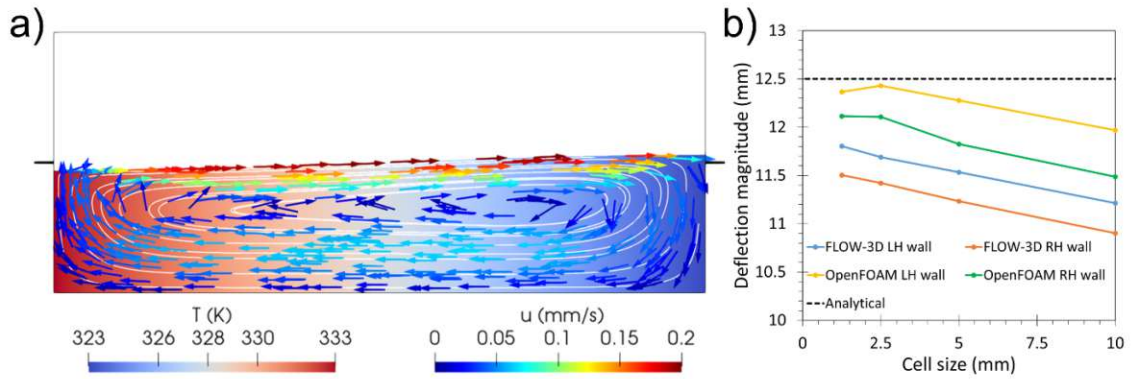

Figure 2: Marangoni verification results showing (a) typical simulation result with temperature contour and velocity vectors coloured by velocity magnitude; and (b) comparison of predicted deflection magnitudes to analytical solution for both solvers at different grid resolutions.

4 Laser Track Model Comparison

4.1 Model setup

To allow a direct comparison between the one- and two-fluid models employed, test cases of a single laser track were set up identically in both software packages. The scenario comprised a rectangular sample of a simplified material, resembling AISI 304L stainless steel, which was illuminated by a moving laser spot at normal incidence with Gaussian intensity distribution and constant power. The domain and sample geometry, as well as the computational grid, are displayed in Figure 3. The domain, spanning 1 x 1.4 x 3 mm^3, was initialized as solid metal, except for the top 100 µm where an ambient atmosphere was present. The domain was discretized using cubic cells of 50 µm side length, with two levels of mesh refinement in the region of interest, down to the finest cells of 12.5 µm side length covering the central 2.3 x 0.3 mm^2 plane in the upper 0.2 mm of the domain. The gas boundaries of the domain were assigned an inlet-outlet condition, with any inflow set to a temperature of 298.15 K and a pressure of 1 bar. The remaining (solid) boundaries were treated as adiabatic. Initial checks were conducted on a larger domain which confirmed that the adopted domain size was sufficient that the choice of boundary conditions did not affect the melt pool results. Radiative heat loss was not applied in the models as it is currently not implemented in the OpenFOAM solver used. In any case, separate testing with

FLOW-3D (Appendix A) shows that radiation constitutes only a very minor fraction of surface heat loss so its omission is inconsequential to the aims of the investigation. Most material properties (Table 8) were chosen to be constant for easier reproducibility, exceptions being surface tension, to allow Marangoni forces, and gas densities. Simulations without a Fresnel angular dependence used a constant material absorptivity A of 0.32, equal to the Fresnel value at normal incidence. Linear laser scan tracks of 2 mm length along the $\vec{e}_Z$-direction (cf. Figure 3) were performed with the laser parameters listed in Table 1. The laser powers used were 30, 120, 300 or 500 W, depending on the particular test case.

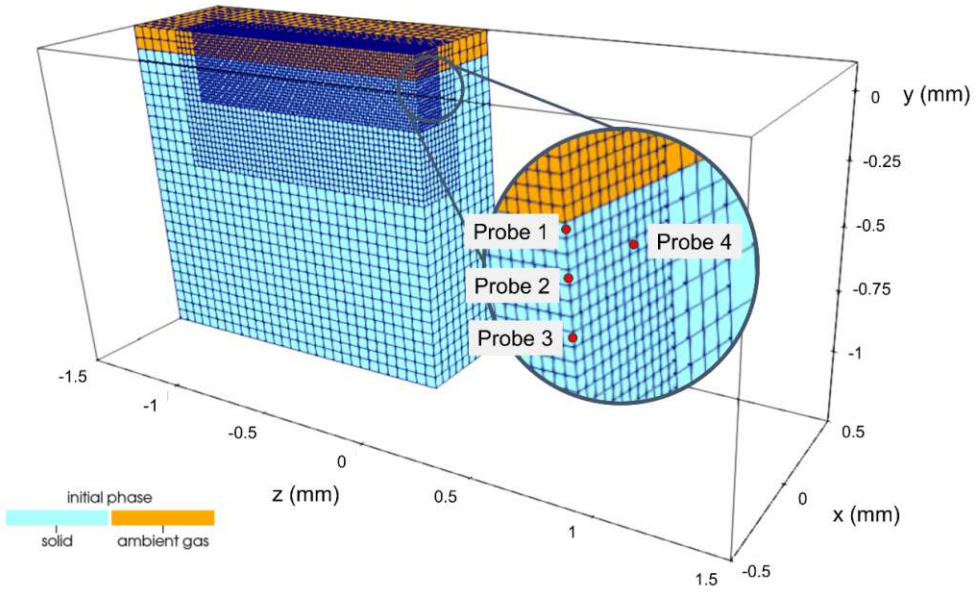

Figure 3: Computational domain used for laser track comparison simulations. Mesh and initial phase distribution are shown for a quarter of domain. The four probes (cf. Table 2) are located at the centre of the respective cells marked with red dots.

Parameter		Value	Unit
Wavelength	λ	$1070{\cdot}10^{-9}$	m
Intensity distribution	–	Gaussian	–
Spot diameter at focus	D	$176{\cdot}10^{-6}$	m
Power	P	variable	W
Beam quality factor	M^2	1	–
Focus position	v_L	0.75	$\mathrm{m{\cdot}s^{-1}}$

Table 1: Laser parameters used in laser track comparison simulations.

Probe number	Description	Coordinates x, y, z (µm)
1	Center at top of melt pool	6.25, -6.25, -6.25
2	Center within melt pool	6.25, -43.75, -6.25
3	Center underneath melt pool	6.25, -93.75, -6.25
4	Beside melt pool	93.75, -43.75, -6.25

Table 2: Locations of temperature probes. The description is only applicable for cases with sufficient melt pool size.

To enable quantitative comparisons of the temperature evolution, results were extracted at the four probe locations listed in Table 2. Care was taken to position the probes precisely at cell centers to avoid any interpolation errors, since this is where variables are solved in both software packages. For reference, note that the location $(0, 0, 0)$ corresponds to the center of the sample top surface in the xz-plane. To better understand where differences in the two solver approaches arise, physical processes were introduced to the model one by one. Starting from the simplest case of laser heating with no melt, we progressively added melting/solidification, Marangoni stirring, vaporisation heat loss and recoil, multiple laser reflections and (finally) Fresnel reflection behaviour. At each stage, we compared the solver results. It would be impractical and repetitive to show pictures of all the laser track results. Instead, to provide some overall context, Figure 4 shows some pictures of the track geometry and temperature distributions for the final model which includes all the processes. It illustrates the key features common to most laser tracks, e.g. the hot spot at laser incidence, the melt pool depression, the solidified profile behind and slight humping on either side of the track. It also demonstrates that the two solvers give broadly similar results, but differing in detail as we now explore.

4.2 Pure conduction laser heating and melting

For the first set of analyses, we set all momentum sources (buoyancy, Marangoni, evaporation) to zero to enable solver comparisons for the simplest scenario of no melt or gas flow. Heat losses from the metal top surface by convection and radiation were also switched off. The only active processes were thus thermal conduction and phase change by melting/solidification. At a laser power of 30 W, the peak temperature is less than 900 °C and no melt pool is formed. In these conditions, the OpenFOAM and FLOW-3D temperature traces are virtually indistinguishable (Figure 5). When laser power is increased to 120 W (Figure 6), a melt pool begins to form, observable as a step in the cooling curve for probe 1. The two solvers still produce nearly identical temperatures, the largest discrepancy being only ≈ 6 °C in probe 1. The melt pool quickly reaches a steady volume (Figure 7) and remains quite shallow at this laser power, only two computational cells deep. Importantly, the good agreement between the two solvers demonstrates that they are calculating cell melt fractions in a consistent manner.

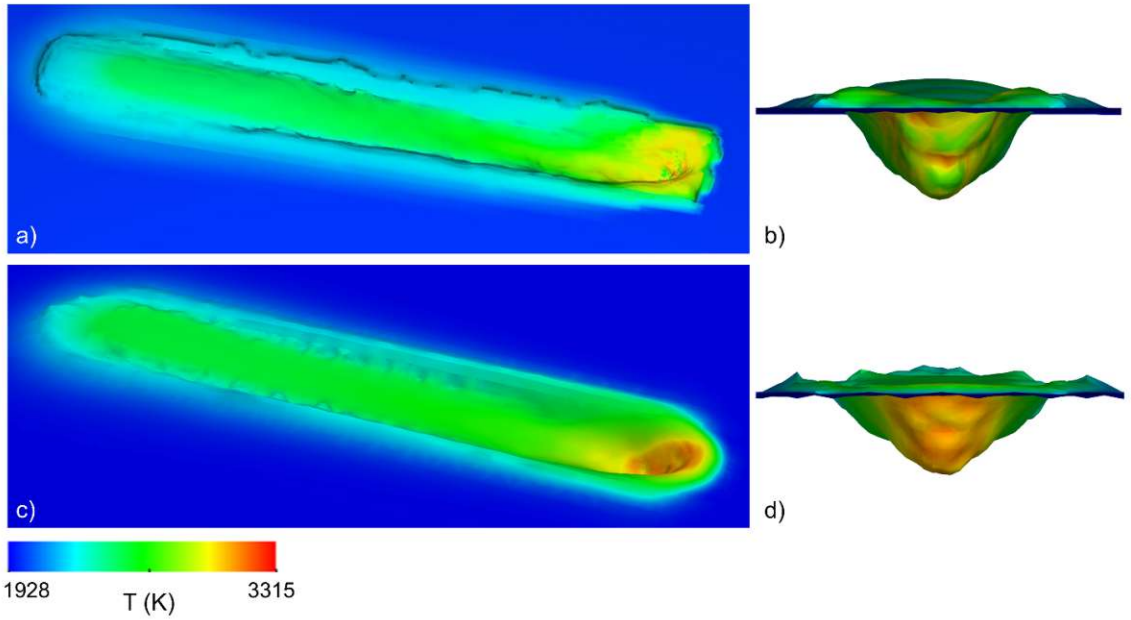

Figure 4: Laser vaporisation at $P = 500$ W, with Marangoni convection, Fresnel absorption and multiple reflections. 3D views of vapour depression predicted by FLOW-3D (a,b) and OpenFOAM (c,d). In (a) and (c), condensed matter is shown, while in (b) and (d), an iso-surface at $\alpha_c = 0.5$ is depicted as seen from in front of the vapour depression (looking in negative $\vec{e}_Z$-direction).

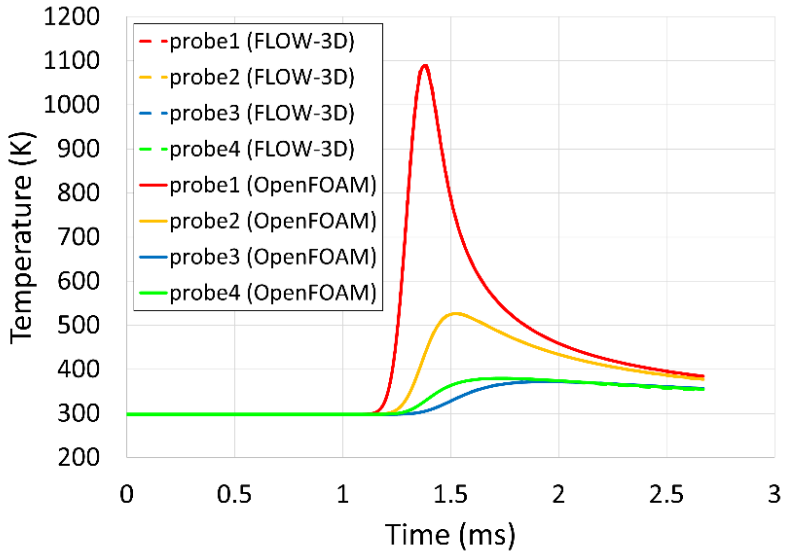

Figure 5: Laser heating without melting at $P = 30$ W, comparing temperatures at different probe locations. Note that the solver results are nearly identical and hence the respective curves coincide.

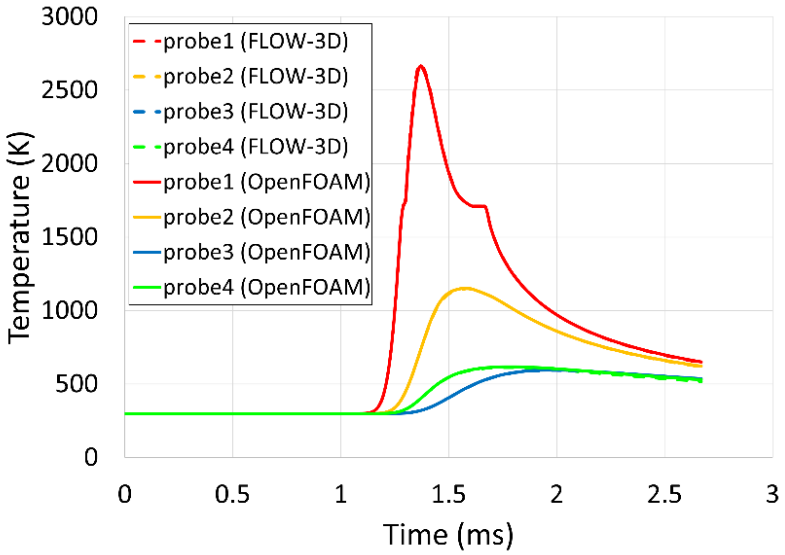

Figure 6: Laser melting without evaporation at $P = 120$ W, comparing temperatures at different probe locations. Note that the solver results are nearly identical and hence the respective curves coincide.

4.3 Addition of Marangoni effect

Having established fundamental agreement between the solvers for heat transfer and melting/solidification calculations, the next step was to add melt flow. This also required allowing gas flow because melt circulation causes movement of the free surface which then affects the gas phase. The treatment of convective heat loss from the metal to the atmosphere above is one of the points of difference between the two solvers and needed up-front consideration. In a two-fluid solution like OpenFOAM, the transport of heat from the metal top surface by gas flow is directly calculated. In FLOW-3D, as in all one-fluid solutions, this heat loss mechanism must instead be approximated as a fixed heat transfer coefficient (HTC) to an ambient temperature. The HTC values employed in published LPBF simulations vary widely [16], from 10 to more than 100 $W{\cdot}m^{-2}{\cdot}K^{-1}$, with little or no explanation. The availability of both solver types in the current study provided an excellent opportunity to instead find a realistic HTC value by a calibration approach. As explained further in Appendix B, this involved adjusting the HTC in FLOW-3D solutions to match the metal temperature differences between OpenFOAM solutions with gas flow on and off. In this way, the effective HTC values were determined to be 80 $W{\cdot}m^{-2}{\cdot}K^{-1}$ at 120 W laser power and 130 $W{\cdot}m^{-2}{\cdot}K^{-1}$ at 200 W laser power. These HTC values were then used in subsequent FLOW-3D simulations to minimise this source of possible difference between the one-and two-fluid solutions. It is emphasised that the convective heat loss is in any case a very small term, at 130 $W{\cdot}m^{-2}{\cdot}K^{-1}$ reducing surface temperatures by a maximum of only 3 °C on the melt pool surface and less than 0.5 °C elsewhere. The HTC may increase above 130 when vaporisation starts but then surface heat loss is dominated by evaporation anyway.

The first driver of melt flow examined was the Marangoni force. Vaporisation was left switched off. Analyses were run at both 120 W and 300 W, but for brevity only

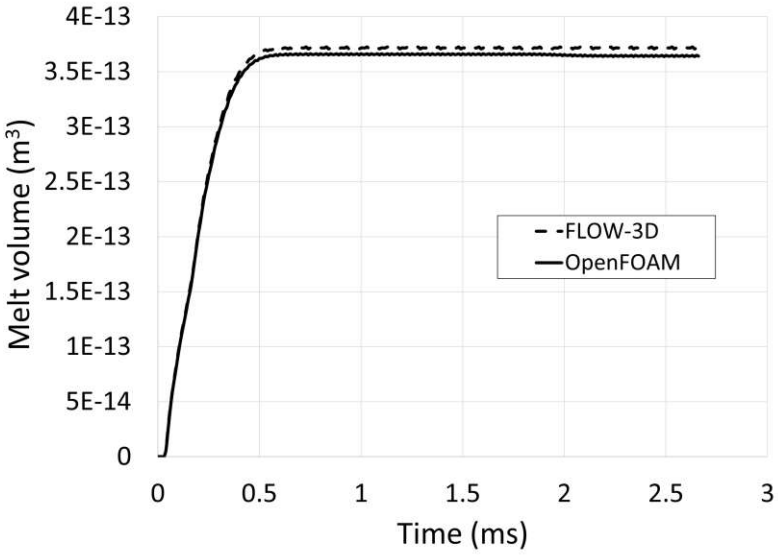

Figure 7: Comparison of melt volumes for laser melting without evaporation at $P = 120$ W.

the results at 300 W are shown because the much greater melt volume makes the Marangoni effects more evident. Figure 8 plots the melt volume for the two solvers with and without the Marangoni force. Without Marangoni, the melt pool velocities are zero and the free surface remains flat. Compared to Figure 7 at 120 W, it can be seen that raising the laser power to 300 W has increased the melt pool volume by a factor of about 9. Addition of the Marangoni force significantly diminishes the melt pool volume, mainly by reducing its lateral extent rather than depth. The overall volume reduction occurs because the circulation created by the Marangoni force moves hot melt from the pool's top surface to its peripheries and thereby increases heat transfer to the solid substrate. With Marangoni enabled, there is noticeably less melt volume with OpenFOAM than with FLOW-3D. It should be noted that the relatively low resolution of the melt pool (up to only four cells deep at 300 W) magnifies the relative effect of any algorithmic differences and instabilities. The two solvers yield slightly different temperature curves with Marangoni enabled (Figure 9), whereas the solutions for the same simulations without Marangoni convection coincided (Figure 6). Unsurprisingly, the greatest temperature difference between the solvers occurs at probe 1, closest to the top of the melt. The largest effect on the temperature traces of adding Marangoni also occurs at probe 1. Comparing Figure 9 with Figure 6, both at 120 W laser power, the peak temperature at probe 1 is seen to be several hundred degrees less due to the Marangoni current transporting heat away.

4.4 Addition of vaporisation

The next stage of the solver comparison was to add vaporisation effects to the solution. To ensure a significant rate of vaporisation, the laser power was increased further to 500 W. Analyses were run with vaporisation alone and also with combined vaporisation and Marangoni. The melt cross-sections along the centre-line of the

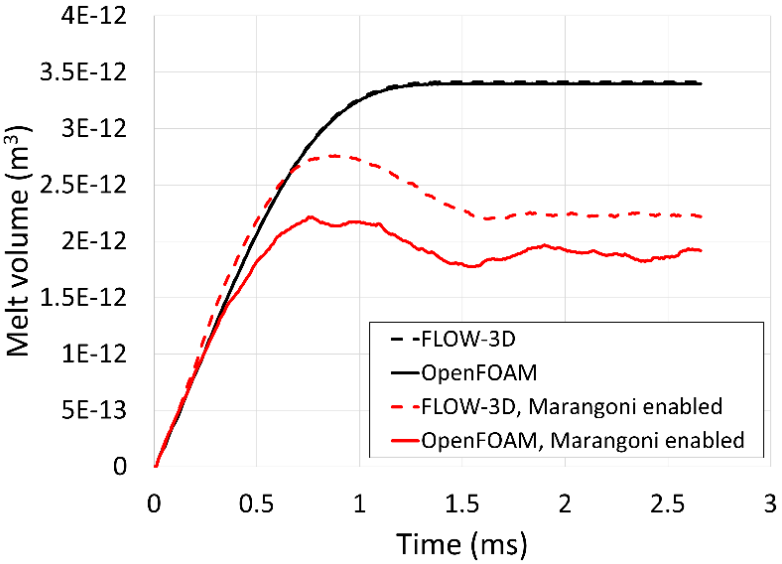

Figure 8: Laser melting without evaporation at $P = 300$ W. Melt volume comparison with and without Marangoni convection.

laser track (plane $x = 0$) are plotted in Figure 10. In both situations, the profiles are quite similar for the two solvers, with the melt pool depression slightly deeper for FLOW-3D. The addition of Marangoni tends to reduce the curvature of the melt depression for both solvers, flattening it by making the trailing surface less steep. Looking more quantitatively at the melt volume (Figure 11), the two solvers give essentially the same results for vaporisation in isolation, within the simulation uncertainties. Adding Marangoni forces reduces the melt volume, by slightly more for OpenFOAM than for FLOW-3D. These observations are both consistent with those made in the absence of vaporisation in the previous section.

Examination of the amount of mass lost by evaporation (Figure 12) reveals some interesting behaviour. Firstly, since this graph plots the cumulative mass loss, the linearity of the curves implies that the rate of mass loss very rapidly reaches a constant value, after an initial period < 0.1 ms for the surface to heat from 25 °C to the boiling point. The melt volume, in comparison, takes much longer to attain a quasi-steady state, around 2 ms (Figure 11), the time being controlled mainly by the thermal diffusivity of the substrate. Secondly, adding Marangoni markedly lowers the vaporisation rate, which can be explained by surface cooling due to the increased melt pool circulation. Lastly, the predicted vaporisation rate is significantly greater for FLOW-3D than OpenFOAM, both with and without Marangoni, which we discuss later.

4.5 Addition of multiple laser reflections

Having seen the effects of adding vaporisation and Marangoni, we next turned on the calculation of multiple laser reflections, with vaporisation and Marangoni still enabled. Both solvers use a ray tracing method in which each ray is tracked, apply-

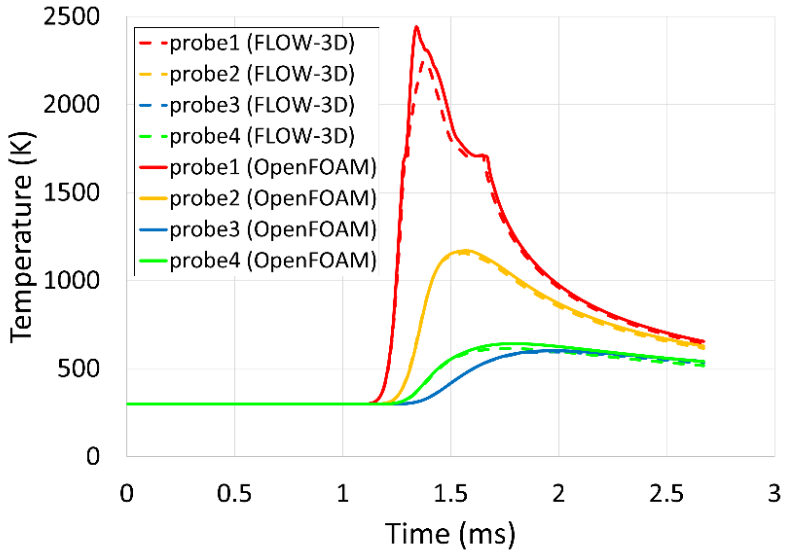

Figure 9: Laser melting without evaporation at $P = 120$ W, including Marangoni convection. Comparison of solver temperatures at four probe locations.

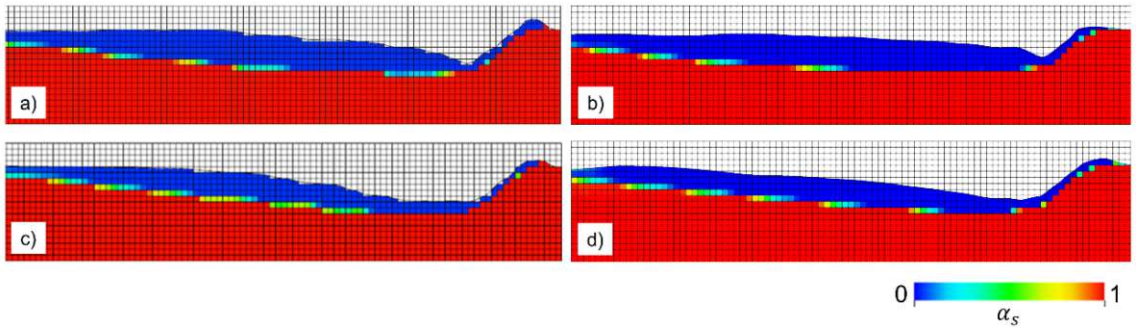

Figure 10: Laser vaporisation at $P = 500$ W. Melt pool without Marangoni convection (top): a) FLOW-3D, b) OpenFOAM, and with Marangoni convection (bottom): c) FLOW-3D, d) OpenFOAM.

ing some absorption at each reflection, until the ray either leaves the domain or is reduced to less than 1 % of initial intensity. The effect on melt volume for each solver of including multiple laser reflections (absorptions) is shown in Figure 13. Since the same laser power of 500 W was used, the results for the base case of a single reflection repeat those in Figure 11. Multiple reflections transfer a greater proportion of laser energy to the sample with the increase being dependent on the concavity and roughness of the surface. We deliberately created a case with a significant melt pool depression to more fully test the solvers. The difference in condensed phase enthalpy between the start and end of track (i.e., the laser energy absorbed by condensed matter and not yielded to the vapour phase via evaporation) increases by 50 % for FLOW-3D and 62 % for OpenFOAM. The lower value in FLOW-3D can be ascribed to a larger increase in evaporation (and hence more of the additional absorbed energy being utilized to overcome latent heat of vaporisation), and potentially differences in ray tracing implementations. Melt volumes increase much faster than linearly with absorbed energy, ending 176 % higher for FLOW-3D and 234 % higher for Open-

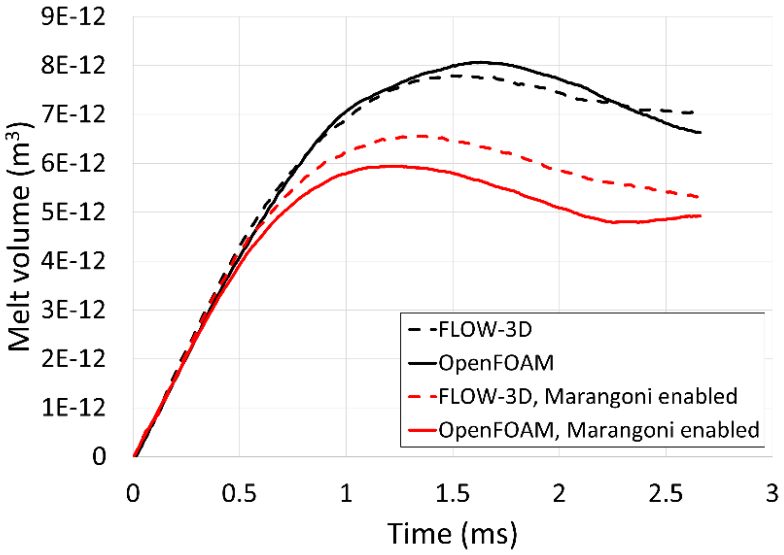

Figure 11: Laser vaporisation at $P = 500$ W. Melt volume with and without Marangoni convection.

FOAM (Figure 13).
The rate of vaporisation (Figure 14) also increases dramatically when multiple reflections are added, with the cumulative evaporated mass being 180 % greater for FLOW-3D and 76 % for OpenFOAM. The much lower sensitivity of vaporisation rate to heat input in OpenFOAM can be attributed to the coupling between pressure and evaporation rate in OpenFOAM, cf. Eq. (10). A larger amount of evaporated mass will lead to a build-up of pressure in the vicinity of the evaporating interface, yielding a self-limiting process. This coupling, and hence limiting effect, is absent in the FLOW-3D rate equation.

4.6 Addition of Fresnel reflection behaviour

The final physical feature added to the models was the Fresnel absorption behaviour, as per Eqs. (18) to (22), in which laser absorption increases at high angles of incidence. The effects on melt volume (Figure 15) and vaporisation rate (Figure reffig:16) are significant, around 10 % for FLOW-3D and 5 % for OpenFOAM, respectively in this case. The augmentation of both quantities, melt volume and vaporisation, is greater for FLOW-3D than for OpenFOAM which can be mainly ascribed to a greater increase in heating for FLOW-3D (5.8 % vs. 1.6 %) due to a higher angle of incidence at the absorption front.

The laser heat flux distributions from the two solvers are compared in Figure 17. Heat spots away from the primary laser incidence are associated with multiple reflections. Due to the stochastic variability of the melt pool geometry, the flux pattern fluctuates at every analysis timestep so that the differences between the two solvers are not statistically significant. This is supported by the fact that the melt pool volumes, driven by laser heat input, are quite similar.

In Figure 18 and Figure 19, we compare the melt velocity patterns of the two solvers in the final timestep of each analysis, when the conditions are essentially steady. ig-

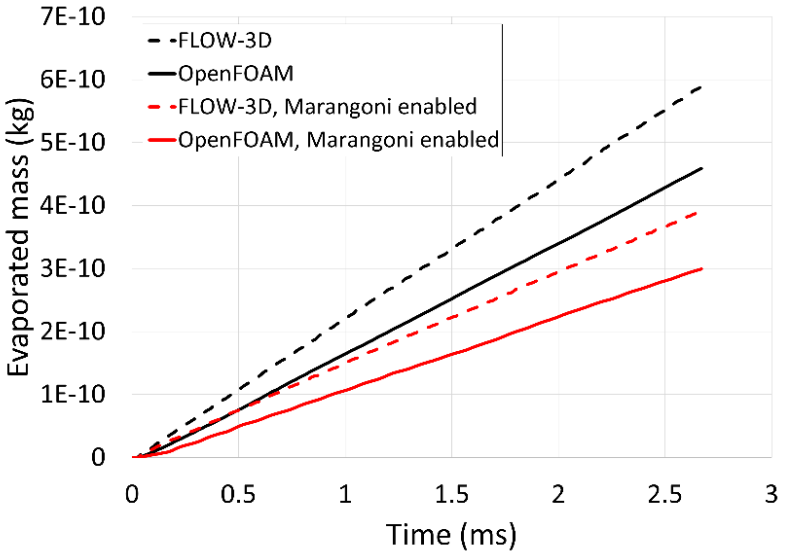

Figure 12: Laser vaporisation at $P = 500$ W. Evaporated mass with and without Marangoni convection.

ure 18 looks at a slice along the laser travel plane while Figure 19 plots the velocity pattern on three transverse slices, at the locations marked in Figure 18. Looking first at the longitudinal slice, we see some significant differences. The melt pool depression depth and the profile of the track behind the laser are quite similar. However, there is a clear sub-surface recirculation in the FLOW-3D simulation, moving material in the $\vec{e}_Z$-direction from the rear of the melt pool toward the front (vectors pointing to right in Figure 18). By contrast, the sub-surface flow directions are quite disordered in OpenFOAM. The transverse plots do not show any distinct differences, except for the higher surface velocities for FLOW-3D already described.

An extensive investigation was conducted to identify why FLOW-3D displays a longitudinal recirculation zone below the surface whereas OpenFOAM does not. First, two features of the OpenFOAM solution which are not present in FLOW-3D (drag by gas on the liquid surface, liquid compressibility) were checked but found to have negligible influence. Then the sensitivity of the flow pattern to changes in recoil force, vaporisation rate, mushy zone treatment, Marangoni effect and the thermal conductivity equation for partially frozen cells was examined. Although large changes in melt volume and surface profile could be produced, as expected, none of these factors altered the fundamental disparity in recirculation behaviour between FLOW-3D and OpenFOAM. We also ran analyses with longer tracks, extended by a factor of three, and found that the respective circulation patterns were unchanged. Finally, the key factor responsible for the difference in melt flow pattern was discovered to be the treatment of the meeting point between melt and the solid surface of the substrate, i.e. what is normally termed the contact angle. Results presented in the Appendix (Section C) show that for FLOW-3D the recirculation is reduced considerably as the contact angle is increased from the default of 0 degrees, whereas in OpenFOAM the same change actually creates some recirculation, bringing it closer to FLOW-3D. We discuss contact angles further in the next section.

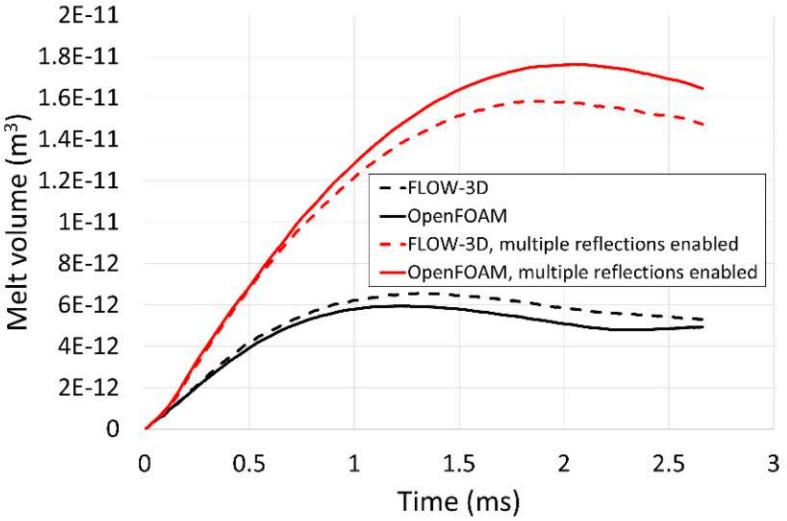

Figure 13: $P = 500$ W. Influence of multiple reflections (no Fresnel) on melt volume.

4.7 Discussion of laser track investigation

We now seek a coherent explanation of the differences between the one-fluid and two-fluid solver results observed in the preceding sections. When evaluating the significance of these differences, we must recognise the stochastic variability which occurs in LPBF and simulations thereof, which receives inadequate attention in the LPBF simulation literature. The greatest variability occurs in the most severe conditions, of course, which in the current work was the 500 W test with all laser terms, as presented in Section 4.6. We ran four additional FLOW-3D analyses of this case with tiny (< 0.01 W) changes in laser power to determine the inherent variability of the final results. The standard deviations of the final melt volume, energy increase and cumulative evaporated mass were 2.5 %, 0.14 % and 1.4 %, respectively. A similar analysis of the 300 W case with only Marangoni enabled (Section 4.3) yielded standard deviations in melt volume and energy increase of 1.6 % and 0.01 % respectively. These inherent variabilities provide some context for the following discussion.
The two models differ somewhat in their treatment of surface heat losses (radiative, convective and evaporative).

- As described earlier, radiative heat loss was omitted as it is negligible in the test case.

- Convective heat losses were made as similar as possible by the HTC calibration method described in Section 4.3, and, as noted there, are small anyway. To confirm that point, we re-ran the 500 W case with the HTC doubled and found that the final melt volume and energy increase were reduced by only 1 % and 0.3 %, respectively. Since the HTC calibration leaves only residual differences in what is already a very small quantity, convective heat losses can also be dismissed as contributors to solver differences.

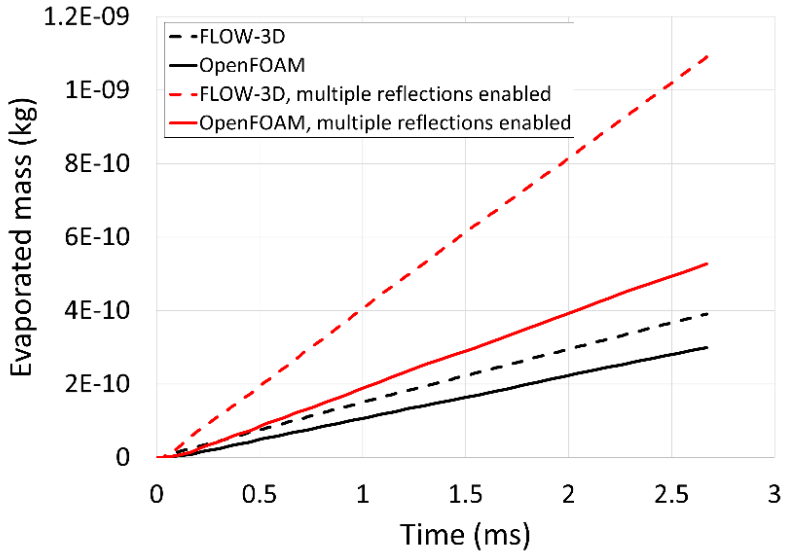

Figure 14: $P = 500$ W. Influence of multiple reflections (no Fresnel) on evaporated mass.

- Vapour heat losses, though, do have some influence. Sensitivity tests were run with FLOW-3D by altering the coefficient of 0.82 in Eq. (12) which controls evaporative mass rate and heat loss (Note this did not directly affect evaporative recoil as in FLOW-3D that is applied separately.) Doubling the rate coefficient increased mass loss by 83 %, less than linearly because surface temperatures are reduced. Melt volume declined by 5.1 % and the energy increase was 2.2 % less. Conversely, and more relevantly to the actual situation, halving the coefficient reduced evaporation by 47 % and increased melt volume by 2.6 % and energy gain by 1.3 %.

The greater vaporisation rate with FLOW-3D is the most obvious difference in the solver results. As more heat is added to the system by adding first multiple laser reflections and then Fresnel effects, this disparity increases further. The difference is attributed to the handling of the ambient pressure in the vaporisation mass flux Eqs. (10) and (11) for OpenFOAM compared to Eq. (12) for FLOW-3D. In OpenFOAM, vaporisation increases more slowly with surface temperature due to the self-damping effect from the greater vapour pressure. The OpenFOAM results in the vapour phase display an elevated ambient pressure above the melt surface, averaging 1.25 bar and reaching nearly 3 bar (refer Appendix D for details on the averaging method used and pressure distribution data). In FLOW-3D, as in nearly all one-fluid models, the ambient pressure for vaporisation is fixed during the analysis, and is normally set to 1 atm. The OpenFOAM results suggest that perhaps this value should be increased. However, in further testing, it was found that the ambient pressure required to match the OpenFOAM results is unrealistically large, which emphasises the limitations of trying to match dynamic pressure effects seen in a two-fluid model with fixed pressures in a one-fluid model. As an illustration, when the ambient pressure in Eq. (12) for the FLOW-3D analysis was increased from 1 atm to 2.0 atm, the evaporated mass dropped from $1.22{\cdot}10^{-9}$ to $0.67{\cdot}10^{-9}$ kg, much closer to the OpenFOAM result (Figure 16). The melt volume increased slightly, as expected from the

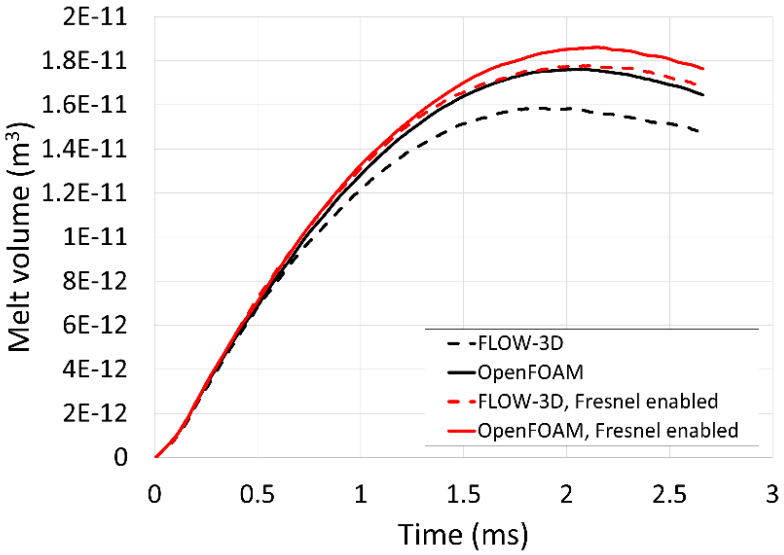

Figure 15: $P = 500$ W. Influence of Fresnel absorption on melt volume.

reduced vapour heat loss, from $1.68{\cdot}10^{-11}$ to $1.73{\cdot}10^{-11}$ m^3, therefore also closer to OpenFOAM (Figure 15).

Another important way in which the solvers differ is in their handling of recoil pressure. In one-fluid models, like FLOW-3D, recoil is applied independently of vaporisation, apart from a shared temperature dependence, whereas in two-fluid architectures like our OpenFOAM model they can be intimately linked. Virtually all one-fluid models employ the formulation in Eq. (7), originally derived by Anisimov with a 0.54 factor. However, this Anisimov equation does not account for vapour pressure variations, with p_{amb} a fixed value during the analysis. Detailed investigations by Wang et al. [3] and Pang et al. [55] determined that the Anisimov equation often over-estimates recoil pressure. That finding is consistent with the current work in which we find that the melt depression is slightly deeper and steeper for FLOW-3D than OpenFOAM when recoil is added. That can be seen most clearly when there is no additional Marangoni contribution, as shown in the results of Figure 10 (a) and (b). We also find evidence that the Anisimov equation can over-estimate recoil in validations against stationary laser experiments, presented in the next section. A sensitivity test of the effect of reducing the recoil term by 50 % was conducted with FLOW-3D for the 500 W test case of Section 4.6. The enthalpy gain was reduced by 2.6 %, consistent with less multiple reflections due to a slightly shallower melt depression, and there was an associated melt volume reduction of 3.4 %. However, the highly variable nature of the melt surface as the laser progresses means it is not possible to see this small change in average surface profile.

In Section 4.6, we observed that the difference in contact angle formulation between the one-and two-fluid models leads to noticeable modification of the melt circulation pattern. It is also believed to create the melt volume differences between solvers seen in Figure 9 when Marangoni flow is introduced. Without Marangoni (and vaporisation), the melt surface is flat so contact angle does not play a part, and the solvers match closely in temperatures and melt volume. The Marangoni verification tests

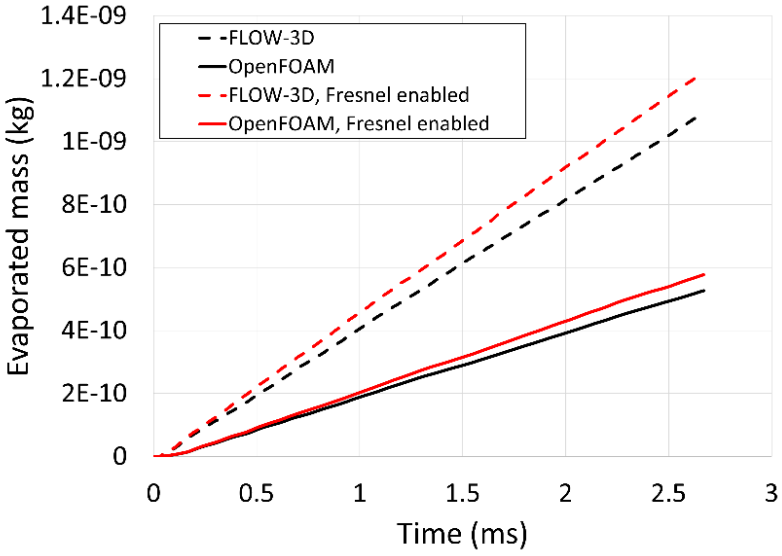

Figure 16: $P = 500$ W. Influence of Fresnel absorption on evaporated mass.

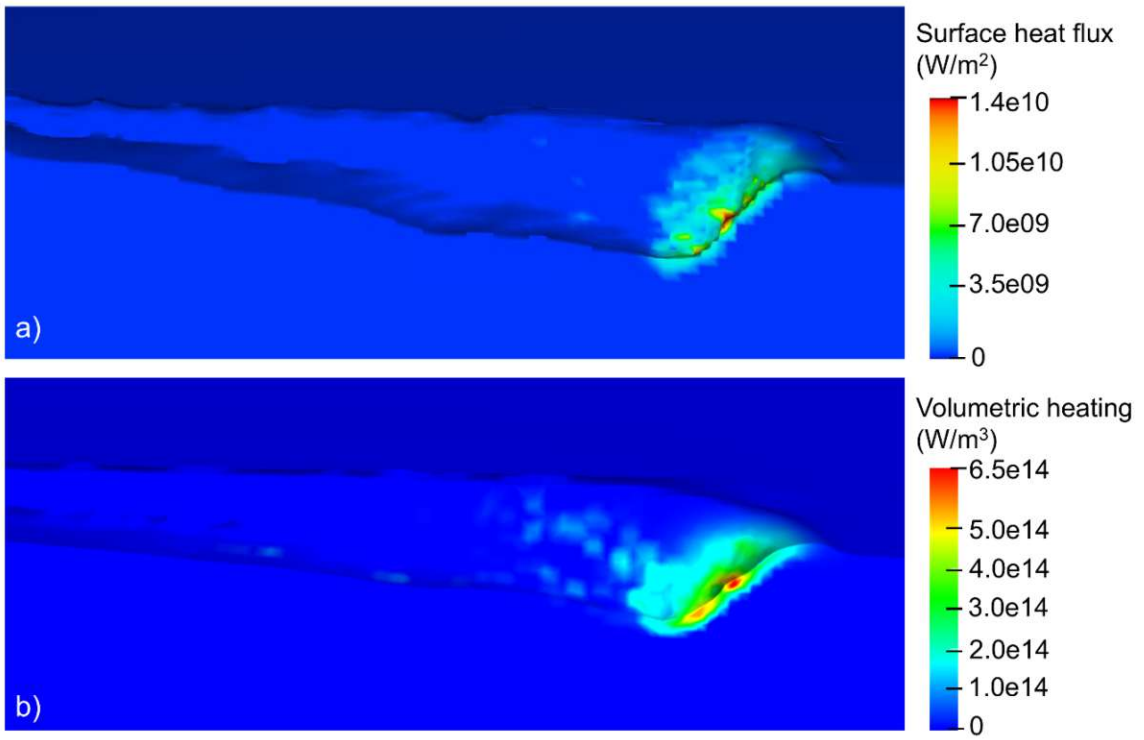

Figure 17: $P = 500$ W, including Marangoni forces, multiple reflections and Fresnel absorptivity. Comparison of laser heat flux on liquid surface, top (a): FLOW-3D, bottom (b): OpenFOAM. The difference in units and magnitude stems from a surface heat flux being applied in FLOW-3D vs. a volumetric heat source being applied in OpenFOAM.

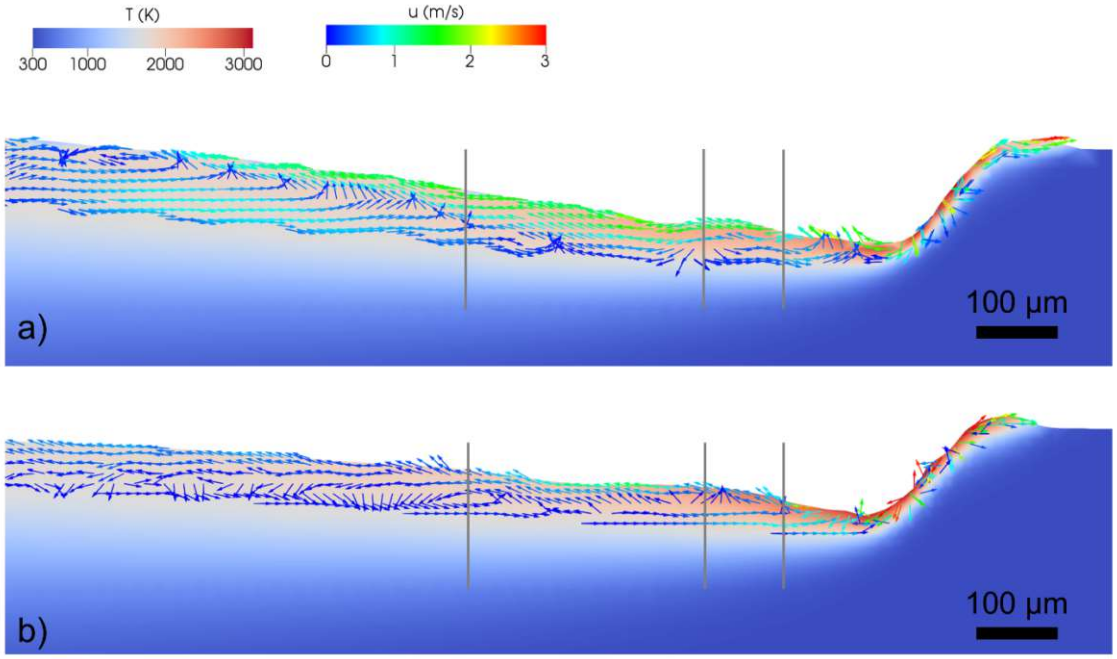

Figure 18: $P = 500$ W, including Marangoni forces, multiple reflections and Fresnel absorptivity. Comparison of melt velocity and temperature at longitudinal center plane (zy-plane). Top (a): FLOW-3D, bottom (b): OpenFOAM. Vertical grey lines denote locations of cross-sectional views shown in Figure 19.

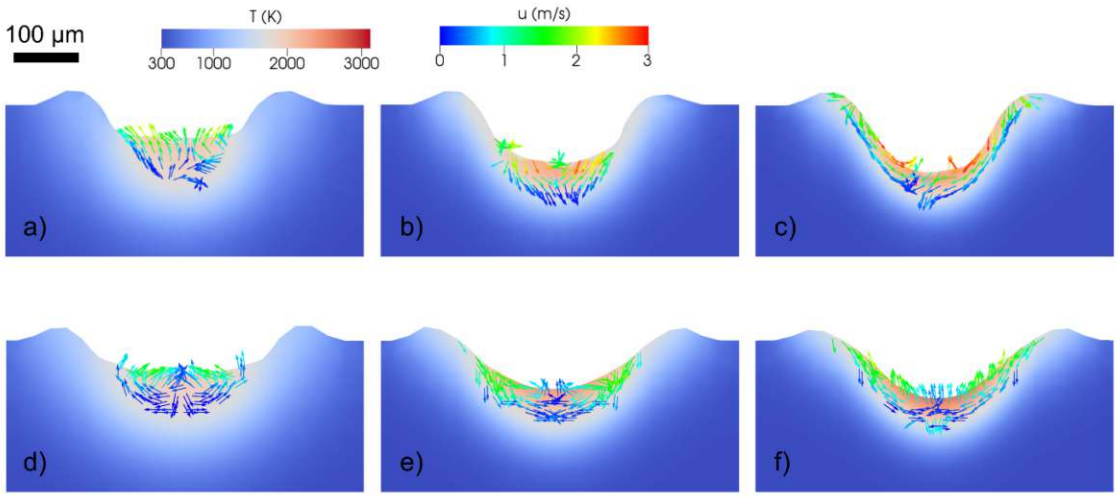

Figure 19: $P = 500$ W, including Marangoni forces, multiple reflections and Fresnel absorptivity. Comparison of melt velocity and temperature at transversal planes (xy-planes). Top: FLOW-3D at z-distances of a) 600 µm, b) 300 µm, c) 200 µm behind laser position, Bottom: OpenFOAM at z-distances of d) 600 µm, e) 300 µm, f) 200 µm behind laser position. Cf. vertical grey lines in Figure 18 for locations of these cross-sectional views.

in Section 3.1.2 established that the solvers agree well in the absence of melt-solid contact, so Marangoni flow is not itself the cause.
The treatment of the contact angle between melt and solid is thus an important consideration but rarely mentioned in publications dealing with CFD simulation of LPBF. In FLOW-3D, a melt-solid contact angle can be set but the theoretical form assumed is not provided. Presumably it is similar to the method applied for general liquid contact with an unrelated solid, in which surface forces are applied to liquid cells at the interface to achieve the desired angle. In OpenFOAM, the situation is further complicated by the need to deal with a 3-way contact. The individual phase surface energies are each specified, yielding surface tension values for each phase pair. Given a set of surface energy values at the triple line, a theoretical equilibrium contact angle can be calculated by Young's formula (or the surface energies specified to yield a desired contact angle). In practice, the contact angle is dynamic, tending toward but never maintaining the equilibrium value due to continual melt pool disturbances and solidification possibly occurring before reaching equilibrium. Notably, surface energy values producing a zero-degree equilibrium contact angle could, depending on initial conditions and perturbations, lead to the surfaces of the melt and adjacent solid remaining coplanar (Figure 20 (a)) or to perfect wetting by a thin liquid film spreading over the solid surface (Figure 20 (b)).

For all contact angle methods, geometrical approximations to define the relevant

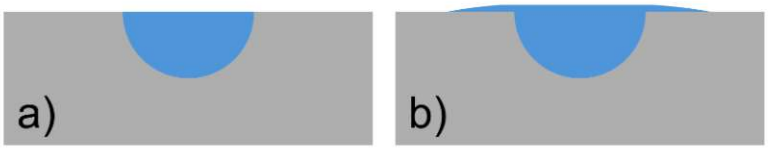

Figure 20: Schematic of melt pool sections for two possible scenarios yielding a zero-degree contact angle. If no melt flow or perturbations are present, the initially flat melt pool will remain as in (a). Given sufficient melt pool perturbation, the triple line forces resulting from a zero-degree specification of surface energies will lead to a scenario as in (b).

directions necessarily entail significant error due to the discrete nature of the surrounding computational cells. Even the correct theory to be applied is ambiguous. For example, it is likely that the wetting behaviour of melt advancing ahead of the laser spot differs from that behind the laser where the melt is cooling, and the melt front is retreating across re-solidified material.
A variety of values for the equilibrium contact angle (i.e., the angle determined by Young's equation) between liquid and re-solidified material or unmelted substrate can be found in studies of melt pool simulations, ranging from zero [56], 10 degrees [57], 30 degrees [8], 60 degrees [58], up to 90 degrees [59]. The same is true for the contact angle between liquid and unmelted powder material, with examples ranging from good wetting (e.g., 30 degrees [8]) to relatively poor wetting (e.g., 105 degrees [57]). The actual values depend on the material state (such as the surface roughness and presence of oxide layers) and even the ambient conditions (type of ambient gas, presence of vacuum), so are often not known. As demonstrated by Korneev et al. [57] in additive manufacturing simulations, the contact angle choice greatly influences the resulting track morphology and build quality. Hu et al. [60] show experimentally that

the contact angle obtained differs from the equilibrium contact angle, approaching an asymptotic limit over the course of consecutive melting tracks due to heat accumulation and hence increased solidification times. To conclude, the choice of wetting conditions or equilibrium contact angle has a strong effect on the resulting flow patterns, and while it is difficult to obtain reliable input values for a given case in the first place, the introduction of the three-phase line into a model depends strongly on whether all three phases are part of the modelling domain. We observed that it is not possible to yield exactly the same flow behaviour for the two solvers investigated here even if setting the same equilibrium contact angle. Further investigation of these effects and suitable modelling approaches are needed but outside of the scope of the present work.

5 Model Application to Real-World Case

5.1 Model setup

To compare the two models in a real-world scenario, the stationary bare plate illumination experiments of Cunningham et al. [61] are chosen, as they provide in-situ measurements of the keyhole morphology with high spatial and temporal resolution. While the setup is fairly simple, with well-defined and reported conditions, the observed physical phenomena span two different process regimes within one experiment. These regimes are characterised by initially a stable thermocapillary exhibiting a quasi-constant drill rate and, at later times, a highly unstable, fluctuating thermocapillary. Therefore, this experiment proves useful for assessing a model's predictive capabilities, and has been used in many studies for validating numerical models [3, 10, 62], becoming a sort of benchmark.
The authors have published the results of the here-presented OpenFOAM model previously [26] but reproduce them here to permit direct comparison with FLOW-3D. Close attention was paid to setting up the FLOW-3D simulations in exactly the same way as the corresponding OpenFOAM simulations, to eliminate the possibility of discrepancies stemming from differences in model setup rather than the models themselves. While a detailed description of the case setup is provided in [26], we briefly repeat it here for easier reproducibility. Figure 21 shows the computational domain, mesh and initial distribution of phases used in the simulations. Table 9 lists the material parameters employed for the Ti6Al4V sample. Two simulations were conducted with a laser diameter at the sample surface of $D = 140$ µm and $D = 95$ µm, respectively, while the power was fixed at $P = 156$ W in both cases.
The keyhole depth measurements over time are presented in Figure 22 and for both solvers were performed by constructing an isosurface at $\alpha_g = 0.5$ and measuring its deepest point. Hence, there is a slight bias in the reported data towards greater depths as sealed-off bubbles were counted as keyhole until they fully collapsed. (As an example, the last two frames in Figure 25 (b) yield the same depth measurement). This choice of definition is of course arbitrary, and it is not known which definition was used in the published experiments. Furthermore, since the isosurface is constructed via linear interpolation, any fluctuations below the cell could be due to interpolation errors. Notably, the initial fluctuations in both simulation results of

the 140 µm spot size case in Figure 22 are approximately of the order of the cell size (6.25 µm).

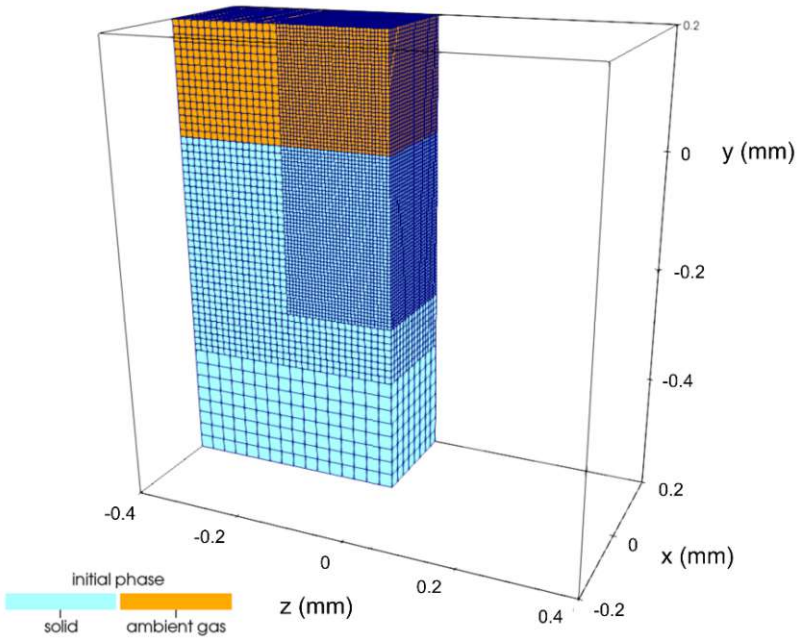

Figure 21: Computational domain used for real-world keyhole drilling simulations. Mesh and initial phase distribution are shown for a quarter of domain.

5.2 Results

In Figure 22, the temporal evolution of keyhole depth obtained from the FLOW-3D and OpenFOAM simulations are compared to experiment for the small (left) and large (right) laser spot size. Agreement of both models with experimental data is better in the small spot size case, which can be attributed to the less pronounced regime separation, compared to the large spot size case, where two distinct regimes can be identified. Interestingly, the FLOW-3D model slightly underestimates the keyhole depth in the small spot size case, while overestimating it in the large spot size case. Additional tests have shown that by choosing a different prefactor value for the evaporative recoil pressure in FLOW-3D, reducing the evaporative recoil pressure to approximately 30 % of its original value, the experimental values can be matched closely for the 140 µm spot size case. However, using the same prefactor to simulate the 95 µm case leads to significant underestimation of keyhole depths. These additional results are provided in Section E in the Appendix.

In Figure 23, the keyhole morphology of the 140 µm spot size case is shown at similar exemplary stages for FLOW-3D (a-d) and OpenFOAM (e-h), but not at the same times due to the stochastic behaviour of the two solutions. All frames are coloured by temperature, with a colour scheme cut off at the boiling temperature. It is noticeable that large parts of the keyhole are strongly superheated in the OpenFOAM simulation which can be attributed to the coupling between evaporation and vapour pressure.

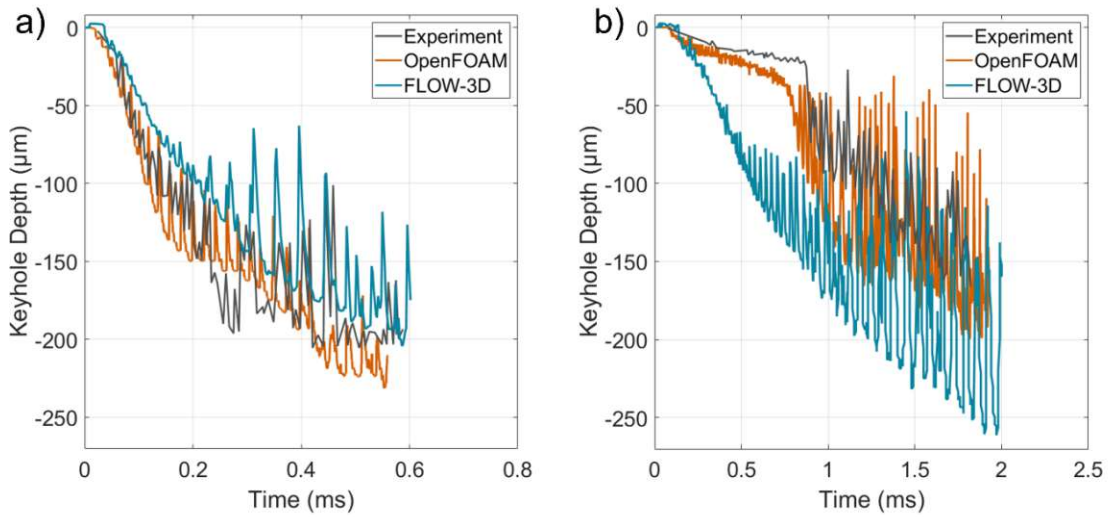

Figure 22: Comparison of simulation results with Cunningham data for (a): 95 µm, and (b): 140 µm spot size at $P = 156$ W.

With a static laser, the pressure inside the keyhole is significantly higher than ambient pressure so that evaporation requires temperatures well above the boiling point to occur, cf. the Clausius-Clapeyron Equation, Eq. (9). Figure 24 shows OpenFOAM results of the keyhole across one drill – collapse cycle in the fluctuating regime of the 140 µm spot size case, with gaseous phases being coloured by pressure (in multiples of ambient pressure). The pressure at the keyhole bottom is relatively high during the entire drilling phase, locally peaking at the maximum depth, and creating a sudden halt in the evaporation process when the surface cannot be sufficiently superheated to sustain evaporation anymore, leading to a collapse. Figure 25 (a) shows some of the frames from Figure 24 (but using a different pressure range for colouring), comparing to the 95 µm spot size case in Figure 24 (b). The entire drill-collapse cycle happens significantly faster in the 95 µm spot size case, and there is a strong overlap between the phases, with the bubble generated from pinching off the bottom of the keyhole still collapsing while the subsequent drilling phase is well progressed. Also, the pressure ranges are much higher (both above and below ambient pressure), when comparing to the large spot size case.

As contact angle settings had a large effect on results for the laser track cases, we performed additional simulations of the stationary illumination cases with the contact angle set to 22.5 rather than 0 degrees. We found that the keyhole evolution was unaffected in terms of frequency, amplitude or the onset of deep fluctuations, just noise deviations that any chaotic system will exhibit given small perturbations. We suggest that contact angle affects these results much less than in the laser track cases because the thinner and more extended melt layer within a deep keyhole restricts the contact influence to the top of the plate.

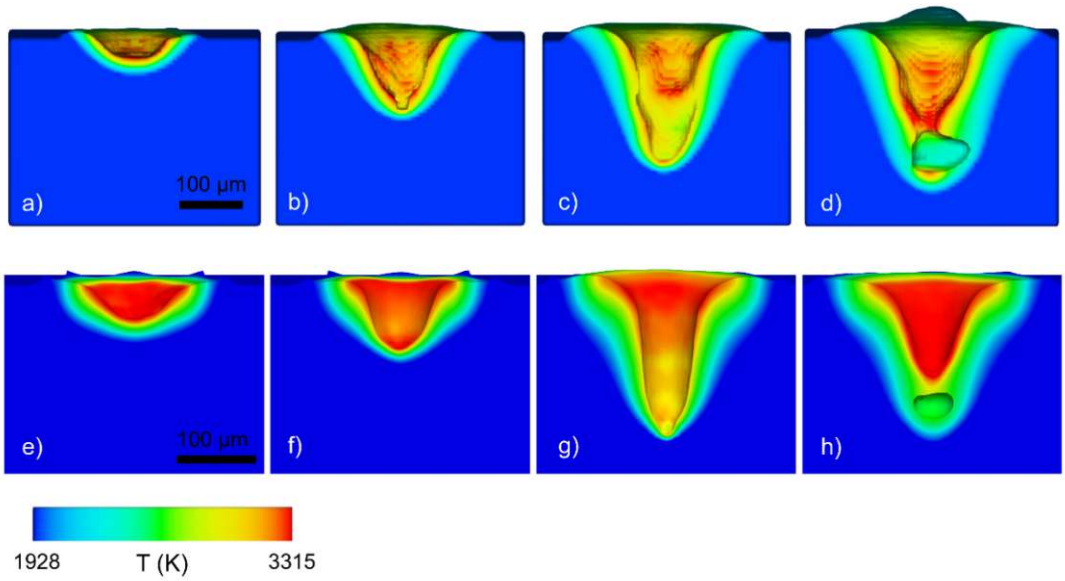

Figure 23: Comparison of keyhole shape and temperature in condensed matter at different process stages for 140 µm spot size and $P = 156$ W. Top: FLOW-3D at a) $t = 30$ µs, b) $t = 600$ µs, c) $t = 1150$ µs, d) $t = 1500$ µs; bottom OpenFOAM at e) $t = 800$ µs, f) $t = 920$ µs, g) $t = 1630$ µs, h) $t = 1650$ µs. Due to the stochastic nature of the fluctuations (cf. Figure 22), different times from the two solutions are shown to enable comparison of similar physical states of the process.

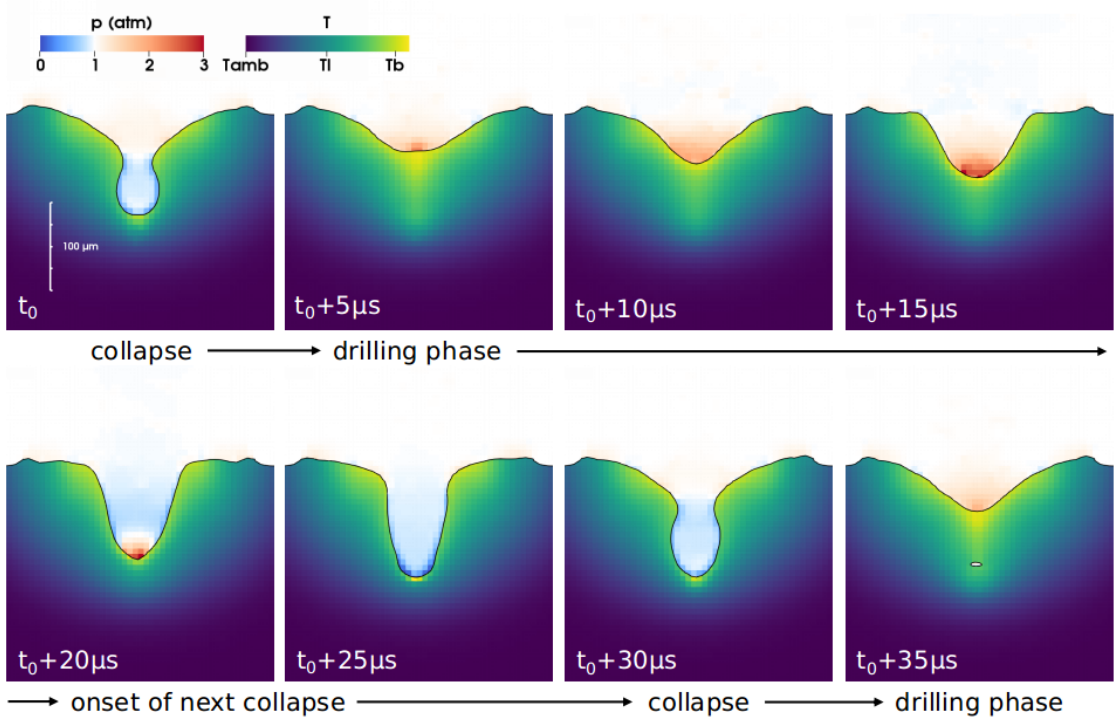

Figure 24: OpenFOAM results showing keyhole morphologies for 140 µm spot size case over one drill – collapse cycle during fluctuating process phase ($t > 1$ ms). Gaseous phases are coloured by pressure and condensed phases by temperature.

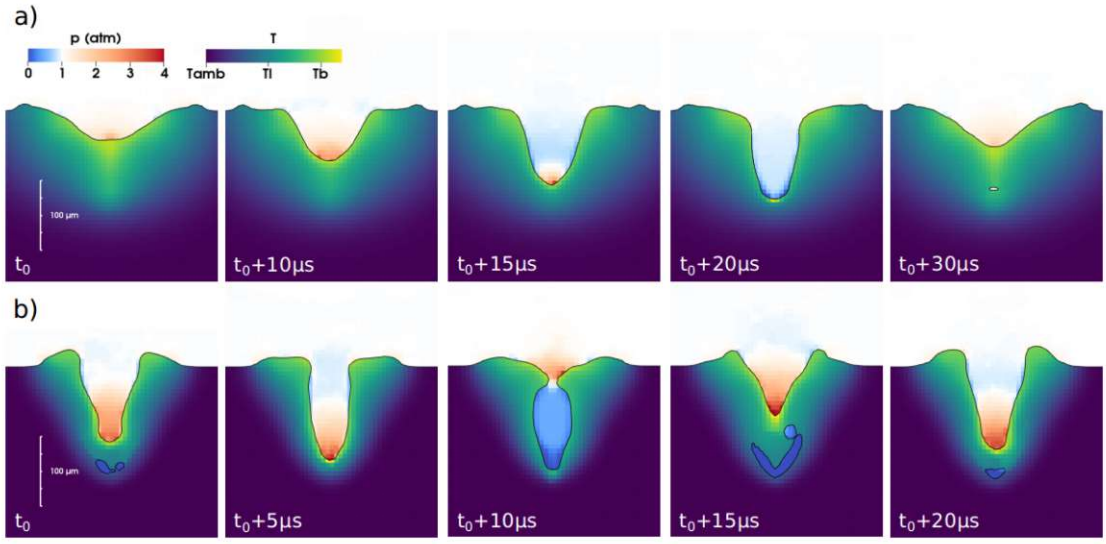

Figure 25: OpenFOAM results showing keyhole morphologies for a) 140 µm spot size case, and b) 95 µm spot size case over one drill – collapse cycle during fluctuating process phase ($t > 1$ ms for (a), $t > 0.2$ ms for (b)). Gaseous phases are coloured by pressure and condensed phases by temperature. The data in a) are a subset of Figure 24, coloured differently to enable comparison with b).

5.3 Discussion of stationary laser case

Both models can qualitatively predict the unstable, fluctuating drilling process that is observed in the corresponding experiments. However, the quantitative prediction of average keyhole depth and drill rates is more accurate in the OpenFOAM simulation for both investigated spot sizes. As outlined above, FLOW-3D slightly underestimates the keyhole depth in the 95 µm spot size case, while strongly overestimating it in the 140 µm spot size case. This is most likely a consequence of the lower degree of coupling employed in FLOW-3D, where the evaporation rate is independent of local vapour pressure, and only a function of temperature. Strong evaporation will lead to a build-up of vapour (as the newly generated vapour can only escape at a finite rate) which increases pressure and limits the ultimate evaporation rate, yielding a self-limiting mechanism in the OpenFOAM model. This also explains the higher keyhole surface temperatures observed in the OpenFOAM simulation, as shown in Figure 23. Essentially, most of the keyhole surface temperature is above boiling temperature in the OpenFOAM simulation, as this is required to yield a saturation pressure above ambient pressure, such that evaporation can occur even when pressures increase above ambient at the evaporation interface.
As shown in Figure 24 and Figure 25, the pressure inside the keyhole plays an important role in the dynamic evolution of the keyhole shape and the development of instabilities. While it is possible to adjust the evaporation rate prefactor in Eq. (7) to match experiments, the inherent predictive power of one-fluid simulations is questionable if they require calibration against experimental or higher fidelity simulation results. When moving towards industrial applications, it remains an open question how complex spatial (and even temporal) laser intensity distributions as introduced through static or dynamic beam shaping could be modelled via a one-fluid model without any pressure-evaporation coupling. Different features of the laser intensity

distribution would likely require calibrated evaporation prefactor values which vary in space and time. A more complex formulation of recoil pressure than Eq. (7), taking better account of the Knudsen layer physics in the recondensation term, has shown some promise by improving the match to keyhole results over a range of laser powers [63]. Fundamentally, though, the recoil pressure depends on local vapour conditions whose variations are more accurately determined with a two-fluid model. The increased predictive capabilities of the OpenFOAM model do, however, come at a high computational cost. As an example, the 140 µm spot size simulation in FLOW-3D required approx. 3.5 hours on 10 CPU cores (Intel Xeon E5-2697 v4), while the corresponding OpenFOAM simulation required approx. 22 hours on 10 CPU cores (AMD EPYC 7713). Since the single core performance of the AMD EPYC processor is approx. 30 % higher than that of the Intel Xeon processor, we see that the OpenFOAM solution was slower by approx. a factor of 10. Part of the extended OpenFOAM calculation time stems from the smaller time step necessary to satisfy the CFL condition when resolving high velocities in the gas phase. The required OpenFOAM time step was smaller by approx. a factor of 2 to 4. The remaining speed difference could potentially be attributed to the greater overall complexity of the solution algorithm, but the proprietary nature of the FLOW-3D code makes it difficult to confidently compare the algorithms' complexities. However, we expect the FLOW-3D solution algorithm to be greatly optimized for speed, probably to a larger extent than that of OpenFOAM. To conclude, for performing a large parameter study within a confined process regime, a calibrated and validated one-fluid model is likely a good choice. However, when aiming to predict behaviour across broader processing regimes, or under very unstable conditions, employment of a two-fluid model is advised to enable reliable process prediction, albeit at a higher computational cost.

6 Conclusions and outlook

We have presented a systematic and reproducible comparison of one- and two-fluid modelling approaches for laser-induced melt pool modelling under conditions relevant to additive manufacturing applications, the first in-depth investigation of this nature to be published.

- Providing that material properties, discretization and equation parameters are carefully matched, both modelling strategies yield nearly identical results for cases where evaporation and melt flow play a minor role. Furthermore, it is found that surface heat loss by convection and radiation are small in the tested scenarios and can be adequately accounted for by simple, calibrated models.

- Although remaining qualitatively similar, the one- and two-fluid solutions begin to diverge as soon as an evaporation-induced vapour depression is visible and melt flow starts to become significant. The two main sources of this divergence are found to be the coupling to vapour pressure (affecting evaporation-induced recoil pressure and evaporative mass flux), and the handling of the contact angle at the solid-melt-vapour interface. Since both aspects are inherent features

of the modelling choice, we expect that the same behaviour will be exhibited by other one- and two-fluid models, not restricted just to those investigated here.

- In the phenomenological recoil pressure term usually employed in one-fluid models, we find that the absence of coupling to increasing vapour pressure during the evaporation-condensation process leads to a tendency to overestimate recoil forces in keyhole conditions. In principle, as demonstrated here, it is possible to adjust the recoil pressure by calibration. However, any such calibration coefficient is specific to process conditions and omits the space and time dependencies. Similarly, the quantity of evaporated mass can be overpredicted by one-fluid models, and again it is not possible to satisfactorily calibrate this quantity, for example against two-fluid model predictions.

- Three-phase line forces (and associated contact angles) play a significant role in laser-based AM but have not received sufficient attention in model development. Our investigation revealed them to be a major contributor to solver differences since their treatment is inherently different in one- and two-fluid models.

- In addition to the above fundamental distinctions between one- and two-fluid models, numerical or algorithmic differences can also be significant, as seen here in the differences in laser beam resolution and handling of multiple reflections.

The application of both solver types to a real-world example showed that two-fluid models have significantly stronger predictive capabilities, whereas one-fluid models need to be properly calibrated to the specific conditions of interest. However, the superior capabilities of two-fluid models come with a computational cost, being higher by a factor of approximately 10.
Our comparison of modelling approaches highlights further areas that need to be addressed to enhance the accuracy of additive manufacturing simulation. One requirement is improved algorithms for the control of contact angle between melt and solid, seeking robust methods which are also self-consistent between one- and two-fluid models. Another important area of research is to compare the responses of one- and two-fluid models to process, material and powder bed parameters. Such sensitivity analyses are especially important to lay the groundwork for multi-fidelity models for process optimization. In this concept, computationally expensive models with high predictive capabilities perform extrapolation tasks and calibrate computationally inexpensive models, which can then extend simulation predictions across multidimensional parameter spaces.

Funding Acknowledgement

C. Zenz gratefully acknowledges funding through the TU Wien Doctoral School, within the Doctoral College *DigiPhot*. The authors acknowledge TU Wien Bibliothek for financial support through its Open Access Funding Programme.

CRediT authorship contribution statement

C. Zenz: Conceptualization, Methodology, Software (OpenFOAM), Validation, Investigation, Visualization, Writing- Original Draft. **P. Cook:** Conceptualization, Methodology, Software (FLOW-3D), Validation, Investigation, Visualization, Writing- Original Draft. **L. Vörös:** Investigation, Validation, Visualization, Writing - Review & Editing. **A. Otto:** Conceptualization, Supervision, Funding acquisition, Writing - Review & Editing.

Data availability statement

The datasets generated during and/or analysed during the current study are available from the corresponding author on reasonable request.

Declaration of competing interests

The authors declare that they have no known competing financial or non-financial interests, personal relationships or other conflicts of interest that could have appeared to influence the results, discussions or conclusions reported in this article.

Appendix A Effect of radiative heat loss

We conducted analyses using FLOW-3D to determine the effect of radiative heat loss on surface temperatures, to check whether the omission of radiation could influence our findings. The tests were deliberately constructed to maximise any radiation effects by turning off other surface heat loss sources (zero HTC and evaporation) and setting zero melt flow. Results were obtained at three laser powers with radiation 'on' (uniform emissivity of 0.32 over the entire top surface) or 'off' (zero emissivity). Other laser conditions and material properties were as described in Section 4.1.
The results are provided in Table 3. The temperatures shown are the maximum values reached at two probe locations (listed in Section 4.1) as the laser moves past. The final melt volumes, which have reached a steady state within a very tight tolerance due to there being no melt flow, are also listed in the table. The percentage effects of radiative heat loss are seen to be very small, despite running the tests in extreme scenarios, reaching more than 5000 K at 300 W and 8000 K at 500 W. Therefore, we can be confident that radiative heat loss has negligible effect for the more realistic conditions of our main investigation and can safely be omitted.

Result quantity		120 W	300 W	500 W
Probe 1 temperature (K):	Radiation on	2683.07	5432.13	8518.77
	Radiation off	2683.48	5441.90	8578.58
	Difference (%)	0.016	0.180	0.697
Probe 4 temperature (K):	Radiation on	1149.97	2091.59	2929.49
	Radiation off	1150.16	2094.85	2946.61
	Difference (%)	0.017	0.156	0.581
Final melt volume (m^3):	Radiation on	$3.717 \cdot 10^{-13}$	$3.402 \cdot 10^{-12}$	$9.914 \cdot 10^{-12}$
	Radiation off	$3.717 \cdot 10^{-13}$	$3.416 \cdot 10^{-12}$	$1.007 \cdot 10^{-11}$
	Difference (%)	0.000	0.405	1.535

Table 3: Effect of radiative heat loss on peak temperatures and final melt volume at three laser powers

Appendix B Calibration of heat transfer coefficient

In FLOW-3D, as in most one-fluid solutions, convective heat loss from the metal to the atmosphere above is approximated by a constant heat transfer coefficient to an ambient temperature. However, for OpenFOAM, the transport of heat from the metal top surface by gas flow is directly calculated which provided a means to find a realistic HTC value for FLOW-3D. The calibration approach involved adjusting the HTC in FLOW-3D solutions to match the metal temperature and enthalpy differences between OpenFOAM solutions with and without convective heat transfer from the metal to the gas phase.

Identical baseline conditions were set up for the FLOW-3D and OpenFOAM models with zero melt flow and no surface heat loss sources except convection. Other laser conditions and material properties were as described in Section 4.1, except that the analyses were extended to 10 ms to determine the cooling curves following laser removal at 2.667 ms.

The first step was to obtain OpenFOAM solutions for the two cases of surface heat loss on and off. The latter case was produced by reducing gas thermal conductivity effectively to zero and also stopping gas movement by setting zero gas buoyancy. The results obtained at laser powers of 120 W and 200 W (Figure 26) plot the increases in temperature at the four probe locations if surface heat loss is removed. It should be noted that the actual surface temperatures reach 2000 – 3000 K so these are very small differentials. Consequently, they exhibit some interpolation-related fluctuations, from $\approx$ 1.5 to 2.7 ms, due to the large temperature changes between timesteps as the laser passes by.

The next calibration step was to run the same analyses in FLOW-3D with and without an applied HTC. Analyses were repeated, varying the HTC value, until the temperature changes (Figure 27) were very similar to those found for OpenFOAM. The HTC values obtained were 80 $W \cdot m^{-2} \cdot K^{-1}$ for the 120 W case and 130 $W \cdot m^{-2} \cdot K^{-1}$ for the 200 W case. The matching process focused on probe 1 since this is closest

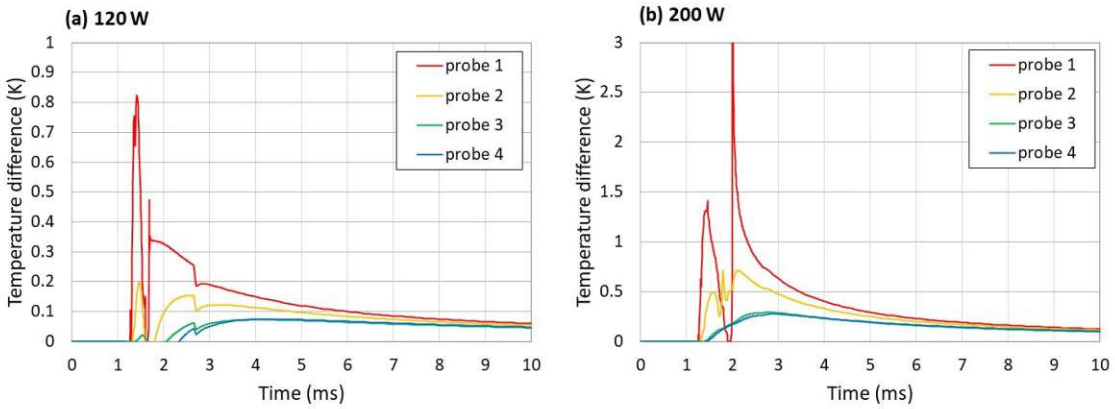

Figure 26: Increase in temperatures when convective heat loss turned off for OpenFOAM analyses at (a) 120 W and (b) 200 W.

to the surface, and at a time of 4.0 ms which falls within a smooth region of the cooling curve with minimal interpolation error. However, the agreement between Figure 26 and Figure 27 is quite good across the whole range. As an additional calibration check, the total enthalpies with and without convective heat loss were also compared. Since the model boundaries were adiabatic and there were no other surface heat losses, the change in the total enthalpy of the condensed material is due solely to convection. Being a global rather than point measure, the enthalpy results enhance confidence in the HTC calibration. The results summarised in Table 4 and Table 5 show that a good HTC calibration has been achieved.

The HTC values thus calibrated are physically reasonable for the natural convection flow produced by surface temperatures reaching 2000 – 3000 K. It should also be noted that the amount of energy lost by convection is very small. For the 200 W case, it is only 0.00009 J out of 0.17 J transferred from the laser to the metal. Therefore, at least in the current work, convective heat loss is a very small term and has little influence on the overall melt pool results.

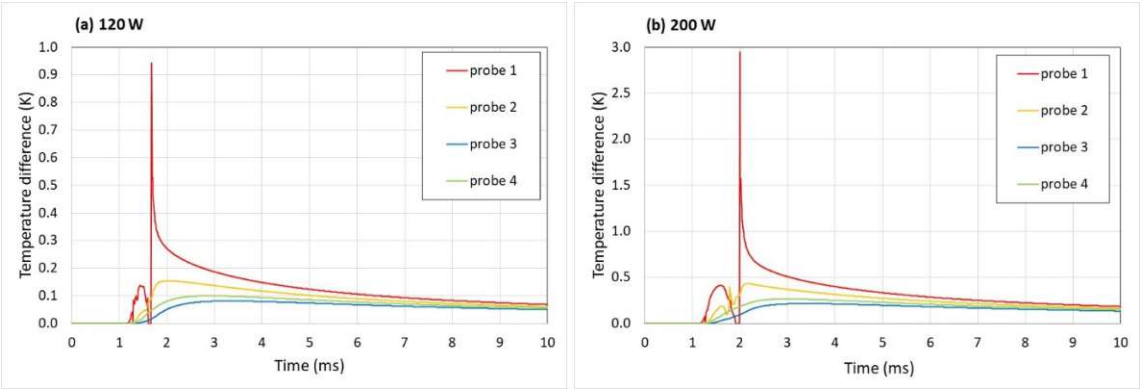

Figure 27: Increase in temperatures when HTC turned off for FLOW-3D analyses at (a) 120 W and (b) 200 W.

	Probe 1 temperature increase at 4 ms (°C)	Condensed matter enthalpy increase (J)
OpenFOAM. Turn off surface heat loss	0.149	$4.7 \cdot 10^{-5}$
FLOW-3D. Remove HTC	0.148	$3.4 \cdot 10^{-5}$

Table 4: Convective heat loss results at 120 W laser power, using HTC = 80 $W \cdot m^{-2} \cdot K^{-1}$ for FLOW-3D.

	Probe 1 temperature increase at 4 ms (°C)	Condensed matter enthalpy increase (J)
OpenFOAM. Turn off surface heat loss	0.401	$8.9 \cdot 10^{-5}$
FLOW-3D. Remove HTC	0.400	$8.8 \cdot 10^{-5}$

Table 5: Convective heat loss results at 200 W laser power, using HTC = 130 $W \cdot m^{-2} \cdot K^{-1}$ for FLOW-3D.

Appendix C Effect of contact angle

As discussed in Section 4.7, the strong difference in recirculation patterns within the melt pool between OpenFOAM and FLOW-3D could be associated with the difference in handling contact angles. The initial aim of setting a 0-degree equilibrium contact angle did not yield identical results once the case setup was sufficiently complex to perturbate the melt pool surface in a way that contact angle forces started to play a role. In Figure 28 and Figure 29, the results of the final laser track case (P = 500 W, including multiple reflections and Fresnel absorption) are presented again, but with a set equilibrium contact angle of 22.5°(set directly in FLOW-3D and via the surface energy value of solid phases yielding the respective contact angle according to Young's formula in OpenFOAM). Now, a larger recirculation zone can be seen at the bottom of the melt pool in the OpenFOAM results, where previously (cf. Figure 18) only a very thin layer at the bottom was moving in scanning direction. Contrarily, the recirculation slightly decreases in the FLOW-3D results, with slightly more backwards direction of flow now in the melt pool. Further, systematic tests at various equilibrium contact angles were conducted, and no equilibrium contact angle value could be found where both solvers agree better in terms of recirculation flow patterns.

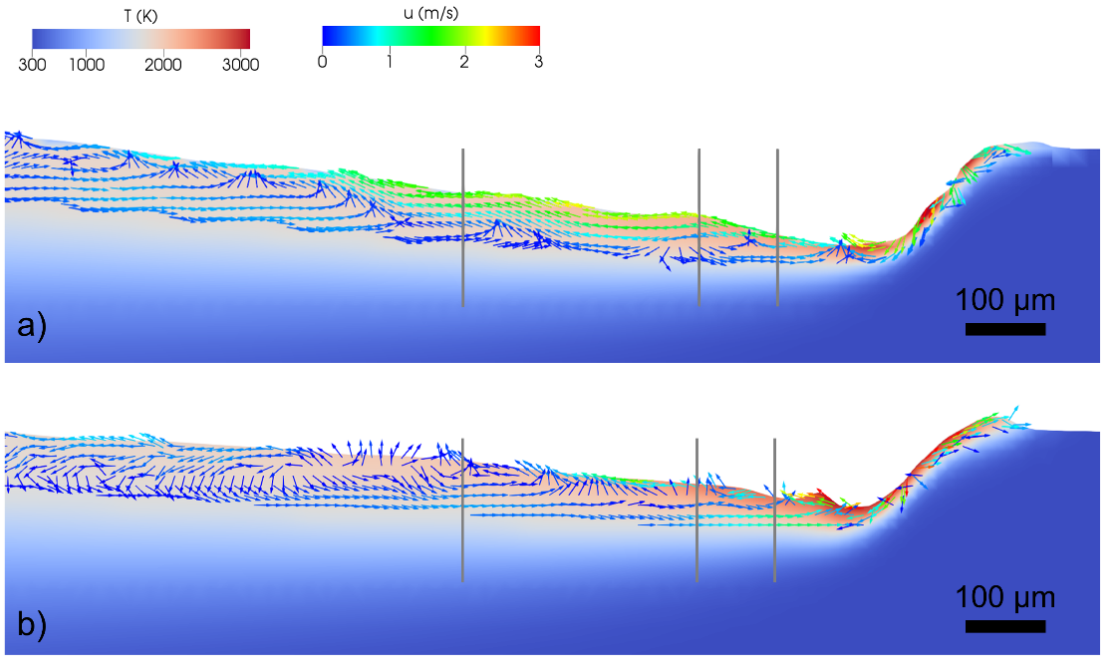

Figure 28: $P = 500$ W, including Marangoni forces, multiple reflections and Fresnel absorptivity for a contact angle of 22.5°: Comparison of melt velocity and temperature at longitudinal center plane (zy-plane). Top (a): FLOW-3D, bottom (b): OpenFOAM. Vertical grey lines denote locations of cross-sectional views shown in Figure 29.

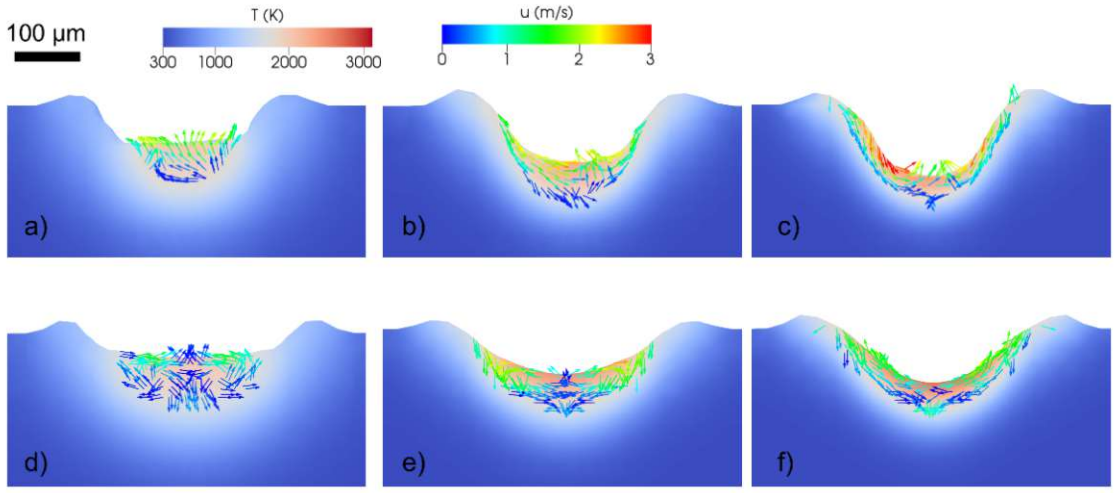

Figure 29: $P = 500$ W, including Marangoni forces, multiple reflections and Fresnel absorptivity for a contact angle of 22.5°: Comparison of melt velocity and temperature at transversal planes (xy-planes). Top: FLOW-3D at z-distances of a) 600 µm, b) 300 µm, c) 200 µm behind laser position, Bottom: OpenFOAM at z-distances of d) 600 µm, e) 300 µm, f) 200 µm behind laser position. Cf. vertical grey lines in Figure 28 for locations of these cross-sectional views.

Appendix D Pressure distribution throughout the vapour depression in the OpenFOAM laser track simulation

Figure 30 shows three exemplary longitudinal sections in the vicinity of the vapour depression as calculated by the OpenFOAM solver towards the end of the process ($t > 2.5$ ms) for the full complexity case ($P = 500$ W, including Marangoni forces, multiple reflections and Fresnel absorptivity). Regions fulfilling $\alpha_c > 0.5$ are coloured by temperature while remaining regions are coloured by pressure. Due to the vapour depression moving through space and changing in shape even in the pseudo-steady state, it is difficult to calculate a spatiotemporal average of pressure. To estimate of the average pressure present on the vapour side of the melt depression, we measured an average pressure value across five times, $t = 2.50$ ms, 2.51 ms, 2.52 ms, 2.53 ms and 2.54 ms. At each time, we calculated the volume-weighted average of pressure, p, over all cells lying within a sphere of 125 µm radius centred on the current optical axis of the laser beam at a point 50 µm below the workpiece surface, which had positive evaporative mass flux, $S_{Mv,e} > 0$, and also fulfilled $0.05 > \alpha_c > 0.5$. Only considering cells with $S_{Mv,e} > 0$, the vapour pressure is expected to be below the saturation pressure. Figure 31 shows an exemplary set of cells fulfilling these criteria for one of the evaluated times. In this manner, we arrived at a spatiotemporal average pressure of $p_{avg} = 1.253$ bar, with the spatial average taking minimum and maximum values over the analysed times of 1.175 bar and 1.407 bar, respectively. One quick way of obtaining an estimate of the saturation pressure in this region is via a spatiotemporal average of temperature, which is approx. 3274 K, corresponding to a saturation pressure, according to the Clausius-Clapeyron Equation, Eq. (9), of 1.789 bar. However, the relevance of the saturation pressure calculated from an average temperature value is questionable given the nonlinear relationship between temperature and saturation pressure.

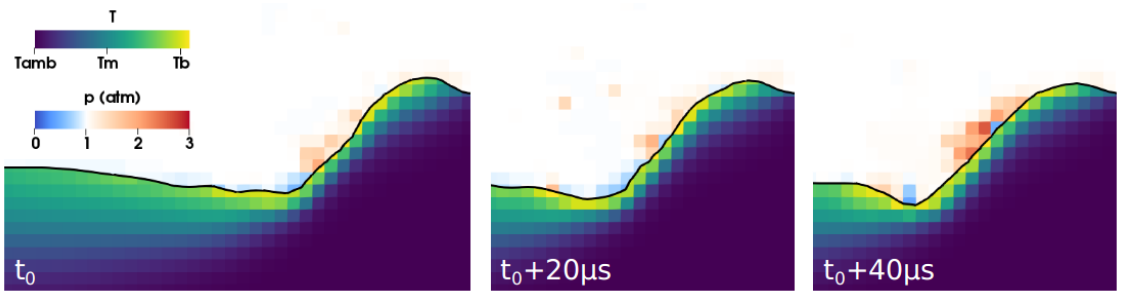

Figure 30: $P = 500$ W, including Marangoni forces, multiple reflections and Fresnel absorptivity (OpenFOAM simulation), showing exemplary (at $t > 2.5$ ms) longitudinal sections at vapour depression, with vapour coloured by pressure and condensed matter coloured by temperature.

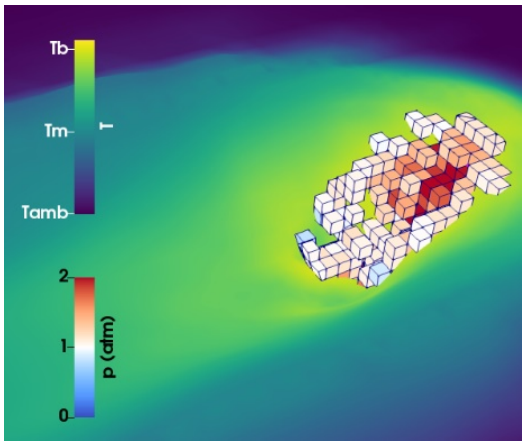

Figure 31: Exemplary view of cells falling within selection criteria for average pressure evaluation, coloured by pressure. Contour of condensed matter at $\alpha_c = 0.5$ is coloured by temperature.

Appendix E Effect of recoil factor in one-fluid model

Figure 32 shows the keyhole depth results obtained with FLOW-3D for the real-world case presented in Section 5 when the evaporative recoil factor value in Eq. (7) is varied. In this context, the standard value of 0.54 is regarded as 100 %. Interestingly, the 140 µm laser spot size simulation (Figure 32 (b)) is well matched to experiment if a recoil value of 30 % is chosen (i.e., an absolute value of 0.162). However, keyhole depth is strongly underestimated for the 95 µm spot size case with the same recoil factor (Figure 32 (a)). Generally, keyhole depth is more sensitive to recoil pressure for the larger (140 µm) laser spot. It is not possible to match both the 95 and 140 µm spot size simulations to experiment just by varying recoil pressure.
The transition between regimes for the 140 µm spot size is visible as a distinct acceleration in the rate at which the keyhole depth increases with time. This transition seems to be determined by geometry (rather than by time or energy accumulation) since it occurs at a depth of around 40 µm for all three FLOW-3D simulations in Figure 32 and also for the OpenFOAM simulation in Figure 22.

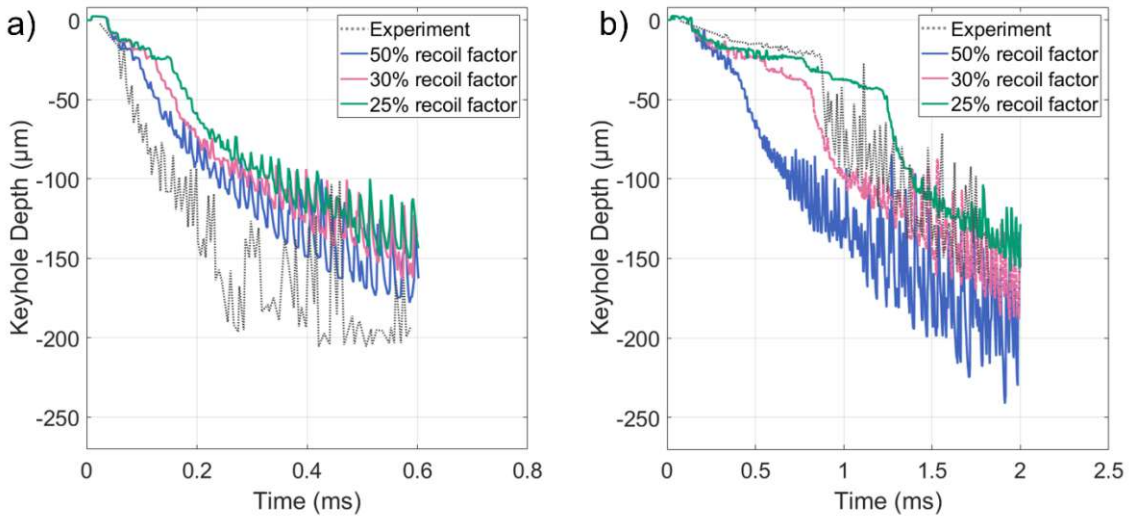

Figure 32: Comparison of FLOW-3D simulation results using different values for the evaporative recoil factor for (a): 95 µm, and (b): 140 µm spot size at $P = 156$ W (Case of 100 % recoil pressure was shown in Figure 22).

Appendix F Simulation parameters and material properties

The following tables contain the material properties, process parameters and simulation settings used for the test cases presented in the main body of the article, as referenced within the respective Sections.

Parameter		Value	Unit
Thermal conductivity	k	16.2	$W{\cdot}m^{-1}{\cdot}K^{-1}$
Density	ρ	7850	$kg{\cdot}m^{-3}$
Specific heat	c_p	483.5	$J{\cdot}kg^{-1}{\cdot}K^{-1}$
Latent heat of fusion	L	$2.4711{\cdot}10^5$	$J{\cdot}kg^{-1}$
$T_m - T_c$		200	K
$T_h - T_m$		200	K
Liquid Stefan number	St_L	0.3913	–
Solid Stefan number	St_S	0.3913	–

Table 6: Data for the Stefan verification case.

Parameter		Value	Unit
Liquid average depth		200	mm
Cavity width		1000	mm
Aspect ratio	A	0.2	–
Temperature at hot wall	T_h	60	°C
Temperature at cold wall	T_c	50	°C
Surface tension at T_r	σ_r	0.01	$N{\cdot}m^{-1}$

Thermal coefficient of surface tension	$\frac{\partial\sigma}{\partial T}$	$4.0{\cdot}10^{-5}$	$N{\cdot}m^{-1}{\cdot}K^{-1}$
Normalised capillary number	C_n	5.0	–
Contact angle	θ	90	°
Contact parameter	M	0.0	–

Table 7: Data for the Marangoni verification case.

Parameter		Value	Unit
Molar mass	M	$55.845{\cdot}10^{-3}$	$kg{\cdot}mol^{-1}$
Melting temperature	T_m	1710	K
Boiling temperature	T_b	3134	K
Latent heat of solidification	L_m	$247.11{\cdot}10^{3}$	$J{\cdot}kg^{-1}$
Latent heat of condensation	L_b	$6344.1{\cdot}10^{3}$	$J{\cdot}kg^{-1}$
Density (solid)	$\langle\rho_s\rangle$	7850	$kg{\cdot}m^{-3}$
Density (liquid)	$\langle\rho_l\rangle$	7850	$kg{\cdot}m^{-3}$
Density (vapour)	$\langle\rho_v\rangle$	*ideal gas law*	–
Specific heat capacity (solid)	$c_{p,s}$	483.5	$J{\cdot}kg^{-1}{\cdot}K^{-1}$
Specific heat capacity (liquid)	$c_{p,l}$	824.1	$J{\cdot}kg^{-1}{\cdot}K^{-1}$
Specific heat capacity (vapour)	$c_{p,v}$	477.0	$J{\cdot}kg^{-1}{\cdot}K^{-1}$
Thermal conductivity (solid)	k_s	16.2	$W{\cdot}m^{-1}{\cdot}K^{-1}$
Thermal conductivity (liquid)	k_l	27.0	$W{\cdot}m^{-1}{\cdot}K^{-1}$
Thermal conductivity (vapour)	k_v	0.10233	$W{\cdot}m^{-1}{\cdot}K^{-1}$
Surface energy (solid)	σ_s	0.5	$N{\cdot}m^{-1}$
Surface energy (liquid)	σ_l	1.8	$N{\cdot}m^{-1}$
Thermal coefficient of surface tension (liquid)	$\frac{\partial\sigma}{\partial T}$	$-5.0{\cdot}10^{-4}$	$N{\cdot}m^{-1}{\cdot}K^{-1}$
Surface energy (vapour)	σ_v	0	$N{\cdot}m^{-1}$
Kinematic viscosity (liquid)	ν_l	$6.91{\cdot}10^{-7}$	$m^2{\cdot}s^{-1}$
Kinematic viscosity (vapour)	ν_v	$1.48{\cdot}10^{-5}$	$m^2{\cdot}s^{-1}$
Refractive index (solid, liquid)	n_r	3.8	–
Extinction coeff. (solid, liquid)	κ_r	5.0	–

Table 8: Material properties of simplified stainless steel used in laser track comparison simulations.

Parameter		T(K)	Value	Unit
Molar mass	M		$46.77{\cdot}10^{-3}$	$kg{\cdot}mol^{-1}$
Liquidus temperature	T_l		1928	K
Solidus temperature	T_s		1878	K
Boiling temperature	T_b		3315	K
Latent heat of solidification	L_m		$2.90{\cdot}10^{5}$	$J{\cdot}kg^{-1}$
Latent heat of condensation	L_b		$9.82{\cdot}10^{6}$	$J{\cdot}kg^{-1}$
Density (solid)	$\langle\rho_s\rangle$		4457	$kg{\cdot}m^{-3}$
Density (liquid)	$\langle\rho_l\rangle$	1923	4100	$kg{\cdot}m^{-3}$
		2073	4025	$kg{\cdot}m^{-3}$
		2573	3800	$kg{\cdot}m^{-3}$
Density (vapour)	$\langle\rho_v\rangle$		*ideal gas law*	–
Specific heat capacity (solid)	$c_{p,s}$	293	580	$J{\cdot}kg^{-1}{\cdot}K^{-1}$

		873	668	$J \cdot kg^{-1} \cdot K^{-1}$
		1073	691	$J \cdot kg^{-1} \cdot K^{-1}$
		1278	643	$J \cdot kg^{-1} \cdot K^{-1}$
		1373	660	$J \cdot kg^{-1} \cdot K^{-1}$
		1923	759	$J \cdot kg^{-1} \cdot K^{-1}$
Specific heat capacity (liquid)	$c_{p,l}$		1126	$J \cdot kg^{-1} \cdot K^{-1}$
Specific heat capacity (vapour)	$c_{p,v}$	3631	732	$J \cdot kg^{-1} \cdot K^{-1}$
		4000	774	$J \cdot kg^{-1} \cdot K^{-1}$
		4800	853	$J \cdot kg^{-1} \cdot K^{-1}$
Thermal conductivity (solid)	k_s	430	5.957	$W \cdot m^{-1} \cdot K^{-1}$
		1270	17	$W \cdot m^{-1} \cdot K^{-1}$
		1383	19.87	$W \cdot m^{-1} \cdot K^{-1}$
		1888	27	$W \cdot m^{-1} \cdot K^{-1}$
Thermal conductivity (liquid)	k_l	1913	28.8	$W \cdot m^{-1} \cdot K^{-1}$
		2666	42.2	$W \cdot m^{-1} \cdot K^{-1}$
Thermal conductivity (vapour)	k_v	3315	0.1281	$W \cdot m^{-1} \cdot K^{-1}$
		5000	0.1588	$W \cdot m^{-1} \cdot K^{-1}$
Surface energy (solid)	σ_s	300	0.375	$N \cdot m^{-1}$
		1500	1.0	$N \cdot m^{-1}$
		1878	1.505	$N \cdot m^{-1}$
Surface energy (liquid)	σ_l	1928	1.505	$N \cdot m^{-1}$
		3315	1.1	$N \cdot m^{-1}$
Surface energy (vapour)	σ_v		0	$N \cdot m^{-1}$
Kinematic viscosity (liquid)	ν_l	1732	$3.9 \cdot 10^{-6}$	$m^2 \cdot s^{-1}$
		1931	$2.53 \cdot 10^{-6}$	$m^2 \cdot s^{-1}$
		2045	$2.14 \cdot 10^{-6}$	$m^2 \cdot s^{-1}$
Kinematic viscosity (vapour)	ν_v		*ideal gas law**	$m^2 \cdot s^{-1}$
Refractive index (solid)	$n_{r,s}$		3.86	–
Extinction coeff. (solid)	$\kappa_{r,s}$		6.1	–
Refractive index (liquid)	$n_{r,l}$	1901	4.01	–
		2603	4.08 –	
Extinction coeff. (liquid)	$\kappa_{r,l}$	1901	4.7	–
		2603	4.83	–

Table 9: Material properties of Ti6Al4V used in simulations. Temperature-dependent values are kept constant outside the specified range. *Using analytical viscosity model based on ideal gas law [64].

References

[1] Y. C. Shin, B. Wu, S. Lei, G. J. Cheng, and Y. Lawrence Yao. "Overview of Laser Applications in Manufacturing and Materials Processing in Recent Years". In: *Journal of Manufacturing Science and Engineering* 142, Oct. 2020, p. 110818. DOI: https://doi.org/10.1115/1.4048397.

[2] Y. Shu, D. Galles, O. A. Tertuliano, B. A. McWilliams, N. Yang, W. Cai, and A. J. Lew. "A critical look at the prediction of the temperature field around a

laser-induced melt pool on metallic substrates". In: *Scientific Reports* 11, 2021, p. 12224. DOI: https://doi.org/10.1038/s41598-021-91039-z.

[3] L. Wang, Y. Zhang, and W. Yan. "Evaporation Model for Keyhole Dynamics during Additive Manufacturing of Metal". In: *Physical Review Applied* 14, 2020, p. 064039. DOI: https://doi.org/10.1103/PhysRevApplied.14.064039.

[4] N. Much, M. Schreter-Fleischhacker, P. Munch, M. Kronbichler, W. A. Wall, and C. Meier. "Improved accuracy of continuum surface flux models for metal additive manufacturing melt pool simulations". In: *Adv. Model. and Simul. in Eng. Sci.* 11, 2024, p. 16. DOI: https://doi.org/10.1186/s40323-024-00270-6.

[5] J. Zhou, H. L. Tsia, and T. F. Lehnhoff. "Investigation of transport phenomena and defect formation in pulsed laser keyhole welding of zinc-coated steels". In: *Journal of Physics D: Applied Phyiscs* 39, 2006, pp. 5338–5355. DOI: https://doi.org/10.1088/0022-3727/39/24/036.

[6] M. Courtois, M. Carin, P. Le Masson, S. Gaied, and M. Balabane. "A new approach to compute multi-reflections of laser beam in a keyhole for heat transfer and fluid flow modelling in laser welding". In: *Journal of Physics D: Applied Phyiscs* 46, 2013, p. 505305. DOI: https://doi.org/10.1088/0022-3727/46/50/505305.

[7] S. Pang, W. Chen, and W. Wang. "A Quantitative Model of Keyhole Instability Induced Porosity in Laser Welding of Titanium Alloy". In: *Metall Mater Trans A* 45, 2014, pp. 2808–2818. DOI: https://doi.org/10.1007/s11661-014-2231-3.

[8] C. Körner, E. Attar, and P. Heinl. "Mesoscopic simulation of selective beam melting processes". In: *Journal of Materials Processing Technology* 211, 2011, pp. 978–987. DOI: https://doi.org/10.1016/j.jmatprotec.2010.12.016.

[9] M. Russell, A. Souto-Iglesias, and T. Zohdi. "Numerical simulation of Laser Fusion Additive Manufacturing processes using the SPH method". In: *Computer Methods in Applied Mechanics and Engineering* 341, 2018, pp. 163–187. DOI: https://doi.org/10.1016/j.cma.2018.06.033.

[10] T. Yu and J. Zhao. "Quantitative simulation of selective laser melting of metals enabled by new high-fidelity multiphase, multiphysics computational tool". In: *Computer Methods in Applied Mechanics and Engineering* 399, 2022, p. 115422. DOI: https://doi.org/10.1016/j.cma.2022.115422.

[11] L. Wang, Y. Zhang, and H. Y. Chia. "Mechanism of keyhole pore formation in metal additive manufacturing". In: *npj Comput Mater* 8, 2022. DOI: https://doi.org/10.1038/s41524-022-00699-6.

[12] M. Bayat, S. Mohanty, and J. H. Hattel. "Multiphysics modelling of lack-of-fusion voids formation and evolution in IN718 made by multi-track/multi-layer L-PBF". In: *International Journal of Heat and Mass Transfer* 139, 2019, pp. 95–114. DOI: https://doi.org/10.1016/j.ijheatmasstransfer.2019.05.003.

[13] W. Yan, Y. Qian, W. Ge, S. Lin, W. K. Liu, F. Lin, and G. J. Wagner. "Meso-scale modeling of multiple-layer fabrication process in Selective Electron Beam Melting: Inter-layer/track voids formation". In: *Materials & Design* 141, 2018, pp. 210–219. DOI: https://doi.org/10.1016/j.matdes.2017.12.031.

[14] Y. Lee and W. Zhang. "Modeling of heat transfer, fluid flow and solidification microstructure of nickel-base superalloy fabricated by laser powder bed fusion". In: *Additive Manufacturing* 12, 2016. Special Issue on Modeling & Simulation for Additive Manufacturing, pp. 178–188. DOI: https://doi.org/10.1016/j.addma.2016.05.003.

[15] P. S. Cook, A. Phua, C. H. Davies, and G. W. Delaney. "Modelling the influences of powder layer depth and particle morphology on powder bed fusion using a coupled DEM-CFD approach". In: *Powder Technology* 429, 2023, p. 118927. DOI: https://doi.org/10.1016/j.powtec.2023.118927.

[16] P. S. Cook and A. B. Murphy. "Simulation of melt pool behaviour during additive manufacturing: Underlying physics and progress". In: *Additive Manufacturing* 31, 2020, p. 100909. DOI: https://doi.org/10.1016/j.addma.2019.100909.

[17] J. A. Turner, J. Belak, N. Barton, M. Bement, N. Carlson, R. Carson, S. DeWitt, J.-L. Fattebert, N. Hodge, Z. Jibben, W. King, L. Levine, C. Newman, A. Plotkowski, B. Radhakrishnan, S. T. Reeve, M. Rolchigo, A. Sabau, S. Slattery, and B. Stump. "ExaAM: Metal additive manufacturing simulation at the fidelity of the microstructure". In: *The International Journal of High Performance Computing Applications* 36, 2022, pp. 13–39. DOI: https://doi.org/10.1177/10943420211042558.

[18] A. S. Sabau, L. Yuan, N. Raghavan, M. Bement, S. Simunovic, J. A. Turner, and V. K. Gupta. "Fluid dynamics effects on microstructure prediction in single-laser tracks for additive manufacturing of IN625". In: *Metallurgical and Materials Transactions B* 51, 2020, pp. 1263–1281. DOI: https://doi.org/10.1007/s11663-020-01808-w.

[19] G. Parivendhan, P. Cardiff, T. Flint, Ž. Tuković, M. Obeidi, D. Brabazon, and A. Ivanković. "A numerical study of processing parameters and their effect on the melt-track profile in Laser Powder Bed Fusion processes". In: *Additive Manufacturing* 67, 2023, p. 103482. DOI: https://doi.org/10.1016/j.addma.2023.103482.

[20] T. F. Flint, G. Parivendhan, A. Ivankovic, M. C. Smith, and P. Cardiff. "beamWeldFoam: Numerical simulation of high energy density fusion and vapourisation-inducing processes". In: *SoftwareX* 18, 2022, p. 101065. DOI: https://doi.org/10.1016/j.softx.2022.101065.

[21] T. F. Flint, J. D. Robson, G. Parivendhan, and P. Cardiff. "laserbeamFoam: Laser ray-tracing and thermally induced state transition simulation toolkit". In: *SoftwareX* 21, 2023, p. 101299. DOI: https://doi.org/10.1016/j.softx.2022.101299.

[22] T. F. Flint, J. D. Robson, P. Esmati, N. Grilli, G. Parivendhan, and P. Cardiff. "Version 2.0 — LaserbeamFoam: Laser ray-tracing and thermally induced state transition simulation toolkit". In: *SoftwareX* 25, 2024, p. 101612. DOI: https://doi.org/10.1016/j.softx.2023.101612.

[23] T. F. Flint, L. Scotti, H. C. Basoalto, and M. C. Smith. "A thermal fluid dynamics framework applied to multi-component substrates experiencing fusion and vaporisation state transitions". In: *Communications Physics* 3, 2020, p. 196. DOI: https://doi.org/10.1038/s42005-020-00462-7.

[24] M. Schreter-Fleischhacker, N. Much, P. Munch, M. Kronbichler, W. A. Wall, and C. Meier. "A consistent diffuse-interface finite element approach to rapid melt–vapor dynamics with application to metal additive manufacturing". In: *Computer Methods in Applied Mechanics and Engineering* 442, 2025, p. 117985. DOI: https://doi.org/10.1016/j.cma.2025.117985.

[25] S. Jabar, Q. Hayat, A. B. Barenji, G. Chianese, H. Kotadia, D. Ceglarek, and P. Franciosa. "Investigations of weld profiling and intermetallic formation in laser welding of steel-to-aluminium: a multi-physics CFD approach using beam shaping". In: *Procedia CIRP* 124, 2024, pp. 559–564. DOI: https://doi.org/10.1016/j.procir.2024.08.174.

[26] C. Zenz, M. Buttazzoni, T. Florian, K. E. Crespo Armijos, R. Gómez Vázquez, G. Liedl, and A. Otto. "A compressible multiphase Mass-of-Fluid model for the simulation of laser-based manufacturing processes". In: *Computers & Fluids* 268, 2024, p. 106109. DOI: https://doi.org/10.1016/j.compfluid.2023.106109.

[27] "Combining in situ synchrotron X-ray imaging and multiphysics simulation to reveal pore formation dynamics in laser welding of copper". In: *International Journal of Machine Tools and Manufacture* 204, 2025, p. 104224. DOI: https://doi.org/10.1016/j.ijmachtools.2024.104224.

[28] T. Flint, G. Parivendhan, M. Smith, A. Ivankovic, and P. Cardiff. "Numerical modelling approaches for simulating powder bed fusion processes". In: *16th OpenFOAM Workshop* (Dublin, Ireland, 2021). 2021.

[29] Y. A. Mayi, A. Queva, M. Dal, G. Guillemot, C. Metton, C. Moriconi, P. Peyre, and M. Bellet. "Multiphysics simulation of single pulse laser powder bed fusion: comparison of front capturing and front tracking methods". In: *International Journal of Numerical Methods for Heat & Fluid Flow* 32, Sept. 2021, pp. 2149–2176. DOI: https://doi.org/10.1108/HFF-04-2021-0282.

[30] A. Kidess, S. Kenjereš, B. W. Righolt, and C. R. Kleijn. "Marangoni driven turbulence in high energy surface melting processes". In: *International Journal of Thermal Sciences* 104, 2016, pp. 412–422. DOI: https://doi.org/10.1016/j.ijthermalsci.2016.01.015.

[31] V. Jacquier, J. Zollinger, P. Zeller, M. Dal, F. Schuster, H. Maskrot, and W. Pacquentin. "Melt Pool Turbulence Effects on the Interface between Dissimilar Materials Manufactured by Directed Energy Deposition with Laser and Powder". In: *Journal of Materials Engineering and Performance* 30, 2021, pp. 8810–8820. DOI: https://doi.org/10.1007/s11665-021-06279-x.

[32] M. Jamshidinia, F. Kong, and R. Kovacevic. "Temperature distribution and fluid flow modelling of electron beam melting (EBM)". In: *Proceedings of the ASME International Mechanical Engineering Congress & Exposition*. Houston, 2012, pp. 3089–3101.

[33] P. S. Cook and D. J. Ritchie. "Determining the laser absorptivity of Ti-6Al-4V during laser powder bed fusion by calibrated melt pool simulation". In: *Optics & Laser Technology* 162, 2023, p. 109247. DOI: https://doi.org/10.1016/j.optlastec.2023.109247.

[34] A. De and T. DebRoy. "A smart model to estimate effective thermal conductivity and viscosity in the weld pool". In: *Journal of Applied Physics* 95, May 2004, pp. 5230–5240. DOI: https://doi.org/10.1063/1.1695593.

[35] J. Shinjo, A. Kutsukake, H. Wakabayashi, K. Arakawa, A. Ogawara, H. Uchida, C. Panwisawas, and R. C. Reed. "In-process monitoring and direct simulation of Argon shielding gas and vapour dynamics to control laser-matter interaction in laser powder bed fusion additive manufacturing". In: *Additive Manufacturing* 80, 2024, p. 103953. DOI: https://doi.org/10.1016/j.addma.2023.103953.

[36] H. Chen, Y. Zhang, A. Giam, and W. Yan. "Experimental and computational study on thermal and fluid behaviours of powder layer during selective laser melting additive manufacturing". In: *Additive Manufacturing* 52, 2022, p. 102645. DOI: https://doi.org/10.1016/j.addma.2022.102645.

[37] H. Ki, J. Mazumder, and P. S. Mohanty. "Modeling of laser keyhole welding: Part I. mathematical modeling, numerical methodology, role of recoil pressure, multiple reflections, and free surface evolution". In: *Metall Mater Trans A* 33, 2002, pp. 1817–1830. DOI: https://doi.org/10.1007/s11661-002-0190-6.

[38] A. Queva, G. Guillemot, C. Moriconi, C. Metton, and M. Bellet. "Numerical study of the impact of vaporisation on melt pool dynamics in Laser Powder Bed Fusion - Application to IN718 and Ti–6Al–4V". In: *Additive Manufacturing* 35, 2020, p. 101249. DOI: https://doi.org/10.1016/j.addma.2020.101249.

[39] T. Yamamoto, Y. Okano, and S. Dost. "Validation of the S-CLSVOF method with the density-scaled balanced continuum surface force model in multiphase systems coupled with thermocapillary flows". In: *International Journal for Numerical Methods in Fluids* 83, 2017, pp. 223–244. DOI: https://doi.org/10.1002/fld.4267.

[40] T. Heeling, M. Cloots, and K. Wegener. "Melt pool simulation for the evaluation of process parameters in selective laser melting". In: *Additive Manufacturing* 14, 2017, pp. 116–125. DOI: https://doi.org/10.1016/j.addma.2017.02.003.

[41] J. Brackbill, D. Kothe, and C. Zemach. "A continuum method for modeling surface tension". In: *Journal of Computational Physics* 100, 1992, pp. 335–354. DOI: https://doi.org/10.1016/0021-9991(92)90240-Y.

[42] É. Ruiz-Gutiérrez, J. Hasslberger, M. Klein, K. Dalgarno, and N. Chakraborty. "Physically consistent modelling of surface tension forces in the Volume-of-Fluid method for three or more phases". In: *Journal of Computational Physics* 513, 2024, p. 113149. DOI: https://doi.org/10.1016/j.jcp.2024.113149.

[43] M. Ruths. “Surface Forces, Surface Tension, and Adhesion”. In: *Encyclopedia of Tribology*. Ed. by Q. J. Wang and Y.-W. Chung. Boston, MA: Springer US, 2013, pp. 3435–3443. ISBN: 978-0-387-92897-5. DOI: https://doi.org/10.1007/978-0-387-92897-5_463.

[44] V. Semak and A. Matsunawa. “The role of recoil pressure in energy balance during laser materials processing”. In: *Journal of Physics D: Applied Physics* 30, Sept. 1997, p. 2541. DOI: https://doi.org/10.1088/0022-3727/30/18/008.

[45] C. J. Knight. “Theoretical modeling of rapid surface vaporization with back-pressure”. In: *AIAA Journal* 17, 1979, pp. 519–523. DOI: https://doi.org/10.2514/6.1978-1220.

[46] J. A. Dantzig and M. Rappaz. *Solidification: -Revised & Expanded*. EPFL press, 2016. ISBN: 978-0-84938-238-3.

[47] C. Zenz, C. Durán, T. Florian, R. Bielak, and A. Otto. “Multiphysical simulation of hot cracking in Laser-Based Powder Bed Fusion”. In: *Procedia CIRP* 124, 2024, pp. 341–346. DOI: https://doi.org/10.1016/j.procir.2024.08.130.

[48] E. Beyer. *Schweißen mit Laser*. Springer: Berlin/Heidelberg, Germany, 1995. DOI: https://doi.org/10.1007/978-3-642-75759-4.

[49] S. Tatra, R. Gómez Vázquez, C. Stiglbrunner, and A. Otto. “Numerical Simulation of Laser Ablation with Short and Ultra-short Pulses for Metals and Semiconductors”. In: *Physics Procedia* 83, 2016, pp. 1339–1346. DOI: https://doi.org/10.1016/j.phpro.2016.08.141.

[50] H. G. Weller, G. Tabor, H. Jasak, and C. Fureby. “A tensorial approach to computational continuum mechanics using object-oriented techniques”. In: *Computers in Physics* 12, 1998, pp. 620–631. DOI: https://doi.org/10.1063/1.168744.

[51] T. Flint, T. Dutilleul, and W. Kyffin. “A fundamental investigation into the role of beam focal point, and beam divergence, on thermo-capillary stability and evolution in electron beam welding applications”. In: *International Journal of Heat and Mass Transfer* 212, 2023, p. 124262. DOI: https://doi.org/10.1016/j.ijheatmasstransfer.2023.124262.

[52] A. Otto, H. Koch, and R. Gómez Vázquez. “Multiphysical Simulation of Laser Material Processing”. In: *Physics Procedia* 39, 2012, pp. 843–852. DOI: https://doi.org/10.1016/j.phpro.2012.10.109.

[53] A. K. Sen and S. H. Davis. “Steady thermocapillary flows in two-dimensional slots”. In: *Journal of Fluid Mechanics* 121, 1982, pp. 163–186. DOI: https://doi.org/10.1017/S0022112082001840.

[54] Z. S. Saldi. “Marangoni driven free surface flows in liquid weld pools”. PhD thesis. Delft University of Technology, 2012.

[55] S. Pang, X. Chen, J. Zhou, X. Shao, and C. Wang. “3D transient multiphase model for keyhole, vapor plume, and weld pool dynamics in laser welding including the ambient pressure effect”. In: *Optics and Lasers in Engineering* 74, 2015, pp. 47–58. DOI: https://doi.org/10.1016/j.optlaseng.2015.05.003.

[56] A. Rai, M. Markl, and C. Körner. "A coupled Cellular Automaton–Lattice Boltzmann model for grain structure simulation during additive manufacturing". In: *Computational Materials Science* 124, 2016, pp. 37–48. DOI: https://doi.org/10.1016/j.commatsci.2016.07.005.

[57] B. Korneev, A. Zakirov, M. Bogdanova, S. Belousov, A. Perepelkina, I. Iskandarova, and B. Potapkin. "A numerical study of powder wetting influence on the morphology of laser powder bed fusion manufactured thin walls". In: *Additive Manufacturing* 74, 2023, p. 103705. DOI: https://doi.org/10.1016/j.addma.2023.103705.

[58] C. Meier, S. L. Fuchs, A. J. Hart, and W. A. Wall. "A novel smoothed particle hydrodynamics formulation for thermo-capillary phase change problems with focus on metal additive manufacturing melt pool modeling". In: *Computer Methods in Applied Mechanics and Engineering* 381, 2021, p. 113812. DOI: https://doi.org/10.1016/j.cma.2021.113812.

[59] R. Andreotta, L. Ladani, and W. Brindley. "Finite element simulation of laser additive melting and solidification of Inconel 718 with experimentally tested thermal properties". In: *Finite Elements in Analysis and Design* 135, 2017, pp. 36–43. DOI: https://doi.org/10.1016/j.finel.2017.07.002.

[60] Z. Hu, H. Zhu, C. Zhang, H. Zhang, T. Qi, and X. Zeng. "Contact angle evolution during selective laser melting". In: *Materials & Design* 139, 2018, pp. 304–313. DOI: https://doi.org/10.1016/j.matdes.2017.11.002.

[61] R. Cunningham, C. Zhao, N. Parab, C. Kantzos, J. Pauza, K. Fezzaa, T. Sun, and A. D. Rollett. "Keyhole threshold and morphology in laser melting revealed by ultrahigh-speed x-ray imaging". In: *Science* 363, 2019, pp. 849–852. DOI: https://doi.org/10.1126/science.aav4687.

[62] M. Schreter-Fleischhacker, N. Much, P. Munch, M. Kronbichler, W. A. Wall, and C. Meier. "A consistent diffuse-interface finite element approach to rapid melt–vapor dynamics with application to metal additive manufacturing". In: *Computer Methods in Applied Mechanics and Engineering* 442, 2025, p. 117985. DOI: https://doi.org/10.1016/j.cma.2025.117985.

[63] Y. A. Mayi, M. Dal, P. Peyre, M. Bellet, and R. Fabbro. "Physical mechanisms of conduction-to-keyhole transition in laser welding and additive manufacturing processes". In: *Optics & Laser Technology* 158, 2023, p. 108811. DOI: https://doi.org/10.1016/j.optlastec.2022.108811.

[64] R. B. Bird, W. E. Stewart, and E. N. Lightfoot. *Transport Phenomena*. New York: John Wiley & Sons, 1960.